THE UNIVERSITY OF CHICAGO

# CAVITY QUANTUM ELECTRODYNAMICS IN A TOPOLOGICAL PHOTONIC METAMATERIAL

A DISSERTATION SUBMITTED TO
THE FACULTY OF THE DIVISION OF THE PHYSICAL SCIENCES
IN CANDIDACY FOR THE DEGREE OF
DOCTOR OF PHILOSOPHY

DEPARTMENT OF PHYSICS

BY
MARGARET GORHAM PANETTA

CHICAGO, ILLINOIS
DECEMBER 2023

To Peg Gorham, the original hardware girl

*… Me tabula sacer*

*votiva paries indicat uvida*

*suspendisse potenti*

*vestimenta maris deo.*

Quintus Horatius Flaccus, *Odes* 1.5

# TABLE OF CONTENTS

# LIST OF FIGURES

# LIST OF TABLES

# ACKNOWLEDGMENTS

I am often met with some proportion of disbelief when I tell folks that I decided to study experimental physics because it's such a social, people-oriented activity; but that's the case! After a year spent studying history of science and a particularly reclusive quarter spent researching Victorian botanical texts in the dead-silent manuscripts reading room of the Cambridge University Library, during which my main form of workday communication was pantomime with the librarians, I decided that a research direction focused on teamwork, frequent ideas-sharing, and collaboration to build and run experiments was the path for me.

I contend that scientific work in academic institutions is substantially about community-building: we share stories (as my advisor Jon likes to argue), share time, resources, and craft knowledge, and make the core of our work communication in order to persuade. The specific artisanal practices (ask anyone who's spent time in a cleanroom) that we transmit and develop are built through mentorship. And the infrastructure that supports us, both physically and institutionally, relies on community connection and political will.

Acknowledging the people who formed my community during this PhD is then not just about their impact on me and my personal experience, but is part of the substance of this thesis and is not separable from the results. I would like to thank:

**My advisors:** Dave Schuster and Jon Simon, for their support of me and this project through the pandemic and afterward. Dave for his infectious enthusiasm for ideas, the limitless resources he provides to students trying to reach their goals, and the warm lab community he's helped to foster. Jon for the attention he pays to teaching the method of doing things, the time he puts into working with students, and the expectation he sets for, and belief he holds regarding, his students' substantial growth and change.

**Members of the Schuster lab:** Gabrielle Roberts for navigating this PhD trajectory alongside me physically as an officemate, intellectually on the quantum simulation team, and emotionally as a friend. Brendan Saxberg for his contributions in the quantum simulation team and his willingness to share wild ideas at any time. Andrei Vrajitoarea for his cryptic sense of humor, the love of scientific inquiry that he carries into all his work, and his dedication to helping this thesis project (and me) to launch through ups and downs. Fang Zhao for her fascinating office conversation, her great taste in takeout orders, and the mentorship she provided me in nanofabrication.

Clai Owens, for his gentle and engaging mentoring of me when I inherited his experiment with only a few months of overlap – his approach to getting experiments done and testing things quickly was amazing to behold. Andrew Oriani, for his provision of a flow of subtleties regarding experiment and technical work to me and the lab at large. Srivatsan Chakram for his enthusiastic encouragement of me when I was a young student. Alex Ruichao Ma for his support in finishing the first paper and for his interest in thinking deeply about how to craft a lab environment. Ziqian Li and Tanay Roy for their generosity in sharing time, experimental support, and ideas as officemates. Kevin He for helping with this project's 3D qubit fabrication during the pandemic-era nanofabrication facility restrictions. Sasha Anferov for supplying the rhinestone stickers necessary to properly operate this project's room-temperature apparatus, and also microwave physics advice.

BlueFors 1 team (Brennan Dizdar, Chris Wang, Connie Miao, and Andrei Vrajitoarea) for their teamwork in retrofitting the dilution refrigerator to host a particularly convoluted array of tubes and cables, and for navigating the rapid cycling and helium leak debacles with a spirit of persistence and collaboration. Brennan Dizdar for helping me grow as a technician and collaborator by so freely discussing his scientific thoughts, opinions, and concerns. Chris Wang for his scientific support, his emotional support, and the rich perspectives he brought on working with quantum circuits. Connie Miao for applying her remarkable skills at jumping into new problems, for her dedication to working only in dark mode, and for sending donuts. Chunyang Ding for the enthusiasm for organization and community he brought to the lab. Brenda Thomas for her logistical support, her bravery in sending faxes abroad, and her humorous yet welcoming spirit. Thanks also to the rest of the lab!

**Members of the Simon lab:**

Aziza Suleymanzade for blazing a trail in the lab and for the substance with which she values mentorship and paying it forward. Claire Baum for her enthusiastic leadership presence and the example she set in finding her passion. Lavanya Taneja for her thoughtful and deep opinions, Chuan Yin for her pointed and funny opinions, and both for their work to shape the lab. Lukas Palm for his companionship in last-minute writing of DAMOP 2023 talks just after the labs' move. Thanks also to the rest of the lab!

**My UChicago community:**

My roommate Jonathan Colen for his horrible ideas and for agreeing not to install a SpongeBob-themed shower curtain in our apartment. Jon and his wife Chloe Downs for their companionship and pancakes during the deep pandemic. Alexander McDonald and Gabrielle Roberts for their co-leadership of Forget The Year 2019. Pratiti Deb for pushing me to enrich my view of how our work fits into society and for her stream of extremely niche professional gossip. Leaders and members of the Graduate Recruitment Initiative Team, in particular Jake Higgins who was a mentor and example to me, and the other co-directors of GRIT in my year: Jessy Morgan, Jimmy Elias, and Ross Mansouri-Rad.

**My family:** Patti Gorham for her lifelong example of how to balance career achievement with personal priorities, and her support of all my niche, enthusiastic ideas and phases. Ed Panetta for the even-keeled sense of balance he attempts to teach me, his unending toolbox of very specific professional advice, and the example he set in making the core of his academic career about building community and uplifting people. Eli Panetta for being on this journey of young adulthood with me.

Special mention should go to Gabrielle Roberts' family, Susan Dunn and Eric Dunn, who graciously hosted me in their guest house so that I could be near the Stanford lab while I was completing this thesis, completing a paper, and working on finding a job.

# ABSTRACT

Cavity quantum electrodynamics, which explores strong light-matter interaction at the single-photon level, has provided a foundation for work to study, manipulate, and build systems managing quantum states. A parallel site of richness has been the study of topology in condensed matter physics; beyond its intrinsic value, the robustness to disorder afforded by topological structure, sometimes generated via a time-reversal-symmetry-breaking gauge field as in the case of the quantum Hall effect, has become of interest as a route to protection of quantum excitations.

In this thesis, we mix these two regimes, exploring cavity quantum electrodynamics in a topological metamaterial which breaks time-reversal symmetry for microwave photons by realizing a synthetic gauge field 'felt' by these photons. We strongly couple the edge of this quarter-flux Harper-Hofstadter lattice, a 2D array of coupled superconducting cavity resonators, to a single transmon qubit, demonstrating Rabi oscillations between the excited transmon and each individual mode of the topological band structure and profiling the multimode Lamb shift on the qubit from the forest of the synthetic vacuum.

Then, inspired by recent efforts to achieve chiral emission and transport of photons for use in quantum information science, we introduce a second transmon qubit to another site along the lattice edge and use this to detect a single photon confined to propagate in the chiral edge of this topological photonic bulk. This demonstration of non-reciprocal transport between quantum emitters coupled to an engineered chiral channel offers opportunities to use this platform to build and probe entangled states of light which gain structure from the system topology, and is a step along the path to exploring topological quantum matter.

# CHAPTER 1

# INTRODUCTION

## 1.1 Motivation: topological photonics

### *1.1.1 Why topology?*

A hallmark of topological order in matter is the global protection of system states which are made robust to small, smooth perturbation and local disorder. Of particular interest to this thesis is the expectation that when one supplies an edge to an insulator characterized by a nonzero topological invariant (the Chern number), the boundary between that topological system and vacuum will give rise to directional, conducting edge states engendered and protected by the structure of the topological bulk.

An excitation propagating in one of these edge channels set up at a boundary may encounter disorder in the form of barriers to tunneling like contortions in the edge or distortions in the energies of materials lattice sites. But because it requires a substantial modification to the energy-momentum landscape of the bulk material, closing the gap between bulk insulating bands in which this edge state lives, to disrupt the system's topological invariant (see Chapter 3), small alterations that register as smooth perturbations to the Hamiltonian will leave the system topology undamaged [72], preserving directional conduction against local imperfection. Topologically-protected directional conduction arises not just in quantum matter, but in classical systems hosting wave physics: topological order stemming from the Coriolis force has been shown to produce directional currents in the Earth's atmosphere and ocean [207], and lattice-like fluid stratification in the oceans is theorized to support bulk waves and surface states that can be described with topological band theory [63].

The characteristic protection against backscatter – protection against the halting or redirection of transport by a barrier to tunneling – makes topological systems attractive to researchers seeking to engineer, in the messy context of experiment, platforms which control and probe the dynamics of materials states. Such insulation against local disorder is of particular interest to those seeking to leverage this control for use in quantum information science; when trying to manipulate, move around, and probe quantum states subject to decoherence and decay, it is valuable to to be able to draw on the globally-rooted protection afforded by topological structure [131].

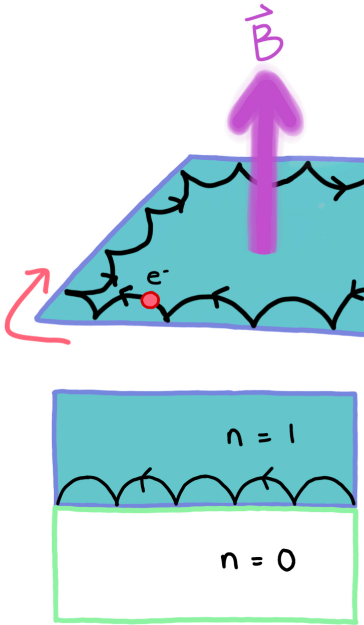

Figure 1.1: **Conducting edge of a topological bulk.** At **top**, a magnetic flux applied through a conducting plane causes an electron bouncing off the boundary to be redirected by the Lorentz force and transported chirally along the system edge. Even if there exist barriers in the edge, this overall transport can be maintained by a strong flux. At **bottom**, a generic boundary between such a quantum Hall regime and one with a different topological invariant $n$ supports a chiral edge mode. Panel adapted from Hasan and Kane [72].

As the Hilbert space of a quantum-mechanical system with $N$ two-level (spin-$\frac{1}{2}$) elements scales as $2^N$, storing the details of a macroscopic quantum state scales exponentially with system size, putting full representations of large entangled quantum materials states out of the range of classical tractability. The superposition and entanglement attainable across a system of many quantum bits (qubits) [70] provide a powerful opportunity, in combination with good design choices, to simulate such large entangled systems and to leverage quantum states as computational resources [154]. In quantum computing, where error rates are high compared to classical computing, the imperative to protect quantum states is core to current and future capacities. Gottesman [64] explains that it is a goal of the field to achieve fault-tolerance in quantum computing, a way of encoding states that allows all aspects of a computation (state preparation, gates between quantum bits, and measurement) to persist in the face of local error.

A branch of work sees a route to fault-tolerant quantum computing by leveraging the long-range structure inherent to topological order [39] to encode quantum bits in a way that brings about resistance to local errors. As an example, Raussendorf [159] argues that 3D cluster states, states of multidimensionally entangled photonic qubits, manipulated in a way that incorporates topology, are sufficient as a substrate for universal fault-tolerant quantum computation. Nayak et al. [131] review the approach debuted by Kitaev [86] to realize fault-tolerant quantum computation in a two-dimensional system hosting topology: generating a topological Hamiltonian in a 2D operator-space lattice and performing operations by moving its excitations, quasiparticles called non-Abelian anyons which are structured by the long-range topological order, around each other renders the logical states less-sensitive to local-qubit decoherence and decay. This approach, like spin-based magnetic information storage in classical computing, is “fault tolerant by its physical nature” [86].

A set of recent landmark results from two quantum computing firms demonstrated computational operations performed by exchange of non-Abelian anyons. These are a genre of quasiparticles which are predicted to be present in fractional quantum Hall systems and which obtain their fractional statistics from the interplay of many-body interactions and the topology that results, in ‘real’ systems, from the application of a gauge field. Both groups [3, 77] generate non-Abelian anyonic states in operator-space lattices built from arrays of physical qubits, and perform a set of operations to ‘braid’ these quasiparticles around each other, generating an observable which reflects the phase accumulated during the braiding operation. Google then uses a set of non-Abelian anyons to generate three logical qubits, which it entangles via a braiding operation to realize a Greenberger-Horne-Zeilinger state [3]. Both groups argue, as laid out above, that non-Abelian topological order might provide a route to fault-tolerant quantum communication, as the globally-encoded states used for operations are undisturbed by local perturbations associated with individual physical qubits.

Note that, while these applications of system topology to error resistance in quantum computing are a major motivation for the study of topology in the quantum information context, the topological metamaterial detailed in this thesis achieves a *different* sort of protection (from local disorder's impact on dynamics) than the sort (protection from local errors and decay, as quantum states are broadly encoded across a topological space) afforded by the above two approaches to fault-tolerant topological quantum computing.

Beyond its application to protection of quantum states for computing, topological order may be valuable in systems where a state needs both to be protected and to go somewhere fast for a reason, as in the case of quantum communication [85, 42, 133]. The option to flexibly engineer a topological system to shape the form and direction of state dynamics [140], and even alter that topological system on-the-go to direct the flow of light [213], is a powerful tool in the modern paradigm of work in quantum information science that seeks to design and control systems as a route to understanding [211]. In this thesis we realize one such system which leverages engineered topology to shape, speed, and protect against disorder the dynamics of photons. Excitations propagating in the conducting edge channel of our two-dimensional topological lattice are afforded a steep dispersion (speed of propagating light in a direction) by the system's topological Hamiltonian and would need to meet with disorder close to the size of the band gap [37] to cease their edge-propagation.

Our system also allows photons to be interfaced with photon-number-sensitive oscillators, here superconducting quantum bits, to explore the dynamics of topologically structured quantum light. Such investigation of topological structure in quantum systems is further motivated in Section 1.2.2. Introducting further nonlinearity, in the form of the photon-number-sensitive oscillators, would open future avenues to exploring the combination of topology and quantum many-body interactions which underpins the fractional quantum Hall effect. With a system modeling this phenomenon (see Section 1.2.1), we might ask questions about how state localization, thermalization, and transport occur in a system afforded global structure by its topology. How, in this complicated case, can we connect the microscopic physics of interacting quantum particles with a very distinctive macroscopic observable?

The intellectual richness of quantum many-body physics has served as a historical anchor for the discipline of condensed matter physics. Some industrial ‘solid state’ physicists practicing in the Cold War US leveraged this richness to re-describe their work as ‘condensed matter’ physics, framing it as ‘pure’ enough of an activity to remain an academic pursuit and shaping their scientific discipline in the process [114, 115]. Topological, and topological many-body, phenomena in materials continue to hold an influential place in condensed matter, photonic, and atomic physics; the response of bulk material properties like the quantized plateaus of conductivity in the quantum Hall effect to disorder [189], and the depth of interest afforded by the interplay of topology and quantum many-body interactions in the fractional quantum Hall effect [196, 185], remain generators of interest for today’s research.

### *1.1.2 Why photonics?*

Fabry-Pérot cavities, which can be understood as houses of mirrors with partially transmitting walls [186], are by definition good photon holders, or at least better photon holders than their surrounding non-resonator terrain. Photons confined to Fabry-Pérot cavities can be largely shielded from the environment, maintained within the cavity for extended lifetimes relative to other system dynamics or leaked out with a specific rate or energy. This fine control of photons’ environments – the rate at which they decay and leak or jump between neighboring photon holders – provides a playground to engineer photons’ preservation, dissipation specifics, and band structure and density of states.

Restricted to a small volume, cavity-confined photons see their densities of states inflated so high that it is possible to attain dramatically enhanced light-matter interaction by placing an atom within the cavity. This physics is the core of cavity quantum electrodynamics. Rather than working with actual atoms, in this thesis we realize this interaction using transmon qubits, superconducting circuits which are macroscopically ‘quantum’. These superconducting qubits are quantum anharmonic oscillators that act like artificial atoms and achieve strong light-matter interaction [175] via their circuit elements which couple capacitively to the cavity mode field landscape.

In purely photonic systems, arrays of connected cavities localizing photons can be engineered generally to shape the dispersion (speed and direction) of propagating light, enabling researchers to construct localized [84, 35] and traveling [66, 13, 55] states of light with the frequencies and spatial profiles they need. In some cases, it is possible to exploit the tight confinement of light for spin-momentum locking, imparting light with an effective sort of angular momentum in its polarization [102]. Arrays of weakly connected photon-holders afford a photon effective mass and can thus be used to construct a Hamiltonian for a propagating single photon which is a convenient analog of a particle hopping in some material, following the tight-binding model (see Section 2.2) in which we treat nuclei as static and electrons as free to hop between potential wells [199].

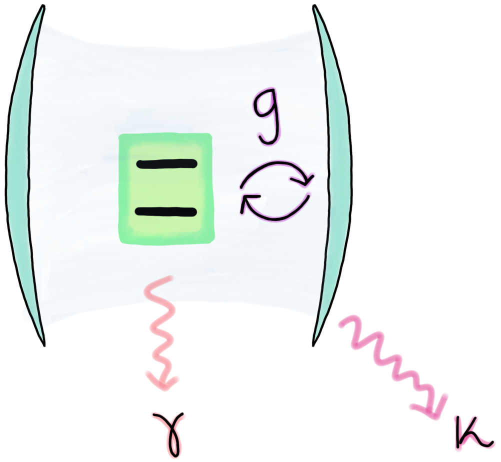

Figure 1.2: **Two-level emitter coupled to photon in Fabry-Pérot cavity.** In this archetypal model of cavity quantum electrodynamics [70, 174, 186], a Fabry-Pérot cavity (blue walls) traps photons (pale blue) and supports coherent interactions between these photons and a two-level quantum emitter (green) with rate $g$. Photons decay from the cavity at rate $\kappa$, and from the emitter at rate $\gamma$.

Such flexible, controllable photonic systems are exciting on their own; a rich range of work [103, 140, 155], detailed in Chapter 3, has sought to introduce topology to photonic systems via interventions in both physical and synthetic dimensions. Being able to cause photons to move in a bespoke way with engineerable access to band structure and band gaps has intrinsic value across the field of optics. But adding sufficiently strong nonlinearity to a photonic system, through strongly coupling in an atom or artificial atom, also opens access to studying interactions between photons, which natively do not 'feel' each others' presence.

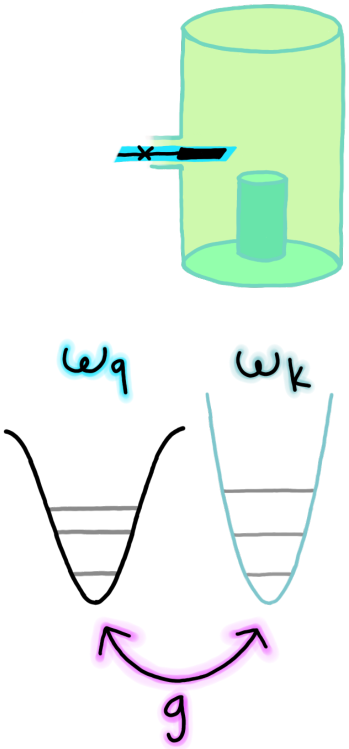

Figure 1.3: **Transmon qubit coupled to superconducting cavity resonator.** At **bottom**, we schematize the anharmonic potential of the nonlinear transmon and the resonator's bare harmonic potential, with some specific transition coupled at rate $g$.

Coupling a photon-holder to another oscillator (see Figure 1.3) allows energy to pass between the two, setting up a new set of system eigenstates that are hybrid mixtures of both components [174]. If a harmonic oscillator is coupled to a nonlinear one, the formerly linear photonic cavity becomes mildly nonlinear, as it inherits a bit of anharmonicity through its coupling to the nonlinear oscillator (see Chapter 2). With strong enough coupling, this means that photons populating the cavity no longer see a 'bosonic ladder' of evenly-spaced quantum harmonic oscillator energy states – the spacing between each set of energy levels becomes idiosyncratic, so a photon incident upon the cavity will 'know' if another photon is already present, depending on whether its resonant transition is available to excite. This 'blockade' effect [20, 35] gives rise to effective photon-photon interactions.

Combining the creative playground of photonic platforms with nonlinearity, introduced through either (1) coupling-in of nonlinear oscillators at specific locations or (2) use of an intrinsically nonlinear material as part of the photonic structure, allows us to shape and make use of this oscillator hybridization. Following option (1) can provide a route to explore light-matter interaction in a controllable landscape more dynamically interesting than a single cavity. The burgeoning subdiscipline of waveguide quantum electrodynamics (waveguide QED), introduced further in Section 1.2.2 and Xueyue Zhang's PhD thesis [211], does just this, exploring the physics of nonlinear emitters interacting through, or passing photonic wavepackets along, continuum waveguides and engineered photonic metamaterials [120, 101, 79]. In this thesis, 'quantum emitter' generically describes a two-level quantum system or quantum anharmonic oscillator, such as a transmon qubit, in which a distinctive level transition may be isolated, supplying a site of absorption and emission of a single photon. Proposals in waveguide QED argue that strongly coupling many quantum emitters to a waveguide might offer a chance to realize collective phenomena like many-body localized phases [54] and interaction-induced topology [152]. Experiments in waveguide QED have generated chiral scattering from emitters [120] and emitter pairs coupled to waveguides [106]. Work in this area with superconducting circuits seeks to develop control of traveling photons using strongly-coupled single-photon-sensitive nonlinear emitters [91, 10, 25, 92], or to use engineered waveguides to mediate emitter-emitter interactions [84, 212], directions of interest as quantum information systems scale up in size and towards communication between modules.

Option (2), building photonic systems from intrinsically nonlinear materials, can be limited by the generally weak nonlinearity available in optical photonic materials, and is particularly relevant for work combining topological photonics with gain and loss [87, 136, 155]. A recent thread of work realizes lasing in edge modes of synthetic topological insulators [11, 12], introducing nonlinearity via semiconductor metamaterials and contending that topology can enhance lasing properties. Another thread of work seeks to profile the combination of topology and non-Hermitian physics through pairing drives and engineered losses [136, 155].

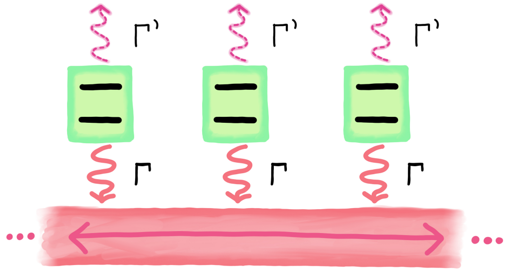

Figure 1.4: **Paradigm of multi-emitter waveguide quantum electrodynamics.** Two-level systems emit to a waveguide at rate $\Gamma$ and elsewhere at rate $\Gamma'$. The Purcell factor, $\Gamma/\Gamma'$, describes emitter-waveguide coupling strength. Adapted from [211].

The potential of cavities and photonic systems to intensify light-matter interaction, allowing us to profile quantum light inhabiting engineered landscapes, is powerful for studying the generation and transport of quantum states and the waveguide-assisted emitter-emitter interactions valuable for quantum networking [211]. In this thesis, we contribute to this line of work, connecting a set of quantum emitters to a few-mode channel to probe a regime intermediate between coupling an emitter to some continuum waveguide or near-continuum photonic crystal (the standard in waveguide quantum electrodynamics) and coupling it to a single-mode cavity or few-mode landscape without long-distance dispersion.

The same strong light-matter interaction in a system designed from the ground up is also powerful for modeling materials. Combining photon-photon interactions with bandstructure engineering opens the possibility of constructing synthetic materials, incorporating many-body interactions, out of light [157, 31, 32]. Using techniques from photonics to isolate and prolong the lifetimes of quantum states, and using techniques from cavity or circuit quantum electrodynamics to enable interactions of quantum-mechanical excitations, can allow us to prepare and measure quantum many-body dynamics in growing sizes of systems, and perhaps eventually to probe the boundary between quantum systems and the classical ones which lack entanglement [70].

## 1.2 Motivation: circuit quantum electrodynamics

### *1.2.1 Circuits for analog quantum simulation*

Research in analog quantum simulation seeks to build, from the ground up, systems which emulate the expected Hamiltonians of quantum materials. This approach stands in contrast to digital quantum simulation, in which a target Hamiltonian is Trotterized (time evolution under it is cumulatively executed via gates representing short-time chunks under split-apart Hamiltonians) and the target dynamics is simulated rather than emulated. As dynamics and observables in analog quantum simulation remain tangible even in the presence of currently realistic quantum errors [43], it is not necessary to await the advent of a fault-tolerant digital quantum computer in order to gain a “practical quantum advantage” [47] in using analog quantum simulation to study problems in quantum many-body physics. This statement especially applies to out-of-equilibrium dynamics and thermalization of many-body systems in two dimensions, which are intractable to classical methods [65].

Taking advantage of the power of interacting quantum bits to contend with a Hilbert space that rapidly balloons with system size, work in the discipline of analog quantum simulation spins off the paradigm of isolating, controlling, and measuring single quantum particles and states developed in quantum information science and uses these techniques to find the ground states of many-particle quantum systems and measure out-of-equilibrium system dynamics [43]. Work in quantum simulation is presently moving past methods development and recapitulation of understood physics and towards drawing novel connections between the microscopic mechanisms underlying quantum materials physics and the observed macroscopic phenomena of function.

A recent analog quantum simulation experiment pushed past the limits of empiricism with ‘real’ matter and made first observation of a new many-body phenomenon, quantum many-body scars [177, 18], in a 51-element Ising spin model realized with cold atoms which were excited to interact in their Rydberg states. Here, after state preparation and a quench of the system to resonance, some starting many-body states experienced revivals at later times, realizing an unexpected oscillation in system ordering, while the rest thermalized ergodically without revival as might be expected.

Superconducting circuits and resonators provide great resources with which to approach analog quantum simulation because of the long photon lifetimes, particularly strong light-matter coupling strength, and flexibility of design and engineering available with these fabricated systems. Circuit platforms also provide convenient options to engage engineered dissipation or dissipative stabilization of steady states of light [74, 82, 96, 110], as it is relatively straightforward to couple in another antenna, connect the system with a lossy resonator, or just supply another drive to pump the system to a target state. The tools of engineered dissipation, dissipative stabilization, and reservoir engineering are a particularly powerful advantage of modeling materials with circuits.

A range of analog quantum simulation platforms realized in superconducting circuits explore how to generate and probe quantum fluid states of computationally tractable models [172, 168, 83], or move towards regimes of engineered long-range couplings [212] which might support simulation of systems that look quite different from the circuit array initially visible [211]. Recent work implemented both with circuits [198] and later with trapped ions [191] has also pushed to model a real-world-relevant chemical reaction, simulating quantum dynamics important to light-driven processes in photosynthesis and vision.

The set of experiments detailed in this thesis do not approach the limit of analog quantum simulation of interacting materials; our topological photonic metamaterial realizes the Hamiltonian of a single noninteracting electron (no Pauli exclusion here!) hopping in the lattice of a material. To approach the limit of modeling interactions between particles, we would need to include nonlinearity at sites throughout the metamaterial, emulating electron-electron interactions with the photon-photon interactions that our experimental system is designed to allow. Instead, we introduce several localized sites of nonlinearity, and explore the quantum optics of specific quantum emitters coupled to a topological band structure.

### *1.2.2 Circuits + topological photonics for chiral quantum optics*

The strong coupling rates attainable between superconducting circuits and superconducting transmission lines or resonators [174] are standout among light-matter-interaction platforms and offer a significant advantage to those (like us, here) seeking to employ superconducting qubits as sources of nonlinearity in topological photonic metamaterials. Other emitters coupled to topological photonic platforms, even if they reach above the strong-coupling threshold of Purcell factor $\Gamma/\Gamma'$ (see Figure 1.4) for Purcell enhancement of emission from a nonlinearity coupled to a resonator [14], do not currently display the easy access to coherent emitter-cavity interactions needed to spur and probe dynamics.

In this thesis, we strongly couple two superconducting qubits to a topological photonic metamaterial and access coherent Rabi oscillations between each nonlinearity and this resonator array. Our metamaterial is a 25-site square lattice of coupled cavity resonators which realizes a synthetic magnetic field ‘felt’ by the microwave photons propagating within it. Coupling qubits to this 25-eigenmode system allows us to probe the boundary between the classic single-mode cavity quantum electrodynamics (QED) paradigm [70] and the classic paradigm of waveguide QED, in which a quantum bit, or set of quantum bits, couple(s) to some photonic mode continuum. Past work combining superconducting qubits with a topological photonic crystal [84] has been done in one dimension; by moving to a two-dimensional $5 \times 5$ system, although we are limited to 25 eigenmodes, we also gain access to conducting chiral edge channels that support multi-round-trip wavepacket propagation rather than the 1D topological edge states which show an exponential falloff of amplitude with distance from the coupling site [194]. An initially apparent use of such channels might be to use them for topologically robust state transfer [209, 50] in some quantum network. While we do not work with attention towards the scalability needed for networking, we do explore edge channel transport here as a topic itself of interest in a chiral quantum optics platform.

There exists an incentive for those broadly interested in networking between distant sites of quantum state preparation and measurement to use the strong coupling attainable in circuit QED to attach multiple quantum emitters to some channel for transmission. This channel might be a transmission line, waveguide, or photonic system with a sloped dispersion which sets up a group velocity that permits the use of transmissible, malleable-in-envelope photonic wavepackets to move quantum information around between quantum network nodes [85, 42]. Since the platform used in this thesis is not extensively scalable due to its size, and involves substantial decay-based losses due to the permanent magnetic field involved, we steer away from such a networking-based direction when motivating our work.

Significant work has been done to achieve photonic state transmission between superconducting quantum bits, first to show coherent interaction of superconducting qubits coupled to the same transmission line [193], and then to deterministically transfer single photons between qubits coupled via a multimode landscape [100] and use superconducting circuits to prepare, launch, and efficiently capture 'flying' or 'itinerant' photons, i.e. single- or multi-photon propagating wavepackets employed to transmit quantum information, in bidirectional transmission lines [129, 91, 30, 10, 25, 167].

A breadth of research is developing a toolbox for, in particular, *directional* coupling between superconducting qubits and waveguides. In contrast to work at optical wavelengths which largely relies on spin-momentum locking of confined light [102] to generate chiral emitter-waveguide coupling, these experimental interventions with superconducting qubits at microwave frequencies lean on interference effects between emission points or couplings to generate chiral scattering [165] and emission [80, 81, 79] from these qubits to intrinsically bidirectional landscapes for photonic propagation. This work is chiral quantum optics in the sense that it is quantum optics with chiral emission.

We reverse the above paradigm, working in chiral quantum optics by spurring *a priori* directionally-unrestricted emission from superconducting qubits to a channel that is itself chirally structured. Coupling quantum emitters to the chiral edge of a topological bulk can help us to see the connections between chiral structure of emitter-emitter interaction and long-range entanglement, which can be understood as synonymous with topological order [39]. Already some work has been done in topological photonics to propose and show topological protection of correlated states of light propagating in the chiral edges of topological photonic setups [123, 22, 200]. Regardless of whether the waveguide or the emission is chiral, though, systems of multiple quantum emitters interacting through a directional channel (chiral waveguide QED) are of interest for those invested in studying nonlocal entanglement between multiple quantum bits [102].

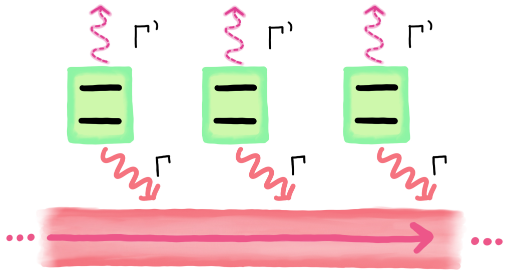

Figure 1.5: **Paradigm of multi-emitter chiral waveguide quantum electrodynamics.** We picture two-level systems emitting at rate Γ to a chiral waveguide and $\Gamma'$ elsewhere. In this thesis, our transmon qubits do not emit to a mode continuum but rather couple coherently at rate $\tilde{g}_k$ to a set of discrete waveguide modes $k$.

Theoretical works in chiral quantum optics [179] have interrogated the physics of waveguide-mediated collective interaction between multiple emitters chirally coupled to a waveguide [29, 182] and the behavior of many-photon bound states in such a system [113]. Experiments have demonstrated "topology-dependent cooperative radiation effects" between qubits coupled to a 1D topological photonic waveguide [84] and measured statistics of correlated photonic states in a waveguide made nonlinear by chiral coupling to many atoms [153]. Many-emitter setups chirally coupled to a shared waveguide are termed 'cascaded quantum networks' [184, 158, 148]. In a result that a review by Lodahl [102] flags as 'quite remarkable', application of drive and dissipation to such networks is predicted to generate pure entangled steady states of many emitters, and many-site decoupled 'dark states' of these two-level systems, supported by the chiral structure of the coupling or the waveguide itself. Authors argue that while quantum entanglement is generally sensitive to degradation due to interactions with the environment, in the case of multi-emitter chiral quantum optics, an environment-oriented driven-dissipative approach might actually be used to instead distill or distribute entanglement over a distance [195, 184].

When dealing with driven-dissipative approaches, our cavity-array system has an advantage: it admits many sites of coupling that might be straightforwardly used to introduce drives and losses. In the topological photonic setup described in this thesis, introduction of generalized dissipation is anticipated to stabilize entangled steady states of light that draw their character from the system structure [82, 148]. Introducing a specific engineered reservoir [208] or a non-Hermitian pairing operation [151] at some local site can access, respectively, stabilization of a pure, entangled steady state or onset of a new system instability.

## 1.3 What we do in this thesis

*Introductory chapters:* In Chapter 2, we introduce basics of the physics of coupled oscillators, as well as qubit-cavity interactions, helpful for those seeking to understand the rest of the document. We present an introduction to the four-wave mixing process, accessible under strong classical drive, that will allow us to transfer excitations between fixed-frequency transmon qubits and the modes of the topological lattice that are natively over 1 GHz detuned. In Chapter 3, we provide theoretical background introducing the physics of a particle hopping on a 2D lattice under a magnetic field, survey other experimentalists' work to build topological photonic platforms with and without added nonlinearity, and provide an introduction to how one constructs a quarter-flux Harper-Hofstadter lattice for microwave photons.

*Experimental chapters:* In Chapter 4, we detail the experimental specifics of assembling this topological photonic metamaterial, and describe site- and time-resolved measurements of photon dynamics in this platform which show transport of excitations in two nondegenerate chiral lattice edge channels. In Chapter 5, we summarize the final result of the first paper of this thesis, demonstrating strong coupling between a superconducting transmon qubit and the edge of this lattice, and measuring, for the first time, a Lamb shift on the qubit resulting from the global effect of a multimode synthetic vacuum. In Chapter 6, we detail the second paper of this thesis, characterizing non-reciprocal transport of a single photon between two quantum emitters coupled to a chiral lattice edge channel. Here we explore challenges and subtleties of the multiphoton drive needed to access resonant qubit-lattice interactions.

*Conclusion:* In Chapter 7, we consider options for modifications to this experiment and share some potential future directions of work.

# CHAPTER 2

# OSCILLATORS, LATTICES, AND QUBIT-CAVITY INTERACTIONS

## 2.1 Coupled oscillators

The core physics of this thesis – a microwave cavity array realizing a particular topological Hamiltonian for photons, and a pair of superconducting qubits strongly coupled to it – is built up from coupled harmonic and anharmonic quantum oscillators. Our experimental work goes towards keeping states of light trapped and un-decayed long enough for dynamics to occur, shaping the phase structures and tunneling behavior of light to achieve the dynamics of interest, and doing these things in a cold enough environment that we can use anharmonic oscillators to prepare, manipulate, and count single quanta of energy resolvably above the threshold of thermal noise.

### *2.1.1 Two coupled harmonic oscillators*

As Aziza Suleymanzade explores at greater length in her thesis [186], much of the physics of resonance and coherence that underpins our work in cavity quantum electrodynamics can be accessibly modeled with sets of classical, harmonic oscillators. As moving energy around between resonators is a central tool deployed in this thesis, it is worth considering the simplest paradigm of this, two coupled classical harmonic oscillators.

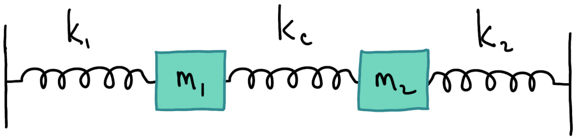

Figure 2.1: **Coupled oscillators.**

If a single, undamped mass-on-spring of mass $m$ and spring constant $k$ has the equation of motion $m\ddot{x} = -kx = -m\omega^2 x$ with resonance frequency $\omega = \sqrt{\frac{k}{m}}$ and displacement $x$, we can write the equations of motion of coupled oscillators experiencing damping rates $\gamma_1, \gamma_2$ as:

$$\begin{aligned} m_1\ddot{x}_1 + m_1\gamma_1\dot{x}_1 + m_1\omega_1^2 x_1 &= k_c(x_2 - x_1) \\ m_2\ddot{x}_2 + m_2\gamma_2\dot{x}_2 + m_2\omega_2^2 x_2 &= k_c(x_1 - x_2) \end{aligned} \tag{2.1}$$

We can characterize how this system responds to injected power – what kinds of shaking make the masses respond with the most movement? – by applying a periodic drive with angular frequency $\omega_D$ to one of the masses:

$$\begin{aligned} m_1\ddot{x}_1 + m_1\gamma_1\dot{x}_1 + m_1\omega_1^2 x_1 &= k_c(x_2 - x_1) + Fe^{i\omega_D t} \\ m_2\ddot{x}_2 + m_2\gamma_2\dot{x}_2 + m_2\omega_2^2 x_2 &= k_c(x_1 - x_2) + 0 \end{aligned} \tag{2.2}$$

We can write these equations out in matrix form for $X = \begin{bmatrix} x_1 \\ x_2 \end{bmatrix}$:

$$\begin{bmatrix} m_1 & 0 \\ 0 & m_2 \end{bmatrix} \ddot{X} + \begin{bmatrix} m_1\gamma_1 & 0 \\ 0 & m_2\gamma_2 \end{bmatrix} \dot{X} + \begin{bmatrix} m_1\omega_1^2 + k_c & -k_c \\ -k_c & m_2\omega_2^2 + k_c \end{bmatrix} X = \begin{bmatrix} F \\ 0 \end{bmatrix} e^{i\omega_D t} \tag{2.3}$$

And condense this equation by defining a mass matrix, a decay rate matrix, and a matrix for the various spring constants involved:

$$\mathbf{M} = \begin{bmatrix} m_1 & 0 \\ 0 & m_2 \end{bmatrix}, \quad \mathbf{\Gamma} = \begin{bmatrix} \gamma_1 \\ \gamma_2 \end{bmatrix}, \quad \mathbf{K} = \begin{bmatrix} m_1\omega_1^2 + k_c & -k_c \\ -k_c & m_2\omega_2^2 + k_c \end{bmatrix} \tag{2.4}$$

$$\mathbf{M}\ddot{X} + \mathbf{M\Gamma}\dot{X} + \mathbf{K}X = \begin{bmatrix} F \\ 0 \end{bmatrix} e^{i\omega_D t} \tag{2.5}$$

We can introduce an ansatz for $X$, an oscillatory solution for this set of linear equations which we pick to rotate with the frame of the drive: $X = \begin{bmatrix} A_1 \\ A_2 \end{bmatrix} e^{i\omega_D t} = \mathbf{A}e^{i\omega_D t}$. Introducing the ansatz and pulling off the rotation allows us to generate a steady-state equation describing the system response:

$$\mathbf{A}(\omega_D) = \left(-\mathbf{M}\omega_D^2 + i\omega_D\mathbf{M\Gamma} + \mathbf{K}\right)^{-1} \begin{bmatrix} F \\ 0 \end{bmatrix} \tag{2.6}$$

Solving for $\|\mathbf{A}\|^2$ as a function of $\omega_D$ will provide us with the system response (heuristically, how perturbed the masses' positions are by the drive) across the space of drive frequencies. When we plot this for a pair of masses with the same $k$ and $m$, we see two big spikes at the frequencies of the system's two normal modes: $\omega = \sqrt{\frac{k}{m}}$, where both masses are oscillating together at their uncoupled bare frequency, and $\omega = \sqrt{\frac{(k+2k_c)}{m}}$, where the masses oscillate out-of-phase [125]. As we increase the coupling strength $k_c$, we see these two peaks split more and more, and the scale of the higher-frequency response shrink. For small $\gamma_i$, these peaks are at the system eigenfrequencies.

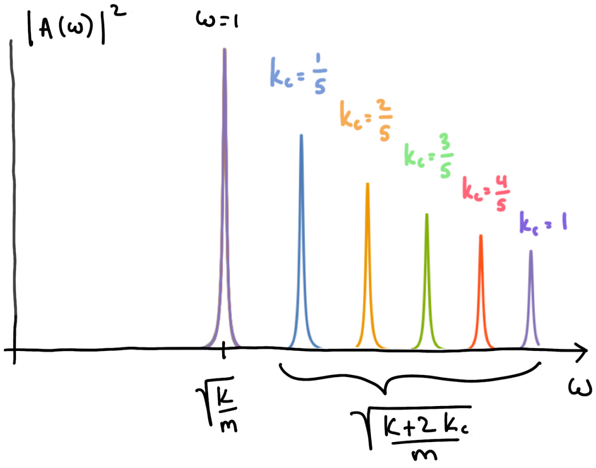

Figure 2.2: **Response of pair of coupled oscillators when one is driven.** We plot $\|A_1(\omega)\|^2$ for a range of $k_c$ values between coupled oscillators with weak damping across a range of drive frequencies $\omega$.

We can also numerically solve these coupled differential equations in Equation 2.1.1 to probe time dynamics; if we start with one of the masses displaced, and plot displacement coordinates $x_1$ and $x_2$ in time, we see amplitude of displacement swap back and forth between the resonators. We plot an example, with some damping $\gamma$ on both oscillators, in Figure 2.3 – starting out with oscillator 1 displaced, we see displacement amplitude trade back and forth between the resonators at a steady rate on top of an underlying resonant frequency.

The core idea to take away here is that providing a coupling between a pair of independent resonators provides a way for energy to slosh from one to the other at some rate that's related to the coupling strength, as we'll see later and throughout this thesis.

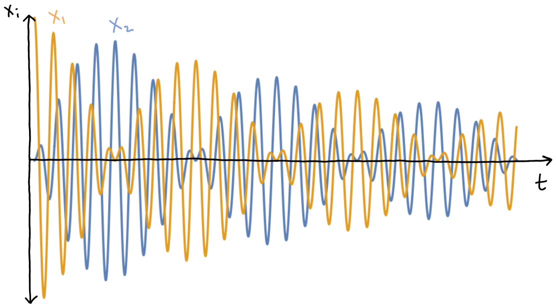

Figure 2.3: **Oscillation of displacement amplitude between coupled resonators.**

Alongside this coupling rate comes an alteration of the system eigenstates – what would be a pair of degenerate system eigenfrequencies $\sqrt{\frac{k}{m}}$ for on-resonance independent oscillators sees its degeneracy broken as the coupling $k_c$ splits off one of the system response peaks in the response plot above. To address the phenomenon of this energy splitting a bit more, let's find the eigenenergies of a more generic system of coupled, undriven and undamped oscillators, following Novotny's classical treatment of avoided level crossings [134]:

We allow different spring constants $k_i$ for masses $m$ and couple them using a spring with $k_c$:

$$\begin{aligned} m\ddot{x}_1 + k_1 x_1 + k_c(x_1 - x_2) &= 0 \\ m\ddot{x}_2 + k_2 x_2 + k_c(x_2 - x_1) &= 0 \end{aligned} \tag{2.7}$$

We again seek oscillatory solutions $X = \mathbf{A}e^{i\omega t}$, resulting in:

$$\begin{pmatrix} -m\omega^2 + k_1 + k_c & -k_c \\ -k_c & -m\omega^2 + k_2 + k_c \end{pmatrix} \begin{bmatrix} A_1 \\ A_2 \end{bmatrix} = 0 \tag{2.8}$$

This matrix equation has nontrivial solutions only if the determinant is 0 – otherwise the solution is that the masses don't go anywhere, ever! From this requirement we extract system eigenfrequencies $\omega$. If we were to have no coupling ($k_c = 0$), we would have just the bare resonant frequencies of the uncoupled oscillators:

$$\omega^2 = \frac{1}{2}\left(\omega_{1,0}^2 + \omega_{2,0}^2 \pm \sqrt{\left(\omega_{1,0}^2 - \omega_{2,0}^2\right)^2}\right) = \omega_{1,0}^2 \text{ or } \omega_{2,0}^2 \tag{2.9}$$

Here $\omega_{1,0}^2 = \frac{k_1}{m}$, the bare frequency of mass 1. For $k_1 = k_2$ these are degenerate. If we go ahead and include the contribution of $k_c$ to the diagonal elements of the matrix equation we've been solving,

$$\begin{pmatrix} -m\omega^2 + k_1 + k_c & 0 \\ 0 & -m\omega^2 + k_2 + k_c \end{pmatrix} \begin{bmatrix} A_1 \\ A_2 \end{bmatrix} = 0, \tag{2.10}$$

and redefine $\omega_1 = \sqrt{\frac{k_1+k_c}{m}}$ and $\omega_2 = \sqrt{\frac{k_2+k_c}{m}}$ to involve the presence of the coupling spring, we still don't see any splitting of eigenfrequencies at $k_1 = k_2$, as altering the diagonals of an eigenvalue equation just shifted both the energies:

$$\omega^2 = \frac{1}{2}\left(\omega_1^2 + \omega_2^2 \pm \sqrt{\left(\omega_1^2 - \omega_2^2\right)^2 + 0}\right) = \omega_1^2 \text{ or } \omega_2^2 \tag{2.11}$$

We can pick a different energy baseline at any time without altering the system dynamics (this baseline shows up as a total time derivative in the system Lagrangian, so can't have an impact) – for an oscillating system we do this by rotating frame. Adding in the off-diagonal couplings, though, does alter system dynamics and produce the desired eigenenergy splitting!

If we solve all of Equation 2.1.1, we retrieve:

$$\begin{gathered}\omega^2 = \frac{1}{2}\left(\frac{k_1}{m} + \frac{k_2}{m} + \frac{2k_c}{m} \pm \sqrt{\left(\frac{k_1 - k_2}{m}\right)^2 + 4\left(\frac{k_c}{m}\right)^2}\right) \\ \omega^2 = \frac{1}{2}\left(\omega_1^2 + \omega_2^2 \pm \sqrt{\left(\omega_1^2 - \omega_2^2\right)^2 + 4\left(\frac{k_c}{m}\right)^2}\right)\end{gathered} \tag{2.12}$$

If we work in the condition that $k_1 = k_2$, so the modified frequencies $\omega_1$ and $\omega_2$ of the harmonic oscillators are on resonance, then we get:

$$\omega_\pm^2 = \omega_1^2 \pm \left(\frac{k_c}{m}\right) = \omega_2^2 \pm \left(\frac{k_c}{m}\right) \tag{2.13}$$

The off-diagonal couplings in the eigenequation matrix produce an eigenfrequency difference of $2\frac{k_c}{m}$. We depict this in Figure 2.4.

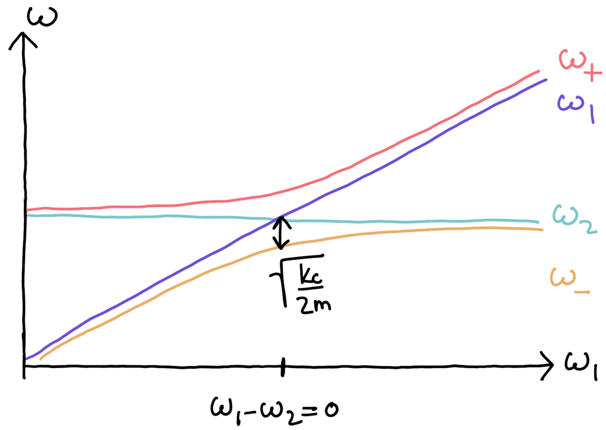

Figure 2.4: **Avoided level crossing of eigenfrequencies for system of two coupled oscillators.** We plot system eigenfrequencies $\omega_\pm$ for a range of values of uncoupled $\omega_1 = \sqrt{\frac{k_1+k_c}{m}}$, with $\omega_2$ held constant. At resonance, $\omega_+$ and $\omega_-$ are split by $\sqrt{\frac{2k_c}{m}}$.

By coupling the two formerly independent oscillators, we have created a set of 'dressed' system eigenstates, each of which is a mixture of the states of both oscillators. Accordingly with this dressing, the system eigenfrequencies at former resonance are split apart by an amount proportional to the strength of the coupling which hybridizes the eigenstates. We see this avoided crossing feature throughout cavity and circuit quantum electrodynamics, as a level splitting larger than the state linewidths is an indicator of strong coupling between two resonators. Avoided crossing is often thought of a quantum phenomenon, but it is not intrinsically related to quantum mechanics or to specifically anharmonic oscillators like atoms and transmon qubits.

We see this avoided crossing again when dealing with quantum oscillators – in Figure 2.5, we adapt a plot from David Schuster's PhD thesis [174] to depict bare resonant frequencies of a cavity resonator and transmon qubit, and show the avoided crossing that occurs when these oscillators are coupled with rate $g$. Here $|g,1\rangle$ is the system state with 1 cavity photon and none in the two-level qubit, and $|e,0\rangle$ is the state with 1 photon in the qubit and none in the cavity. As we sweep the resonant frequency of the qubit past that of the cavity, the coupling causes eigenstates to hybridize into 'phobit' and 'quton' states (written out in pink and purple) with eigenenergies split by $2g$.

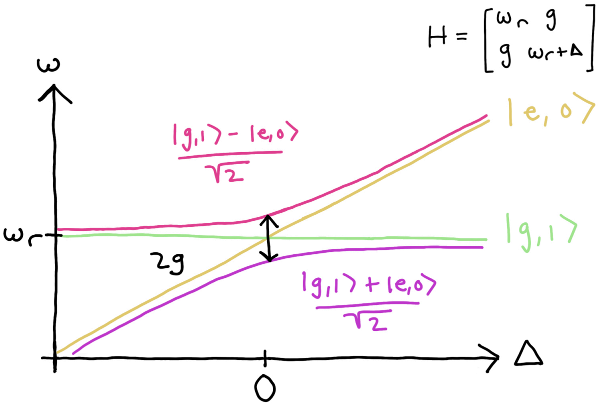

Figure 2.5: **Avoided crossing of coupled qubit-cavity eigenenergies.** Adapted from Figure 2.3 in David Schuster's thesis [174].

Here we only consider two qubit energy levels, $|g\rangle$ and $|e\rangle$, so the qubit is indistinguishable from a harmonic oscillator as long as we do not excite it outside of this two-state manifold. However, the nonlinearity of the Hamiltonian describing a transmon qubit ensures that its level structure is anharmonic, with each pair of higher levels differently spaced. Excitations of hybrid states of such a nonlinear oscillator with a linear one are referred to as polaritons, and even if they 'live' primarily in the linear resonator, the states are afforded some nonlinearity by hybridization with the qubit. To be discussed further later, this sharing of nonlinearity is a core tool we will use for assessing qubit states by making measurements on weakly-hybridized cavity resonators, and for generating single-photon states in qubit and resonator by the application of classical microwave drives.

### *2.1.2 Three-oscillator ring*

It's worth briefly considering a ring of three identical, identically-coupled oscillators, as this system is a good analog of the microwave cavity resonator with three quarter-wavelength posts which we implement later in this thesis.

We can model a ring of three nearby-spaced conducting posts as a ring of coupled resonators – individually, each would host an electromagnetic resonance, and here excitations, in the form of electric field amplitude, can propagate around the ring of resonators via post-post coupling. The equations of motion for this ring of oscillators are:

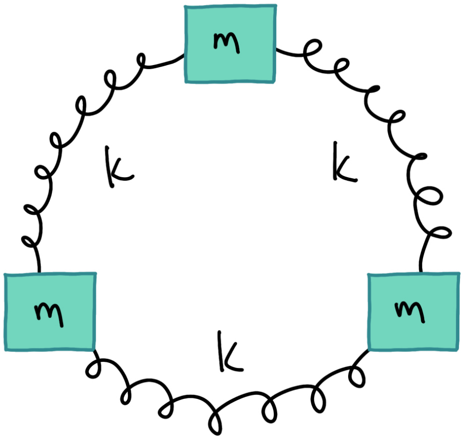

Figure 2.6: **Ring of three coupled oscillators.** We could include a spring with $k_b$ coupling each mass $m$ to some ground, but this would just rotate the bare resonance frequency of each mass, so we neglect it.

$$
\begin{aligned}
m\ddot{x}_1 &= -k(x_1 - x_3) - k(x_1 - x_2) \\
m\ddot{x}_2 &= -k(x_2 - x_1) - k(x_2 - x_3) \\
m\ddot{x}_3 &= -k(x_3 - x_2) - k(x_3 - x_1)
\end{aligned}
\tag{2.14}
$$

Implementing the now standard complex exponential ansatz for $X$,

$$
\begin{bmatrix} -\omega^2 + 2\omega_0^2 & -\omega_0^2 & -\omega_0^2 \\ -\omega_0^2 & -\omega^2 + 2\omega_0^2 & -\omega_0^2 \\ -\omega_0^2 & -\omega_0^2 & -\omega^2 + 2\omega_0^2 \end{bmatrix} \begin{bmatrix} A_1 \\ A_2 \\ A_3 \end{bmatrix} = 0 \tag{2.15}
$$

The eigenvalues and eigenvectors of the matrix at left are:

$$-\omega^2, \begin{bmatrix} 1 \\ 1 \\ 1 \end{bmatrix}, -\omega^2 + 3\omega_0, \begin{bmatrix} -1 \\ 0 \\ 1 \end{bmatrix}, -\omega^2 + 3\omega_0, \begin{bmatrix} -1 \\ 1 \\ 0 \end{bmatrix} \tag{2.16}$$

The leftmost eigenvector realizes the displacement of all three masses together in the ring – this is the lowest-frequency three-post eigenmode, in which the three resonator posts act like one distributed post and host one fundamental resonance. The other two eigenvectors, associated with a pair of degenerate eigenenergies $-\omega^2+3\omega_0$, encode opposite-direction phase windings for excitations (displacement waves) propagating around the resonator ring. These will map onto right- and left-handed degenerate chiral modes that arise in the three-post cavity resonators discussed later.

### *2.1.3 Long chain of coupled oscillators: Wavepackets!*

For some $j$th oscillator in a boundary-less one-dimensional chain of identical coupled oscillators, we can write down an equation of motion in terms of the impact on the oscillator from its nearest neighbors to which it is coupled:

$$\ddot{x}_j = \frac{k}{m}(x_{j+1} - 2x_j + x_{j-1}) \tag{2.17}$$

Our ansatz for $x_j$ should include $e^{i\omega t}$ but also includes a spatial oscillatory component, $e^{ikx_j} = e^{ikna}$, where $a$ is the unperturbed oscillator spacing and $n$ indexes how many oscillator-spacings $x_j$ is from some hypothetical $x = 0$. The new spatial oscillatory component of the ansatz encodes spatial periodicity of any excitation along this boundless chain. Plugging in $x_j = Ae^{inka}e^{i\omega t}$, we get the dispersion relation, or energy-wave momentum relationship, for excitations on the oscillator chain:

$$\begin{aligned} -\omega^2 e^{ijka} &= \frac{k}{m}(e^{ika}e^{ijka} - 2e^{ijka} + e^{-ika}e^{ijka}) \\ \omega^2 &= \frac{2k}{m}(1-\cos ka) \\ \omega(k)^2 &= \frac{4k}{m}\sin^2(\frac{ka}{2}) \\ \omega(k) &= 2\sqrt{\frac{k}{m}}\sin(\frac{ka}{2}) \end{aligned} \tag{2.18}$$

Here $k = \frac{2\pi}{\lambda}$ is the spatial oscillation frequency for wavelength $\lambda$. The smallest possible $\lambda$ for an identifiable oscillation in this chain is $2a$, so the largest value of $k$ is $\pi/a$. From this dispersion, we can extract the group and phase velocity for excitations in this chain – the phase velocity $\frac{\omega}{k}$ describes the speed of a single-$k$ sinusoid through the chain. If we'd like to instead send a wavepacket, some kind of spatially-localized bump or wiggle, it's necessary to synthesize this from multiple Fourier components with different spatial oscillation frequencies $k$ [125]. The velocity of this wavepacket is described by the group velocity, $\frac{d\omega}{dk}$. As each Fourier component has a different phase velocity, this wavepacket will eventually decohere.

Much work in photonics has been done to design dispersions for photons confined to, and hopping in, engineered photonic resonators and waveguides. Controlling the velocity of wavepackets of light and designing the localization/delocalization of states is of broad interest to efforts seeking to prepare information in quantum states and move those states around. Ferreira et al. [55] used a photonic crystal to engineer a slow-light waveguide, allowing them to prepare a photonic qubit in a wavepacket, and sent that wavepacket out to a mirror and back to a generating transmon with enough time gap to resolve an ensuing entangling interaction. Martinez, Chiu, et al. [116] use a small lattice of transmon qubits, in their role as nonlinear photon-holders, to engineer a flat dispersion for photons, so that the excitations they study stay localized until interactions enter the picture and break that localization.

## 2.2 Bloch equations and the tight binding model

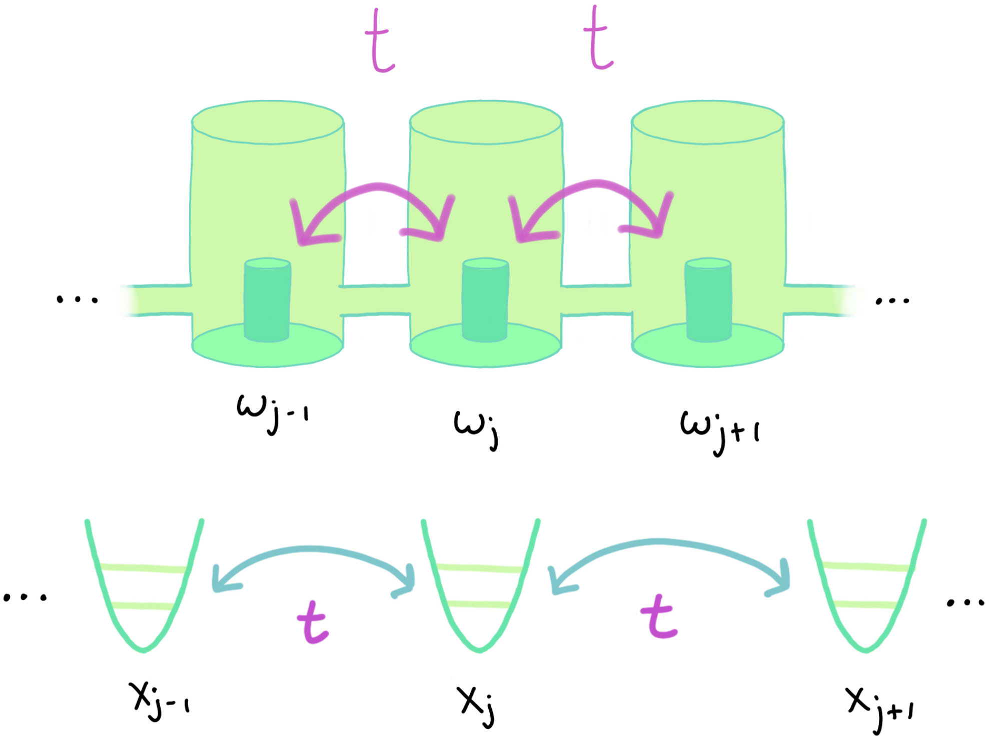

Figure 2.7: **Tight-binding model realized in cavities.** At **top**, we picture a 1D array of superconducting cavity resonators with fundamental modes at $\omega_j$, with holes milled between them allowing a photon to hop between them at rate $t$. At **bottom**, we schematize these resonators as quantum harmonic oscillators at sites $x_j$ in a tight-binding chain.

We can 'make a material' out of coupled quantum oscillators – if we imagine each atomic nucleus in a material as supplying a potential well to a tunneling electron, we can cartoonishly describe the motion of that electron as hopping between a discrete array of harmonic oscillator lattice sites [190] (see Figure 2.7). This combination of the ingredients of locality and hopping applies also to our cavity array, in which a photon is held in a harmonic potential, but some overlap between field landscapes of neighboring cavities through small holes presents some rate of that photon hopping between cavities. Following Tong [190], the Hamiltonian for a photon seated somewhere on an array of uncoupled quantum harmonic oscillators with transition energy $E_0 = \hbar\omega_0$ and $|n\rangle$ representing the photon's presence on the $n^{th}$ oscillator is:

$$\frac{H_0}{\hbar} = \omega_0 \sum_n |n\rangle\langle n| \tag{2.19}$$

Allowing the photon to hop between nearest-neighbor sites in the chain at some rate $t$ produces the Hamiltonian:

$$\frac{H_0}{\hbar} = \omega_0 \sum_n |n\rangle\langle n| - t\sum_n \left(|n\rangle\langle n+1| + |n+1\rangle\langle n|\right) \tag{2.20}$$

If we use the language of second quantization and identify the $n^{th}$ site's occupation number operator $|n\rangle\langle n|$ as $\hat{a}_n^\dagger \hat{a}_n$, where $\hat{a}_n^\dagger$ is the creation operator for a photon on site $n$ and move to a two-dimensional lattice, we can write out the two-dimensional tight-binding model as:

$$\frac{H}{\hbar} = \sum_{i,j} \omega_{i,j} \hat{a}_{i,j}^\dagger \hat{a}_{i,j} - t\sum_{i,j} \left(\hat{a}_{i,j+1}^\dagger \hat{a}_{i,j} + \hat{a}_{i,j}\hat{a}_{i+1,j}^\dagger + h.c.\right) \tag{2.21}$$

The first term describes the holding of photons at site $(i, j)$ – although this expression admits multiple photons, we consider just the one excitation and think of each oscillator as a two-level system – and the second term inscribes hopping of a particle vertically and horizontally between adjacent sites with a rate $t$.

Since we are working not in a continuum but in a lattice of photon holders – which we give spacing $a$ in both dimensions of a square lattice – when we produce solutions to the Schrodinger equation for this Hamiltonian, we can place some expectation on the resulting states that has to do with the lattice periodicity.

Following an early paper by Wannier on 'dynamics of band electrons' [205], we can use the lattice vector $\vec{r} = ma\hat{x} + na\hat{y}$, which encodes the lattice periodicity by connecting sites that 'look the same' upon translation in the lattice along that vector, to describe position indexed by (m,n) on this square lattice with spacing $a$, since all the sites 'look the same'!

We can then define a variety of lattice translation operators

$$\hat{T}(\vec{k}) = e^{i\vec{k}\cdot\vec{r}} \tag{2.22}$$

using crystal momentum $\vec{p} = \hbar\vec{k}$ for a lattice-tunneling particle. By definition, these translation operators commute with the Hamiltonian. Wannier defines Fourier expansions of Bloch wavefunctions for lattice position $\vec{x}$ and lattice momentum $\vec{k}$, which are eigenfunctions both of this tight-binding Hamiltonian on a lattice and of the translation operators:

$$\Psi_q(\vec{x};\vec{k}) = \sum_{\vec{r}} e^{i\vec{k}\cdot\vec{r}}\psi_q(\vec{x}-\vec{r}) \tag{2.23}$$

In the above expression, $q$ indexes the band of energies, useful when more broadly describing materials – in this particular tight-binding model, we'll restrict ourselves to low momentum and neglect $q$. $\psi(\vec{x}-\vec{r})$ is the Wannier function, describing the wavefunctions of states on the localized oscillators. As the lattice spacing is $a$, the largest $\|\vec{k}\|$ can be is $\frac{\pi}{a}$. This condition defines the first Brillouin zone for the tunneling particle. If $\|\vec{k}\| = \|\vec{k}\| + \frac{2\pi}{a}$, the exponential $e^{i\vec{k}\cdot\vec{r}}$ will look the same, but the ultimate particle energy $E(\vec{k})$ will be different – this is a higher-energy band indexed by different $q$, and we neglect it here.

Inserting the Bloch equations into the time-independent Schrodinger equation $\hat{H}\Psi = E\Psi$, we can extract a dispersion $E(\vec{k})$.

$$\begin{aligned}
\hat{H}\Psi((ma\hat{x}, na\hat{y});\vec{k}) &= E\Psi((ma\hat{x}, na\hat{y});\vec{k}) \\
\omega_0 - t\left(e^{i\vec{k}\cdot a\hat{x}} + e^{i\vec{k}\cdot(-a\hat{x})} + e^{i\vec{k}\cdot a\hat{y}} + e^{i\vec{k}\cdot(-a\hat{y})}\right) &= E(\vec{k}) \\
\omega_0 - t\left(2\cos k_x a + 2\cos k_y a\right) &= E(\vec{k})
\end{aligned} \tag{2.24}$$

We'll deploy this dispersion in the following chapter when we consider modifying the tight-binding model by applying a magnetic field!

## 2.3 Circuit quantum electrodynamics

### 2.3.1 The transmon Hamiltonian

Superconducting transmon qubits are microwave resonators which incorporate Josephson junctions that act as nonlinear inductors [88]. When these circuits are cooled below the superconducting transition, it is possible to leverage the existence of the global superconducting quantum-mechanical state across the resonator to describe this large circuit as something *quantum*, a quantum oscillator with some added nonlinearity that makes it anharmonic. The canon of theses describing the physics of transmon qubits, and circuit quantization [132], is already extensive and I will evade recapitulating much of the introductory material already laid out in theses by many others [174, 163, 199, 21]. I encourage the reader to search for a resource which is most accessible to them, as the options are numerous.

We introduce the Hamiltonian of the transmon, written in terms of charge $\hat{n}$ on the superconducting island in the circuit, and phase $\hat{\phi}$. The Josephson energy $E_J$ and charging energy $E_C$ shape the circuit properties and must take on certain values for the circuit to work in the transmon regime [174, 21].

$$\hat{H} = 4E_C(\hat{n} - n_g)^2 - E_J \cos(\hat{\phi}) \tag{2.25}$$

Here $\hat{\phi}$ is the phase across the Josephson junction, one of the two quantized conjugate variables (charge, phase) that play the roles of position and momentum for this quantum oscillator. $n - n_g$ is a relative charge, with $\hat{n}$ the other conjugate variable. If we set $n_g = 0$, choosing a gauge, and expand the cosine, we can write this as:

$$\hat{H} = 4E_C\hat{n}^2 - E_J \left(1 - \frac{\hat{\phi}^2}{2!} + \frac{\hat{\phi}^4}{4!} + ...\right) \tag{2.26}$$

Following a similar presentation in Chris Wang's thesis [199], we recast the conjugate variables $\hat{n}$ and $\hat{\phi}$ using the second-quantization language of creation and annihilation operators for excitations in a resonator:

$$\hat{n} = i \left( \frac{E_J}{8E_C} \right)^{\frac{1}{4}} \frac{\hat{a}_q - \hat{a}_q^\dagger}{\sqrt{2}}; \quad \hat{\phi} = i \left( \frac{8E_C}{E_J} \right)^{\frac{1}{4}} \frac{\hat{a}_q + \hat{a}_q^\dagger}{\sqrt{2}} \tag{2.27}$$

We can eliminate $-E_J$, a total derivative offset, and use these operators to rewrite the above transmon Hamiltonian as a quantum harmonic oscillator with a perturbation from the nonlinear inductance that the Josephson junction supplies [163]. A great number of the multiplicative terms here are scooped into lowest qubit transition frequency $\omega_q$.

$$\hat{H} = \hbar\omega_q \hat{a}_q^\dagger \hat{a}_q + \hat{H}_{\text{nonlinear}}; \quad \hat{H}_{\text{nonlinear}} = -E_J \left( \cos\hat{\phi} \right) - \frac{E_J}{2}\hat{\phi}^2 \tag{2.28}$$

So by expanding the cosine up in Equation 2.26, we were ordering the nonlinear contributions to the transmon Hamiltonian by their perturbative strength. Keeping terms up to fourth order and removing ones that don't conserve energy or are aggressively off-resonant ('counterrotating', in this frame), we retrieve the lowest-order nonlinear effect in the transmon Hamiltonian, the Kerr nonlinearity which supplies the transmon anharmonicity $\alpha \approx -E_C$:

$$\hat{H} \approx \hbar\omega_q \hat{a}_q^\dagger \hat{a}_q - E_C \hat{a}_q^\dagger \hat{a}_q^\dagger \hat{a}_q \hat{a}_q \tag{2.29}$$

Sticking with the un-expanded Hamiltonian for now, we can introduce a resonator coupled to the transmon qubit via a dipole interaction, as pictured in one of the halves of Figure 2.8. We've done a lot of work above to explore this physics of coupled oscillators – here the resonator to which we couple the transmon can be treated as a quantum harmonic oscillator, resulting in the Hamiltonian [21]:

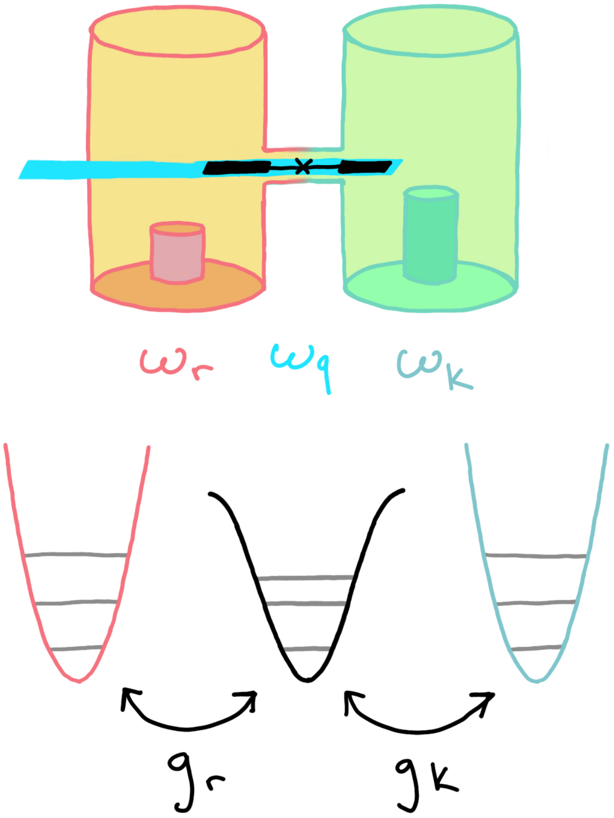

Figure 2.8: **Coupling of transmon qubit to a pair of resonators.** In this thesis, we couple each transmon qubit both to a readout resonator with frequency $\omega_r/2\pi \sim 10.8$ GHz and to some eigenmode $k$ of the chiral lattice with frequency $\omega_k/2\pi \sim 8.9$ GHz. The transmon (in blue at **top**, frequency $\omega_q/2\pi \sim 7.8$ GHz) is dipole-coupled to the electric field landscape in each cavity via a capacitive pad. At **bottom**, we draw schematic harmonic potentials for each cavity mode and the central anharmonic potential of the transmon. We couple the transmon to the readout resonator at rate $g_r$ and to the lattice mode $k$ at rate $g_k$.

$$H = \hbar\omega_q \hat{a}_q^\dagger \hat{a}_q - E_J \left(\cos\hat{\phi}\right) - \frac{E_J}{2}\hat{\phi}^2 + \hbar\omega_r(a_r^\dagger a_r + \frac{1}{2}) + \beta\hat{n}(a_r^\dagger + a_r) \tag{2.30}$$

Here the last term expresses the dipole coupling between the resonator and transmon, proportional to the voltage of the resonator $(a_r^\dagger + a_r)$ and the transmon charge $\hat{n}$. Coupling these resonators will create some dressed eigenstates of the hybrid system, and accordingly, $\hat{\phi}$ across the Josephson junction can be recast in terms of contribution from the coupled-in resonator [199, 132, 99], providing a mechanism by which a transmon 'shares' its nonlinearity through hybridizing with strongly-coupled photons.

If we move to approximating the transmon as a system of its two lowest levels (describable by a Pauli spin operator), we can present the above Equation 2.30 in the classic form of the Jaynes-Cummings Hamiltonian for coupled two-level quantum bit and resonator:

$$\begin{aligned} \frac{\hat{H}_{JC}}{\hbar} &= \omega_q \frac{\hat{\sigma}_z}{2} + \omega_r(\hat{a}_r^\dagger \hat{a}_r + \frac{1}{2}) + g\hat{\sigma}_x(\hat{a}_r + \hat{a}_r^\dagger) \\ &\approx \omega_q \frac{\hat{\sigma}_z}{2} + \omega_r(\hat{a}_r^\dagger \hat{a}_r + \frac{1}{2}) + g(\hat{\sigma}^+\hat{a}_r + \hat{\sigma}^-\hat{a}_r^\dagger) \end{aligned} \tag{2.31}$$

The rate of coupling $g$ between qubit and resonator is again scaling a product of their operators. To reach the final approximation in Equation 2.31 above, we perform the rotating wave approximation, arguing that only operations that stay near zero relative energy in the frame of the qubit transition are likely to occur, as the rest appear to be oscillating 'fast' enough to be neglected from the Hamiltonian-described dynamics.

### *2.3.2 Jaynes-Cummings Hamiltonian in the dispersive limit*

A wide range of resources in this field discuss how to make the dispersive approximation for the above Hamiltonian, in which the qubit-resonator $\Delta = \omega_q - \omega_r$ or (for lattice modes $k$ detailed later) $\Delta = \omega_q - \omega_k$ is much larger than $g_r$ or $g_k$. In general one perturbatively expands and retains only the lowest-order elements of the nonlinear term in the Hamiltonian, in the style of Equation 2.26. We can write the Jaynes-Cummings Hamiltonian for qubit and resonator in the dispersive limit [199] as:

$$\frac{\hat{H}_{JC}}{\hbar} = \left(\frac{\omega_q}{2} + \frac{g^2}{2\Delta}\right)\hat{\sigma}_z + \omega_r \hat{a}_r^\dagger \hat{a}_r + \frac{\omega_r}{2} + \frac{g^2}{\Delta}\hat{\sigma}_z \hat{a}_r^\dagger \hat{a}_r \tag{2.32}$$

This expression accounts for the alterations to system eigenenergies due to qubit-resonator coupling $g$. The $\frac{\omega_r}{2}$ is just some total time derivative stemming from vacuum fluctuations in the resonator that we can neglect when considering dynamics. The qubit's resonant frequency, represented by the first multiplier on $\hat{\sigma}_z$, is shifted by an amount

$$\frac{g^2}{2\Delta}, \text{ the Lamb shift.} \tag{2.33}$$

The Lamb shift holds a stable value and results purely from off-resonant coupling to a resonator hosting vacuum quantum fluctuations. The qubit and the resonator also now 'see' each other in the form of a *dispersive shift*, seen in the last term hosting operators for both oscillators – when a photon populates the resonator (note that the resonator photonic number operator is $\hat{a}_r^\dagger \hat{a}_r$), the qubit's frequency will shift over by an amount

$$2\chi = \frac{g^2}{\Delta}, \text{ the dispersive shift.} \tag{2.34}$$

For a resonator prepared with some average photon number (e.g. if we inject a coherent state, supplying a Poisson-distribution-weighted set of cavity Fock states), we expect the qubit line to shift by $2\chi\bar{n}$, where $\bar{n}$ is the photonic population of the coupled resonator. This photon-number-dependent *AC Stark shift* will become relevant later when we explore putting more and more photons into relevant resonators in our system. As a note to the reader, it is important to discern whether an author is quoting $\chi$ or $2\chi$ as the dispersive shift, as this can vary across the field and affect calculations. It is also important to note that this expression for the dispersive shift must be modified to accommodate a further transmon level if one ceases to approximate the transmon as a two-level system [21, 137].

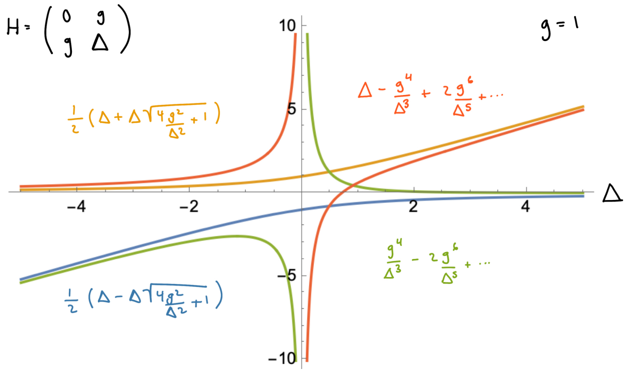

Figure 2.9: **Regimes of validity of the dispersive limit.** We plot eigenvalues for the Hamiltonian listed at top left – orange and blue are the originals, and red and green (labeled at right) are expansions of the eigenvalues in small $\frac{g}{\Delta}$ with the lowest-order term $\frac{g^2}{\Delta}$ removed. Setting $g = 1$, we see that as long as $\frac{g}{\Delta} < \frac{1}{4}$, the higher-order terms in expansions of the eigenvalues don't do much to change these values from their full values, so staying in the dispersive limit and considering expansions in $\frac{g}{\Delta}$ to only lowest order is warranted.

It is quite straightforward to write down the dispersive-limit Hamiltonian for a qubit coupled to *multiple* cavity resonators, expressing the situation dealt with in this thesis. Here we couple in the corner site of our topological photonic metamaterial to the transmon, and decompose a localized excitation in that site in terms of the 25 eigenmodes, indexed by $k$, available in the 25-coupled-resonator lattice. $g_k$ is the coupling between the transmon and a particular lattice mode, smaller than the overall $g_l$ between transmon and lattice corner site and scaled proportionally to the participation ratio of each lattice mode at that site.

$$\frac{\hat{H}_{JC}}{\hbar} = \left(\frac{\omega_q}{2} + \frac{g_r^2}{2\Delta_r} + \frac{g_l^2}{2\Delta_l}\right) + \omega_r \hat{a}_r^\dagger \hat{a}_r + \omega_l \hat{a}_l^\dagger \hat{a}_l + \frac{g_r^2}{\Delta}\hat{\sigma}_z \hat{a}_r^\dagger \hat{a}_r + \frac{g_l^2}{\Delta_l}\hat{\sigma}_z \hat{a}_l^\dagger \hat{a}_l$$

$$\frac{\hat{H}_{JC}}{\hbar} = \left(\frac{\omega_q}{2} + \frac{g_r^2}{2\Delta_r} + \sum_k \frac{g_k^2}{2\Delta_k}\right)\hat{\sigma}_z + \omega_r \hat{a}_r^\dagger \hat{a}_r + \sum_k \omega_k \hat{a}_k^\dagger \hat{a}_k + \frac{g_r^2}{\Delta}\hat{\sigma}_z \hat{a}_r^\dagger \hat{a}_r + \sum_k \frac{g_k^2}{\Delta_k}\hat{\sigma}_z \hat{a}_k^\dagger \hat{a}_k \tag{2.35}$$

In Figure 2.9, we explore the expansion of the nonlinear term in the dispersive Jaynes-Cummings Hamiltonian in powers of $\frac{g}{\Delta}$. We trace the eigenenergies of resonators detuned by $\Delta$ and coupled (via off-diagonal terms in the Hamiltonian) at rate $g$, which should be modified by this coupling as detailed in earlier sections. We conclude that as long as $\frac{g}{\Delta} \leq \frac{1}{4}$ or so, the departure between the full-expansion system eigenvalues and the simple lowest-order system eigenvalues is minimal. This qualitative and vague judgement sets an approximate threshold for the validity of the dispersive approximation.

The canonical signal of strong interaction between dispersively ($g \ll \Delta$) coupled nonlinear and linear resonators like the above is number-splitting of resonances (see results detailed in Chapter 5 and Schuster's original paper [175]), in which the resonant frequency of some transition moves by more than its linewidth in response to photonic population in a coupled resonator. We leverage the effect of this dispersive shift to read out qubit states, watching for a dip in reflected power when a qubit-coupled readout resonator sees its resonant frequency shifted due to qubit population.

## 2.4 Four-wave-mixing path to resonance

We've just dealt with dispersive interaction due to nonlinearity shared between resonators and transmon qubits. It's also possible to leverage the $g$ between these oscillators to produce coherent interactions, supplying a drive to close the energy gap and access resonant processes otherwise significantly detuned. By supplying a multiphoton drive, we can access effective couplings $\tilde{g}$ that appear, counterrotating, in the generally-neglected higher-order terms of the expanded Jaynes-Cummings Hamiltonian for coupled qubit and resonator, and use these couplings to permit movement of photons around the system.

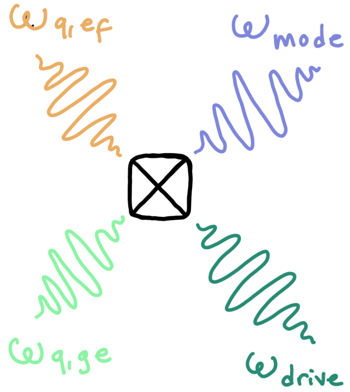

Figure 2.10: **Schematic of driven four-wave mixing process used to prepare single lattice photons.** The transmon nonlinearity (black cross at center) provides access to four-wave mixing. This depiction style is inspired by other work [10] which deploys this process.

Following the supplement of [99], we can write the

Hamiltonian for a transmon qubit with bare $\omega_q$ coupled to two cavity modes, the readout mode $\omega_r$ and the lattice mode $\omega_k$, with drive $\epsilon_D e^{-i\omega_D t}$ applied to the readout mode, as follows:

$$\frac{\hat{H}}{h} = \bar{\omega}_q \hat{a}_q^\dagger \hat{a}_q + \bar{\omega}_r \hat{a}_r^\dagger \hat{a}_r + \bar{\omega}_k \hat{a}_k^\dagger \hat{a}_k - \frac{E_J}{\hbar}\left(\cos\left(\phi\right) + \frac{\phi^2}{2}\right) + 2\mathrm{Re}\left(\epsilon_D e^{-i\omega_D t}\right)\left(\hat{a}_r + \hat{a}_r^\dagger\right),$$
$$\phi = \phi_q\left(\hat{a}_q + \hat{a}_q^\dagger\right) + \phi_r\left(\hat{a}_r + \hat{a}_r^\dagger\right) + \phi_k\left(\hat{a}_k + \hat{a}_k^\dagger\right) \tag{2.36}$$

Bars are placed on the resonator frequencies to indicate that these are the bare versions unmodified by the nonlinear Josephson portion of the Hamiltonian – un-barred frequencies are what we'll measure if we probe frequencies of the hybridized modes. We decompose $\phi$, the phase across the Josephson junctions, as a hybrid combination of its contributions from the qubit and both of the coupled-in oscillator modes. The last term in the Hamiltonian, built from operators $(\hat{a}_r + \hat{a}_r^\dagger)$, expresses the application of an oscillatory drive to the resonator, much as we earlier applied drives $F_0 \cos\left(\omega_D t\right)$ to an oscillator in a coupled-classical-oscillator system.

We can perform a unitary transformation to rotate out some of the system frequencies $\omega_q$ and $\omega_D$. We use the operator $U$:

$$U = e^{i\bar{\omega}_q t \hat{a}_q^\dagger \hat{a}_q} e^{i\omega_D t \hat{a}_r^\dagger \hat{a}_r} \tag{2.37}$$

and perform the transformation according to:

$$\frac{\hat{\tilde{H}}}{\hbar} = U\frac{\hat{H}}{\hbar}U^\dagger - iU\dot{U}^\dagger \tag{2.38}$$

We can additionally perform a displacement transformation in order to translate the system frame to follow the displacement of the cavity state introduced by the drive $\epsilon_D e^{-i\omega_D t}$, which should place the resonator $r$ into a coherent state of light. The operator for this transformation incorporates a quantity $\xi_D$ which represents the effective scale of the displacement drive in the cavity and, when run through the time-derivative portion of the unitary transformation, can be described with a differential equation:

$$U = e^{-\xi_D \hat{a}_r^\dagger + \xi_D^* \hat{a}_r}; \quad \frac{d\xi_D}{dt} = -i\bar{\omega}_r \xi_D - i2Re\left(\epsilon_D e^{-i\omega_D t}\right) - \frac{\kappa_r}{2}\xi_D \tag{2.39}$$

For readout cavity with $\kappa_r$, after some ringup time $\frac{1}{\kappa_r}$, we have the ‘field trajectory’ [199]:

$$\xi_D = e^{-i\omega_D t}\frac{-i\epsilon_D}{\frac{\kappa_r}{2} + i(\bar{\omega}_r - \omega_D)} \approx e^{-i\omega_D t}\frac{-i\epsilon_D}{\frac{\kappa_r}{2} + i(\omega_r - \omega_D)} \tag{2.40}$$

The effect of executing the displacement transformation on the whole Hamiltonian is to pull the classical drive term $\xi_D$ inside the cosine which stems from the Josephson nonlinearity, moving the applied drive from something that acts on that resonator in particular to something that participates in the transmon operator and thus scales nonlinear elements of the hybridized Hamiltonian, allowing us to access drive-sensitive multiphoton processes.

After executing these transformations on the system Hamiltonian, we are left with:

$$\begin{gathered}
\frac{\hat{\tilde{H}}}{\hbar} = (\bar{\omega}_r - \omega_D)\hat{\tilde{a}}_r^\dagger \hat{\tilde{a}}_r + \bar{\omega}_k \hat{a}_k^\dagger \hat{a}_k + \frac{E_J}{\hbar}\left(\cos(\tilde{\phi}) + \frac{\tilde{\phi}^2}{2}\right), \\
\tilde{\phi} = \phi_q\left(\hat{\tilde{a}}_q + \hat{\tilde{a}}_q^\dagger\right) + \phi_r\left(\hat{\tilde{a}}_r + \hat{\tilde{a}}_r^\dagger\right) + \phi_k\left(\hat{a}_k + \hat{a}_k^\dagger\right) + \phi_r\left(\xi_D + \xi_D^*\right), \\
\hat{\tilde{a}}_q = e^{-i\bar{\omega}_q t}\hat{a}_q, \; \hat{\tilde{a}}_r = e^{-i\omega_D t}\hat{a}_r
\end{gathered} \tag{2.41}$$

If we expand $\cos(\tilde{\phi})$ to fourth order, the $E_J$ term in the above Hamiltonian becomes

$$\frac{E_J}{\hbar}\left(1 - \frac{\tilde{\phi}^2}{2} + \frac{\tilde{\phi}^2}{2} + \frac{\tilde{\phi}^4}{4!}\right) = \frac{E_J}{\hbar}\frac{\tilde{\phi}^4}{4!} \tag{2.42}$$

Plugging in $\tilde{\phi}^4$, we generate an enormous number of cross-multiplied terms due to the contributions each mode and the drive make to $\tilde{\phi}$. We keep only those that conserve energy – other terms, while they exist in the Hamiltonian, are energetically far counterrotating and can be neglected. In a situation without the applied classical drive $\xi_D$, that would mean that we only kept terms with an equal number of $\hat{a}^\dagger$ and $\hat{a}$. As we now incorporate the classical drive, we can use it to close energetic gaps, and keep terms with odd numbers of creation and annihilation operators. In particular, we keep a term that looks like:

$$\frac{E_J}{\hbar}\frac{12}{24}\phi_q\phi_q\phi_k\phi_k\|\xi_D\|\hat{a}_q^\dagger\hat{a}_q^\dagger\hat{a}_k = \frac{\chi_{qk}}{2}\|\xi_D\|\hat{a}_q^\dagger\hat{a}_q^\dagger\hat{a}_k = \tilde{g}\|\xi_D\|\hat{a}_q^\dagger\hat{a}_q^\dagger\hat{a}_k \tag{2.43}$$

which resonantly converts a pair of photons in the transmon to one in the lattice mode $k$ and other in the classical drive applied to the readout resonator.

Here $\chi_{qk}$ is the cross-Kerr interaction between qubit and readout resonator that stems from the Josephson nonlinearity. We define an effective coupling rate $\tilde{g} = \frac{\chi_{qk}}{2}\|\xi_D\|$ describing the coupling the coupling strength between two-photons-in-qubit and one-photon-in-mode-$k$.

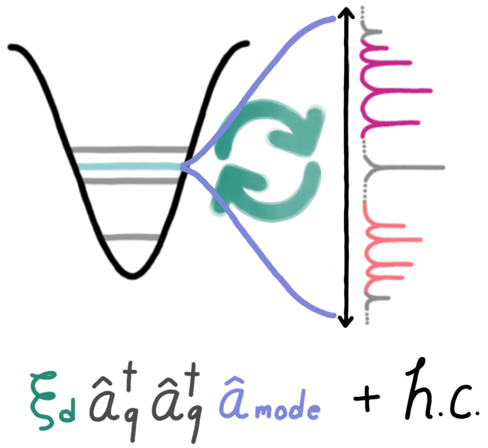

Figure 2.11: **Dressed-state picture of four-wave swap process.** We can understand this particular multiphoton process in Equation 2.43 as bringing a 'dressed' excited state of the transmon (teal level) onto resonance with modes in the spectrum of our topological lattice (drawn at right) via a classical drive (drawn in green).

This same operation, performing a displacement transformation to incorporate the role of a drive inside the transmon nonlinearity in the Hamiltonian, also provides other more common drive-dependent shifts like the Stark shift: keeping only energy-conserving terms in the expansion of the cosine, we also hold onto a term which (possibly missing a scalar multiplier) represents the AC Stark shift on the qubit due to application of the classical drive to the readout resonator, quadratic with amplitude $\xi_D$:

$$\frac{E_J}{\hbar}\frac{6}{24}\phi_q\phi_q\phi_r\phi_r\|\xi_D\|^2\hat{\tilde{a}}_q^\dagger\hat{\tilde{a}}_q = \frac{1}{4}\chi_{qr}\|\xi_D\|^2\hat{\tilde{a}}_q^\dagger\hat{\tilde{a}}_q \tag{2.44}$$

We refer to the process that elicits these now-resonant terms as a 'four-wave process' (see Figure 2.10), as it is an example of 'four-wave mixing', an umbrella term for processes in the higher-order $\phi^4$ portion of the hybrid qubit-cavity nonlinearity, which involve four photons through invocation of either classical drive amplitude $\xi_D$ or resonator ladder operators. Without the transmon nonlinearity, this mixing would not be possible.

### *2.4.1 Effective coupling under drive*

Imagine (see Figure 2.8) that we have a transmon qubit, with the transition frequency between its lowest two states $|g\rangle \leftrightarrow |e\rangle$ being $\omega_q/2\pi$ and anharmonicity of level spacings $-\alpha/2\pi$, coupled to a readout resonator which has frequency $\omega_r/2\pi$ and some other cavity with harmonic $|0\rangle \leftrightarrow |1\rangle$ transition $\omega_k/2\pi$ (for us, this is relevantly an eigenmode $k$ of the chiral lattice to which the transmon is coupled). We can employ the scheme detailed above, applying a strong multiphoton drive to access the transition found in Equation 2.43 and converting two photons prepared in the qubit to one in the lattice and another in the drive. The effective displacement amplitude $\xi_D$, as shown in Equation 2.43, sets the 'importance' of this process in the Hamiltonian. In the experiments in this thesis, we apply the strong drive through the readout resonator, accessing a four-wave process between qubit and lattice mode $k$, as executed in the derivations above. It is also reasonable to write this drive as acting directly on qubit operators to start out.

To bring the relevant process, which is normally counterrotating and easily neglected, onto resonance in our rotating frame, we need to pick a drive frequency $\omega_D/2\pi$ which 'closes the loop' between the detuned states and makes the relevant term pop out as resonant in the step between Equations 2.42 and 2.43. To close the energy loop for this process, we apply the drive at the energy difference between that of two photons in the qubit ($|g\rangle \leftrightarrow |e\rangle + |e\rangle \leftrightarrow |f\rangle$)

and that of one photon in the lattice ($|0\rangle \leftrightarrow |1\rangle$), using angular frequency

$$\omega_D = \omega_{ef} + \omega_{ge} - \omega_k = 2\omega_q - \alpha - \omega_k. \tag{2.45}$$

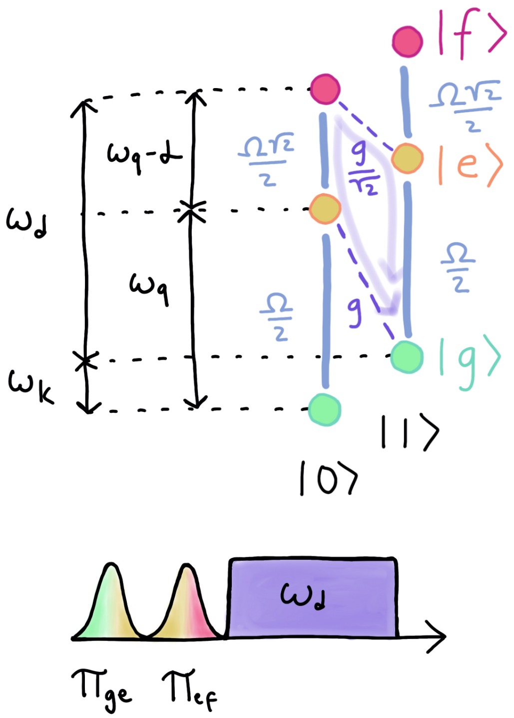

Figure 2.12: **Level diagram of the $|f,0\rangle \leftrightarrow |g,1\rangle$ swap process** Adapted from Pechal et al. [145]. Vertical state axis represents the state of the qubit, and horizontal state axis represents that of the coupled cavity mode $k$.

This operation takes the qubit-cavity state from $|f,0\rangle$ to $|g,1\rangle$ and is referred to throughout this thesis as an $|f,0\rangle \leftrightarrow |g,1\rangle$ swap process, as the drive-dependent coupling $\tilde{g}$ generated between these two system states permits resonant swapping of excitations, in a quantum-mechanical analog of Figure 2.3. We can calculate an approximate effective $\tilde{g}$, the coupling rate between $|f,0\rangle$ and $|g,1\rangle$. We can write the applied classical drive, which Pechal et al. [145] apply directly to the qubit as $\Omega(t) = \Omega_0 \cos(\omega_D t + \phi(t))$. Representing the Hamiltonian of a qubit with anharmonicity $-\alpha$ and ladder operator $\hat{a}_q^\dagger$, and a single resonator $\hat{a}_r^\dagger$, in the rotating frame of this drive, we write, for bare qubit-resonator coupling $g$ [145],

$$H(t) = (\omega_q - \omega_d)\hat{a}_q^\dagger \hat{a}_q - \frac{1}{2}\alpha \hat{a}_q^\dagger \hat{a}_q^\dagger \hat{a}_q \hat{a}_q + (\omega_r - \omega_D)\hat{a}_r^\dagger \hat{a}_r + g(\hat{a}_r \hat{a}_q^\dagger + \hat{a}_r^\dagger \hat{a}_q) + \frac{1}{2}(\Omega(t)^* \hat{a}_q + \Omega(t)\hat{a}_q^\dagger) \tag{2.46}$$

Note that because we're representing the qubit in terms of harmonic oscillator ladder operators, the second term here encodes the Kerr nonlinearity which realizes the transmon anharmonicity. The level structure of this setup is diagrammed in Figure 2.12; the two most dominant perturbative paths the coupling and drive set up between $|f,0\rangle$ and $|g,1\rangle$ are illustrated in purple. We can treat this as a Raman process, effectively adiabatically eliminate the middle states [210], and extract an effective $|f,0\rangle \leftrightarrow |g,1\rangle$ transition rate $\tilde{g}$ by combining paths. Below, $\Delta = \omega_k - \omega_q$, and we neglect a factor of two used later.

$$\begin{aligned} \tilde{g} \approx \frac{g\Omega\sqrt{2}}{(-\Delta)} + \frac{g\Omega}{\sqrt{2}(\Delta-\alpha)} = \frac{g\Omega}{\sqrt{2}}\left(\frac{\alpha-\Delta}{\Delta(\Delta-\alpha)} + \frac{\Delta}{\Delta(\Delta-\alpha)}\right) &= \frac{g\Omega}{\sqrt{2}}\frac{\alpha}{\Delta(\Delta-\alpha)} \\ \tilde{g}(t) \approx \frac{g\Omega_0 e^{i\phi(t)}}{\sqrt{2}}&\frac{\alpha}{\Delta(\Delta-\alpha)} \end{aligned} \tag{2.47}$$

We largely neglect the phase $\phi$ of the process drive – but it will become relevant again right at the end of this thesis! To execute the swap process (Figure 2.12), we prepare the qubit in its $|f\rangle$ state with a set of $\pi$ pulses prior to pulsing the process drive; see, e.g., references [128, 169] for introductions to qubit control. It is important to note that the application of a strong microwave drive will induce a substantial Stark shift on the $|g\rangle \leftrightarrow |e\rangle$ and $|e\rangle \leftrightarrow |f\rangle$ transitions of the qubit involved in this process. Zeytinoğlu et al. [210] derive a subtle way to calculate the scale of this shift, which is quadratic in drive amplitude at low drive powers but diverges at higher powers (see this experimentally demonstrated in Figure 6.17).

This tool of using a strong classical drive to gain access to higher-order nonlinear processes that are normally far counterrotating is really powerful; despite the fact that the transmon qubits used in this thesis have fixed transition frequencies $\omega_q$, we are able to dress the excited states of this qubit onto and off of resonance with relevant cavity modes by using a strong drive, and the presence of nonlinearity in the Hamiltonian, to close the energetic gap. This opens up a world of exploration where one can turn on and off qubit-resonator couplings to move energy between the qubits, our single-photon preparers and detectors, and a landscape of largely linear cavity modes of the topological metamaterial we will discuss next.

# CHAPTER 3

# A TOPOLOGICAL INSULATOR FOR PHOTONS

This thesis chapter, and the chapter that follows, are in part based on the first paper of this PhD [139], with additional details added on the setup, simulation, and measurement. In that paper, we demonstrated a scalable architecture for probing interacting topological physics with light. Building on a prior experiment realizing a chiral photonic lattice at room temperature [138], we demonstrated a similar lattice at cryogenic temperatures. This $5 \times 5$ array of superconducting resonators acts as a quarter flux ($\alpha = \frac{1}{4}$) Hofstadter lattice [73], exhibiting topological bulk and edge modes for the photons that reside within it.

This chapter will address the design and modeling of a synthetic gauge field for microwave photons. The following chapter will explore its implemetation in the platform used in this thesis.

## 3.1 Introduction: Making materials out of light

Materials made of light are a frontier in quantum many-body physics [31]; relying upon non-linear emitters to generate strong photon-photon interactions and ultra-low-loss metamaterials to manipulate the properties of the individual photons, this field explores the interface of condensed matter physics and quantum optics, while motivating production of devices for manipulating light [180, 16]. Recent progress in imbuing photons with topological properties [140], in particular those that lead the photons to undergo circular time-reversal-symmetry-breaking orbits, promises opportunities to explore photonic analogs of such solid-state phenomena as the (fractional) quantum Hall effect [196, 185], Abrikosov lattices [1], and topological insulators [72].

In electronic materials, the circular electron orbits result from magnetic or spin-orbit couplings [72]. Unlike electrons, photons are charge-neutral objects and so do not directly couple to magnetic fields. In order to cause photons to behave like they 'feel' a magnetic field, much work has been done in photonic platforms to create a 'synthetic' magnetic field for photons by modifying properties of the Hamiltonian which a tunneling photon obeys.

Significant progress in this arena has been made in both optical- and microwave-based topological photonics: in silicon photonics [164, 66] and optics [173, 45], synthetic gauge fields have been achieved while maintaining time-reversal symmetry by encoding a pseudo-spin in either the polarization or spatial mode. In RF and microwave meta-materials, both time-reversal-symmetric [78, 105] and time-reversal-symmetry-broken models have been explored, with the T-breaking induced either by coupling the light to ferrimagnets in magnetic fields [203, 138], by Floquet engineering [170], by pumping to generate a synthetic lattice dimension with time-reversal symmetry breaking [75], or by building geometries for twisted qubit-qubit coupling [116].

We want to end up with photons that have effective mass, effective charge, and are confined to two dimensions, the necessary ingredients for quantum Hall physics [196]. To achieve this, in our platform, microwave photons are trapped in a 2D array of microwave resonators, and thereby confined to two transverse dimensions and imbued with an effective mass due to the finite tunneling rate between the resonators. Photons are afforded an effective charge by the assignment of a synthetic gauge field (see Section 3.2) which they 'feel' as though they were electrons tunneling in a two-dimensional material under an applied flux; we execute this synthetic gauge field by coupling the photonic landscape of certain cavities to ferrimagnets in magnetic fields, modifying the phase landscape of those cavities and ultimately realizing a Harper-Hofstadter model for microwave light.

## 3.2 Harper-Hofstadter model realized in a microwave cavity array

### *3.2.1 The Harper-Hofstadter model*

The behavior of a photon traveling in our cavity lattice platform can be described by the Harper-Hofstadter model: this model is a lattice-physics description of the behavior of a single charged particle propagating in two dimensions under the influence of an out-of-plane magnetic field [71, 73]. In the most general version of this model, a tight-binding description of a particle hopping on a lattice sees some of these hopping rates modified to be complex, a change which encodes the field:

$$\frac{H}{\hbar} = \sum_{m,n} \omega_{m,n} \hat{a}^{\dagger}_{m,n} \hat{a}_{m,n} - t \sum_{m,n} \left( e^{i\phi^{y}_{m,n}} \hat{a}^{\dagger}_{m,n+1} \hat{a}_{m,n} + e^{i\phi^{x}_{m,n}} \hat{a}_{m,n} \hat{a}^{\dagger}_{m+1,n} + h.c. \right) \tag{3.1}$$

As illustrated in Figure 3.1, $t$ is the rate of particle hopping between sites and the magnetic flux orthogonal to the tunneling plane is encoded by the value of the complex phase on each hopping term. Assuming the phases are nontrivial, their introduction breaks time-reversal symmetry in the formerly time-reversal-symmetric tight-binding system. If the magnetic field is uniform across the area of the two-dimensional lattice, phases $\phi^{x}_{m,n}$ and $\phi^{y}_{m,n}$ will retain their same values for any specific lattice coordinate $(m, n)$.

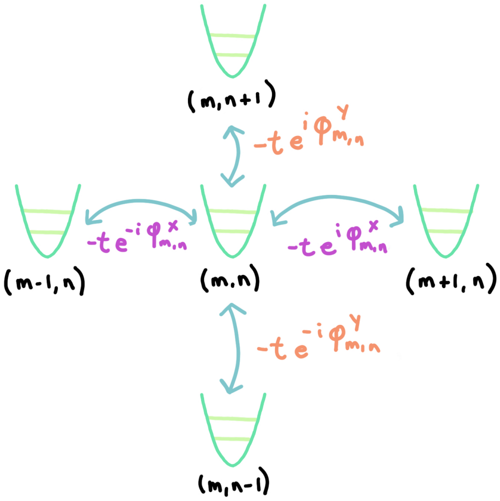

Figure 3.1: **Onsite potentials and hopping rates in the most general Harper-Hofstadter model.** Cartoon quantum harmonic oscillators represent sites $(m, n)$ in a two-dimensional tight-binding lattice for photons. The hopping rate $t$ is modified by a different complex phase for each direction.

The Harper-Hofstadter Hamiltonian can

also be represented (see Figure 3.2 and equation 3.2) in a gauge such that the flux is encoded in complex hopping multipliers along only one dimension.

$$\frac{H}{\hbar} = \sum_{m,n} \omega_{m,n} \hat{a}^{\dagger}_{m,n} \hat{a}_{m,n} - t \sum_{m,n} \left( \hat{a}^{\dagger}_{m,n} \hat{a}_{m+1,n} + h.c. \right) - t \sum_{m,n} \left( e^{i2\pi\alpha m} \hat{a}^{\dagger}_{m,n} \hat{a}_{m,n+1} + h.c. \right) \tag{3.2}$$

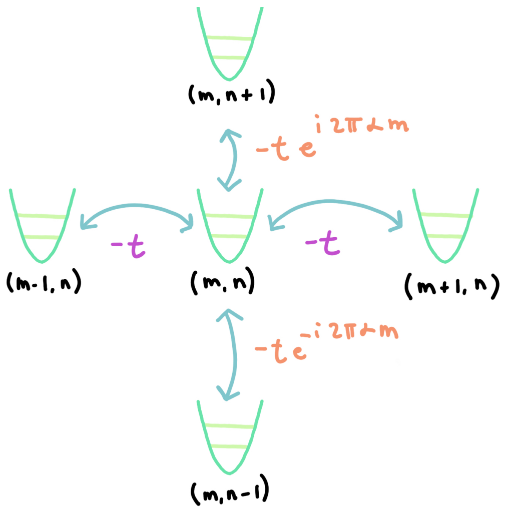

Figure 3.2: **Onsite potentials and hopping rates in the Landau gauge Harper-Hofstadter model.** If the field is uniform across the lattice, y-direction hopping rates are the same for all m.

What is going on here? Why does sticking some complex phases on tunneling terms encode a magnetic field? [1]

Let's take a very big step back and think about a charged, massive particle propagating in a magnetic field. A particle of mass $m$ and charge $-e$ traveling with $\vec{v}$ will experience a Lorentz force, $m\frac{d\vec{v}}{dt} = -e\vec{v}\times\vec{B}$, under field $\vec{B}$. For a particle propagating in two dimensions $(x, y)$ under a uniform orthogonal-to-plane magnetic field $\vec{B} = B\vec{z}$, the above equation of motion will render the coupled equations $m\ddot{x} = -eB\dot{y}$ and $m\ddot{y} = eB\dot{x}$. Solving these equations shows that the particle will travel in a circle (Figure 3.3) at the cyclotron frequency $\omega_B = eB/m$. The thing to note here is that the cyclotron frequency for a specific particle is fixed purely by the strength of the field and its direction on that circle set by the sign of the field along $\vec{z}$ [189].

---

[1] The following presentation of representing magnetic fields in the Harper-Hofstadter model follows a mixture of Hofstadter's original 1976 paper [73] calculating the eigenspectrum of Harper's equation, Wannier's 1962 paper describing Bloch electrons tunneling in fields [205], the legendary David Tong's online lecture notes on the quantum Hall effect [189], and Monika Aidelsburger's PhD thesis [6] introducing one of the two contemporaneous first implementations of the Harper-Hofstadter model in cold atoms.

### *3.2.2 Hofstadter's approach to a Bloch electron in a magnetic field*

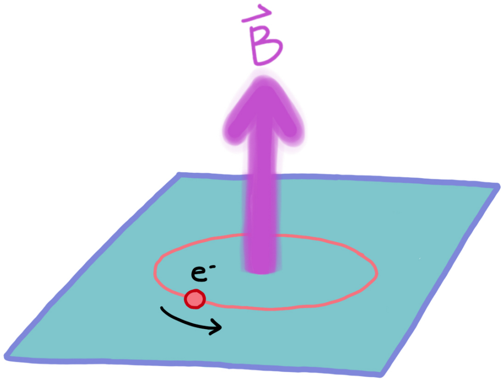

Figure 3.3: **Cartoon of an electron's cyclotron orbit in an out-of-plane magnetic field.**

The modification the magnetic field inflicts upon the dynamics of the particle means that the vector potential $\vec{A}$ which generates $B\vec{z} = \nabla \times \vec{A}$ goes into the particle's Lagrangian; that Lagrangian yields a canonical momentum (the variable conjugate to position) that also reflects $\vec{A}$:

$$L = \frac{1}{2}m\dot{\vec{x}}^2 - e\dot{\vec{x}} \cdot \vec{A}; \quad \vec{p} = \frac{\partial L}{\partial \dot{\vec{x}}} = m\dot{\vec{x}} - e\vec{A} \tag{3.3}$$

We can explore the effect of this new canonical momentum for a Bloch electron (see Section 2.2) moving in a two-dimensional periodic tight-binding potential in the lowest band of its energy spectrum. We will eventually see that the applied field causes this band to fragment into several sub-bands in a way that reflects the strength of the field. Let's start with the dispersion of the lowest-energy band for a Bloch electron hopping along in a two-dimensional tight-binding model without any applied field, which Hofstadter defines, for lattice spacing $a$ and crystal momenta $k_x$ and $k_y$, as

$$W(\vec{k}) = 2E_0 \left(\cos k_x a + \cos k_y a\right) \tag{3.4}$$

We insert for the quantum particle's momentum an expression which incorporates the vector potential's modification to the dynamics, thus carrying out the 'Peierls substitution':

$$\vec{p} = h\vec{k} \rightarrow \vec{p} = m_p\dot{\vec{x}} - e\vec{A} \tag{3.5}$$

Expressing $k_x$ and $k_y$ in Equation 3.4 in terms of the modified $\vec{p}$ using $\hbar\vec{k} = m_p\dot{\vec{x}} -$

$e\vec{A}$. If we promote $W(\vec{k})$ to an operator, we can now use $W(\vec{k})$ as an 'effective single-band Hamiltonian' [73, 71]. Preparing to deploy this Hamiltonian in the time-independent Schrodinger equation, we can write momentum-space Bloch wavefunctions $\Psi(\vec{x};\vec{k})$ (assumed to be normalized) on the 2D lattice in terms of sums on excitations localized on specific lattice sites $\psi(\vec{x};\vec{r})$. Here $\vec{r} = m\hat{x} + n\hat{y}$ is the lattice vector for site $(m,n)$ based on lattice primitive vectors $\hat{x}$ and $\hat{y}$ (which are just coordinates for a square lattice), $\vec{r'}$ is a hypothetical spatial translation vector, and $\vec{k}$ is the reciprocal lattice vector corresponding to $\vec{r}$.

$$\begin{aligned} \Psi(\vec{x};\vec{k}) &= \sum_{\vec{r}} e^{i\vec{k}\cdot\vec{r}}\psi(\vec{x};\vec{r}); \\ \Psi(\vec{x}-\vec{r'};\vec{k}) &= \sum_{\vec{r}} e^{i\vec{k}\cdot\vec{r}}\psi(\vec{x}-\vec{r'};\vec{r}) \end{aligned} \tag{3.6}$$

Wannier [205] defines lattice translation operators for a situation without magnetic field using the lattice vector $\vec{r}$:

$$\hat{T}(\vec{r}) = e^{\frac{i\vec{p}\cdot\vec{r}}{\hbar}}; \quad \hat{T}(\vec{r})f(\vec{p},\vec{x}) = f(\vec{p},\vec{x}+\vec{r})\hat{T}(\vec{r}) \tag{3.7}$$

Keeping this in mind, we follow Wannier to further rewrite the Bloch wavefunction above (3.6), which is an eigenstate of the lattice translation operator, two ways, the latter with the index $\vec{r}$ relabeled a lattice site over from the first:

$$\begin{aligned} \Psi(\vec{x}-\vec{r'};\vec{k}) &= \sum_{\vec{r}} e^{i\vec{k}\cdot(\vec{r}-\vec{r'})}\psi(\vec{x};\vec{r}) \\ \Psi(\vec{x}-\vec{r'};\vec{k}) &= \sum_{\vec{r}} e^{i\vec{k}\cdot\vec{r}}\psi(\vec{x};\vec{r}+\vec{r'}) \end{aligned} \tag{3.8}$$

If we, following Wannier's somewhat arcane choices, capitalize upon the translatability of an infinite lattice, we can call both indices $\vec{r}$ the same. If we also set the coordinate $\vec{r}$ to

0, recall the effect of translation operators, and then neglect the 0, we get:

$$\begin{aligned} \sum_{\vec{r}} e^{i\vec{k}\cdot(\vec{r}-\vec{r'})}\psi(\vec{x};\vec{r}) &= \sum_{\vec{r}} e^{i\vec{k}\cdot\vec{r}}\psi(\vec{x};\vec{r}+\vec{r'}) \\ \psi(\vec{x}-\vec{r'};0) &= \psi(\vec{x};0+\vec{r'}) \\ \psi(\vec{x}-\vec{r'}) &= \psi(\vec{x};\vec{r'}) \end{aligned} \tag{3.9}$$

We can redeploy this understanding to re-express the $\vec{k}$-space Bloch wavefunction (3.6) in terms of what Wannier himself terms the 'Wannier functions' $\psi(\vec{x}-\vec{r})$ for this particular band which represent the localized wavefunction on each site:

$$\Psi(\vec{x};\vec{k}) = \sum_{\vec{r}} e^{i\vec{k}\cdot\vec{r}}\psi(\vec{x}-\vec{r}) \tag{3.10}$$

We can express the time-independent Schrodinger equation using $W(\vec{k})$ and the Bloch wavefunction in Equation 3.10:

$$\begin{aligned} H\Psi(\vec{x};\vec{k}) &= E\Psi(\vec{x};\vec{k}) \\ W(\vec{k})\sum_{\vec{r}} e^{i\vec{k}\cdot\vec{r}}\psi(\vec{x}-\vec{r}) &= E\sum_{\vec{r}} e^{i\vec{k}\cdot\vec{r}}\psi(\vec{x}-\vec{r}) \\ \sum_{\vec{r}} e^{i\vec{k}\cdot\vec{r}}W(\vec{k})\psi(\vec{x}-\vec{r}) &= \sum_{\vec{r}} e^{i\vec{k}\cdot\vec{r}}E\psi(\vec{x}-\vec{r}) \end{aligned} \tag{3.11}$$

We then deploy the Peierls substitution (Hofstadter simply articulates that "work to justify this substitution has been done" [73] and we similarly sweep some subtlety under the rug). With lattice spacing $a$, and x-position $m = ax$ in $\vec{r} = m\hat{x} + n\hat{y}$, we retrieve the resulting expressions:

$$\sum_{\vec{r}} e^{i\vec{k}\cdot\vec{r}}2E_0\left(\cos k_x a + \cos k_y a\right)\psi(\vec{x}-\vec{r}) = \sum_{\vec{r}} e^{i\vec{k}\cdot\vec{r}}E\psi(\vec{x}-\vec{r}) \tag{3.12}$$

$$\begin{aligned}\sum_{\vec{r}} e^{i\vec{k}\cdot\vec{r}} 2E_0 \left(\cos\left((\frac{m_p\dot{x'}}{\hbar} - \frac{e\vec{A}\cdot\hat{x'}}{\hbar})a\right) + \cos\left((\frac{m_p\dot{y'}}{\hbar} - \frac{e\vec{A}\cdot\hat{y'}}{\hbar})a\right)\right)\psi(\vec{x}-\vec{r}) \\ = \sum_{\vec{r}} e^{i\vec{k}\cdot\vec{r}} E\psi(\vec{x}-\vec{r})\end{aligned} \tag{3.13}$$

We go ahead and choose the Landau gauge in which the vector potential is all along $\vec{y}$: $\vec{A} = B\ (0\hat{x} + x\hat{y} + 0\hat{z})$ where $B$ is the field strength. We also recall that $\frac{m\dot{x}a}{\hbar} = \frac{p_x}{\hbar}$, the momentum in the $\hat{x}$ direction where the vector potential $\vec{A}$ has no participation.

$$\begin{aligned}\sum_{\vec{r}} e^{i\vec{k}\cdot\vec{r}} 2E_0 \left(\cos\left((\frac{m_p\dot{x'}}{\hbar})a\right) + \cos\left((\frac{m_p\dot{y'}}{\hbar} - \frac{e\vec{A}\cdot\hat{y'}}{\hbar})a\right)\right)\psi(\vec{x}-\vec{r}) \\ = \sum_{\vec{r}} e^{i\vec{k}\cdot\vec{r}} E\psi(\vec{x}-\vec{r}) \\ E_0 \sum_{\vec{r}} e^{i\vec{k}\cdot\vec{r}} \left(e^{\frac{imp\dot{x}a}{\hbar}} + e^{\frac{-imp\dot{x}a}{\hbar}} + e^{\frac{imp\dot{y}a}{\hbar}} e^{\frac{-ieBxa}{\hbar}} + e^{\frac{-imp\dot{y}a}{\hbar}} e^{\frac{ieBxa}{\hbar}}\right)\psi(\vec{x}-\vec{r}) \\ = \sum_{\vec{r}} e^{i\vec{k}\cdot\vec{r}} E\psi(\vec{x}-\vec{r})\end{aligned} \tag{3.14}$$

Implementing the sum on $\vec{r}$ in Equation 3.14, we retrieve:

$$E_0\left(\psi(x+a,y;\vec{k}) + \psi(x-a,y;\vec{k}) + e^{\frac{-ieBax}{\hbar}}\psi(x,y+a;\vec{k}) + e^{\frac{+ieBax}{\hbar}}\psi(x,y-a;\vec{k})\right) = E\psi(\vec{x}) \tag{3.15}$$

Looking at the expression for translation operators (Equation 3.7) alongside Equation 3.15, we can see that introducing the vector potential $\vec{A}$ to the tunneling particle's $\vec{p}$ resulted in the application of translation operators scaled to the field strength within the above single-band Hamiltonian. This makes sense given that we were expecting the uniform applied field to alter the dynamics in a broadly regular way that scales with the field strength.

From this application of the time-independent Schrodinger equation to a gauge-field-modified single-band tight-binding dispersion for a particle, we have an equation which says something about the spectrum of a particle hopping under the applied field. To pursue this further, we continue to follow Hofstadter [73]:

We collapse $\psi(x, y; k)$ to $\psi(x, y)$ and write it in terms of indices on lattice sites: $\psi(x, y) = \psi(ma, na)$, as $\vec{r} = m\hat{x} + n\hat{y}$ indexes the discrete $x$ and $y$ coordinates in the lattice using $(m, n)$. We assume that the wavefunctions $\psi(x, y)$ look like Bloch wavefunctions in the $y$ direction, as application of a vector potential introduced no y-translation operators / made no modifications to the tight-binding nature of the y-direction Hamiltonian (Equation 3.15) in this gauge [73]. Therefore, the $y$ portion of $\psi(ma, na)$ should be a periodic in $a$ (already accomplished here!) and look like a plane wave. If $g(m)$ describes the wavefunction's $x = ma$ dependence, we arrive at:

$$\psi(ma, na) = e^{i\nu n} g(m). \tag{3.16}$$

Using this, we can decouple the unmodified $y$ translation portion of the dynamics and write an effective one-dimensional version of Equation 3.15 that represents hopping along $x = ma$. It is important to note that this equation still makes a statement about the eigenenergies for a particle experiencing two-dimensional dynamics; it's simply that our choice of gauge has placed the impact of the applied field along one direction; much like we selected a single band to get $W(\vec{k})$ earlier in this chapter, here we select some specific value of $\nu$ and are left with an equation in the single index $m$ which still contains the information about what the gauge field does to the particle eigenenergies but is friendlier to work with.

$$
\begin{aligned}
e^{i\nu(n)}g(m+1) + e^{i\nu(n)}g(m-1) + e^{\frac{-ieBax}{\hbar}}e^{i\nu(n+1)}g(m) + e^{\frac{+ieBax}{\hbar}}e^{i\nu(n-1)}g(m) \\
= \frac{E}{E_0}e^{i\nu(n)}g(m) \qquad (3.17) \\
g(m+1) + g(m-1) + e^{\frac{-ia^2Bm}{\hbar/e}+i\nu}g(m) + e^{\frac{+ia^2Bm}{\hbar/e}-i\nu}g(m) = \frac{E}{E_0}g(m)
\end{aligned}
$$

At this point, it's worthwhile to define $\alpha$: this is the dimensionless ratio of the flux through one plaquette (ring of four lattice sites in a two-dimensional tight-binding lattice) to one magnetic flux quantum. It is broadly used as the descriptor of the strength the flux through the plane of a Harper-Hofstadter lattice. Here, if we sweep a factor of $c$ a bit under the rug we get:

$$\alpha = \frac{1}{2\pi}\frac{a^2B}{\hbar/e} \qquad (3.18)$$

Deploying this in Equation 3.17, we get 'Harper's equation' in one dimension:

$$g(m+1) + g(m-1) + 2\cos(2\pi m\alpha - \nu)g(m) = \frac{E}{E_0}g(m) \qquad (3.19)$$

We can find the spectrum of eigenvalues $E/E_0$ for this differential equation; since we're now working with a lattice equation in the single dimension indexed by $m$, we can apply some periodicity conditions [73] and conclude that to achieve bounded wavefunctions $g(m)$, it is necessary for $\alpha$ to be rational, $\alpha = p/q$ where $p$ and $q$ are both some integers. $q$ is defined to index how many unit translations in $m$ under application of this hopping differential equation are needed to bring $g(m)$ back to itself. This makes sense – a stronger field, described by a larger $\alpha$, would generate a faster cyclotron orbit for an imaginary free two-dimensional electron. This intuition maps onto an expectation that fewer translations are needed to accomplish a period in the wavefunction along the remaining lattice dimension.

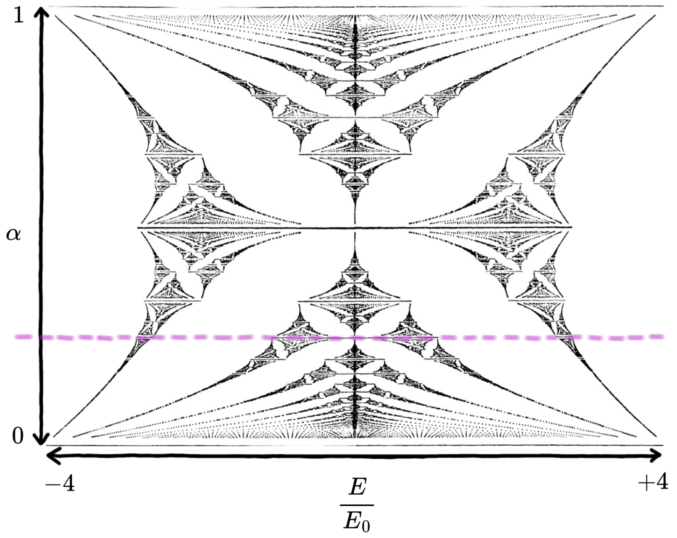

Figure 3.4: **Hofstadter's butterfly, a fractal spectrum for a charged particle hopping on a lattice under applied gauge field.** Energy eigenvalues are plotted for rational $\alpha$ and stretch from $+4$ to $-4$ times the hopping rate, which here is 1. Quarter-flux ($\alpha = 1/4$) is highlighted with a pink dashed line.

We can plot eigenvalues $E/E_0$, which range betwen 4 and -4 times the (unit) hopping, against rational values of $\alpha$ to extract the classic Hofstadter's butterfly. In this thesis we work with $\alpha = 1/4$, or 'quarter flux'. We call this out with a pink dashed line in Figure 3.4, plotted by Hofstadter for rational $\alpha$. At a quarter flux, the spectrum fragments into four bands, and the two center bands touch at a specific point. This leaves two large bulk band gaps to the right and left of band center – these are where edge modes in our finite, edge-possessing Harper-Hofstadter will live.

To summarize, we took the dispersion of a single tight-binding electron tunneling in a two-dimensional lattice, and made the Peierls substitution to include a uniform vector potential $\vec{A} = xB\hat{y}$ in the particle's canonical momentum. This resulted in complex phases $e^{\pm i\left(\frac{-a^2Bm}{\hbar/e}+\nu\right)}$ appearing on terms in the one-dimensional Harper's equation that describes lattice wavefunctions under translation.

Other presentations of the Peierls substitution, including Monika Aidelsburger's [6] which we follow closely in the next section, take this complex phase as axiomatic, and explore its meaning and implementation.

### *3.2.3 Aidelsburger's implementation of the Peierls phase*

In this section we'll describe a slightly different way of arriving at the same Harper equation, which provides the energy spectrum for a tight-binding particle propagating in 2D under an applied magnetic field.

Using the second-quantized creation and annihilation operators for particles on neighboring sites, Aideslburger contrasts the hopping part of a zero-field tight-binding Hamiltonian in two dimensions,

$$\frac{H}{\hbar} = -t \sum_{m,n} \left( \hat{a}^{\dagger}_{m+1,n} \hat{a}_{m,n} + \hat{a}^{\dagger}_{m,n+1} \hat{a}_{m,n} + h.c. \right), \tag{3.20}$$

with a similar Hamiltonan under an applied magnetic field, which now incorporates generic Peierls phases $\phi^{i}_{m,n} = -eA^{i}_{m,n}/\hbar$ on each hopping leg between sites:

$$\frac{H}{\hbar} = -t \sum_{m,n} \left( e^{i\phi^{x}_{m,n}} \hat{a}^{\dagger}_{m+1,n} \hat{a}_{m,n} + e^{i\phi^{y}_{m,n}} \hat{a}^{\dagger}_{m,n+1} \hat{a}_{m,n} + h.c. \right), \tag{3.21}$$

Here, rather than appearing as an addition of the vector potential to the particle's momentum $\vec{p}$, the Peierls substitution is asserted directly as a complex phase multiplier on the translation operators between lattice sites. This is based on the argument, detailed below, that the applied gauge field changes the lattice translations under which the particle's wavefunction can be expected to be periodic. This argument is ultimately the same as the argument delivered above that $q$ in flux $\alpha = p/q$ should be some integer number of single-dimension lattice translations under which the wavefunction, operating in a gauge choice where all of the effects of $\vec{A}$ appear along that dimension, returns to itself.

For a zero-field tight-binding Hamiltonian in two dimensions with lattice sites $(m, n)$, the translation operators, which translate the lattice over by a site, are the site-to-site hopping elements of $\hat{H}$ and commute with each other and with the Hamiltonian [205]:

$$\hat{T}_x = -t\sum_{m,n}\hat{a}^{\dagger}_{m+1,n}\hat{a}_{m,n}; \quad \hat{T}_y = -t\sum_{m,n}\hat{a}^{\dagger}_{m,n+1}\hat{a}_{m,n} \tag{3.22}$$

Introducing a vector potential modifies the Hamiltonian so that these operators don't necessarily commute with it, as there is now possibly some change in $\vec{A}$ on the scale of that translation. If we modify these translation operators to incorporate a complex phase like those we've seen enter into the Hamiltonian in Equation 3.15, and select this phase appropriately for the details of the applied flux and gauge we're using, we can get modified *magnetic* translation operators to commute with the Hamiltonian again:

$$\hat{T}^M_x = -t\sum_{m,n}e^{i\theta^x_{m,n}}\hat{a}^{\dagger}_{m+1,n}\hat{a}_{m,n}; \quad \hat{T}^M_y = -t\sum_{m,n}e^{i\theta^y_{m,n}}\hat{a}^{\dagger}_{m,n+1}\hat{a}_{m,n} \tag{3.23}$$

Aidelsburger [6] derives the requirement that, in order for these new operators to commute with $\hat{H}$ (but not necessarily with each other), they must bear a certain relationship to hopping phases $\phi_{m,n}$, the Peierls phases, acquired on lattice legs adjacent to $(m, n)$ and to the flux per plaquette (here square unit cell) $\Phi_{m,n}$, which can generically vary across the lattice if the field is nonuniform:

$$\theta^x_{m,n} = \phi^x_{m,n} + \Phi_{m,n}n; \quad \theta^y_{m,n} = \phi^y_{m,n} - \Phi_{m,n}m \tag{3.24}$$

$$\Phi_{m,n} = \phi^x_{m,n} + \phi^y_{m+1,n} - \phi^x_{m,n+1} - \phi^y_{m,n} \tag{3.25}$$

These variables are depicted on a schematic lattice section in Figure 3.6. For a uniform synthetic field like we use in this thesis, $\Phi_{m,n} = \Phi$ is constant for each plaquette in the lattice.

The modification of tunneling terms in the Hamiltonian with the multiplication of a complex phase factor $\phi^i_{m,n}$ enforces the acquisition of a Peierls phase for a particle hopping between a pair of sites of the lattice. A particle tracing out some trajectory around the lattice

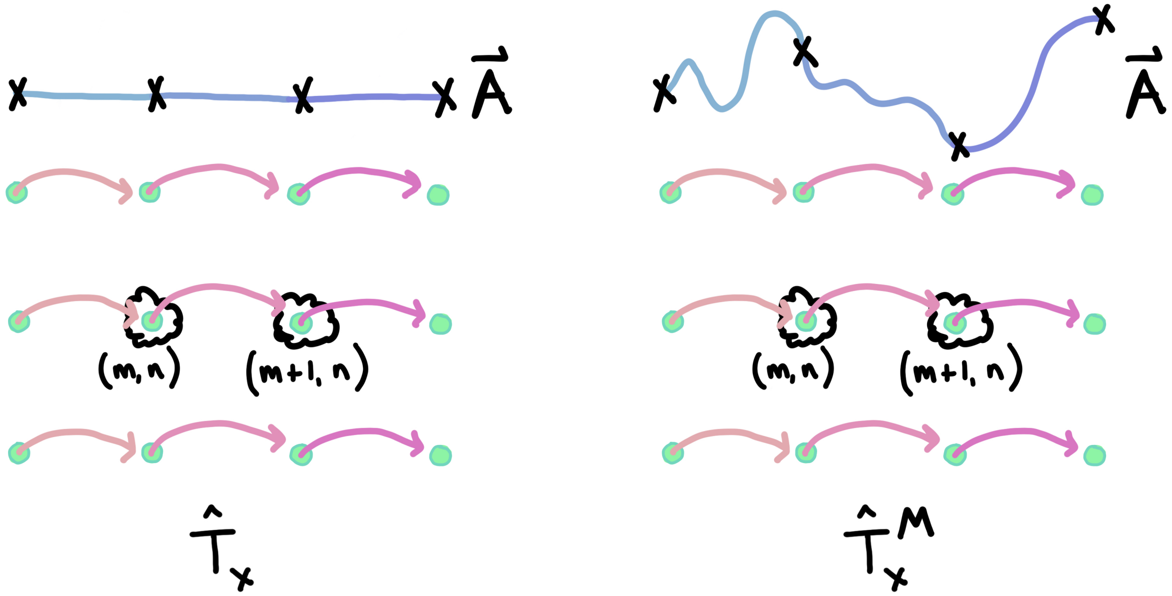

Figure 3.5: **Cartoon of non-magnetic and magnetic translation operators.** A discrete spatial lattice is plotted alongside a continuous spatial vector potential $\vec{A}$. The vertical axis of $\vec{A}$ represents its position in some abstract parameter space; coordinates at the same height indicate that $\vec{A}$ holds all the same parameter values.

Translation operators, in both cases, effect a site-wise translation on the lattice. At left, for a nonexistent vector potential (which is a constant across parameter space), $\hat{T}_x$ commutes with the Hamiltonian. At right, a present vector potential $\vec{A}$ may vary in such a way that it's not constant at each lattice point accessible to the translation operator $\hat{T}_x$. We introduce modified translation operator $\hat{T}_x^M$ for this case that ends up enforcing a complex phase on hopping terms in $\hat{H}$.

will continue acquiring phase as it jumps; if it returns to its original position, that acquired phase may wash out to nothing, or it may hold some other value. In this way, the Peierls phases on tight-binding hopping, which we've asserted inscribe a magnetic field, produce an Aharonov-Bohm phase like that acquired by a particle tunneling in the 2D continuum around a flux-threaded region.

This is the most intuitive explanation for the Peierls phases $\phi_{m,n}$ – whereas here mathematically, and eventually in our experimental implementation, we enforce hopping phases that end up realizing a phase acquisition on a charged particle tunneling in a loop in our system, in a two-dimensional plane threaded by some actual magnetic flux, the presence of that flux will enforce a phase on a charged particle tunneling in a loop.

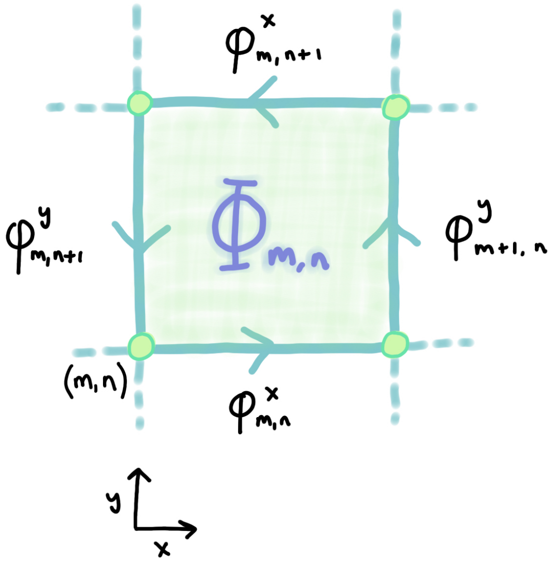

Figure 3.6: **Plaquette schematic.** Adapted from Figure 2.2 of [6]. The Peierls phases are those on the individual hopping legs between lime-green lattice sites.

For a specific uniform gauge field across the lattice, for example the $\alpha = 1/4$ flux we use in this thesis, each plaquette may be threaded by some fraction of a flux quantum, and it helpful to define a set of magnetic translation operators that may generate non-single-site translations such that they cover a 'magnetic unit cell' and tile a region enclosing a full flux quantum. Such translation operators will commute with each other, in addition to commuting with $\hat{H}$, as the vector potential should return to itself under lattice translations by both operators.

Aidelsburger picks a magnetic unit cell, for a quarter-flux ($p/q = 1/4, q = 4$) case, that is 1 lattice coordinate high and 4 long, enclosing a single flux quantum. She thus defines

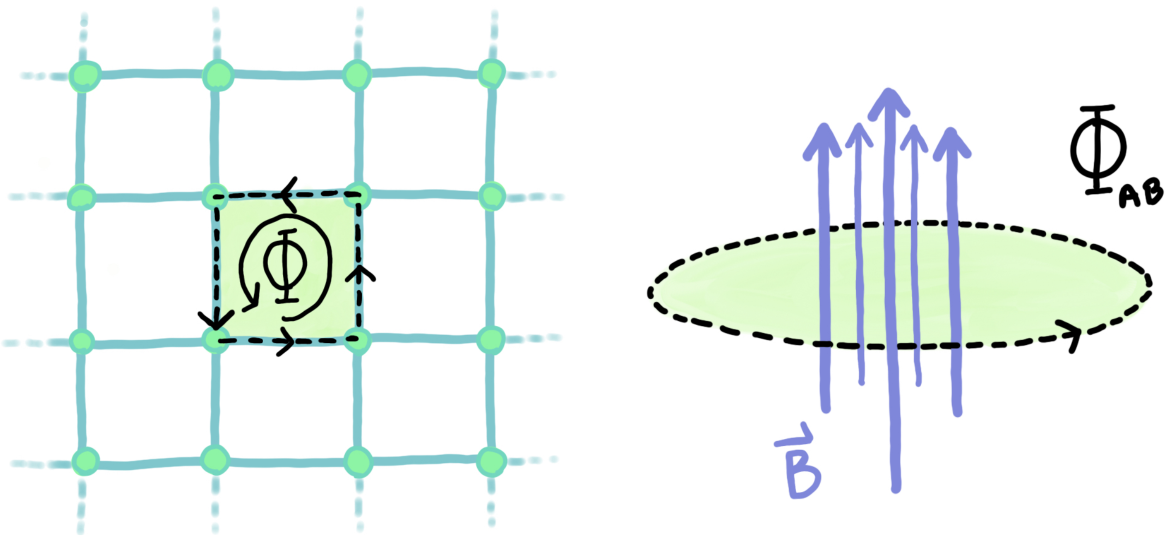

Figure 3.7: **Aharonov-Bohm analogy for Peierls phases.** At left, an excitation, tunneling in our tight-binding model with hopping phases that realize a uniform magnetic field felt by that particle, acquires some phase $\Phi$ per plaquette. At right, an electron, looping in a closed path around a regime threaded by some flux, acquires an Aharonov-Bohm phase $\Phi_{AB}$ commensurate with the flux enclosed.

commuting magnetic translation operators:

$$\hat{M}_x^1 = \sum_{m,n} \hat{a}^\dagger_{m+1,n}\hat{a}_{m,n}; \quad \hat{M}_y^q = \sum_{m,n} \hat{a}^\dagger_{m,n+q}\hat{a}_{m,n} \tag{3.26}$$

She picks a wavefunction that is unchanged under the relevant magnetic translation operators rather than standard lattice translation operators as seen earlier:

$$\begin{aligned} \Psi_{m,n} = e^{ik_x ma} e^{ik_y na}\psi_n; \quad \psi_{n+q} = \psi_n \\ -\pi/a \leq k_x \leq \pi/a; \quad -\pi/(aq) \leq k_y \leq \pi/(aq) \end{aligned} \tag{3.27}$$

This wavefunction fulfills a version of Bloch's theorem that incorporates the acquisition of a geometric phase upon hopping:

$$\begin{aligned}\hat{M}_x^1\Psi_{m,n} &= \Psi_{m+1,n} = e^{ik_xa}\Psi_{m,n}\\ \hat{M}_y^q\Psi_{m,n} &= \Psi_{m,n+q} = e^{qik_ya}\Psi_{m,n}\end{aligned} \tag{3.28}$$

Plugging $\Psi_{m,n}$ into the time-independent Schrodinger equation made with the hopping portion of the Harper-Hofstadter Hamiltonian, we get:

$$\begin{aligned}-t\left(e^{-i\Phi n}\Psi_{m+1,n} + e^{i\Phi n}\Psi_{m-1,n} + \Psi_{m,n+1} + \Psi_{m,n-1}\right) &= E\Psi_{m,n}\\ -t\left(e^{-i\Phi n}e^{ik_xa}\psi_n + e^{i\Phi n}e^{-ik_xa}\psi_n + e^{ik_ya}\psi_{n+1} + e^{-ik_ya}\psi_{n-1}\right) &= E\psi_n\\ -t\left(2\cos\left(k_xa - \Phi n\right)\psi_n + e^{ik_ya}\psi_{n+1} + e^{-ik_ya}\psi_{n-1}\right) &= E\psi_n\end{aligned} \tag{3.29}$$

And we're back to Harper's equation, introduced earlier in Equation 3.19. Here we retrieved this equation by applying Peierls phases to hopping elements in the Harper-Hofstadter Hamiltonian, selecting a gauge that aligns the vector potential $\vec{A}$ with a convenient dimension, and enforcing periodicity expectations for wavefunctions $\Psi_{m,n}$ under the magnetic translation operators $\hat{M}$.

### *3.2.4 An implementation of the Harper equation*

Excitingly, experimental work was done by the now Google-affiliated group at Santa Barbara using a chain of nine coupled superconducting qubits to realize a system governed by Harper's equation [171]. In this case, the experimentalists applied a periodic potential along the single spatial lattice dimension available to them. By altering that potential, they were able to explore a range of synthetic flux strengths and trace out the eigenthings that make up Hofstadter's butterfly.

The Harper model can describe a single-quasimomentum slice of the 2D Harper-Hofstadter model realized on a cylinder (with one periodic boundary condition). Roushan et al. take the hopping part of the Harper-Hofstadter Hamiltonian,

$$\frac{H}{\hbar} = -t\sum_{m,n}\left(\hat{a}^{\dagger}_{m,n}\hat{a}_{m+1,n} + h.c.\right) - t\sum_{m,n}\left(e^{i2\pi\alpha m}\hat{a}^{\dagger}_{m,n}\hat{a}_{m,n+1} + h.c.\right), \tag{3.30}$$

and apply a periodic boundary condition along one dimension, substituting the quantum Fourier transform $\hat{a}^{\dagger}_{m,n} = \sum_k e^{-ikn}\hat{a}^{\dagger}_{m,k}$ to retrieve:

$$\begin{aligned}\frac{H}{\hbar} = -t\sum_{m,n}\left(\sum_k e^{-ikn}\hat{a}^{\dagger}_{m,k}\sum_k e^{ikn}\hat{a}_{m+1,k} + h.c.\right)\\ -t\sum_{m,n}\left(e^{i2\pi\alpha m}\sum_k e^{-ikn}\hat{a}^{\dagger}_{m,k}\sum_k e^{ik(n+1)}\hat{a}_{m,k} + h.c.\right)\end{aligned} \tag{3.31}$$

For a particular quasi-momentum identifier $k$, this leaves the same physics we've now seen twice above:

$$\frac{H_k}{\hbar} = -t\sum_{m}\left(\hat{a}^{\dagger}_{m,k}\hat{a}_{m+1,k} + h.c.\right) - t\sum_{m}\left(2\cos(2\pi\alpha m + k)\hat{a}^{\dagger}_{m,k}\hat{a}_{m,k}\right) \tag{3.32}$$

They [171] realize this for a specific $k$ and trace out Hofstadter's butterfly by looking at eigenenergies in a 9-qubit 1D array at different applied synthetic fluxes achieved by a potential of strength $\Delta$ modulated across the chain.

$$\frac{H}{\hbar} = \Delta\sum_{m}\cos 2\pi n\alpha\hat{n}_m + -t\sum_{m}\left(\hat{a}^{\dagger}_{m}\hat{a}_{m+1} + \hat{a}^{\dagger}_{m+1}\hat{a}_{m}\right) + \sum_{m}\omega_m\hat{n}_m \tag{3.33}$$

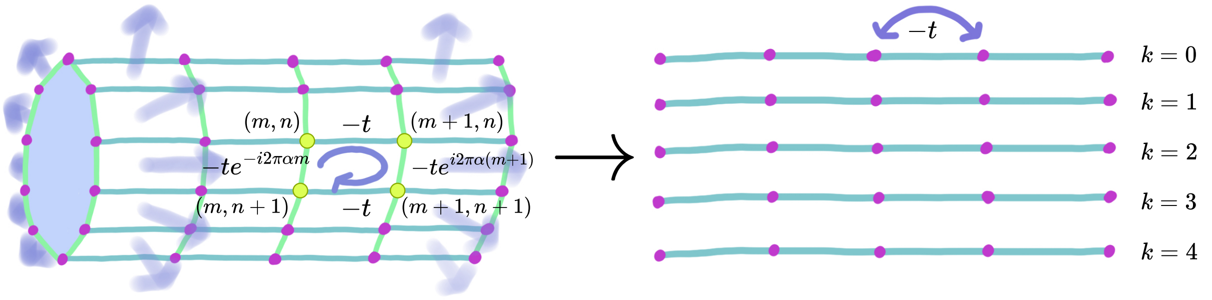

Figure 3.8: **Mapping from Harper-Hofstadter model on a cylinder to 1D Harper model.** Implementing cylindrical boundary conditions on one dimension of a 2D Harper-Hofstadter lattice allows one to decouple bands of lattice physics indexed by different $k$, working with one $k$ value at a time. This figure is adapted from the supplement of the paper [171] implementing the 1D Harper model with superconducting qubits.

### *3.2.5 Berry phase and the Chern number*

Above, we've discussed above how applying a gauge field modifies the lattice translation operators of a tight-binding system, impacting energy-momentum relationships for particles obeying such a Hamiltonian. We've also discussed how a particle hopping in a loop in a Harper-Hofstadter lattice accumulates some Aharonov-Bohm phase made by summing Peierls phases that's related to the hopping trajectory, and directly proportional to the area that trajectory encloses when the gauge field is spatially uniform. This accumulated trajectory-sensitive phase, which persists even if the state of the system returns to itself after the particle hops in some loop, is an example of a Berry phase. What is a Berry phase?

If one prepares a system in an eigenstate and then varies the Hamiltonian parameters slowly (adiabatically), one can move the the system around Hamiltonian-parameter space without ejecting it from an eigenstate. This technique is used by my collaborators [172, 168] to prepare excitations in wildly-detuned lattices of coupled qubits and then move the system into a Bose-Hubbard lattice of resonantly coupled qubits while keeping a single excitation present in an eigenstate. If you slowly wiggle Hamiltonian parameters so that your state of interest traces out a loop in parameter space and comes back to itself, that state $|\psi\rangle$ will accrue a complex phase, $|\psi\rangle \to e^{i\gamma}|\psi\rangle$, which incorporates both the dynamical evolution $e^{-iEt/\hbar}$ that just happens to an eigenstate persisting through time under the Hamiltonian, and an additional 'geometric' (not dynamical) phase $e^{i\gamma+iEt/\hbar}$ from tracing out that parameter-space loop. This geometric phase is the Berry phase [189].

Berry's original paper introducing this phase [19] argues that the Aharonov-Bohm effect [2] is an example of the acquisition of a geometric phase; a particle propagating under the rules of dynamical evolution for an eigenstate will, if it travels in a loop threaded by a flux, acquire some phase from that travel even if it returns to its original location. Here, the gauge-sensitive vector potential associated with the magnetic flux is a version of the more-general 'Berry connection' which one integrates along a particle trajectory in parameter space to produce the gauge-insensitive Berry phase. And the magnetic flux itself, which one can integrate over the area enclosed by the tunneling photon to produce a Berry phase, is a version of the more-general 'Berry flux'.

In the context of a lattice-physics system, like a tight-binding lattice realized, boundaryless, on a torus in $x$ and $y$, we can retrieve the Chern number by integrating the 'Berry flux' across that system's first Brillouin zone. When we move from a tight-binding model to one with an applied gauge field, we alter the system's Hamiltonian-commuting translation operators to be the magnetic ones (Equation 3.2.3). This, in turn, modifies the lattice Brillouin zone as seen in our treatment of the new magnetic translation operators above [9], providing the alteration necessary to yield a nonzero Chern number.

For magnetic Bloch-like wavefunctions $\psi_k(m,n)$ for position $\vec{x} = (ma, na)$ in a lattice, obeying

$$\Psi_k(m,n) = e^{ik_x ma} e^{ik_y na} \psi_k(m,n);\ \ \psi_k(m,n+q) = \psi_k(m,n), \tag{3.34}$$

we recall that in the quarter-flux Harper-Hofstadter lattice we work with $q = 4$, and also that the magnetic Brillouin zone (also defined in Equation 3.27) is spanned by lattice momenta

$$\frac{-\pi}{a} \leq k_x < \frac{\pi}{a};\ \ \frac{-\pi}{qa} \leq k_y < \frac{\pi}{qa}. \tag{3.35}$$

Following David Tong, who presents a wonderful introduction to this material [189], we can express the phase winding of some state around this magnetic Brillouin zone via the Berry connection,

$$\mathcal{A}_i(\vec{k}) = -i\langle\psi_k(\vec{x})|\frac{\partial}{\partial k_i}|\psi_k(\vec{x})\rangle. \tag{3.36}$$

Here generic $i$ indexes the different choices of states $k$ – in two dimensions, these are identified by lattice momenta $k_x$ and $k_y$. The Berry curvature, or Berry flux in the Aharonov-Bohm analogy, is

$$\mathcal{F}_{xy} = \frac{\partial \mathcal{A}_x}{\partial k_y} - \frac{\partial \mathcal{A}_y}{\partial k_x} = -i\langle\frac{\partial\psi}{\partial k_y}|\frac{\partial\psi}{\partial k_x}\rangle + i\langle\frac{\partial\psi}{\partial k_x}|\frac{\partial\psi}{\partial k_y}\rangle \tag{3.37}$$

This certainly does look like a field strength derived from some magnetic vector potential that enforces a phase winding! We obtain the Chern number by integrating this Berry flux over the magnetic first Brillouin zone:

$$C = \frac{-1}{2\pi}\int_{\text{Magnetic Brillouin zone}} \mathcal{F}_{xy} d^2k \tag{3.38}$$

The Chern number is a quantized integer topological invariant, related to the Hall conductance, whose nonzero presence is a common signifier of topology [72]. This invariant is robust under smooth perturbation, accounting for the robustness of the associated topological materials properties; one would have to do a whole lot (perturbing the band structure enough to open or close a band gap! [9]) in the lattice to structurally modify the whole Brillouin zone in order to change this integral's value. This again illustrates how topological properties derive from the global properties of the bulk.

People discussing topology often reference the 'bulk-edge correspondence', the idea that at the interface between some bulk topological material and a regime with a different topological invariant (the 'edge'), some number of localized edge states or modes will exist, dictated and protected by the topological properties of the system bulk. In Chern insulator, the topological invariant of the Chern number sets the number of nondegenerate localized channels spanning the bulk band gaps [6] that arise at the system edge.

The fact that spatially localized, directional conducting channels appear at the edges of Chern insulators is a hallmark of topological insulators and motivates the interest of many people who build engineered versions of these systems. The localization of an edge excitation, and its zippy propagation velocity relative to the speed of excitations in the insulating bulk, are upheld and protected by the overall Chern insulator topology, lending the system robustness to smooth and small perturbation as it takes a lot of effort to alter the Chern number. A classic genre of experiment with synthetic Chern insulators, an example of which is depicted in Figure 3.11, introduces a barrier to tunneling of an edge excitation and profiles the topology-rooted preservation of directional, edge-localized transport.

While conducting edge states of a topological bulk arise at the boundary between this bulk and vacuum (which has no Chern number!), such states more generally arise at interfaces between regimes with different topological invariants, as depicted in Figure 1.1. A range of experimental approaches have leveraged the presence of such edge states at a generic boundary to build topological systems showing transport along a dynamically-modifiable ‘edge’: Cheng et al. [40] physically alter sites in a topological photonic array of copper pillars to change the shape of a domain wall that provides a site for chiral edge-state transport. Pirie et al. [150] offer a simulation-based proposal to use ultrasound heating of a thermally-responsive baseplate supporting a topological phononic crystal of steel pillars to dynamically direct edge conduction between topologically-trivial and topologically spin-Hall regimes, arguing that this could be useful for computing. Zhao et al. [213] leverage non-Hermitian physics, dynamically setting up degenerate right- and left-handed edge modes in a topological photonic ring resonator array by optically pumping parts of it to produce a programmable boundary between regions of gain and loss.

Overall, the presence of a topologically-protected conducting edge, which can suffer some degree of local loss and disorder without shredding the Chern-number-boundary that supports the edge state, is a powerful tool for reliably moving light.

### *3.2.6 Relationship to Bose-Hubbard model*

Because the Harper-Hofstadter model as we've presented describes noninteracting particles, one thinks of it as applying to one boson tunneling around; to get the kind of particle-particle interactions one would hope to see in a model exploring the many-body phases seen in quantum matter, one would need to add more elements to this Hamiltonian.

Another description for tunneling bosons which incorporates particle-particle interactions is the Bose-Hubbard model: here, in addition to nearest-neighbor tunneling, particles experience interactions when occupying the same site, and the system can be subjected to a global chemical potential which supplies a particle number, to which this model is sensitive. For a 1D chain, neglecting the chemical potential, this Hamiltonian can be written as:

$$\frac{H}{\hbar} = -J \sum_{m} \left( \hat{a}_m^\dagger \hat{a}_{m+1} + \hat{a}_{m+1}^\dagger \hat{a}_m \right) + \frac{U}{2} \sum_{m} \hat{n}_m \left( \hat{n}_m - 1 \right) + \sum_{m} \omega_m \hat{n}_m \tag{3.39}$$

Here $\hat{n}_i = \hat{a}_m^\dagger \hat{a_m}$ is the photon number operator for site $m$, $J$ is the same thing as $t$ from above, a hopping rate, and $U$ is the strength of the particle-particle interaction on each site. This is the Hamiltonian of some work, not described in this PhD thesis, in which I also participated [172, 168] – realizing a model which incorporates particle-particle interactions on sites opens up a world of many-body physics to explore.

This particular Bose-Hubbard model is not topological. To more easily compare with the Harper-Hofstadter Hamiltonian shown above, let's look at the Bose-Hubbard Hamiltonian in 2D, with $J$ written as $t$ – this makes it easy to see the lack of complex phases modifying the hoppings, and added particle-particle interactions:

$$\begin{aligned}\frac{H}{\hbar} = \sum_{m,n} \omega_{m,n} \hat{a}^{\dagger}_{m,n} \hat{a}_{m,n} - t \sum_{m,n} \left( \hat{a}^{\dagger}_{m,n+1} \hat{a}_{m,n} + \hat{a}_{m,n} \hat{a}^{\dagger}_{m+1,n} + h.c. \right) \\ + \frac{U}{2} \sum_{m,n} \hat{a}^{\dagger}_{m,n} \hat{a}_{m,n} \left( \hat{a}^{\dagger}_{m,n} \hat{a}_{m,n} - 1 \right)\end{aligned} \tag{3.40}$$

To get a model which incorporated both particle-particle interactions on each site and topology from a synthetic gauge field, we would instead need to write:

$$\begin{aligned}\frac{H}{\hbar} = \sum_{m,n} \omega_{m,n} \hat{a}^{\dagger}_{m,n} \hat{a}_{m,n} - t \sum_{m,n} \left( e^{-i2\pi\alpha m} \hat{a}^{\dagger}_{m,n+1} \hat{a}_{m,n} + \hat{a}_{m,n} \hat{a}^{\dagger}_{m+1,n} + h.c. \right) \\ + \frac{U}{2} \sum_{m,n} \hat{a}^{\dagger}_{m,n} \hat{a}_{m,n} \left( \hat{a}^{\dagger}_{m,n} \hat{a}_{m,n} - 1 \right)\end{aligned} \tag{3.41}$$

## 3.3 Survey: Synthetic gauge fields for photons!

As demonstrated by the implementation of the 1D Harper model via periodic potential in the previous section, there are a range of ways of imparting such a synthetic gauge field on photons, many of which rely on artificially introducing this complex Peierls phase on hopping terms to an engineered lattice model for light.

A set of broad reviews is available describing different ways of imparting topology (a broad regime of pursuits which includes the addition of synthetic gauge fields to mimic the band structures of topological insulators) to photonic systems [140, 155] and those realized in particular in circuit quantum electrodynamics [89, 32]. The work laid out in these reviews falls into five broad categories of methods used to source topology:

*Method 1: Exploit effective spin-orbit coupling in nanophotonically confined light.* Much of the wealth of work done in experimental topological photonics in the past fifteen years has been in silicon photonics, in nanophotonic systems where the tight (subwavelength) confinement of light can enable an effective spin-orbit interaction for that light where its polarization determines its propagation direction. Many works implementing topological band structures in silicon photonics realize the quantum spin Hall effect, in which light with a different 'pseudospin' sees a different propagation direction.

Because this model does not break time reversal symmetry, this results in degenerate right- and left-handed chiral edge channels in engineered quantum spin Hall lattices; selectively coupling, or emitting to, their topological edge modes can be accomplished by choosing the direction of transmission or the state of a coupled emitter. Examples of this work can be found in both photonics [68, 66, 38] and atom-waveguide coupling [147]. Notably, Shomroni et al. [180] use the connection between the state of an emitter and photonic dynamics in a waveguide to realize a switch controlling the propagation direction of light in one such optical system. And Cheng et al. [40] realize spin-Hall physics similar to that mentioned above in optical photonic systems, but using copper and at microwave frequencies!

Achieving strong coupling of nonlinearities to such silicon photonics platforms can be challenging; Barik et al. [13] laid out the platform for this and then realized it [14] by exploiting the bulk-edge correspondence to set up topological edge modes at the boundary between two photonic crystals which host different Berry curvatures. As illustrated in Figure 3.9, they strongly coupled a quantum dot to the counterpropagating modes in this boundary, an effective chiral resonator, emitting selectively to one or the other depending on the polarization ($\sigma^{\pm}$) of the transition excited in the quantum dot. By applying a bias field they achieved energy resolution between emission of opposite chiralities from the quantum dots. Strong coupling was demonstrated by Purcell enhancement of emission from the quantum dot to an edge channel, rather than by any coherent transfer of excitation.

*Method 2: Build a twisted geometry for the light.* In optics, topological states of photons have been realized [173], and used to build Laughlin states [45], by twisting the landscape in which photons propagate rather than putting them in a simple landscape and modifying their

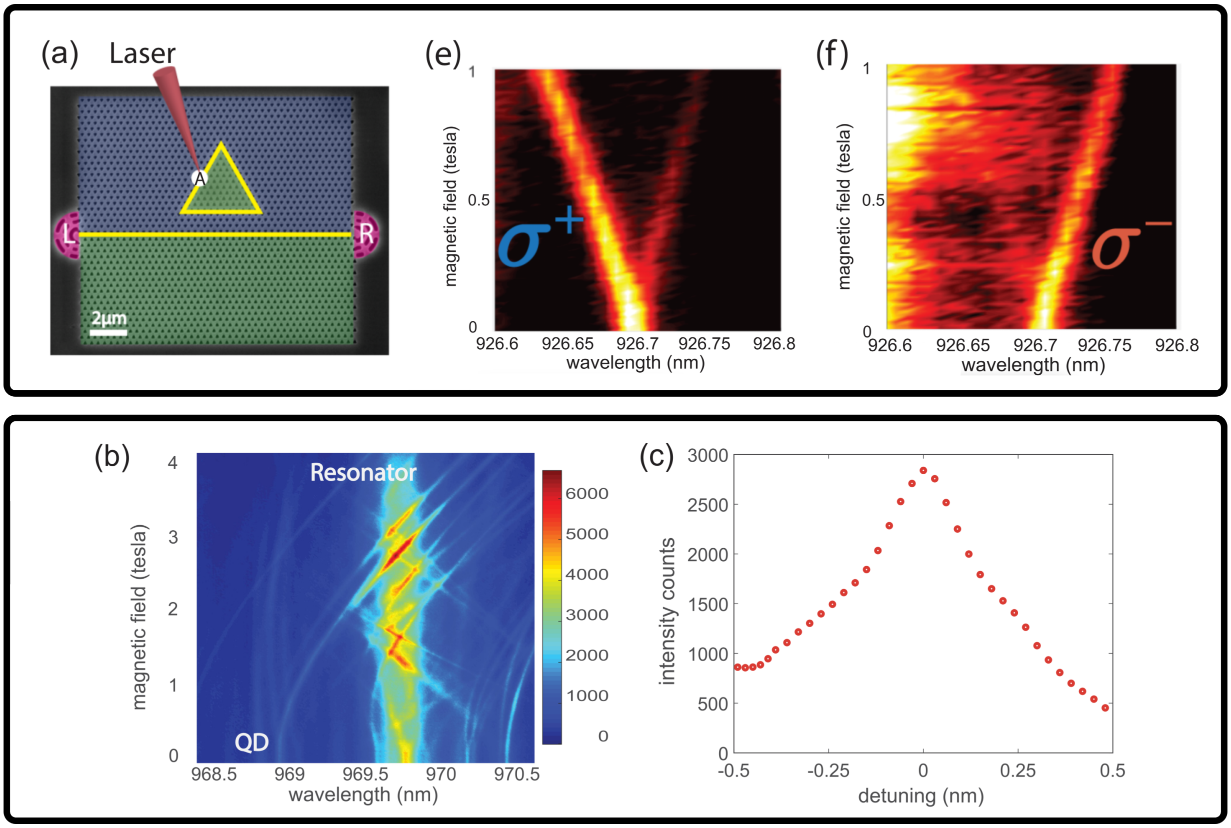

Figure 3.9: **Emission from a quantum dot to chiral channels in a photonic metamaterial.** Reprinted with permission from Mohammad Hafezi and Sabyasachi Barik: *Physical Review B*, 'Chiral quantum optics using a topological resonator', v.1 p.205303, 2020. Copyright (2020) by the American Physical Society [14]. The **top** panel reproduces part of Figure 3: in **a**, the authors use a laser to excite transitions of a quantum dot sited along a triangular chiral channel made of the interface between two materials hosting different topological invariants. Excitations propagating in one direction will preferentially couple out to grating $R$ along a chiral boundary, and those propagating in the other will couple out to grating $L$. In **e** and **f**, photoluminescence measurements taken at grating couplers $L$ and $R$ respectively show that as a bias field splits degenerate quantum dot transitions of opposite polarization apart via Zeeman shift, energy resolution between chiral light-matter interactions emerges as each polarization of dipole transition emits to a channel of opposite chirality. The **bottom** panel reproduces part of Figure 5: in **b**, as a bias field tunes Zeeman-split quantum dot transitions through resonance with the topological resonator, the intensity of their photoluminescence is increased. In **c**, a cut of the intensity of a quantum dot's emission is shown as that dot is tuned across resonance with the chiral channel, showing Purcell enhancement by a factor of $\sim 3$.

propagation properties with applied field or complex hopping. Martinez, Chiu et al. [116] implemented a similar 'twisting' approach in a circuit QED platform – by flipping an asymmetric coupling on one-site of a four-qubit ring, they generated a $\pi$-flux Harper-Hofstradter lattice in a way that amounted to producing a Mobius geometry.

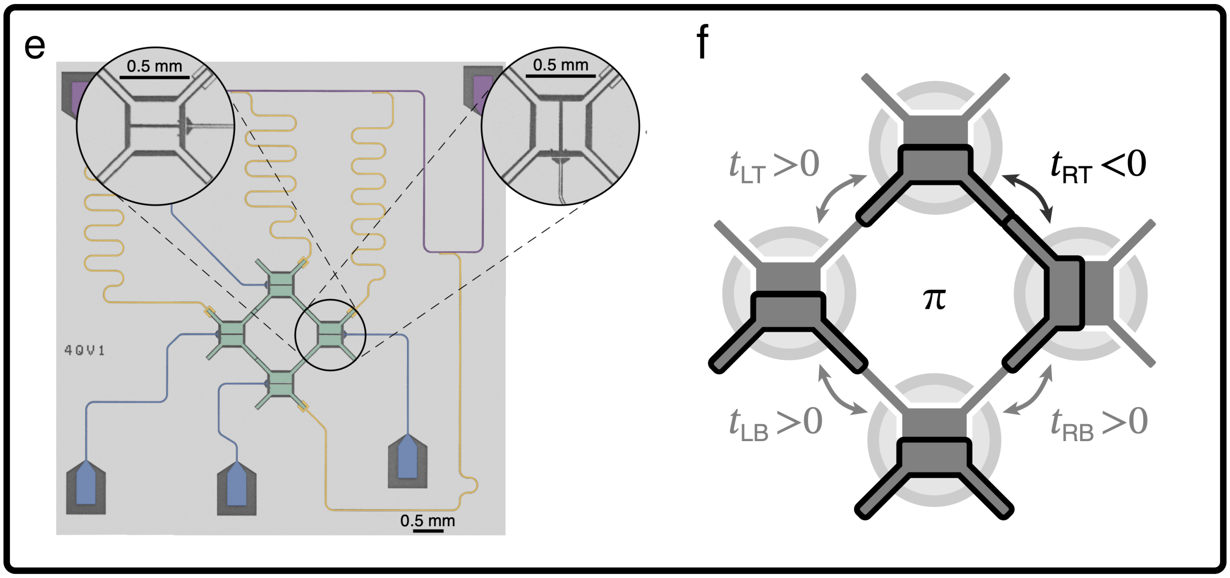

Figure 3.10: **$\pi$-flux lattice formed from a ring of transmon qubits.** Reprinted with permission from Christie Chiu: *arXiv*, 'Flat-band localization and interaction-induced delocalization of photons', arXiv:2303.02170v2, 2023. [116]. Panel reproduces part of Figure 1. In **e**, a false-color of the photograph highlights the transmon ring in green. In **f**, a cartoon schematic shows how flipping the orientation of capacitive couplers of one qubit in the ring asserts a negative tunneling rate between a pair of transmons. The authors use this $\alpha = 1/2$ synthetic flux that enforces a geometric phase of $\pi$ on a loop-tunneling photon to explore localization and delocalization of photons hopping on a lattice that incorporates a flat band (courtesy of the synthetic gauge field) and onsite interactions (courtesy of the transmon nonlinearity, as is possible in Bose-Hubbard chains [172]).

*Method 3: Construct the photonic system out of a material that responds to magnetic field.* Constructing a photonic lattice out of a material that itself hosts a magneto-optical response, and then applying an external field, can enforce the effects of magnetic field on photons exploring the engineered material landscape. The original, pioneering experimental work [203] in topological photonics used this approach, demonstrating a time-reversal-symmetry-broken chiral edge state in a microwave photonic platform realized as an array of field-responsive ferrite YIG posts with a conducting boundary. This work by Wang et al. [203] emerged a year after the theory proposals of Haldane and Raghu [69, 157] suggested that such directional modes were possible to realize in topological photonics platforms and advertised the futures of such platforms, when combined with nonlinearities, to emulate fractional quantum Hall physics. Figure 3.11 illustrates the simulated steady-state electric field and power flow along the edge of a ferrite pillar array subjected to a bias field.

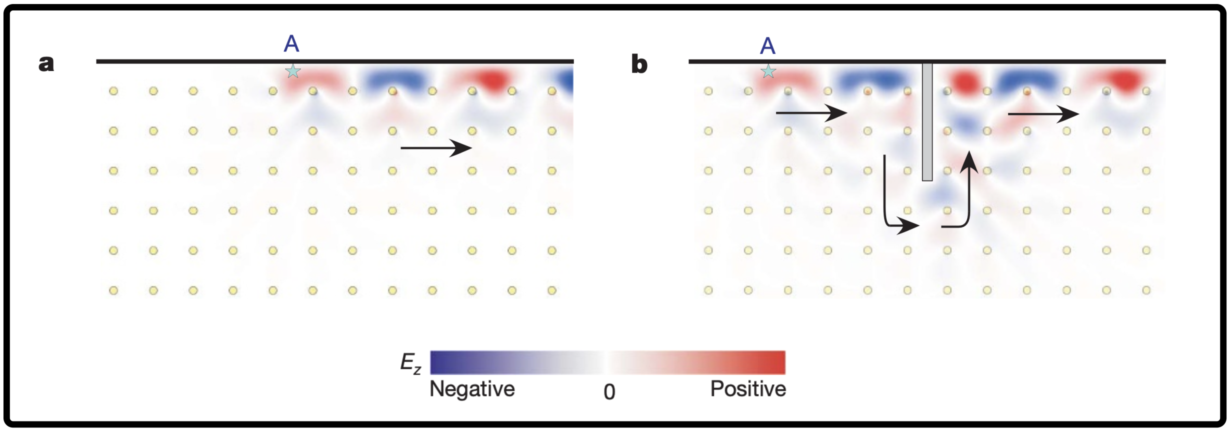

Figure 3.11: **Robust propagation of chiral edge states in a ferrite pillar array.** Reprinted with permission from *Nature*, 'Observation of unidirectional backscattering-immune topological electromagnetic states', v.64 p.772-776, 2009 [203]. Panel reproduces part of Figure 2. In **a**, simulation shows the electric field and direction of power flow (black arrow) when a drive is injected at site A: injected microwaves propagate unidirectionally along the system's chiral edge channel. The black line at the top illustrates the conducting boundary at the edge of the array of ferrite pillars (yellow dots). In **b**, when a chirally propagating edge state is incident upon a conducting intrusion (gray bar), the simulated field pattern wraps around that edge disorder and returns to supporting robust directional movement of power in the chiral system edge.

Other work like this introduced nonlinearity by building a photonic system out of GaAs to investigate topological exciton-polaritons, which were still largely photonic [87]. It could also be argued that the proposal from Wang et al. [201] to make a metamaterial lattice out of SQUIDs and source an effective gauge field from their response to an external flux bias counts too.

The work described in this thesis is best categorized as an application of Method 3 – we generate a synthetic gauge field from a real gauge field, by capitalizing upon the effect said real bias field has upon a material incorporated into our system. We deploy this material (ferrite Yttrium-Iron-Garnet (YIG) crystals) selectively alongside permanent magnetic field to modify the phase windings of local lattice sites in a way that can be re-broadcast as a global Peierls phase on hoppings that generates a Harper-Hofstadter lattice for tunneling photons.

Reviews and commentaries in the field often allude to the challenge of achieving strong enough time-reversal-symmetry breaking via magneto-optical materials responses to see really strong backscatter protection in topological photonic systems at optical frequencies (see, e.g., a proposal to do chiral quantum optics with color centers in diamond coupled to a photonic crystal [146]). Working at microwave frequencies, as Wang et al. [203] do, addresses this issue by allowing use of materials with a stronger field response. But why is achieving strong time-reversal symmetry breaking a concern?

In the example of our chiral lattice platform, a more substantial splitting of lattice site photonic modes of right- and left-handed chirality is ultimately attributable to a stronger applied bias field. The larger splitting provides a wider band of energies in which the realization of the Harper-Hofstadter model is isolated with input from only chiral modes of the appropriate handedness. So stronger response to an applied magnetic field ultimately amounts to a protection of the handedness of the chiral system, and thus protection from backscatter/unintended scatter in the lattice edge channels. In our data, to be detailed later, we see a distinct difference in the group velocity of wavepackets in edge channels on different sides of the lattice band center – the higher-frequency edge eigenmodes are moved around in the spectrum due to the influence of virtual photonic coupling through the (closer to top of band) split-off ‘backwards’-handed chiral site modes. This changes the edge wavepacket dispersion and ultimately makes wavepackets in the higher-frequency edge channel experience a faster group velocity.

*Method 4: Use time modulation to make an effective synthetic gauge field* Instead of relying on static aspects of the system construction, some groups generate a synthetic gauge field for photons by relying on time modulation [53, 46]. In the technique of Floquet engineering, application of a time-periodic external drive can add new attributes to the system Hamiltonian, creating an effective long-time Hamiltonian that incorporates new physics, like the addition of topology to the band structure. If you 'catch' the system at the right periodicity, you see the evolution of the target physics! Examples of experimental work using Floquet engineering to generate synthetic gauge fields include a number of works across photonics [53, 164, 111, 170, 183, 127]. Floquet generation of broader topology (here the Su-Schrieffer-Heeger model, which does not involve a synthetic gauge field) was also realized in circuits by Cai et al. [28].

The 2017 work by Roushan et al. [170] with a ring of three qubits is particularly important in reference to the work in this thesis. The experimenters sinusoidally modulate the couplings between pairs of mutually detuned qubits at the frequencies of the qubit-qubit detunings. This modulation re-builds coupling between the qubits, and the phase of this modulation imparts a phase on the hoppings. The overall phase a photon picks up while hopping around this ring realizes the synthetic flux. By changing the sign of this overall phase, the authors are able to alter the direction of chiral photonic transport, working with a system that also incorporates nonlinearity via the qubits! As shown in Figure 3.12, they measure hopping in both directions along the couplers between qubits in this smallest-possible three-site loop.

*Method 5: Build a synthetic gauge field in synthetic dimensions.* A final method of building a synthetic gauge field for photons is to build part of it in a dimension that departs from real space. It is possible to construct a lattice along some degree of freedom internal to a system, typically momentum (i.e. along a lattice of modes with different frequency), assisting couplings between lattice sites by supplying drives. Lee et al. [98] do this to generate a tight-binding chain across a set of modes that hosts propagating wavepackets. Dutt et al. [51] do

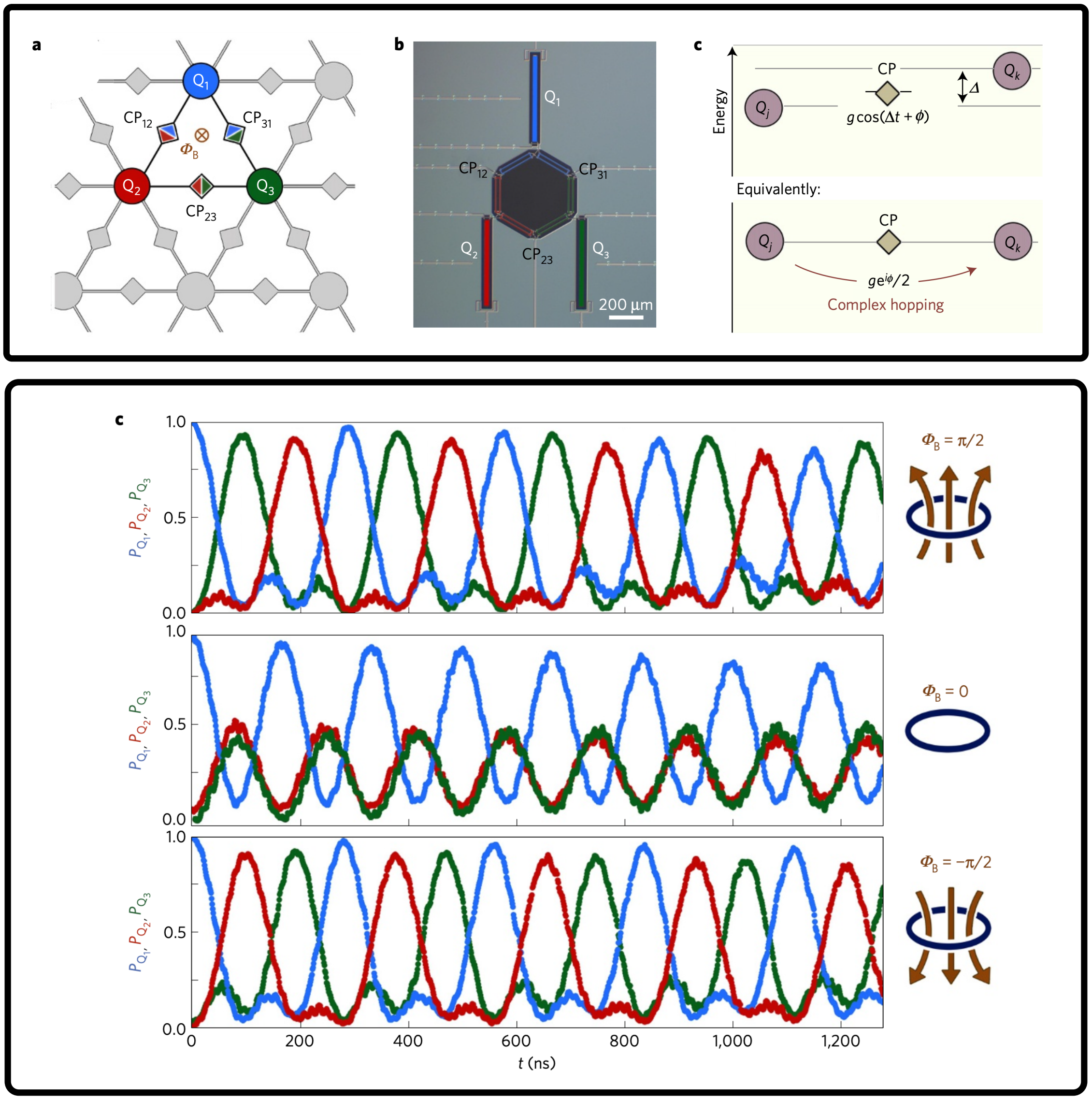

Figure 3.12: **Chiral transport in a three-qubit ring hosting synthetic flux.** Reprinted with permission from *Nature Physics*, ‘Chiral ground-state currents of interacting photons in a synthetic magnetic field’, v.13 p.146-151, 2017. [170] Top panel reproduces part of Figure 1. In **a**, a cartoon shows three qubits and their couplers in a ring threaded by synthetic flux $\Phi_B$. In **b**, a false-color circuit image shows the qubits and their coupler ring. In **c**, a diagram of the involved states shows how parametric modulation of the coupling between detuned qubits results in a complex resonant hopping between the two. Bottom panel reproduces part of Figure 2. In **c**, different choices of coupler modulation produce synthetic fluxes $\Phi_B = \pi/2, 0, -\pi/2$. A photon prepared in $Q_1$ at $t = 0$ propagates directionally around the three-qubit ring in a left- and right-handed manner for nonzero fluxes, whereas for $\Phi_B = 0$ there is no chiral propagation.

this in a ring resonator with a set of two different synthetic dimensions (the ‘pseudospin’, or propagation direction, of modes in the ring and the mode frequencies) to realize a ‘ladder’-style lattice with synthetic flux.

Working in synthetic dimensions can involve less overhead in terms of building lattice sites and their associated control hardware, and supplies access to a more flexible array of lattice connectivities that may not be realizable in real space at all [98]. Working in synthetic dimensions can also make it more accessible to incorporate pump- and reservoir-based processes like pairing interactions ($\hat{a}^{\dagger}_{j+1}\hat{a}^{\dagger}_{j}$) [27], opening up a wider range of physics to exploration in the highly controlled environments of engineered photonic systems.

Excitations can be made to obey the same onsite-energy and hopping physics in a synthetic dimension as is seen in the Harper-Hofstadter model, but in which the relevant complex hopping phase may be easier to impart. Some work in topological photonics [90, 215, 107] builds hybrid lattices which live partially in real-space arrays of coupled sites, and partially in a synthetic dimension. Other work realizes lattice physics with complex hoppings entirely in synthetic dimensions by coupling modes of a system [75].

In addition to the photonic methods for sourcing topology described above, there are some alternative bonus methods available if working with cold atoms (this is not an exhaustive list):

- *Method: Rotate your system!* The Coriolis force experienced by massive particles in a rotating frame behaves effectively like a Lorentz force on a charged particle [46]. If one can coerce a set of bosons to both experience a strong synthetic flux (by rapid rotation) and remain in a low-lying energy state so that single-band dynamics may be investigated [56], it’s even possible to perform experiments exploring the interplay of topology and interactions [126] in a spun-condensate system. This work [56] is spiritually similar to the twisted-geometry work done in a photonic setting by Schine et al. [173].

- *Method: Use lasers to generate desired site-site couplings!* In an accessible review on work towards simulating fractional quantum Hall physics with bosonic atoms, Cooper [46] argues that all drive-based approaches to couple atom lattices with a Peierls phase fall under the heading of Floquet physics.

  Some approaches involve shaking the whole system with a drive to generate an effective Hamiltonian. Another range of works, which use laser-assisted tunneling via resonant modulation as part of a scheme to realize topology in cold atom arrays [4, 124, 5, 188, 108], is spiritually similar to the time-modulation approach listed above, in particular the parametrically-modulated couplings demonstrated by Roushan et al. [170]. The contemporaneous 2013 papers realizing Harper-Hofstadter models for atoms in optical lattices [4, 124] place atoms along the lattice at a potential-energy tilt and close that tilt, while imparting a Peierls phase, via the application of pairs of drives from lasers.

- *Method: Apply a topological pump!* Works which realize topological (Thouless) pumping for cold-atom systems [119] are an atomic-physics version of the synthetic-dimensions preparation scheme described above, where one of the dimensions is time. Thouless pumping – in which slow periodic modulation of system parameters generates a quantized particle current without external bias [44] – can also be thought of as ‘backwards’ from Floquet modulation in the sense that the temporal modulation used to modify system dynamics is slow, rather than fast, relative to system timescales. Topological Thouless pumps apply a slow form of temporal modulation that adiabatically moves states between sites; this externally enforced transport, quantized per pump cycle, can be thought of as effected by a synthetic flux and associated with a Chern number. [33, 140] In this way, it’s possible to build out Harper-Hofstadter physics with one spatial and one temporal dimension!

The above section shares a menagerie of approaches to engineering topological band structures for photons and for atoms. It is important to note that while we mentioned systems with particle-particle interactions in some of the examples provided, the section focused on the interaction-free aspects of systems with hopping and synthetic gauge fields. The introduction of nonlinearity and associated particle-particle interaction will be discussed further in the chapter to follow.

## 3.4 Modeling the chiral lattice

The microwave cavity lattice used in this thesis realizes a synthetic gauge field for tunneling photons without any interactions; sites of nonlinearity are added later in the form of couplings to transmon qubits. An instructive way to think about the Harper-Hofstadter model for such a system is on a cylinder, with one boundary condition of the 2D hopping model made periodic and the other left as an open edge – this setup allows generation of a continuum band structure from the continuum of states allowed by the one periodic dimension, while still providing access to modeling edge modes of interest in the actual doubly-finite system. Code for simulating this partially-periodic 'strip geometry' Harper-Hofstadter model is available in Appendix B.3.

In Figure 3.13, a bandstructure simulated for this strip-geometry Harper-Hofstadter model with $\alpha = 1/4$ ('quarter flux') shows four somewhat flat bulk bands, the center two of which touch at a point as expected for the quarter-flux eigenspectrum seen earlier in Hofstadter's butterfly. A large band gap sits between each outermost bulk band and the central pair of bulk bands; each of these gaps hosts a narrow continuum of edge modes, which are the only excitations able to persist in the band gap.

The edge mode continua above and below the band center have opposite slopes over quasimomentum $k_x$, and central regions where those slopes look basically flat – these are regions of linear dispersion, and a wavepacket excited in these energy regimes would be expected to propagate without decohering, as all of its continuum of Fourier components would share the same group velocity. For more on this, see the section of chapter 2 dealing with wavepacket dynamics in continua and lattices. The specific dispersions of opposite sign indicate that the edge channels above and below the center of this band structure have specific, handed propagation directions which are opposite!

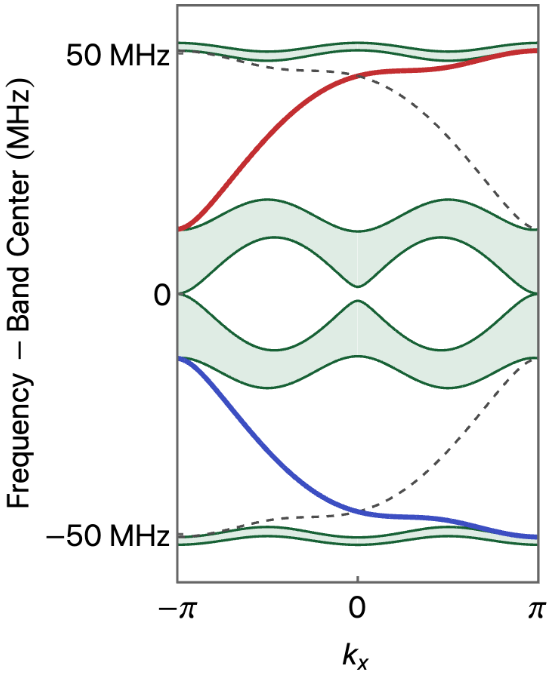

Figure 3.13: **Simulated band structure for strip geometry Harper-Hofstadter lattice.** Simulated for a hopping rate of $-t = 18.5$ MHz, the band structure of a Harper-Hofstadter lattice shows four bulk bands (green). The outer two band gaps host opposite-slope red and blue continua of conducting edge modes.

An important thing to note here is the substantial energy difference between edge channels (regimes of edge modes with pretty-constant dispersion, that could hold a chirally propagating wavepacket) – in spin-Hall models, channels of opposite handedness are degenerate, but in this quantum Hall analog, the time-reversal symmetry breaking introduced by the complex phases on lattice hopping splits that degeneracy. The strength of the synthetic gauge field sets the size of the band gap – Hofstadter's butterfly traces the allowed locations of the bulk bands across different gauge field strengths, visualizing gap openings and closings with different values of flux. The size of this gap is important to protect the edge-ness and thus backscatter protection of edge-propagating wavepackets, as a gap closing is connected to destruction of system topological invariants. In experiments which can realize tunable lattice disorder, it is found (as expected) that edge-ness and directionality are maintained up until the point at which site-energy disorder competes with the scale of the gap opened by the synthetic field. [37]

Because the work in this thesis deals with a finite 5×5 lattice with all boundary conditions

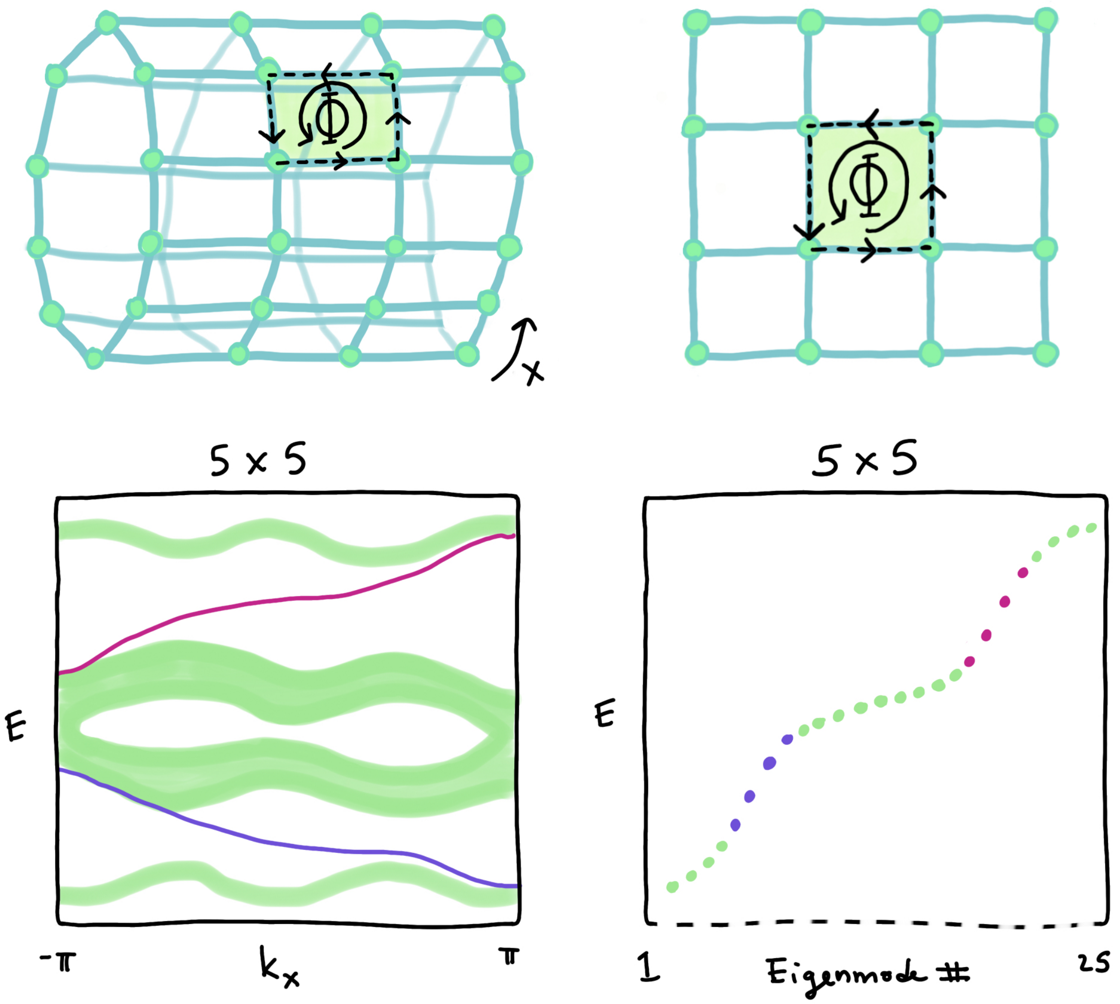

Figure 3.14: **Fragmentation of lattice bandstructure to discrete modes.** Schematic diagrams at top show a Harper-Hofstadter lattice with one (left) and zero (right) periodic boundary conditions. We can calculate a band structure with continua of bulk and edge states for a lattice with one periodic boundary condition (left), which reproduces the edge states classic to topological insulator band structures. At right, for a square 25-site lattice, the 25 discrete eigenmodes 'sample' this band structure.

and no infinite dimension, the discrete 25 eigenmodes which realize the energy landscape of the system 'sample' discretely from the band structure simulated in the above ideal model (Figure 3.13). This fragmentation of the bandstructure into a discrete eigenspectrum is illustrated in Figure 3.14. Generation of a wavepacket in each of the two chiral edge channels is realizable by exciting a set of the geometrically edge-like eigenmodes that live in what would be a bulk band gap. As the smallest lattice which hosts a distinct bulk and edge, a 5-by-5 cavity array allows clear distinctions to be drawn between its 25 eigenmodes, and offers access to explore finite-size effects. In Figure 3.15, we plot a set of simulated eigenmodes of a disorder-free version of this lattice. As the eigenspectrum of a disorder-free Chern insulator should be symmetric around the center mode (pictured near 8.90 GHz), only 13 modes must be plotted.

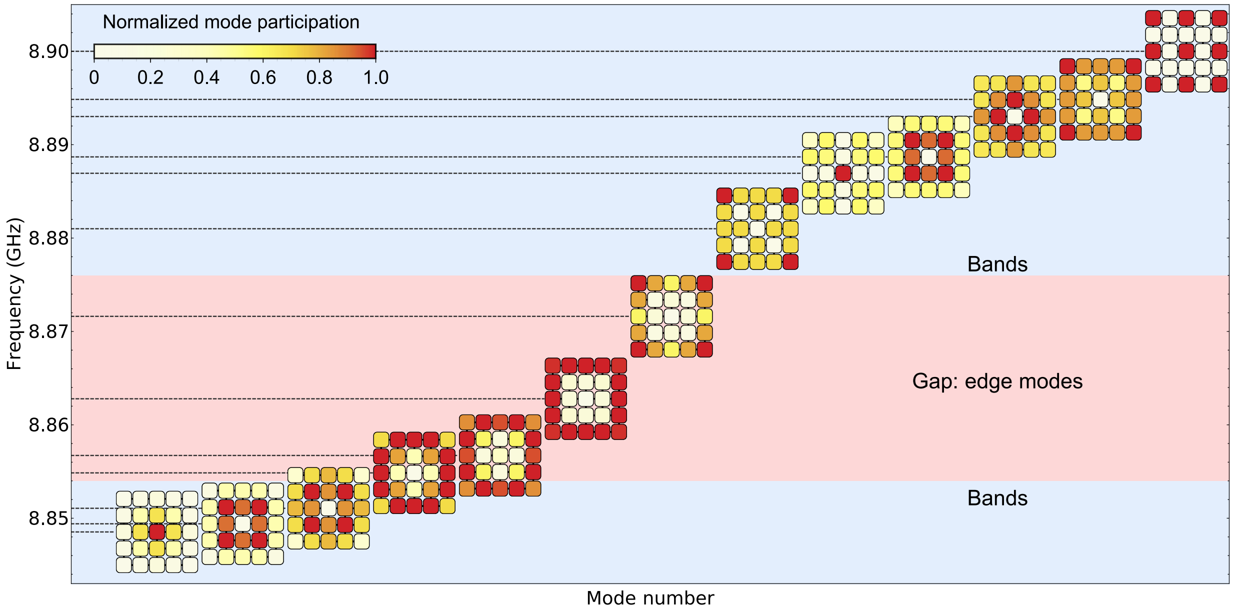

Figure 3.15: **Simulated eigenmodes of a 5x5 Harper-Hofstadter lattice.** Excitation profiles of 13 eigenmodes of the chiral lattice are calculated for the center frequency and hopping rate of the actual platform. The regime highlighted red is the expected bulk band gap, in which four edge-like eigenmodes are located.

For a system this small there are only four modes located in each bulk band gap for a total of eight "edge" modes. However, two of the edge modes in each gap are much closer to the bulk band frequency, which causes the eigenvectors of the these modes to have more participation in the bulk. The 13th (Dirac) mode is located where the two middle bulk bands touch and maintains its large delocalization for a lattice of any size.

In Figure 3.15, these two edge modes that are isolated further from the edge mode have a stronger response in edge-edge transmission, while transmission through the modes located closer to the bulk bands starts to decrease in comparison. This transition from bulk to edge mode at the band edge is seen in larger systems as well. For future experiments where we use the chiral channel to transport quantum states, photons must be transferred into a superposition of edge modes in order to create a localized traveling wave packet. These two modes located closest to the center of the band gap are ideal modes to prioritize in creating a traveling single photon state, since their spatial profiles incorporate less leakage into the bulk.

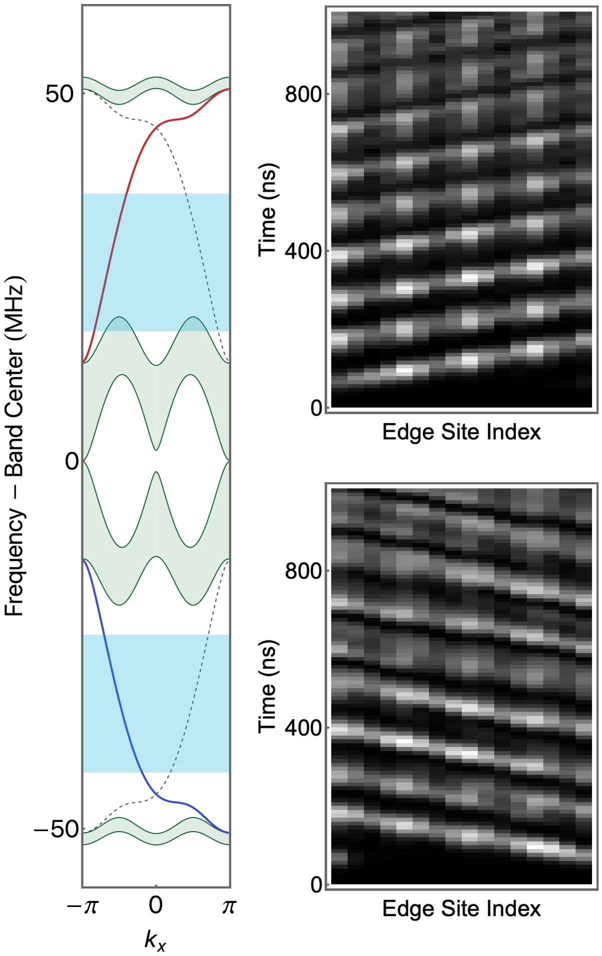

Figure 3.16: **Simulation of wavepacket dynamics in the disorder-free chiral lattice.** Using a Mathematica model of the lattice (Appendix B.3), we model dynamics of Gaussian pulses supplied to lattice corner site 0. Blue highlights on a simulated band structure depict the full width at half-maximum of each pulse.

As we have modeled the eigenthings of this lattice model, we can also trace (linear) dynamics after preparing an excitation in a particular site. In a disorder-free model, we expect the velocities of excitations prepared symmetrically around band center in the upper- and lower-frequency edge channels to be identical. In Figure 3.16 we plot examples of such simulations – one can clearly identify wavepackets with opposite, and approximately identical, velocities propagating around the lattice edge!

In this figure, we place a wavepacket into the lattice edge by driving a corner site with a Gaussian pulse. Excitations in the lower and upper edge channel are tracked at all edge sites and propagate around the edge at approximately the same speed; differences in dynamics are due to slightly different excitation frequencies, chosen to match those used in later experiment with a disordered $5 \times 5$ lattice.

# CHAPTER 4

# REALIZING THE CHIRAL LATTICE

This chapter describes the construction of a synthetic gauge field for photons and addresses microwave transmission and reflection measurements taken on the cryogenic chiral lattice using antennas in the many-photon classical-drive regime. We spectroscopically resolve individual bulk and edge modes of the lattice and make site- and time-resolved measurements of wavepacket transport in both of its chiral edge channels. The following chapter will explore the experiments which concluded this paper that show strong coupling of a transmon qubit to the spectrally resolved modes of this topological band structure.

## 4.1 A superconducting Harper-Hofstadter lattice for microwave photons

We realize an $\alpha = 1/4$ Harper-Hofstadter model using an array of coupled 3D superconducting microwave resonators, cooled to below the superconducting transition so that photons inhabiting these resonators are very long-lived and so that we can later couple them to superconducting qubits, which interact strongly enough with these trapped photons that timescales for photonic dynamics in the qubits and lattice are much shorter than the photon lifetime.

### *4.1.1 Niobium cavity resonators*

The chiral lattice sites are machined in a solid block of niobium and cooled to $\sim 31$ mK when used in conjunction with transmon qubits. The resonators are arranged in a $5 \times 5$ square lattice, which is the minimum lattice size that supports a clear distinction between bulk and edge.

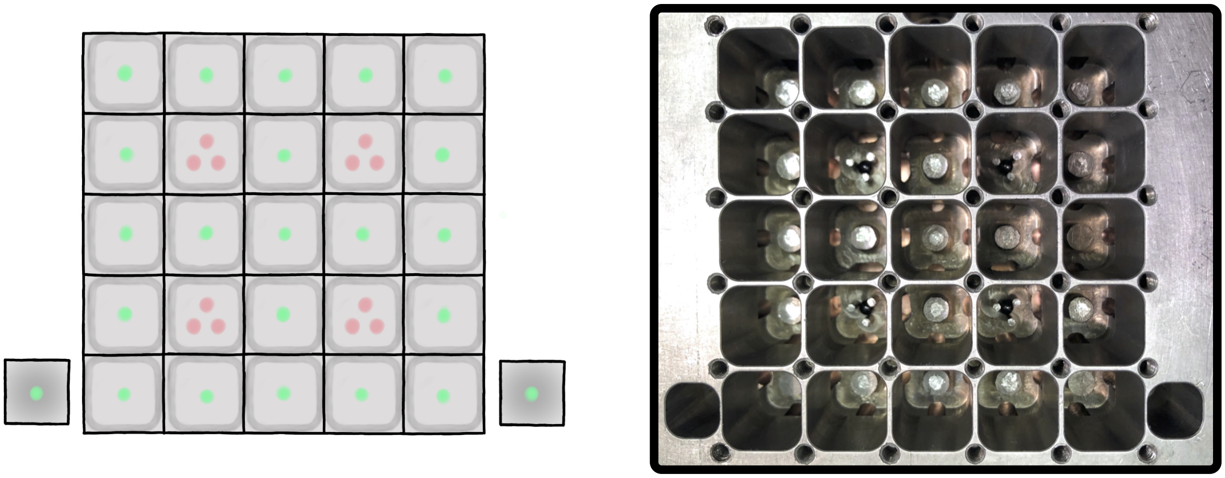

Figure 4.1: **Chiral lattice machined in niobium.** At left, a schematic of coupled 3D microwave resonators in the chiral lattice highlights single-post cavities with green posts and three-post cavities, used to set up the synthetic gauge field, with pink posts. The cavities to either side of the main lattice are used for qubit control and readout. At right, a photograph of the actual apparatus used in this thesis; YIG spheres are visible as black dots inserted in the center of each three-post cavity.

Clai Owens' doctoral thesis [137] is the authority on the design and construction of these microwave resonators and provides much more extensive detail on the development process leading to the final cavity design. Andrew Oriani's thesis [135] and Matt Reagor's thesis [163] offer extensive discussion on principles underlying high-quality-factor superconducting microwave cavities.

Readers seeking to gain more introduction to 3D superconducting cavities for circuit quantum electrodynamics should note that Paik et al. [141] showed the original strong dispersive coupling between a 3D microwave cavity resonator and a superconducting qubit, and Reagor et al. [161] followed up by demonstrating a 3D microwave cavity with lifetime high enough to be compatible with the then- (and still-) current millisecond lifetimes of excited states in superconducting qubits. Reagor et al. [162] then strongly coupled a microwave resonator to a superconducting qubit and kept the resonator lifetime around a millisecond. Chakram et al. [34] developed a multimode seamless cavity coupled to a transmon with mode lifetimes around 2 ms. In his thesis, Oriani [135] describes as-yet-unpublished work demonstrating qubit-coupled cavity lifetimes in the tens of milliseconds. Historically, 3D superconducting cavities have outperformed 2D on-chip superconducting resonators in terms of photon lifetimes, but recent work by Ganjam et al. [60] has demonstrated on-chip superconducting resonator lifetimes of above a millisecond, opening futures in using entirely on-chip platforms to execute tasks like autonomous error correction of bosonic GKP states [94] previously limited to the good photon-holders of 3D cavities.

### *4.1.2 Cavity design priorities*

The core set of design priorities for the cavities forming the chiral lattice were:

*Good electrical conductivity when cold:* To be able to spur and probe dynamics in the chiral lattice, it is necessary to support lattice photon lifetimes that are long on the timescale of qubit/lattice cavity interactions. The less conductor losses and surface dielectric loss contribute to dissipation of energy from the currents on the conducting cavity boundary, the longer the cavity will be able to hold photons before they decay. A cavity material that is a good conductor at cryogenic temperatures (in this case, a superconductor), hosting limited materials and surface dielectric loss, supports the high quality factor needed.

*Avoidance of seam loss:* An important thread of the design innovation by my predecessor Clai Owens [137] was in designing monolithic $\frac{\lambda}{4}$ ('quarter-wave') post coaxial cavities without internal seams (basically, a boundary acting as an impedance to the charge carriers supporting electromagnetic resonances in a cavity which acts as a site of dissipation complementary to materials and dielectric losses [135]) in order to reach higher cavity quality factors. Because of the rotation of the locus of electric field amplitude in time in chiral cavities with a phase winding [137], creative seam placement to limit the current at the seam site (the limitations and use of which are discussed by Brecht et al. [24] in the context of superconducting cavities) was not a feasible option. These reentrant cavities are milled out of a single piece of metal without need for attachment or assembly.

*Dimensions chosen to support quality factor:* The cavities are quarter-wave post resonators, in which the length of the post is dominantly responsible for the frequency of the fundamental cavity mode. Reagor et al. [162] offer an accessible way to think about such cavities: in a transmission line where the post is the inner conductor and the conducting shell is the cavity periphery, a quarter-wave resonator has one end terminated in a short circuit (where the post connects to the cavity floor) and the other in an open circuit (the vacuum/dielectric at the top end of the post). The lowest-frequency resonance supported occurs at wavelength $\lambda$ four times the post length.

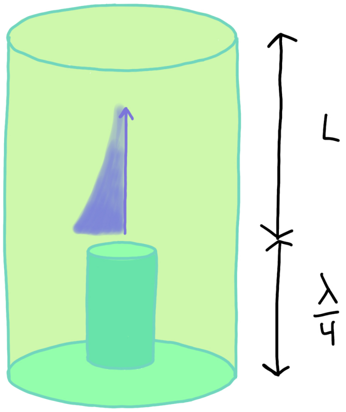

Figure 4.2: **Schematic quarter-wave coaxial resonator.** Adapted from Suleymanzade [186]. The central $\lambda/4$ post sets the fundamental mode frequency. The exponential fall-off of electric field strength is called out in purple. Electric field amplitude should be symmetric and localized near the top of the quarter-wave post.

The shape of the cavity shell affects its loss properties. A larger cavity base footprint (the two smallest dimensions of the 3D cavity) will enable lower surface loss as the field remains localized to the post but the nearby surface area of conducting shell increases [137]. This effect competes with the fact that increasing the footprint brings the cutoff frequency of the roughly-cylindrical-cavity-as-waveguide (higher-frequency than the $\frac{\lambda}{4}$ fundamental mode) closer in frequency to the fundamental mode targeted for use, weakening the fall-off of field amplitude along the long dimension of the cavity and adding strength to an additional loss source [135]. As shown in Figure 4.2, there is an exponential fall-off in (evanescent) field amplitude along the long direction of the cavity [186], so making cavities suitably tall can minimize loss from leakage out of the cavity via that route. Here, in order to maximize the quality factor of each resonator, the depth of the cavity is set so that the evanescent decay from the post mode is much less than the residual resistive loss of the superconductor from which the cavity is fabricated.

*Robustness under DC magnetic field:* As described broadly above and in more detail below, the superconducting properties of the cavity material must persist even when a constant magnetic field penetrates through the chiral lattice wall in order to bias the ferrite spheres used to generate the synthetic gauge field. Niobium is a type-II superconductor, hosting a low $H_{c1}$ (critical applied field at which flux begins to penetrate the superconductor, screened from the conducting regions by formation of current vortices) and high $H_{c2}$ (critical field for the quenching of superconductivity). Thus, when cooled through its superconducting transition with a permanent magnet of the appropriate field strength already in place for ferrite biasing, a block of niobium will support a flux tube that allows the DC field bias to persist [186]. This magnetic field bias ultimately limits the achievable quality factor of the lattice cavities, making it unnecessary to prioritize niobium purity (which would help with conductive loss) in fabricating the lattice.

*Rotational symmetry to support chiral modes:* As is discussed more in the preceding and following sections, modifying some of these cavities to host a right- and left-handed phase winding in their mode structure enables construction of a synthetic gauge field. In order to be able to write the first-excited mode manifold of a three-post cavity as a pair of chiral, rotationally symmetric modes of opposite handedness, it was necessary to preserve rotational symmetry in the field landscape, aided by the rounded-edge-square shape of the cavity bases [137].

### *4.1.3 Splitting chiral modes with YIG spheres*

To produce lattice cavities which host an internal chiral phase winding, we modified some of the quarter-wave post cavities in our lattice, machining them with three quarter-wave posts instead of just one, causing them to host a pair of degenerate modes with right- and left-handed chiral spatial phase windings. The fundamental source of our synthetic gauge field for photons is the introduction of ferrite crystals which support a global magnetic resonance that couples to microwave light and splits the right-and left-handed chiral cavity modes. This precession of the global magnetic moment of such a crystal, frequency-tunable by an applied magnetic field, thus connects an actual gauge field to a phase modification in microwave resonators which is 'felt' by normally field-agnostic photons.

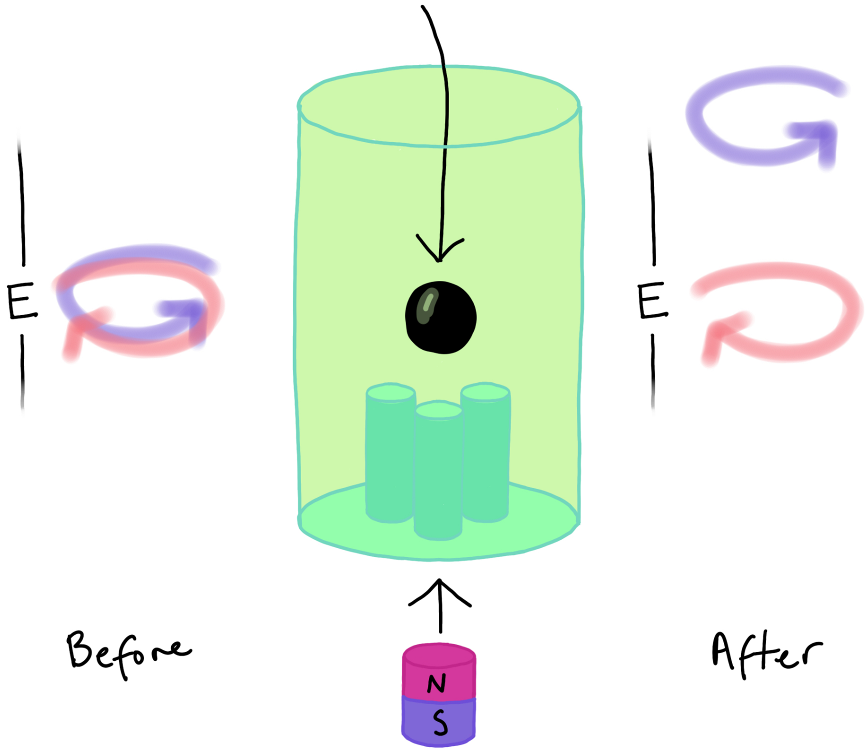

Figure 4.3: **Splitting chiral cavity modes by introduction of a field-biased ferrite.** At left, a three-post cavity hosts a pair degenerate right- and left-handed chiral modes in its first-excited state manifold. At right, introduction of a YIG crystal (black sphere) to the center of the rotationally symmetric cavity, and the application of a permanent bias magnetic field, splits one of these modes off while leaving the other largely unperturbed.

A hangup in explaining the three-post cavities in talks has been in helping audiences understand the pair of degenerate right- and left-handed chiral cavity modes to which the three posts give rise. A simple model of a three-post cavity as a set of three coupled oscillators illustrates the genesis of these modes – see Chapter 2, Section 2.1.2 for more details. In essence, we expect a pair of degenerate modes in which the field amplitude propagates with opposite polarizations.

We place YIG spheres in divots machined between the three posts of the lattice cavities hosting chiral modes. These spheres rest freely until secured in place by their attraction to the permanent magnets used for field bias. To create the bias field, we place a 1.6 mm diameter permanent neodymium cylindrical magnet in a small hole milled into the back of the cavity directly underneath each YIG sphere, leaving a 0.3 mm thick layer of niobium between the magnet and the inside of the cavity and the YIG. Creating a *local* magnetic field in the vicinity of the YIG spheres with small magnets minimizes the magnetic fields permeating the system, which in turn minimizes the amount of niobium which sees its superconductivity quenched by the B-field, as the strongest part of the magnetic field is localized to the area between the ferrite and the magnet, whereas the bulk of the modal surface currents flows in the posts of the cavity, locations where the B-field has decayed substantially.

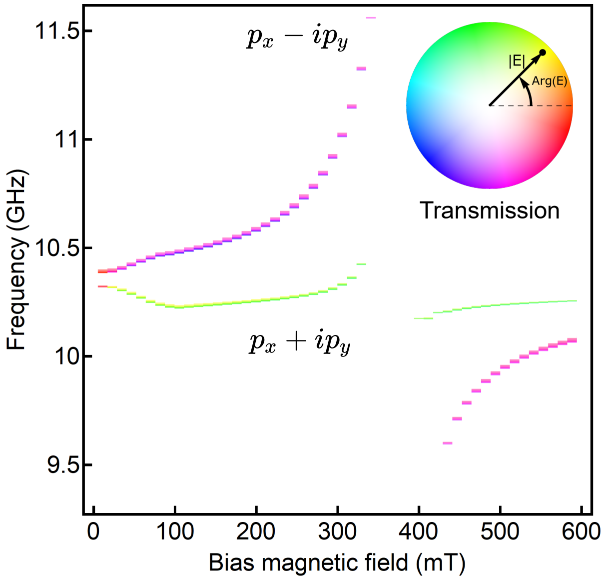

Figure 4.4: **Splitting of chiral cavity modes under applied bias field.** Magnetic field applied to an in-cavity YIG sphere splits the chiral modes of a three-post cavity. Both magnitude and phase of measured transmission between antennas sited 45° apart along the cavity edge are plotted; data hue represents differential phase while saturation represents normalized $S12-S21$ transmission magnitude. For each slice in the y-direction, a test cavity is warmed above the $T_C$ of niobium to 12 K, so that the magnetic field on the YIG sphere can be changed. The cavity is then cooled to 2 K and the magnetic flux is locked in place by the superconducting transition of the cavity. The two cavity modes diverge in frequency when the magnetic field is applied and the $p_x - ip_y$ mode is split off while the $p_x + ip_y$ mode is more minimally perturbed; the accumulated phase differences are $-90°$ and $+90°$ due to the opposite mode chiralities.

We generate sufficient field ($\sim 0.18$ T) to break the degeneracy between the two chiral cavity modes by 180 MHz, while maintaining a cavity quality factor of 200,000. The splitting between these two modes is a measure of how strongly time-reversal symmetry is broken.

This splitting also limits the maximum tunneling rate in the lattice, as the Hofstadter model assumes one orbital per lattice site, requiring the tunneling energy to remain small enough to avoid coupling to the counter-rotating orbitals. The ratio between the tunneling rate and the loss rate in our cavities is then a measure of how fast the dynamics are compared to the loss rate, which is an important benchmark for the system that determines how far the photons move within their lifetimes. In this work, the ratio between tunneling and loss rates is 18 MHz/50 kHz $\approx 400$.

We assemble the Harper-Hofstadter Hamiltonian using the chiral cavity mode which is 'dark' to the field-biased YIG (experiences limited perturbation from coupling and is not split off, colored salmon in Figure 4.3, and referred to by the $p_x + ip_y$ spatial mode structure in Figure 4.4). By coupling this mode resonantly to surrounding fundamental $\lambda/4$ cavity modes, we realize a Hamiltonian for a tunneling photon that experiences hopping and localized additional phase winding on these modified sites (Figure 4.5). The introduction of this phase winding at the proper locations in a $5 \times 5$ lattice produces Peierls phases realizing a uniform synthetic flux.

Because the lattice harnesses the mode which is 'dark' to the YIG, we are insensitive to the precise magnitude of the B-field, its orientation relative to the crystal axis, or coupling to spin-wave modes. Disorder in couplings between YIG resonances and the 'bright' chiral modes does not map to disorder in the Hamiltonian we realize – the exact form of this coupling is less important than the fact that this coupling splits these modes away from resonance, isolating the 'dark' modes for use in the lattice Hamiltonian.

Cavity quality factors were measured after machining the lattice, inserting the ferrites (YIG spheres) to relevant cavities, and applying magnetic fields. After machining but before applying any surface treatment, lattice sites had quality factors of $\sim 2 \times 10^6$. Introducing the YIG sphere to the cavity does not degrade the Q, so long as no additional materials are added to hold the YIG sphere in place. No such additional materials (e.g. adhesive) were used here.

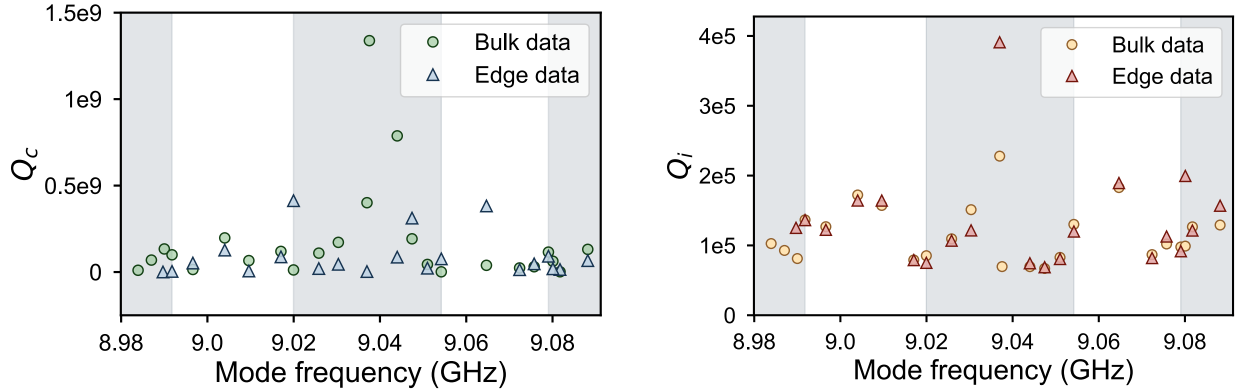

Figure 4.6: **Quality factors of lattice modes from edge and bulk spectra.** Internal ($Q_i$) and coupling ($Q_c$) quality factors are extracted from fits to modes in cryogenically measured lattice spectra taken between pairs of bulk and edge lattice sites. Expected locations of bulk bands are highlighted in gray. Lattice modes with higher edge participation display relatively higher $Q_i$ values, consistent with expectations that these modes suffer less loss due to their smaller relative participation in the lossier bulk sites equipped with YIG spheres.

After applying the magnetic field in the final configuration, cavity quality factors dropped to $\sim 2 \times 10^5$, suggesting that the limiting loss factor of the cavity modes is the resistive losses in the normal regions created by the magnetic field piercing the superconductor. Lifetimes of lattice modes remained stable after long exposure of the lattice to air and potential growth of a penetrating surface oxide, further supporting this suggestion. In Figure 4.6, we plot quality factors of lattice modes measured at cryogenic temperatures.

### *4.1.4 Assembling the chiral lattice*

The cavities which serve as lattice sites are evanescently coupled together via holes milled into the back of the niobium block to form a tight binding model. These holes create coupling by allowing overlap of the Wannier functions of adjacent sites; as the holes also act as higher-frequency resonators themselves, they create additional virtual coupling for virtual photons through these much higher frequency modes. In some (non-cryogenic) lattices earlier in the development of this project [7, 138], my predecessors added a screw that could tune the frequency of the coupler lower, allowing us to achieve greater couplings between lattice sites (up to 150 MHz).

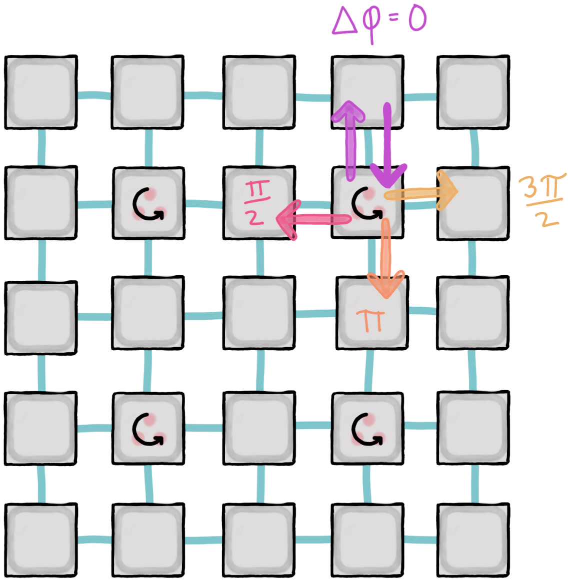

Figure 4.5: **Harper-Hofstadter model constructed with cavities hosting local phase winding.** We assemble a $5 \times 5$ cavity lattice where all sites are connected by tunneling with rate $t$ (blue lines). We modify some sites to host a local phase winding and show the accumulated phase for a photon tunneling into/out of one such site along different tunneling legs. This local modification of cavity phase windings can be recast as a Peierls phase on some of the hoppings $t$ to realize a uniform synthetic gauge field.

The cryogenic lattice realized here saw the tunneling reduced to $t \approx 2\pi \times 18$ MHz, as in order to preserve lattice mode quality factor we deployed weaker bias fields that shrank the amount by which we broke time-reversal symmetry ($\sim 180$ MHz). In the context of the qubit-lattice dynamics explored in this thesis, the slower hopping rate between sites actually provides an advantage, as it allows us to carry out qubit operations several times faster than the round-trip time of a wavepacket in an edge channel.

It is necessary to control disorder in the resonant frequencies of lattices to a level below other energy scales of the system Hamiltonian (tunneling, magnetic field interactions, eventual particle-particle interactions). To achieve this, we tuned the frequencies of lattice sites by application of malleable, superconducting indium to the tops of the cavity posts to alter their lengths without diminishing their quality factors. Three-post YIG-coupled and single-post lattice sites change frequency differently as they are cooled to cryogenic temperatures; the former shift by $\sim$ 40 MHz, while the latter shift by $\sim$ 23 MHz. Adjusting for this difference in cryogenic shift, we tuned and tested the frequencies of lattice sites at room temperature, achieving disorder less than ±1 MHz for the single-post cavities and ±3 MHz for the three-post YIG cavities. We tuned the lattice to $\omega_l \approx 2\pi \times 8.9$ GHz for the measurements detailed in the rest of this thesis.

Figure 4.7a shows the square Hofstadter lattice developed for this work. Each square in the diagram is a lattice site, implemented as a resonator of frequency $\omega_0 \approx 2\pi \times 9$ GHz, tunnel-coupled to its nearest-neighbors with $J = 2\pi \times 18$ MHz. Sites with counter-clockwise red arrows exhibit modes with spatial structure $p_x + ip_y$, while all other sites have $s$-like modes. The phase winding in a $p_x + ip_y$ site causes photons tunneling in/out from different directions to acquire a phase $\phi$ equal to the clockwise angle between input and output directions [138]. This ensures that when photons tunnel around a closed loop in the lattice enclosing $n$ plaquettes, they pick up an Aharonov-Bohm-like phase $\phi_{loop} = n\frac{\pi}{2}$.

Once tuned up, the niobium lattice is mounted between sheets of copper (see Figure 4.8) in order to adequately thermalize the niobium to the mixing chamber plate of the dilution refrigerator in which it is placed. Dipole antennas are mounted onto the lid of the copper box so that a single antenna protrudes into each lattice site from the top of the cavity. The length of the antenna sets the coupling quality factor of each lattice site. For these measurements, each lattice site is weakly coupled to its antenna so that the total quality factor of the lattice is maximized.

## 4.2 Cryogenic setup for lattice spectroscopy and qubit measurement

The lattice is mounted on the mixing chamber (MXC) plate of a Bluefors LD-250 dilution refrigerator at $\sim$31 mK. In order to measure the linear response of the lattice, the weakly-

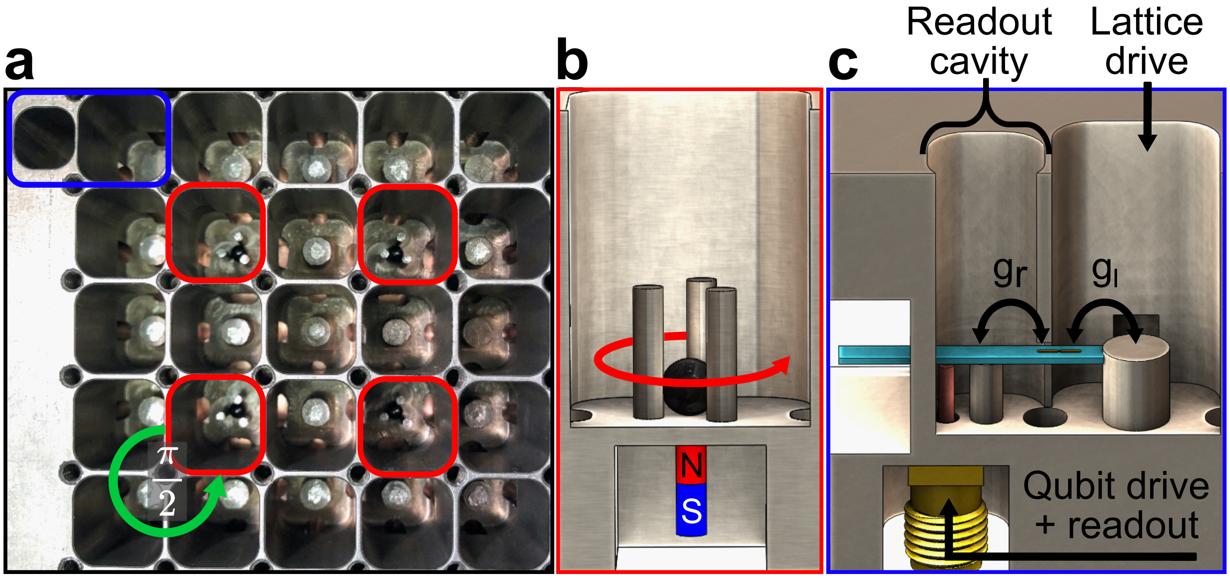

Figure 4.7: **Elements of chiral cavity quantum electrodynamics.** **a,** The apparatus consists of a 5 × 5, $\alpha = \frac{1}{4}$ Hofstadter lattice of resonators in which microwave photons propagate as charged particles in a magnetic field, coupled to a single qubit on the edge that is sensitive to the precise number of photons and their energies. Each site, implemented as a coaxial resonator milled into a block of niobium [161], exhibits a resonance frequency $\omega_0$ determined by the length of a central post, and a nearest neighbor tunneling rate $J$ determined by the size of a machined coupling hole. The synthetic magnetic field manifests as an Aharonov-Bohm flux $\pi/2$ when photons hop around minimal closed loops (green), generated by the spatial structure of the resonator modes: each 2-site by 2-site plaquette includes one lattice site (red) that exhibits a $p_x + ip_y$ orbital, while the other three sites exhibit $s$ orbitals [7, 138]. The additional site (blue) on the system edge serves as readout cavity into which transmons may be inserted. **b,** $p_x+ip_y$ sites instead contain *three* posts and thus support three microwave modes ($s$, $p_x \pm ip_y$). Because our Hofstadter lattice employs only the $p_x+ip_y$ mode, we must isolate it: the $s$ mode is tuned away by the electromagnetic coupling between posts, while a Yttrium-Iron-Garnet (YIG) ferrimagnet (black) couples primarily to the $p_x - ip_y$ mode (due to the orientation of the B-field of the red/blue bar magnet), thereby detuning it in energy and isolating the $p_x+ip_y$ mode. **c,** A transmon qubit is inserted into a gap between readout (left) and lattice (right) cavities on a sapphire carrier (turquoise), and couples to the two cavities with Rabi frequencies $g_r$ and $g_l$ respectively. An SMA connector (gold) allows direct microwave probing of this readout cavity and thus the transmon.

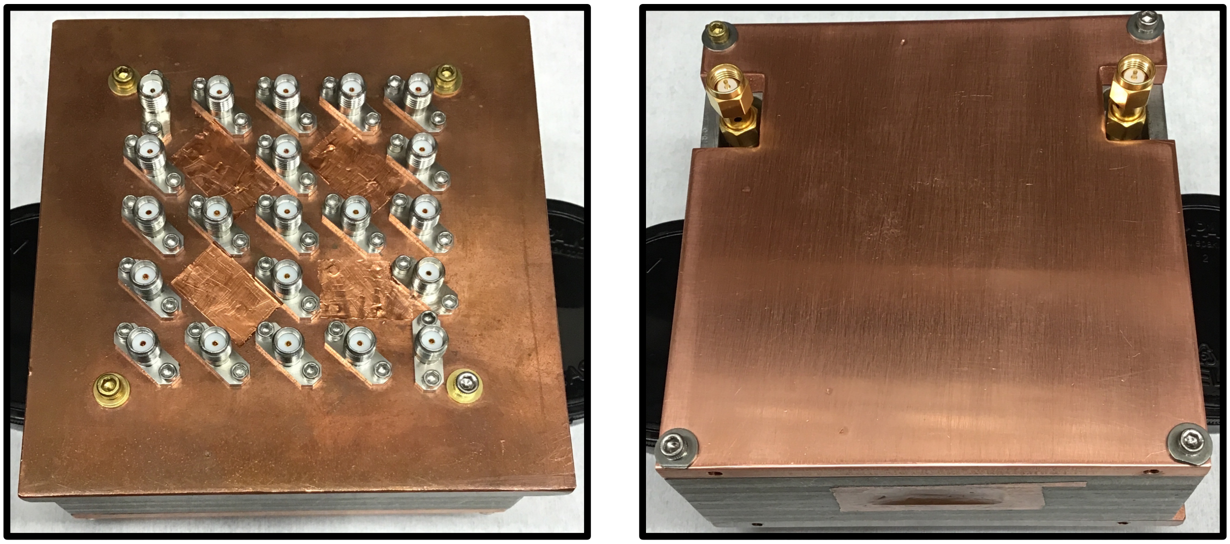

Figure 4.8: **Lattice in box prior to mounting.** At **left**, an array of SMA connectors leads to an array of antennas weakly coupled to lattice sites on the other side of the copper lattice lid. We tape over holes in the lid above three-post chiral sites, as antennas will not couple adequately to their field landscapes without spoiling cavity Q. At **right**, another copper sheet backs the lattice; SMA connectors lead to the antennas coupled to readout cavities for qubits A and B. This whole assembly is eventually mounted on a copper plate that is thermalized to the underside of the mixing chamber plate of a dilution refrigerator.

coupled antennas on each site are connected to one of a pair of 10-way Radiall R574F32005 cryogenic RF switches mounted to the MXC plate and connected to input and output lines with circulators, enabling access to 20 sites. By placing an additional antenna on its own circulator, we are able to perform microwave reflection measurements on all but the 4 three-post chiral cavities, whose modes are more localized in the bottom of the cavity, making coupling to them with a dipole antenna without spoiling the cavity quality factor more difficult.

We measure reflection on each site with an Agilent ENA5071C network analyzer, using the RF switches to select the relevant site-coupled antennas. We then excite propagating pulses and measure lattice site response in time. For this measurement, a microwave tone from a local oscillator is mixed with a pulse generated by an arbitrary waveform generator (Keysight M8195A, 64 GSa/s) and supplied to an edge-site-coupled antenna. Microwave excitation amplitudes of other edge-site-coupled antennas are measured over time: signals exiting the refrigerator are IQ demodulated using the source local oscillator and are fed to an oscilloscope for measurement of time-traces. This specific measurement was performed before I joined the project, and replicated later by me with a different setup.

To make transmission measurements of this lattice after we have coupled a transmon qubit to its corner, the lattice sites depicted in blue in Figure 4.10 have their antennas connected to a single 10-way RF switch leading to a circulator, so that these sites can all connect to either an input line or an output line. Sites in green see their antennas connected to only input lines and thus can only be excited, not measured. The site $(1, 1)$ is connected separately to a circulator so that it can be measured and excited independently. The remaining six sites in the $5 \times 5$ lattice are not connected to a either an input line or output line. The resonator used to read out the qubit (for single-qubit experiments detailed in the following chapter) is also connected to a circulator to support drive and readout. Each output line is filtered by an Eccosorb filter to suppress the incidence of high-frequency photons at base.

A Keysight PNA-X N5242 network analyzer is used to perform lattice spectroscopy for measurements including those depicted in Figures 4.6 and 4.9. In the spectra in Figure 4.9, the lower-frequency bulk band gap hosts four distinct edge modes between 8.86 GHz and 8.88 GHz, while the higher-frequency bulk band gap is seen to host only three distinct edge modes between $2\pi \times 8.92$ and $2\pi \times 8.94$ GHz. The fourth edge mode associated with this band gap is predicted to be much closer to the bulk modes; the peak doublet near $2\pi \times 8.94$ GHz is likely to be a hybridization of one bulk mode and one edge mode that are pushed closer in frequency than in the disorder-free model.

This trend of the top band being asymmetrically compressed in comparison to the bottom band is due to the presence of the opposite-chirality modes in the chiral cavities, explored further in Section 4.3. These modes are located $2\pi \times 140 - 2\pi \times 200$ MHz higher in frequency than the bare lattice frequency and are strongly coupled to the neighboring sites ($\sim 2\pi \times 20$

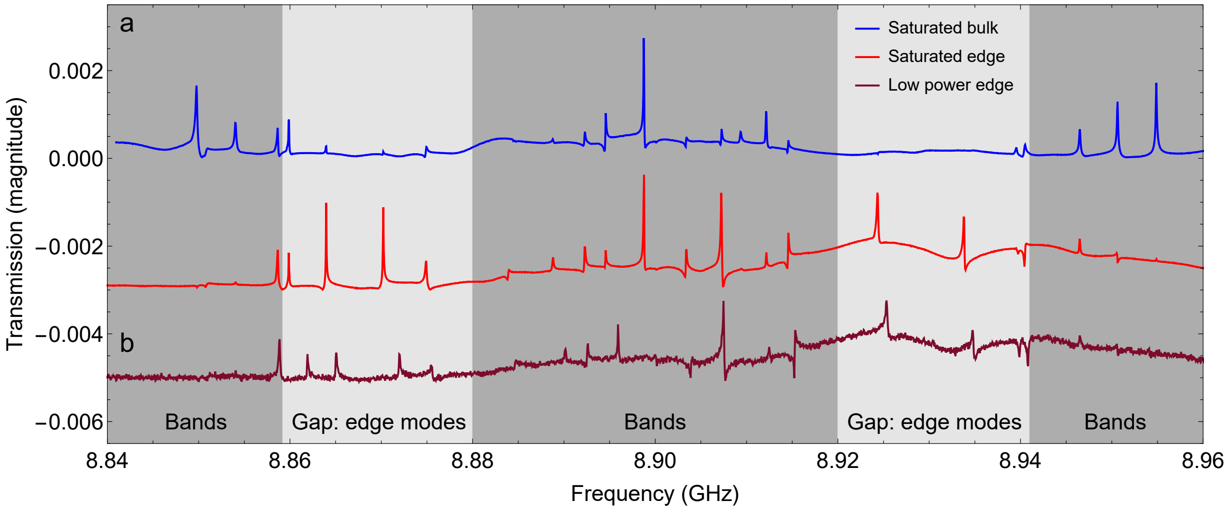

Figure 4.9: **Transmission spectroscopy through the lattice coupled to a qubit.** In **a,** the blue plot and the light red plot compare the transmission between two bulk cavities (site $(3,3)$ and $(2,3)$) and two edge cavities (sites $(1,4)$ and $(3,1)$) at high powers so that the qubit is saturated and the lattice is measured while effectively decoupled from the qubit. As predicted, two large gaps exist in the bulk-bulk transmission and modes in the edge-edge transmission reside in these gaps. The dark red plot in **b** is the edge-edge transmission taken at lower power so that the modes are shifted by their coupling to the qubit. Both plots show four edge modes in each band gap, despite spectrum asymmetry.

MHz). The presence of these modes can shift the higher frequency modes of the lattice by $\sim 2\pi \times 4$ MHz and compress the upper band gap. Figure 4.9b shows the same edge-edge transmission as probe power is varied. When the power is lowered, the lattice modes acquire a dispersive shift from the qubit that is proportional to the lattice corner site's participation in each mode. Edge modes of the lattice experience power dependent shifts of $2\pi \times (1-2)$ MHz while modes constrained to the bulk of the lattice shift by much less than their linewidths.

## 4.3 Effect of backwards-chiral cavity modes

In the insets of Figure 4.12d to come below, we trace pulses propagating on the edge of the lattice when a lattice edge site is excited with a Gaussian pulse with $4\sigma \approx 80$ ns. The pulse to drive the higher-frequency excitation is centered at 9.064 GHz, and the pulse to drive the lower-frequency excitation is centered at 9.004 GHz. Each pulse's 80 ns $4\sigma$ width

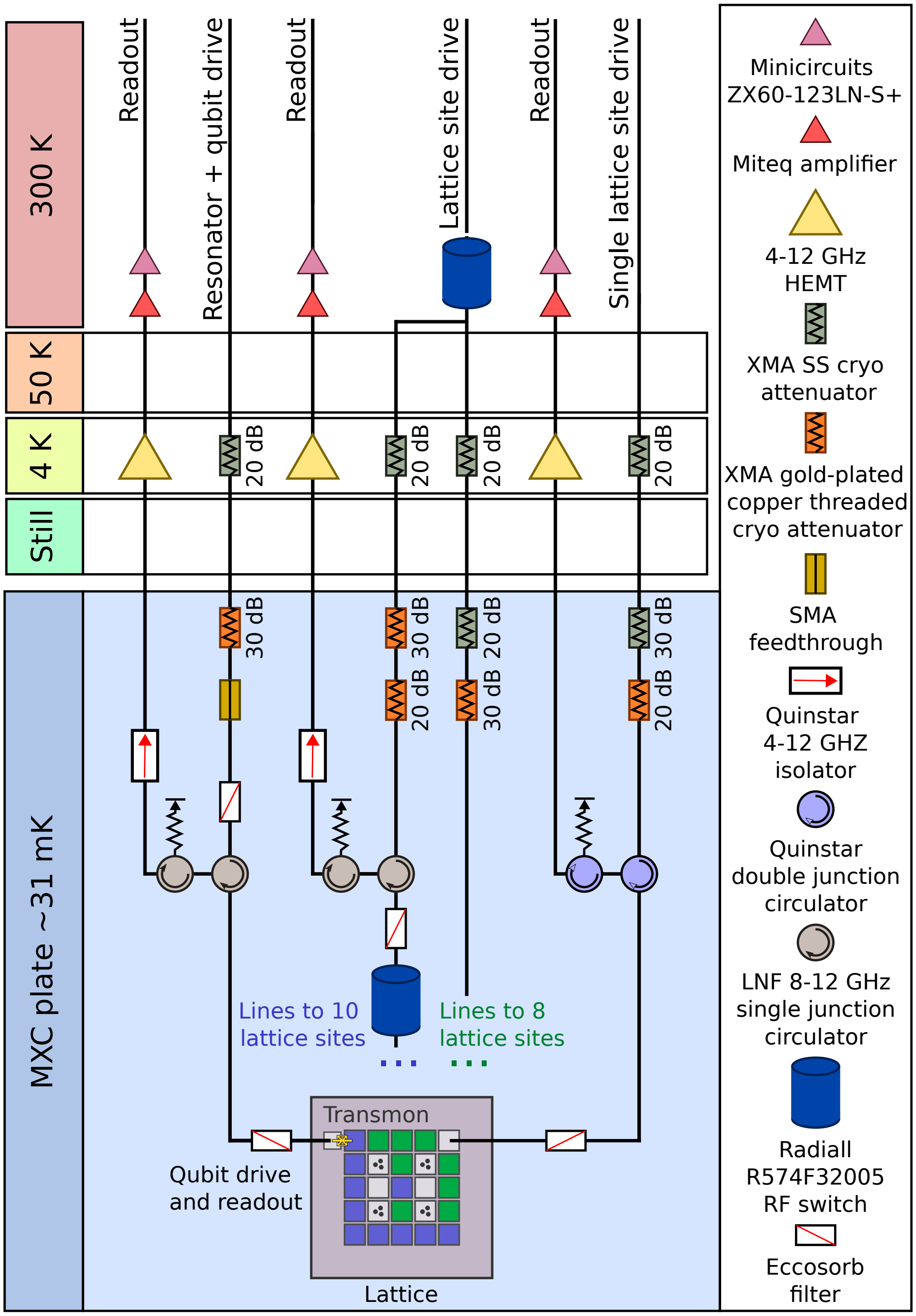

Figure 4.10: **Cryogenic setup for single-qubit measurements.** The antennas coupled to some lattice sites (highlighted in blue) are accessible via an input and readout line connected by a circulator, allowing reflection measurements on individual sites. Other antennas coupled to lattice sites (highlighted in green) are accessible via input line only.

corresponds to a $4\sigma$ frequency width of $\sim 31.8$ MHz, spanning a large portion of the upper or lower band gaps.

Excitations in the opposite-chirality edge channels propagate at different velocities; both channels have round-trip times on the order of a few hundred ns, with the faster reaching $\sim 120$ ns, much faster than the $\sim 3$ us lifetime of lattice excitations. The visually notable difference in velocities of excitations in the two edge channels results from the differing frequency locations of edge modes within the upper and lower band gaps, also pictured in Figure 4.9. In a disorder-free lattice without coupling to the 'bright' chiral modes, the spectrum in Figure 4.9 would be symmetric about its band center. Introducing couplings to the (detuned) 'bright' modes into the model reproduces the asymmetry in the measured spectrum.

Simulations of excitation propagation in chiral edge channels based on this modified Hamiltonian (Figure 4.11) reproduce the observed difference in edge channel propagation velocity. The paired plots at left in this figure show disorder-free simulation of a lattice that incorporates coupling through detuned 'bright' modes, plotted alongside actual data shown in color. The plots at right reproduce the simpler simulations from Figure 3.16 which do not incorporate the detuned chiral cavity modes, and show excitation velocities that appear a bit less accurate to those observed.

## 4.4 Probing the topological lattice: time-resolved wavepacket dynamics

Prior to introducing the transmon nonlinearity, we first characterize the mode structure of the topological lattice itself in the linear regime. Fig. 4.12a shows the anticipated energy spectrum of a semi-infinite strip $\alpha = 1/4$ Hofstadter lattice with four bands and topologically protected edge channels living below the top band and above the bottom band. In a finite system, these continuum bands and edge channels fragment into individual modes satisfying

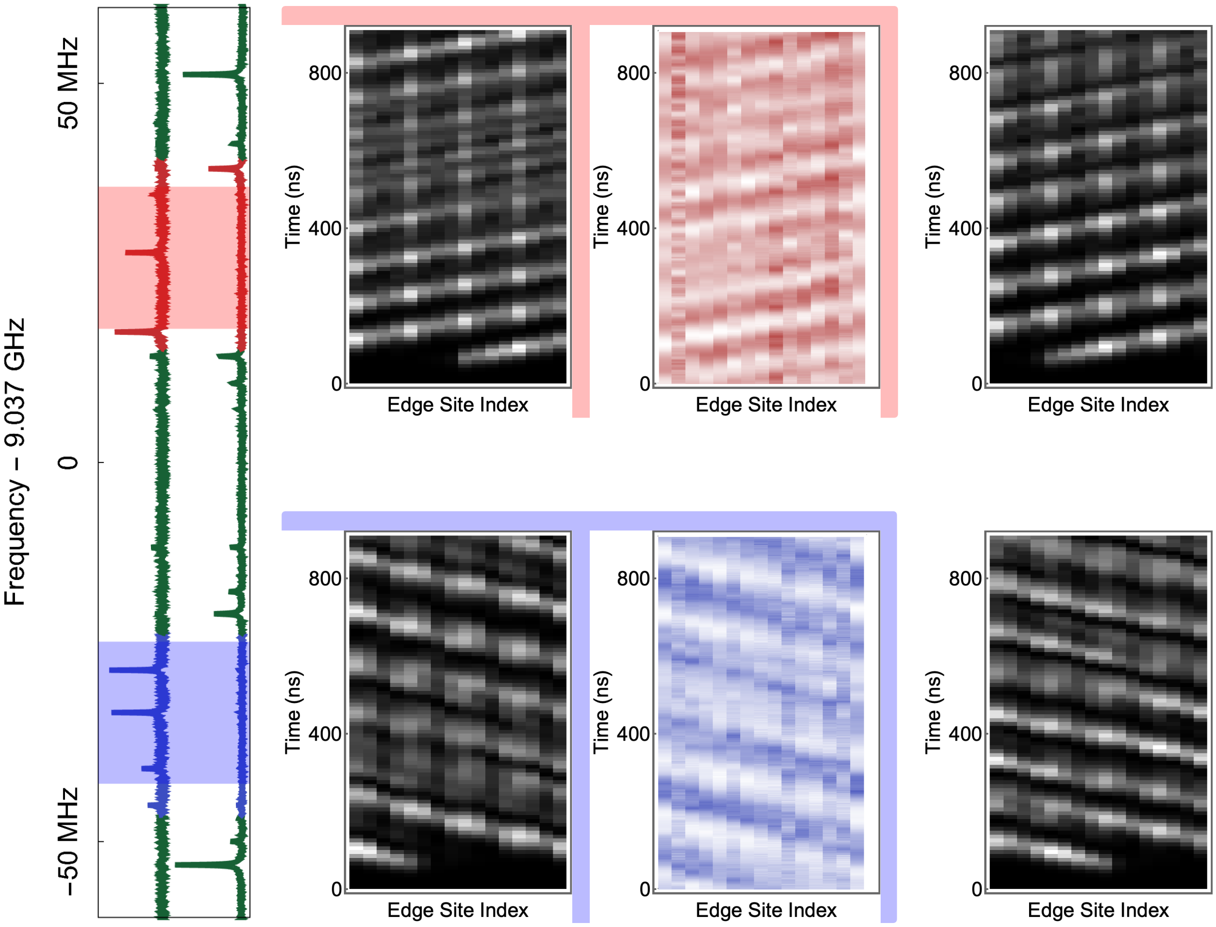

Figure 4.11: **Simulated speeds of edge excitations.** Coupling to detuned $p_x - ip_y$ modes on three-post lattice sites explains the asymmetry in the lattice spectrum and the different propagation speeds of edge excitations in channels of opposite chirality. At left, the measured spectrum from Figure 4.9b depicts the higher-frequency (red) and lower-frequency (blue) edge modes. The two most prominent edge modes on the higher-frequency side of the spectrum have a wider spacing than the two such modes on the lower-frequency side. A simulated spectrum incorporating coupling to detuned $p_x - ip_y$ modes hosts a similar wider gap. This greater spacing gives rise to a faster propagation speed for excitations in the upper chiral edge channel as shown in the upper inset of Figure 4.9d. In leftmost black-and-white plots, we depict lattice edge sites' simulated responses when an initial 80 ns Gaussian excitation is applied to one edge site. The full widths at half-maximum of these pulses are highlighted in red in the higher-frequency bulk band gap and blue in the lower-frequency bulk band gap shown in the spectrum at far left. Red and blue plots in the center panel reproduce data from Figure 4.9d, showing excitation velocities more similar to the simulation results at left. The rightmost black-and-white plots show excitation propagation for a lattice that does not incorporate coupling through detuned chiral cavity modes. Color scales are arbitrary.

the boundary conditions. Fig. 4.12b shows the measured response of the lattice when probed *spatially* both within the bulk (left) and on the edge (right), with the energies aligned to Fig. 4.12a. It is clear that the bulk spectrum exhibits modes within the bands, while the edge spectrum exhibits modes within the bandgaps. We further validate that the modes we have identified as 'bulk' and 'edge' modes reside in the correct spatial location by exciting modes identified with arrows in Fig. 4.12b and performing microscopy of their spatial structure in Fig. 4.12c.

To demonstrate that the excitations of the edge channels are indeed both long-lived and travel in a chiral (handed) manner, we excite the system at an edge site with a short pulse (see Fig. 4.11) that populates the modes within each of the two bulk energy gaps in Fig. 4.12d (see section 4.3 and Figure 3.16). By monitoring the edge-averaged response, we determine that the high Q of the superconducting cavities enables the excitation to travel the full lattice perimeter $>$ 20 times prior to decay (see Fig. 4.12d). The back-scatter-free, unidirectional propagation demonstrates the protection afforded chiral edge channels by this system's topology. In the insets to Fig. 4.12d, we probe in both space *and* time, and observe that the excitations move in opposite directions in the upper and lower band gaps, as anticipated from the bulk-boundary correspondence [72]. The difference in group velocities between upper and lower edge channels arises from second-order tunneling mediated by virtual occupation of the detuned 'bright' $p_x - ip_y$ cavity modes (see section 4.3).

Having demonstrated that the topological lattice hosts distinct 'bulk' and 'edge' modes and can support spectrally distinct and long-lived chiral excitations, we next couple a non-linear emitter to the lattice edge, connecting the chirality of this topological band structure with nonlinear effects seen in cavity quantum electrodynamics.

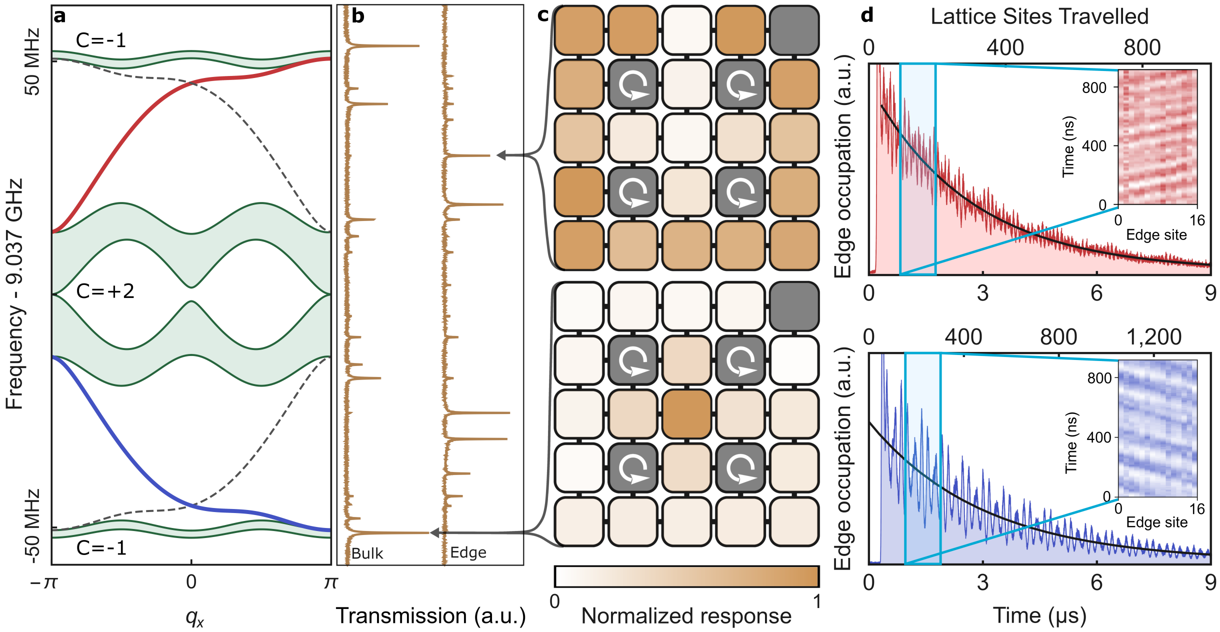

Figure 4.12: **A superconducting Chern circuit.** The central ingredient of a chiral cavity QED platform is a long-lived, spectrally-isolated chiral (unidirectional) mode to couple to a real/synthetic atom. For our experiments this mode lives on the edge of a synthetic Hall system realized in a $\alpha = 1/4$ Hofstadter square lattice. The numerically-computed band structure of this model (as implemented) is depicted in **a,** for an infinite strip geometry. The top/bottom bands exhibit a Chern number $C = -1$, while the middle two bands, which touch at Dirac points, have a total Chern number $C = +2$; chiral edge channels exist above/below the bottom/top bands respectively, as anticipated from the bulk-boundary correspondence. **b** shows microwave transmission spectra measured through our actual $5 \times 5$ lattice, where both the bulk bands and chiral edges manifest as well-resolved modes due to finite system size. "Bulk" measurements are performed by exciting/measuring at two distinct sites on the lattice interior, while "edge" measurements employ two sites on the lattice perimeter. In **c,** we measure the spatial structure of the modes identified with arrows in **b** and observe that the mode residing predominantly in the interior of the lattice is located energetically within band, while the one localized to the edge resides within a gap (see section 4.2 for measurement details). 'Normalized Response' represents the reflected power normalized to the largest measured power at the chosen drive frequency. In **d,** we excite a single edge site with a short pulse spectrally centered in the upper/lower (red/blue) gaps, and observe the response of the resulting traveling excitation as a function of time averaged over the full perimeter (**main panels**) and vs. site index around the system edge (**inset panels**). The excitations in the top/bottom band gaps are centered at 9.064/9.004 GHz. Each Gaussian pulse has a $4\sigma$ length of 80 ns. The insets in **d** demonstrate that upper and lower edge channels have opposite chiralities. The ability of a photon to undergo numerous round trips prior to decay is equivalent to spectroscopic resolution of the individual edge modes.

# CHAPTER 5

# CHIRAL CAVITY QUANTUM ELECTRODYNAMICS

This thesis chapter is based on the conclusion to the first paper of this PhD [139].

In the prior chapters, we explored the construction of a topological metamaterial which is home to purely linear interactions between photons. We also shared the rich and wide range of experimental implementations of photonic systems which yield topological band structures, either with or without time-reversal symmetry breaking. Some are realized in silicon photonics, others in mirror-based cavities, still others in circuits. This thesis implements a photonic lattice of superconducting microwave cavities in particular because of the several advantages superconducting cavities offer: the flexible access to engineering cavities, couplings, and added drives/dissipation, and the strength of the coupling achievable between superconducting qubits, whose Hamiltonians include a Josephson nonlinearity, and these superconducting cavities.

This strong coupling ensures that we can transfer energy between qubit and cavity resonators on timescales faster than the (long!) lifetimes of excitations in the superconducting cavities, allowing us to spur and probe dynamics. Most importantly to the thrust of this work, though, this strong coupling also ensures that a transmon qubit, with a nonlinear component to its Hamiltonian, hybridizes strongly enough with a coupled cavity mode to lend that mode some of its nonlinearity. The cavity mode, then, becomes gently anharmonic, and thus sensitive to photon number, as each further incident photon excites a nondegenerate transition rather than just shunting the cavity state up some bosonic ladder of evenly-spaced states. In this way, coupling in nonlinear elements like transmon qubits to linear photonic landscapes can support interactions between photons at specific sites or modes that are strongly-enough nonlinear, as each photon 'knows' whether another is present there.

Introduction of a nonlinear emitter or an ensemble of nonlinear emitters to a topological photonic system [32] mediates interactions between photons, connecting cavity quantum electrodynamics with topological photonics. This has been realized for optical photons by coupling them to Rydberg-dressed atoms, providing the first assembly of two-photon Laughlin states of light [45]. In quantum circuits, a 3-site lattice of parametrically-coupled transmon qubits enabled observation of chiral orbits of photons/holes [170], and a $1 \times 8$ lattice of transmons enabled exploration of Mott physics [110, 172, 168]. In nanophotonics, a topological interface enabled coupling of quantum dots to a topological channel [13] and a resonator realized by closing such a channel on itself [14].

Taking the synthetic Chern insulator described in the previous chapters, we couple a single superconducting transmon qubit to its edge, and explore the regime of strong-coupling cavity quantum electrodynamics for a highly nonlinear emitter interacting with the spectrally resolved modes of the topological lattice band structure. We detect Rabi oscillations between the excited transmon and each mode, and measure the synthetic-vacuum-induced Lamb shift of the transmon. Finally, we demonstrate the ability to employ the transmon to count individual photons [175] within each mode of the topological band structure. This work opens the field of experimental chiral quantum optics [102], enabling topological many-body physics with microwave photons [7, 48] and providing a route to backscatter-resilient quantum communication.

## 5.1 Coupling a quantum emitter to the topological lattice

To explore quantum nonlinear dynamics in the topological lattice we couple it to a transmon qubit which acts as a quantized nonlinear emitter whose properties change with each photon that it absorbs. Unlike traditional cavity and circuit QED experiments in which a nonlinear emitter couples to a single mode of an isolated resonator, here the transmon couples to all modes of the topological lattice. We induce a controlled resonant interaction (see 2.4) between the transmon and individual lattice modes, investigating the resulting strong-coupling physics.

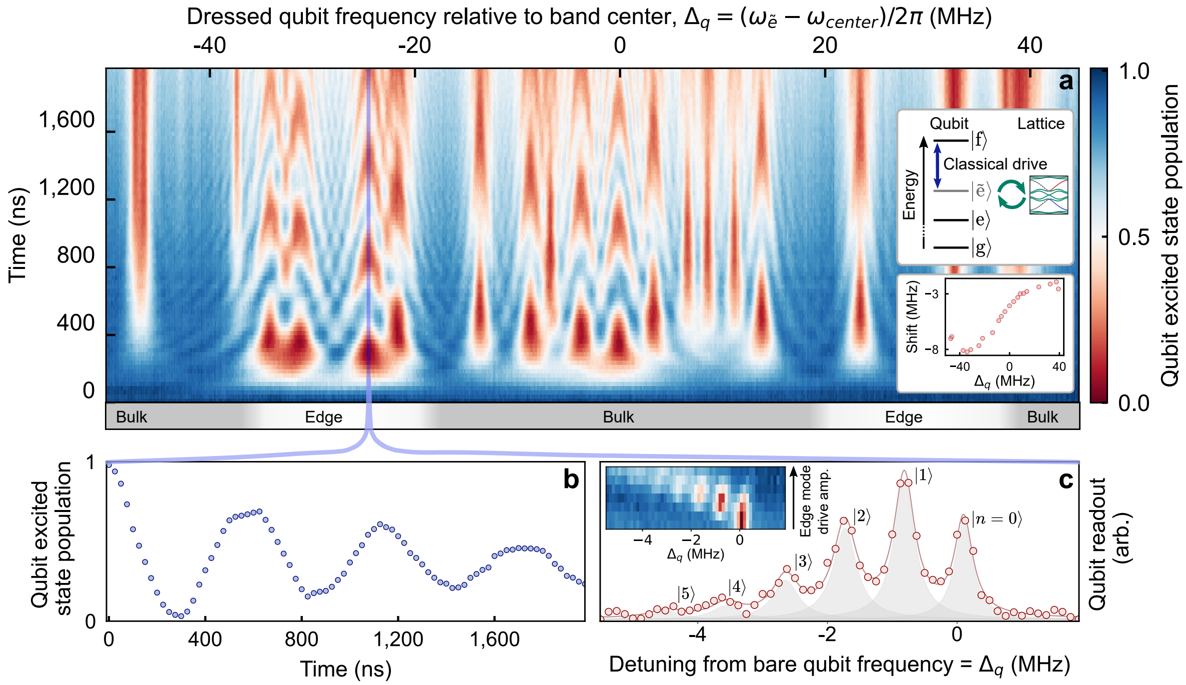

Figure 5.1: **Quantum nonlinear dynamics on a chiral lattice.** When a transmon qubit is coupled to the edge of the topological lattice, many of the properties of the (nonlinear) qubit are transferred to the (linear) lattice modes. In **a,** we prepare the qubit in its second excited state $|f\rangle$ (see **top inset**), and drive it with a classical tone (see Methods), thereby scanning the energy of resulting dressed excited state $|\tilde{e}\rangle$ through the band structure. The qubit can then coherently exchange a single photon with individual lattice modes. The resulting multimode chevron exhibits *fast*, low-amplitude Rabi oscillations when the qubit is detuned from the lattice modes, and slower, high-contrast oscillations on resonance with each mode. The vacuum coupling to each mode is proportional to that mode's overlap with the qubit site (see section 5.6.2); as such the edge modes exhibit fast oscillations, while many bulk modes exhibit slower oscillations. The **bottom inset** shows the Lamb shift of the transmon due to the topological lattice vacuum, measured as the frequency differences between chevrons and linear spectroscopy in Figure 4.12. The chevrons exhibit an additional overall Stark shift from the classical drive. The gray/white at **bottom** highlight band/gap locations. **b,** When the qubit $|\tilde{e}\rangle$ state approaches resonance with a lattice mode (blue line in **a**), vacuum-stimulated Rabi oscillations between qubit and cavity arise, demonstrating strong-coupling cavity QED where information exchange with a single chiral mode is faster than all decay processes. **c,** To count photons in an edge mode, here the highlighted mode in **a**, we directly excite that mode with a coherent pulse and detect the number of photons it contains as a discrete photon-number-dependent shift of the qubit frequency (probed through its readout cavity, see section 5.3). The multi-Lorentzian fit and individual Lorentzians for each photon number are shown in gray. **Inset,** by measuring the qubit excitation spectrum vs. drive amplitude applied to this edge mode, we observe a transition from vacuum (single high-frequency resonance) to the expected Poisson distribution (multiple lower-frequency resonances). Uncertainties are smaller than data points in **b** and **c**.

The $|g\rangle \leftrightarrow |e\rangle$ transition of the transmon ($\omega_q \approx 2\pi \times 7.8$ GHz) is detuned from the lattice spectrum ($\omega_{\text{lattice}} \approx 2\pi \times 9$ GHz) by $\Delta \approx 2\pi \times 1.2$ GHz. We bring the transmon controllably into resonance with individual lattice modes via the dressing scheme in Figure 5.1a inset; this dressing also gives us complete control over the magnitude of the qubit-lattice site coupling.

In Figure 5.1a we tune the excited transmon into resonance with individual lattice modes and observe vacuum-stimulated Rabi oscillations of a quantized excitation between the transmon and the mode. Comparing with the predicted band structure shown in Figure 5.1b, we see that the transmon couples efficiently to both bulk and edge modes of the lattice, despite being physically located on the edge. This is because the lattice is only 5 sites across, comparable to the magnetic length $l_B \sim 1/\alpha = 4$ sites, so the lattice site coupled to the transmon has substantial participation in both bulk and edge modes; furthermore, the system is sufficiently small that the number of bulk sites is comparable to the number of edge sites, so all modes have approximately the same “volume.” The rates of Rabi oscillation shown in Figure 5.1a reflect the participation of the qubit site in each mode.

To unequivocally demonstrate strong coupling between the transmon and a single lattice mode, we examine a single frequency slice of Figure 5.1a versus evolution time. Figure 5.1c shows such a slice and demonstrates high-contrast oscillations that take several Rabi cycles to damp out, as is required for strong light-matter coupling. For simplicity, we choose our dressed coupling strength to be less than the lattice mode spacing; stronger dressing to explore simultaneous coupling to multiple lattice modes opens the realm of super-strong-coupling physics [118, 93], where the qubit launches wavepackets localized to smaller than the system size.

When a qubit is tuned towards resonance with a single cavity mode it experiences level repulsion [57] and then an avoided crossing at degeneracy. The situation is more complex for a qubit coupled to a full lattice, where one must account for interactions with *all* lattice modes, both resonant and non-resonant. In total these couplings produce the resonant oscillations observed in Figure 5.1c plus a frequency-dependent shift due to level repulsion from off-resonant lattice modes, which may be understood as a Lamb shift from coupling to the structured vacuum [95]. We quantify this Lamb shift by comparing the frequencies of the modes observed in linear lattice spectroscopy, as in Figure 4.12a but with the transmon present (see Figure 4.9), to those observed in chevron spectroscopy in Figure 5.1a. These data are shown in the lower inset to Figure 5.1a. When the qubit is tuned near the low-frequency edge of the lattice spectrum it experiences a downward shift from all of the modes above it, and when it is tuned near the upper edge of the lattice, it experiences a corresponding upward shift. These two extremes smoothly interpolate into one another as modes move from one side of the qubit to the other. This effect arises from the multimodedness of our qubit/cavity system, and not the topology explicitly, as the qubit is coupled only to a single site. There is also a near-constant Stark shift of $\sim$ 3.5 MHz arising from the classical dressing tone. To our knowledge, this is the first measurement of the Lamb shift of a qubit in a synthetic lattice vacuum.

Finally, we demonstrate the ability to count photons within an individual lattice mode. If the transmon were coupled to a single lattice site and not to the full lattice, each photon in that site would shift the qubit $|g\rangle \leftrightarrow |e\rangle$ transition by $2\chi$, where $\chi \approx \frac{g_l^2}{\Delta} \times \frac{\alpha_q}{\Delta+\alpha_q} \approx 2\pi \times 5$ MHz, and $\alpha_q$ is the transmon anharmonicity. This photon-number-dependent shift, and thus the intra-cavity photon number, can be measured by performing qubit spectroscopy detected through the readout cavity (see section 5.6.2). When the transmon is coupled to a lattice rather than an isolated cavity, the $\chi$ shift is diluted by the increased volume of the modes. In Figure 5.1d, we inject a coherent state into the highlighted mode in Fig. 5.1a and then perform qubit spectroscopy to count the number of photons within the mode. The observed spectrum corresponds to a coherent state with $\bar{n} \approx 1.4$, with the individual photon occupancies clearly resolved. Indeed, when we perform this experiment as a function of the amplitude of the coherent excitation pulse (Fig. 5.1d, inset), we find a continuous evolution from vacuum into a Poisson distribution over the first six Fock states.

In this work we have demonstrated a photonic materials platform that combines synthetic magnetic fields for lattice-trapped photons with a single emitter. This has enabled us to explore interactions between the individual modes of a topological system and the non-linear excitation spectrum of the emitter, entering the realm of fully-granular chiral cavity QED and thus demonstrating the ability to count and manipulate individual photons in each mode of the lattice. We anticipate that coupling a transmon to a longer edge would enable qubit-mediated photon-induced deformation of the edge channel (in the “super strong” coupling limit of the edge channel [118, 187]), as well as universal quantum computation via time-bin-encoding [149] or blockade engineering [35]. Introduction of a qubit to the bulk of this system would allow investigation of the shell-structure of a Landau-photon polariton [48], a precursor to Laughlin states. Addition of a second qubit on the edge would allow chiral, back-scattering-immune quantum communication between the qubits [102]. Scaling up to one qubit per site will enable dissipative stabilization [109, 82, 67, 96] of fractional Chern states of light [7] and thereby provide a clean platform for creating anyons and probing their statistics.

## 5.2 Setup used for pulsed measurements

As described in more thorough detail in an as-yet-unpublished doctoral thesis by Gabrielle Roberts [169], pulsed time-domain measurements that can probe qubit dynamics, used to generate the data in Figure 5.1, require fast pulse generation and digitization that are not necessary for the continuous-wave microwave measurements detailed in the last chapter, where the response of a system to a steady-state tone is the measurement of interest. Here, it is necessary to shape, on the ns timescale, the pulses used to control the states of superconducting qubits, and to achieve the fine frequency control necessary for good measurement resolution in frequency-space and access to resonant dynamics. Measurements of qubit states executed dispersively through readout resonators must also be phase-sensitive and recordable via digitizer so that many thousands of individual experimental shots can be averaged to produce a distribution that characterizes the quantum dynamics under study. An accessible and thorough introduction to the basics of pulsed measurements on superconducting qubits can also be found in a thesis by Naghiloo [128].

For the qubit measurements described in the section above, a set of room-temperature electronics handle this signal generation and recording: a Keysight arbitrary waveform generator (M8195A, 64 GSa/s) is used to synthesize a local oscillator signal near the qubit frequency, while Berkeley Nucleonics 845-M microwave synthesizers provide separate local oscillator signals near lattice and dressing frequencies. The local oscillators are then I/Q modulated by Keysight PXIe AWGs (M3202A, multichannel, 1GS/s) to generate the individual qubit drive, qubit readout, and dressing pulses. The qubit drive and readout pulses are combined outside the fridge and sent to the readout resonator. The reflected readout signal is routed to the output line via circulators and amplified with a HEMT amplifier at 4 K and additional room temperature amplifiers (Miteq AFS3-00101200-22-10P-4, Minicircuits ZX60-123LN-S+). The signal is then demodulated using an IQ mixer and recorded using a fast digitizer (Keysight M3102A, 500 MSa/s). A layout of the room-temperature components of the experimental setup can be found in Figure 5.2.

## 5.3 Transmon characterization

The transmon chip is clamped in a copper holder that is then mounted on the side of the niobium lattice (see Figure 4.7). Indium foil is added to the inner surface of the copper holder, padding the qubit clamp in order to better thermalize the sapphire chip on which the qubit is printed and secure the qubit in its housing. One measurement port in the system strongly couples to the readout cavity, allowing both supply of strong drive and performance of reflection measurements which dispersively read out the qubit state. The

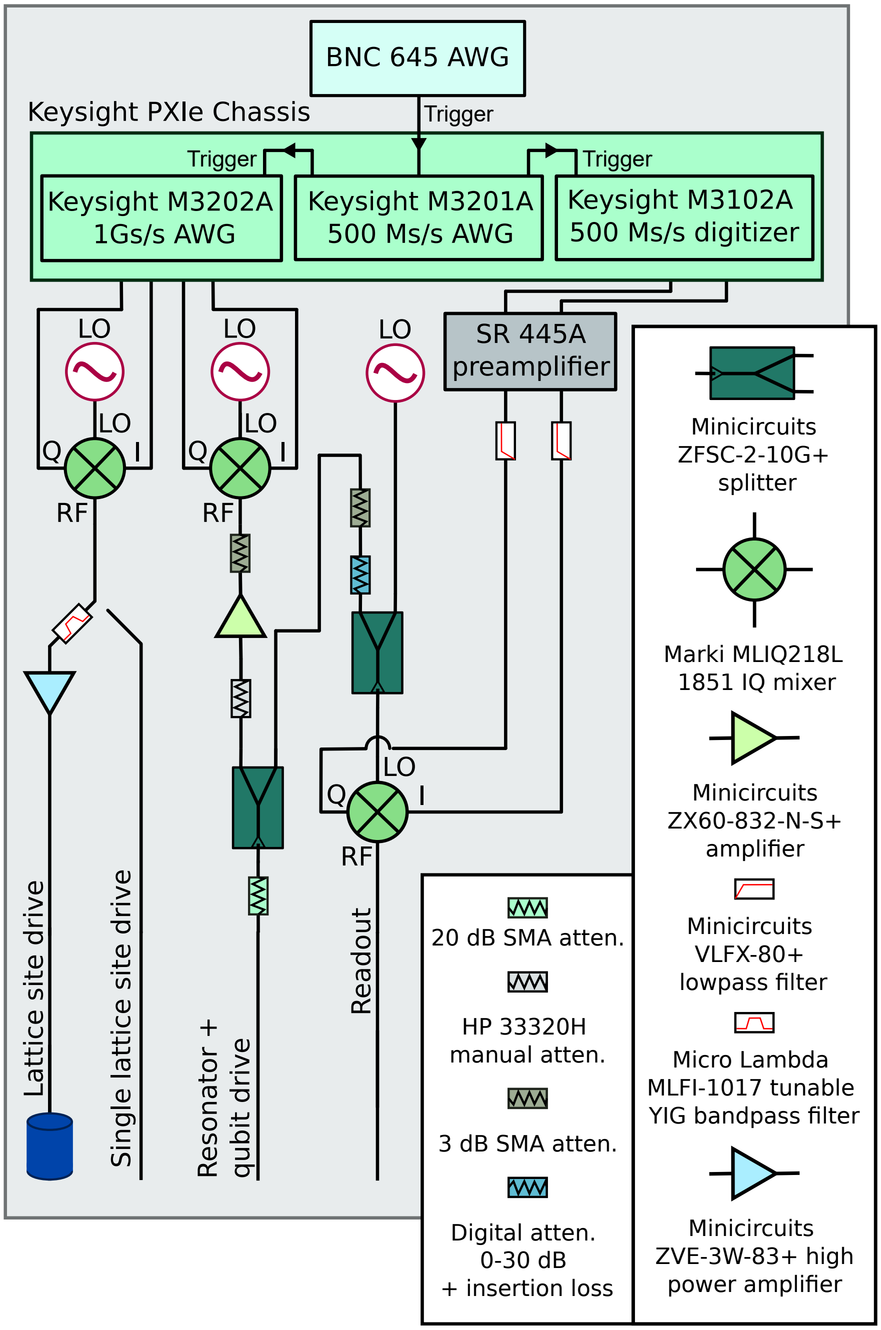

Figure 5.2: **Room-temperature setup for single-qubit measurements.** In any given measurement, one of the three readout lines pictured in Figure 4.10 is selected for use. Drives on lattice sites, important for some pulsed measurements, are either passed directly into the refrigerator after IQ modulation or, in the case of strong dressing tones, are filtered by a tunable bandpass YIG filter with a $\sim 20$ MHz bandwidth and amplified before use.

transmon is fixed-frequency to avoid unnecessary dephasing from sensitivity to the magnetic fields applied to the YIG spheres.

The Hamiltonian of the 25 lattice sites and a readout resonator coupled to the qubit is:

$$
\begin{aligned}
\frac{H}{\hbar} = &\sum_{p=q,r} \left( \omega_p \hat{a}_p^\dagger \hat{a}_p - \frac{\alpha_p}{2} \hat{a}_p^{\dagger 2} \hat{a}_p^2 \right) - 2\chi_r \hat{a}_q^\dagger \hat{a}_q \hat{a}_r^\dagger \hat{a}_r \\
&+ \sum_{l=1}^{N_{\text{modes}}=25} \left( \omega_l \hat{a}_l^\dagger \hat{a}_l - \frac{\alpha_l}{2} \hat{a}_l^{\dagger 2} \hat{a}_l^2 - 2\chi_l \hat{a}_l^\dagger \hat{a}_l \hat{a}_q^\dagger \hat{a}_q \right) \\
&+ \sum_{l \neq m} -2\chi_{lm} \hat{a}_l^\dagger \hat{a}_l \hat{a}_m^\dagger \hat{a}_m,
\end{aligned}
\tag{5.1}
$$

Here $\omega_q = \omega_{ge}$ is the $g \leftrightarrow e$ transition frequency of the transmon, $\alpha_q$ is the transmon anharmonicity (so $\omega_{ef} = \omega_q - \alpha$), $\omega_r$ is the bare readout resonator frequency, $\alpha_r$ is the self-Kerr shift of the readout resonator, $2\chi_r$ is the qubit-readout dispersive shift, $\omega_l$ are the lattice mode frequencies, $2\chi_l$ are the qubit-lattice mode dispersive shifts, $\alpha_l$ are the self-Kerr shifts of the lattice modes, and $\chi_{lm}$ are the cross-Kerr shifts of the lattice modes.

The transmon qubit is controlled and read out dispersively via drive and readout tones applied to its readout resonator, shown enclosed in the left side of the blue boxes in Figure 4.7 and enclosed in red in Figure 4.7.

Initial qubit characterization was done with the single lattice site to which the qubit was coupled tuned to the lattice frequency while the other 24 sites were temporarily blocked off using screws lowered from the lid of the lattice until they contacted the post of the lattice site. My predecessor used this configuration to compare qubit lifetimes with and without magnets present in the chiral lattice; the introduction of the magnets resulted in the lifetime of the qubit dropping from $\sim 9$ to $\sim 3$ $\mu$s, approximately commensurate with the lifetimes of the cavity modes.

Removing the detuning screws, we characterize the qubit coupled to the full tuned-up lattice including the magnets necessary to realize the synthetic flux. Table 5.1 summarizes the qubit parameters. The readout frequency and linewidth and single lattice site frequency are measured and fit via continuous-wave reflection measurements of ther eadout resonator taken with a network analyzer. The qubit transition frequency $\omega_q/2\pi$ is measured through Ramsey spectroscopy, a measurement especially effective at characterizing small differences between the frequencies of applied drive pulses and the frequencies of qubit dipole transitions. $\chi_r$ is measured by $\pi$-pulsing the qubit and measuring the associated dispersive shift in the readout resonator frequency. The $\chi_l$ shifts are measured, for lattice modes strongly-coupled enough to the qubit for this to be seen, by supplying a few-photon coherent drive to the lattice corner on-resonance with each lattice eigenmode and measuring the photon-number-dependent splitting (see section to follow) in the qubit frequency. The self-Kerr $\alpha_l$ of the modes were calculated from the measured dispersive shifts $\chi_l$ and transmon anharmonicity $\alpha_q$, using the relation $2\chi_l = \sqrt{\alpha_q \alpha_l}$ [132].

## 5.4 Structure of pulsed measurements with qubit

To generate number splitting data like that shown in Figure 5.1, a classic demonstration of strong coupling in circuit quantum electrodynamics in which photon-number-resolved peaks in the qubit transition spectrum appear when the dispersive shift between cavity and qubit outstrips the qubit linewidth [175], we populate relevant eigenmodes with photons by providing long and weak drive tones at these modes' frequencies through an antenna weakly coupled to the corner site of the lattice most proximate to, and directly coupled to, the qubit. This pulse sequence is diagrammed in Figure 5.3. While this weak drive is still being supplied to the lattice corner site, we try to excite the qubit from its ground state by supplying its readout resonator with a long Gaussian drive pulse ($\sigma = 1400$ ns) that has a fraction of the amplitude it would take to fully place the qubit in its first excited state. We then measure the degree to which the qubit is excited from its ground state with a readout tone applied at a range of frequencies in the vicinity of the original (zero-lattice-photon) qubit transition. In this way we can characterize the photon-number-dependent shift of the qubit resonance, which depends on photonic population in each lattice eigenmode that has enough edge participation to couple notably to the qubit.

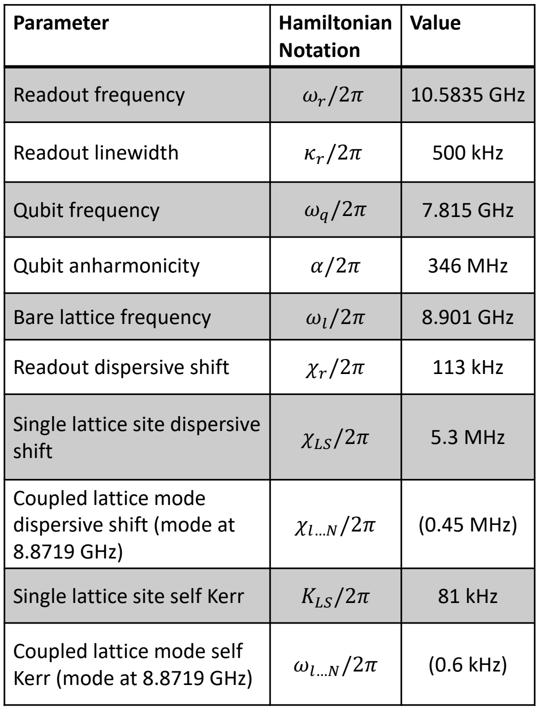

| Parameter | Hamiltonian Notation | Value |
|---|---|---|
| Readout frequency | $\omega_r/2\pi$ | 10.5835 GHz |
| Readout linewidth | $\kappa_r/2\pi$ | 500 kHz |
| Qubit frequency | $\omega_q/2\pi$ | 7.815 GHz |
| Qubit anharmonicity | $\alpha/2\pi$ | 346 MHz |
| Bare lattice frequency | $\omega_l/2\pi$ | 8.901 GHz |
| Readout dispersive shift | $\chi_r/2\pi$ | 113 kHz |
| Single lattice site dispersive shift | $\chi_{LS}/2\pi$ | 5.3 MHz |
| Coupled lattice mode dispersive shift (mode at 8.8719 GHz) | $\chi_{l\ldots N}/2\pi$ | (0.45 MHz) |
| Single lattice site self Kerr | $K_{LS}/2\pi$ | 81 kHz |
| Coupled lattice mode self Kerr (mode at 8.8719 GHz) | $\omega_{l\ldots N}/2\pi$ | (0.6 kHz) |

Table 5.1: **Parameters of qubit, lattice, and readout resonator.** Terms designated "single lattice site" are measured when only the lattice site to which the qubit is directly coupled is tuned to the lattice frequency while the rest of the lattice sites are far detuned. The bare lattice frequency is the target frequency to which each lattice site is tuned before the couplings to adjacent lattice sites are enabled. Values in parentheses are example quantities for the lattice mode investigated in Figures 5.1b and 5.1c.

It's worth asking how we know what frequency of drive to use to generate a coherent state in the relevant eigenmodes! We should expect that coupling between the transmon, a source of nonlinearity, and the lattice modes with which it hybridizes should lend some nonlinearity to the lattice modes, realized as a high-power shift and 'snap' upon qubit saturation by a strong drive in Figure 4.9. Matt Reed's thesis [166] introduces this high-power behavior of a weakly-nonlinear superconducting resonator coupled to a transmon qubit and demonstrates how to use that high-power shift for measurement of qubit states. We have, in figure 4.9, lattice transmission spectra taken at low drive power with a network analyzer that provide a pretty good guide of where the lattice eigenmodes are located. To ensure that we're fully accounting for the qubit's effects on lattice modes at drive powers used for pulsed measurements, we perform lattice spectroscopy via the qubit, supplying long, weak drive tones to the lattice corner at a range of frequencies and attempting to excite the qubit from its ground state. If the qubit is dispersively shifted by the affirmative presence of photons in a lattice resonance, it will fail to excite at the known resonant frequency; this effect is used to trace out a lattice spectrum as ‘seen’ by the qubit.

To generate Rabi oscillations between the qubit and lattice eigenmodes (see section 2.4), we supply a sequential set of $\pi$ pulses at the qubit transition frequencies $\omega_{ge}$ and $\omega_{ef}$ to prepare the qubit in its $|f\rangle$ state. We then supply a square pulse of varying length ($0-2000$ ns) to the qubit's readout resonator to tune the qubit into resonance with targeted lattice eigenmodes and drive oscillations between qubit and lattice. We finally supply an additional $\pi$ pulse at $\omega_{ef}$ before reading out the qubit state. This pulse sequence is also diagrammed in Figure 5.3.

## 5.5 Dilution of global qubit-lattice $\tilde{g}$ between modes

If all other sites in the $5\times5$ lattice, besides the site to which the transmon is directly coupled, are detuned from this single corner resonator, each photon in the corner site induces a shift of the qubit $|g\rangle \leftrightarrow |e\rangle$ transition of $2\chi$, with $\chi_{LS} \approx \frac{g_l^2}{\Delta} \times \frac{\alpha_q}{\Delta+\alpha_q} \approx 2\pi \times 5.3$ MHz. When, after initial qubit characterization, all other lattice sites are tuned back into resonance and hybridize to form the lattice's topological band structure, this qubit-site dispersive shift is diluted between all lattice modes in proportion to their participation on that corner site. Lattice mode $l$ experiences a dispersive shift $2\chi_l = 2\chi_{LS} \times |\langle u_l|LS\rangle|^2$, where $|u_l\rangle$ is the wavefunction of mode $l$, and $|LS\rangle$ is the wavefunction of a photon localized on the corner site coupled to the transmon. Note that $\sum_l \chi_l = \chi_{LS}$.

The mode employed in Figure 5.1c, exhibits a shift per photon of $2\chi_7$ where $\chi_7 = 2\pi\times0.45$ MHz, extracted from the frequency difference between zero- and one-photon resonances of Figure 5.1c. This mode has a wavefunction overlap with the corner site of $|\langle u_7|LS\rangle|^2 = 0.09$, and thus we anticipate a shift of $2\chi_7 = 2\chi_{LS} \times |\langle u_7|LS\rangle|^2 = 2 \times 2\pi \times 5.3$ MHz $\times 0.09 \approx 2 \times 2\pi \times 480$ kHz, in agreement with the measured $\chi_7 = 2\pi \times 450$ kHz. In Figure 5.4 we

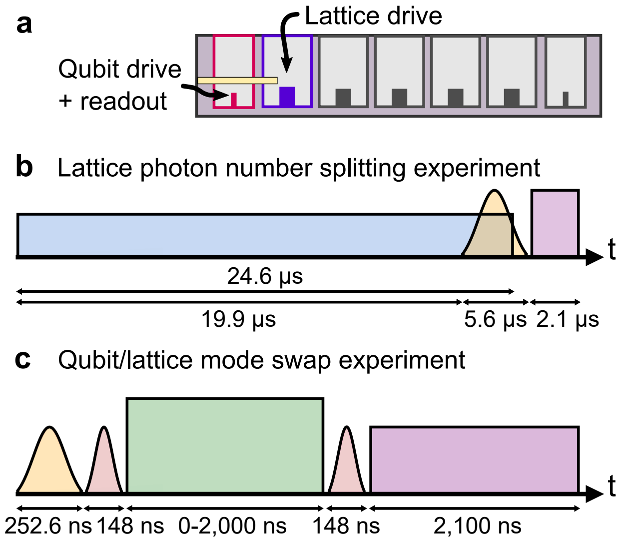

Figure 5.3: **Pulse sequences used for Figure 5.1.** In **a**, locations of qubit drive, readout tone, and lattice corner drive are shown in a schematic cross-section of the lattice edge. The transmon chip is shown in yellow. **b**, To measure the photon-number-dependent shift in the qubit resonance, we apply a very long (24.6 $\mu$s) weak drive (blue pulse) at lattice eigenmode frequencies to the lattice corner site directly coupled to the qubit. After a wait, we apply a slow weak Gaussian pulse (yellow) at $\omega_q$ and then read out (purple pulse) the qubit absorption after the lattice eigenmode drive is completed. **c**, To generate Rabi oscillations between qubit and a swath of the lattice eigenspectrum, we prepare the qubit in its $|f\rangle$ state with two $\pi$ pulses at $\omega_q = \omega_{ge}$ (yellow) and $\omega_{ef}$ (red). We drive dressed vacuum Rabi oscillations with a square pulse of varying length at $\omega_{f0\leftrightarrow g1} = (\omega_{ge} + \omega_{ef} - \omega_l)$, apply a $\pi$ pulse at $\omega_{ef}$ (red) to enable readout on the $|g\rangle \leftrightarrow |e\rangle$ transition, and read out (purple).

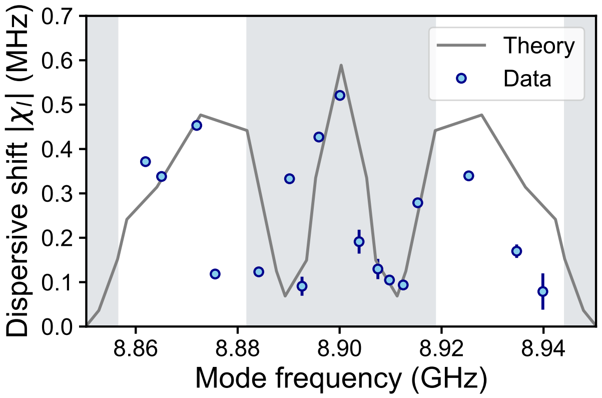

Figure 5.4: **Mode-dependent dispersive shift of qubit.** Theoretical predictions of the dispersive shift between the qubit and each lattice eigenmode are compared to measured values from number splitting data. An example plot of number splitting due to population of a particular lattice eigenmode is seen in inset **c** of Figure 5.1. Theory is based on the measured (single-site) $\chi_{LS}$ scaled by the spectral weight of each lattice mode at the lattice corner site which is coupled to the qubit. Only modes present in the chevron spectrum of the lattice pictured in Figure 5.1 are included. The separation between 0- and 1-photon peaks when mode $l$ is driven is defined as $2\chi_l$. Expected regions of the bulk bands, estimated from mode indices, are highlighted in gray. Error bars are derived from fits to number splitting data.

compare, for each mode, the predicted shift based on simulations of eigenmode structure with the shift extracted from the observed splittings between zero- and one-photon peaks of additional number splitting measurements.

## 5.6 Measurement and analysis of four-wave swap

As the transmon is fixed-frequency, we "tune" the transmon to resonance with various lattice modes by dressing through the readout cavity using the four-wave process detailed in section 2.4: we prepare the transmon in the second excited ($|f\rangle$) state and then provide a detuned drive on the $|f\rangle \leftrightarrow |e\rangle$ transition to create a dressed $|\tilde{e}\rangle \approx |f\rangle - \frac{\Omega}{\Delta}|e\rangle$ state at any energy in the vicinity of the lattice band structure, with a dipole moment for coupling to the lattice which is rescaled by the ratio of the dressing Rabi frequency to the detuning from the $|f\rangle \leftrightarrow |e\rangle$ transition. The resulting vacuum-stimulated $|f,0\rangle \leftrightarrow |g,1_k\rangle$ Rabi frequency is:

$$\tilde{g}_k \approx \sqrt{2}\frac{g_l \alpha}{\Delta(\Delta+\alpha)}\Omega \times \langle x_{\text{transmon}}|\psi_k\rangle = \sqrt{2}\frac{g_k \alpha}{\Delta(\Delta+\alpha)}\Omega \tag{5.2}$$

Here $\alpha$ is the qubit anharmonicity, $\Delta$ is the detuning between qubit $\omega_{ge}$ and the lattice eigenmode frequency $\omega_k$, $\Omega$ is the Rabi frequency of the dressing tone on the $|f\rangle \leftrightarrow |e\rangle$ transition of the transmon, $\langle x_{\text{transmon}}|\psi_k\rangle$ is the participation within mode $k$ of the lattice site where the transmon resides, and $g_l$ is the bare coupling between qubit and the lattice corner site.

Drawn from Pechal et al. [145], this dressing scheme may alternatively be understood as a 2-photon Rabi process, where the $|f,0\rangle \leftarrow |e,0\rangle$ transition is stimulated by the classical drive, and the $|e,0\rangle \leftarrow |g,1_k\rangle$ transition is stimulated by the vacuum field of mode k. For the qubit measurements, the the lattice is tuned to a center frequency of $2\pi \times 8.9$ GHz, corresponding to a dressing frequency of $2\pi \times 6.35$ GHz ±50 MHz. Note that with the additional significant figure, the $|g\rangle \leftrightarrow |e\rangle$ transition has a frequency of $2\pi \times 7.75$ GHz.

### 5.6.1 *Mode dependence of effective $\tilde{g}$*

The stimulated vacuum-Rabi oscillations shown in Figure 5.1 between $|g, 0\rangle$ and $|f, 1\rangle$ display different rates depending on which lattice eigenmode is being populated. These rates should be directly proportional to the participation in the eigenmode of the corner lattice site which couples to the qubit. There is an additional dependence arising from the frequency-dependence of the dressing amplitude.

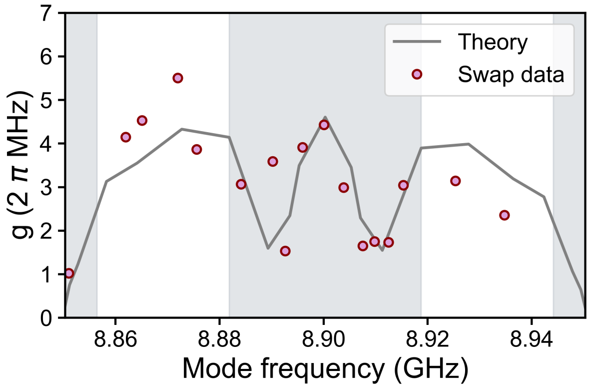

Figure 5.5: **Mode-dependent $|f0\rangle \leftrightarrow |g1\rangle$ coupling.** Theoretical predictions of the coupling $g_k$ seen in stimulated vacuum-Rabi oscillations between dressed $|\tilde{e}\rangle$ of the qubit and a range of lattice eigenmodes are compared with empirical $g_k$ drawn from measurements of the swap frequency close to resonance. Theoretical predictions are derived from rescaling $\tilde{g} = \sqrt{2}\frac{g\alpha}{\Delta(\Delta+\alpha)}\Omega$ by the spectral weight of each lattice mode at the lattice corner site which is coupled to the qubit. A small tilt in the theoretical plot (gray line) can be seen, with the lower-frequency side slightly elevated above the higher-frequency side. We omit characterization of error on the data-based quantities because we believe these errors are likely systematic.

In Figure 5.5, we plot couplings $\tilde{g}_k$ between the dressed $|\tilde{e}\rangle$ state of the qubit and each lattice eigenmode for which resonant swap oscillations are seen. A diagram of this dressed state and the lattice eigenspectrum is presented in the inset of Figure 5.1a. Figure 5.5 compares the above mode-dependent couplings $\tilde{g}_k$ to those that would be expected if we rescaled an effective $|f, 0\rangle \leftrightarrow |g, 1\rangle$ coupling $\tilde{g}$ by the spectral weight of each lattice mode at the lattice corner site which is coupled to the qubit. Figure 5.5 employs a drive strength $\Omega$ chosen to provide the best fit between theory and data. $\Omega$ exhibits an additional weak frequency dependence not included in the Figure 5.5 simulation arising from the frequency-dependent occupation of the driven corner lattice site in response to the classical excitation tone.

We measure $g_k = \omega_{swap,k}/2$ by fitting exponentially decaying sinusoids to slices of Figure 5.1a taken at drive frequencies closest to those that produced resonant oscillations with each mode. Because these data were taken at a discrete set of drive frequencies, many of these slices are likely slightly off-resonance, which could contribute to added scatter in $g_k$ rates found from data. Variations in the eigenmode spatial structure caused by lattice disorder, as well as frequency-dependent attenuation of the RF drive across the almost 100 MHz-wide band, produce the remaining differences between data and theory shown in Figure 5.5.

### *5.6.2 Lamb shift from a synthetic vacuum forest*

In addition to a variation in qubit-mode couplings $g_{swap}$ observed across the lattice spectrum, we also note that the lattice modes 'move' by different amounts to reach their locations in the chevron plot in Figure 5.1a. Another way to say this is that the drive frequencies $\omega_d$ which provide resonant access to coherent interactions between $|f, 0\rangle$ and $|g, 1\rangle$ states of qubit and lattice, differ from the bare expected $\omega_d = 2\omega_q - \alpha - \omega_k$ for each mode $k$. Comparing the swap-based spectrum in Figure 5.1a to low-power lattice spectra in Figure 4.9, one can see that the former spectrum is compressed and sees its lower-frequency resonant process asymmetrically shifted upwards towards band center.

This shift of resonant access to lattice eigenmodes stems from a mixture of Stark shift on the qubit $|f\rangle$ and $|g\rangle$ levels due to the strong classical swap drive, and the Lamb shift experienced by the qubit as its dressed excited state is 'tuned' near resonance with a 25-item forest of vacuum modes.

The scale of the measured shift on each mode (frequency in chevron plot minus frequency in low-power spectrum) is plotted as in inset in Figure 5.1a and here in Figure 5.6. All modes experience a global Stark shift of $\sim 4$ MHz that is largely constant, although mildly diagonal, across the spectrum due to the strong swap drive. On top of that Stark shift, a curved pattern with the strongest divergence from baseline around the edge modes traces out the effect of the global multimode Lamb shift, broadly understandable as:

$$\Delta_{q,\mathrm{Lamb}} = \sum_{\text{modes k below}} \frac{\tilde{g}_k^2}{\Delta_{k,m}} + \sum_{\text{modes k above}} \frac{\tilde{g}_k^2}{\Delta_{k,m}} \tag{5.3}$$

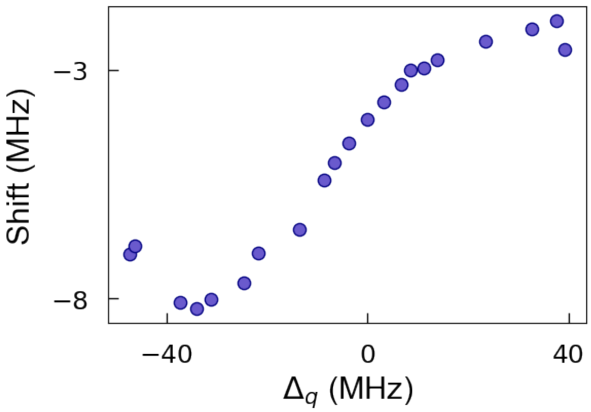

Figure 5.6: **Effect of Stark and Lamb shifts on qubit resonance.** We plot the difference between the frequencies of lattice eigenmodes accessed via four-wave swap and the frequencies of those eigenmodes in low-power transmission spectra. This difference, with this sign, represents the shift on the qubit's $|g\rangle \leftrightarrow |f\rangle$ transition due to the combination of Stark and Lamb shifts it experiences while being 'tuned' near resonance with lattice eigenmodes using a strong multiphoton drive.

Here $\tilde{g}_k$ is the dressed effective coupling rate between the qubit and mode $k$ of the lattice without an applied drive involved. $\Delta_{k,m}$ is the detuning between the frequency of the lattice eigenmode $m$ targeted for resonant swap coupling and the non-$m$ mode $k$'s frequency. Here it's convenient to make the assumption, which has some merit as the strong swap drive is applied on the readout resonator, that the swap drive has only higher-order and minimal effect on the lattice eigenmode frequencies, and that all of the arcane drive-based effects are constrained to the heavily dressed qubit transitions.

Were the lattice spectrum perfectly symmetric, when the qubit's dressed excited state was tuned into resonance with dead-center (the Dirac mode) of the lattice spectrum, we would expect the collective twelve-mode Lamb shifts, which scale inversely with detuning, from either side of band center to cancel each other out. Often when we think of the Lamb shift [95] we conceive of it as between a nonlinearity and a single-mode quantum vacuum; recent work has been done to explore the broadband Lamb shift of an emitter coupled to a mode continuum [181]. In contrast to both of the above situations, here the Lamb shift derives from near-resonant coupling between the qubit and a 25-element vacuum forest. Other work in multimode systems [35] involves a larger free spectral range between these individually addressable modes, whereas here the $\sim 5-10$ MHz detunings between modes of interest brings elements of this forest much closer to resonance with the qubit than is seen in some other multimode systems.

## 5.7 Conclusion

This demonstration of strong coupling between a transmon qubit and a topological lattice leverages the capacity of circuit quantum electrodynamics platforms to reach high coupling strengths in order to gain access to exploring strong light-matter interactions in a chiral system. Measurement of the multimode Lamb shift is particularly intersting because we probe a regime intermediate between qubit-single mode polariton physics and the physics of an emitter coupled to a continuum waveguide, a zone that is fundamentally of interest for researchers hoping to leverage the power of engineered photonic lattices but which is less explored.

# CHAPTER 6

# NON-RECIPROCAL TRANSPORT IN A CHIRAL EDGE CHANNEL

This chapter is based on the as-yet-unpublished second paper [142] of this thesis.

## 6.1 Introduction: Chiral transport of photons

Construction of topological metamaterials for photons provides designer access to the topological phases of fundamental interest in classical [178] and quantum [72, 140] materials physics. The robustness to disorder of chiral edge channels in topological insulators has inspired work [140, 155] across silicon photonics [66, 164, 121], optics [173], and microwave systems [203, 40, 27] to build topological photonic systems which guide backscatter-protected, directional propagation of classical light.

Incorporating nonlinearity into such topological metamaterials enables interactions between the otherwise non-interacting photons [32], opening avenues to investigate the fundamental nature of interactions between particles modified by topological structure [157, 31, 102, 116]. While limited by the strength of emitter-material couplings [14] and magneto-optical response [140] in many photonic platforms, introducing nonlinearity, whether system-wide [170, 28, 45] or spatially local [14, 84], drives work in topological photonics. Topological bandstructures which incorporate nonlinear interactions have the potential for enhancing and stabilizing lasing [11, 12, 176], protecting from loss the correlated and fragile multiphoton quantum states needed for quantum computing [123, 22, 117], stabilizing long-range entangled steady states of light in combination with emitter arrays [184, 148, 102] or (localized sites of) reservoir engineering [82, 208, 151], and enabling directional state transport to build quantum networks [69].

The strong light-matter interaction and flexible, controllable emitter-photon coupling available in circuit quantum electrodynamics offer a powerful toolbox with which to generate and capture photons in both continuum [10, 30, 91, 25, 214, 167] and multimode [100] or band-engineered [84, 212] waveguides. A thread of recent experiments has focused on achieving on-demand chiral emission of photons [120], in particular from superconducting qubits strongly coupled to bidirectional waveguides [80, 81, 79, 165], prioritizing combating loss in order to situate directionally-emitting qubits as nodes in broader quantum networks [42, 85]. These approaches employ interference between coupling points to emit directionally to an intrinsically bidirectional waveguide; we reverse this paradigm, making the waveguide the chiral system of interest and locally coupling non-chiral quantum emitters to it.

In the previous chapter of this thesis, we introduced a local nonlinearity to a synthetic Chern insulator, demonstrating strong coupling of a single transmon qubit [139] to individually-resolved eigenmodes of this superconducting microwave cavity array which breaks time-reversal symmetry for photons [138]. The sixteen-site edge of this superconducting topological lattice can admit couplings to many qubits or engineered reservoirs, opening opportunities for generating non-classical states of light which are specially enabled by the system topology [39, 131, 208, 151, 184, 82, 148, 143] and are of interest as resources for continuous-variable quantum information processing [149, 55].

In this chapter, we demonstrate non-reciprocal transport of itinerant photons via edge-localized wavepackets in a two-dimensional topological photonic metamaterial. We synthesize a wavepacket by spurring emission of a single photon from a transmon qubit strongly coupled to a set of discrete edge modes available in the bulk band gap of this finite-size Harper-Hofstadter lattice, operating in a regime intermediate between cavity and waveguide quantum electrodynamics. The wavepacket propagates along the chiral edge of the lattice and is detected by a second edge-coupled transmon, providing a direct observation of chiral emission. We measure a time delay for a photon launched ‘the long way around’ commensurate with that expected for an edge-propagating excitation. Demonstration of chiral transport between quantum emitters coupled to an engineered topological lattice offers opportunities for using such a system to build and probe entangled states of light which gain structure from [39, 131], or are made accessible by [184, 82, 148, 143, 208, 151], the system topology, and is a step along the path to exploring topological quantum matter [157].

In Section 6.2 we detail the experimental setup used here, and the work done to characterize the updated lattice platform. In Section 6.2 we characterize the transmons used and explain protocols related to cooling, measurement, and handling of these anharmonic oscillators. In Section 6.4 we demonstrate detection of a photon launched between two transmon qubits through individual and multiple edge modes of the topological lattice. In Section 6.5 we use this pair of qubits to demonstrate a time delay in transport through a chiral channel commensurate with this wavepacket propagating along the chiral lattice edge. And in Section 6.6 we explore a range of issues and experimental subtleties related to implementing the multiphoton classical drive used to execute emission and detection of lattice-propagating photons.

## 6.2 Experimental setup and lattice characterization

Our Chern insulator platform consists of a the same 5×5 array of reentrant quarter-wave-post microwave resonators [162] machined in niobium that has been described throughout this thesis. Their bare frequencies are $\omega_{lat}/2\pi = 8.903$ GHz and cavity-cavity couplings $J/2\pi \sim 18$ MHz. Recall that to generate a *synthetic* magnetic field for photons, we employ an *actual* gauge field by introducing magnetic-field-tunable magnon modes to our cavity array. This results in a local phase modification on specific cavities that introduces topology to the lattice band structure.

This realization [138, 139] of a quarter-flux Harper-Hofstadter lattice for light hosts two chiral edge channels of opposite directionality at non-degenerate energies in gaps between its bulk bands. Because the edge channels of this chiral lattice are sparsely sampled by

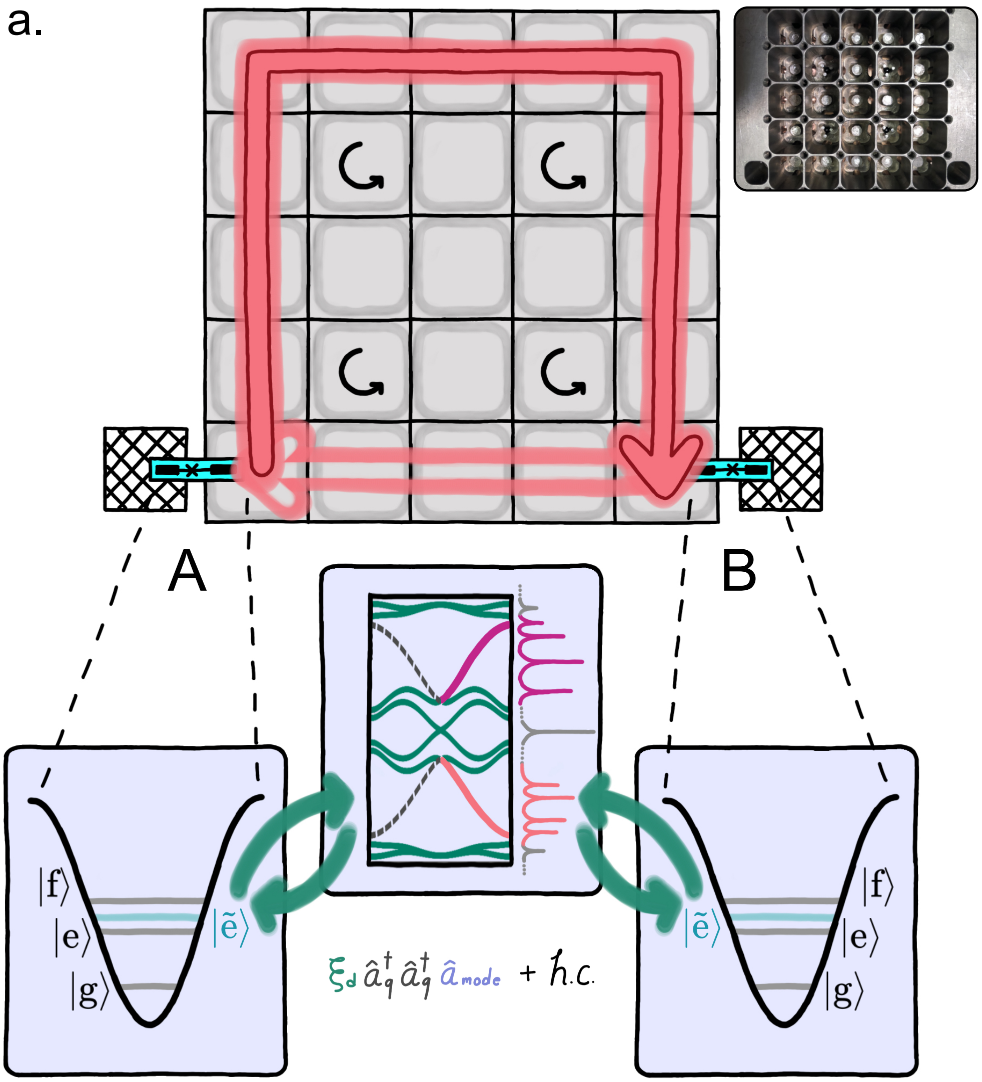

Figure 6.1: **Experimental setup for two-qubit measurements. a,** A 5 × 5 lattice of microwave cavity resonators machined in superconducting niobium (photograph inset at top right) realizes a quarter-flux Harper Hofstadter model for microwave photons. Cavities are evanescently tunnel-coupled; curved black arrows indicate the four such lattice sites engineered to host an in-cavity phase winding that supplies the lattice topology. We couple two fixed-frequency superconducting qubits, to corner sites of this lattice as well as to auxiliary resonators (hashed squares) for readout and control. Undriven, these qubits are more than 1 GHz detuned from the lattice band. A schematic at bottom indicates the four-wave process which brings a dressed excited state of each qubit (left and right boxes) on resonance with elements of the lattice eigensystem (center box), enabling coherent transfer of an excitation between each qubit and the topological lattice.

discrete edge-localized eigenmodes, generation of a wavepacket in each chiral edge channel is realizable by exciting a set of these edge modes. As the smallest lattice which hosts a distinct bulk and edge, a $5 \times 5$ cavity array allows clear distinctions to be drawn between its 25 eigenmodes, and offers access to explore finite-size effects.

We again cool this lattice to $\sim$ 35 mK, ensuring $\sim$ 3 $\mu$s excitation lifetimes in the superconducting niobium cavity array. We diagram the experimental setup used to take lattice spectra and perform qubit measurements in Figure 6.2. Notably, in order to supply a multiphoton drive strong enough to generate speedy resonant swapping of excitations between $|f, 0\rangle$ and $|g, 1\rangle$, while not unduly relying on power amplifiers to send a massive amount of power into the refrigerator, we apply only 40 dB of attenuation (versus the standard 70 dB) to multiphoton drive input lines. These lines are then bandpass filtered with hardware thermalized at base, blocking off unwanted radiation except at a target regime of frequencies near-resonant with the drive. We calculate the blackbody spectrum of a radiating object at 4K (the plate above at which lines are thermalized) and conclude that a minimal amount of thermal radiation from this plate will make it through the bandpass filtering centered around 6.3 GHz. We diagram the room-temperature electronics used to take time-domain pulsed measurements of qubit and lattice in Figure 6.3.

### 6.2.1 Characterizing the lattice and its edge channels

To counter any drift accumulated over the several years' interim between measurements, we assessed the frequencies of the lattice corner sites to which the qubits are coupled with screws inserted to spoil coupling to the rest of the lattice, and then re-tuned the frequencies of single-post sites by adding and removing indium to better match this resonance condition.

Ultimately the room-temperature variation in lattice site frequencies of single-post cavities wass reduced to a maximum of ±5 MHz, with an average of 0.35 MHz (standard deviation 3.53 MHz) departure from resonance with the chiral sites, against a hopping rate

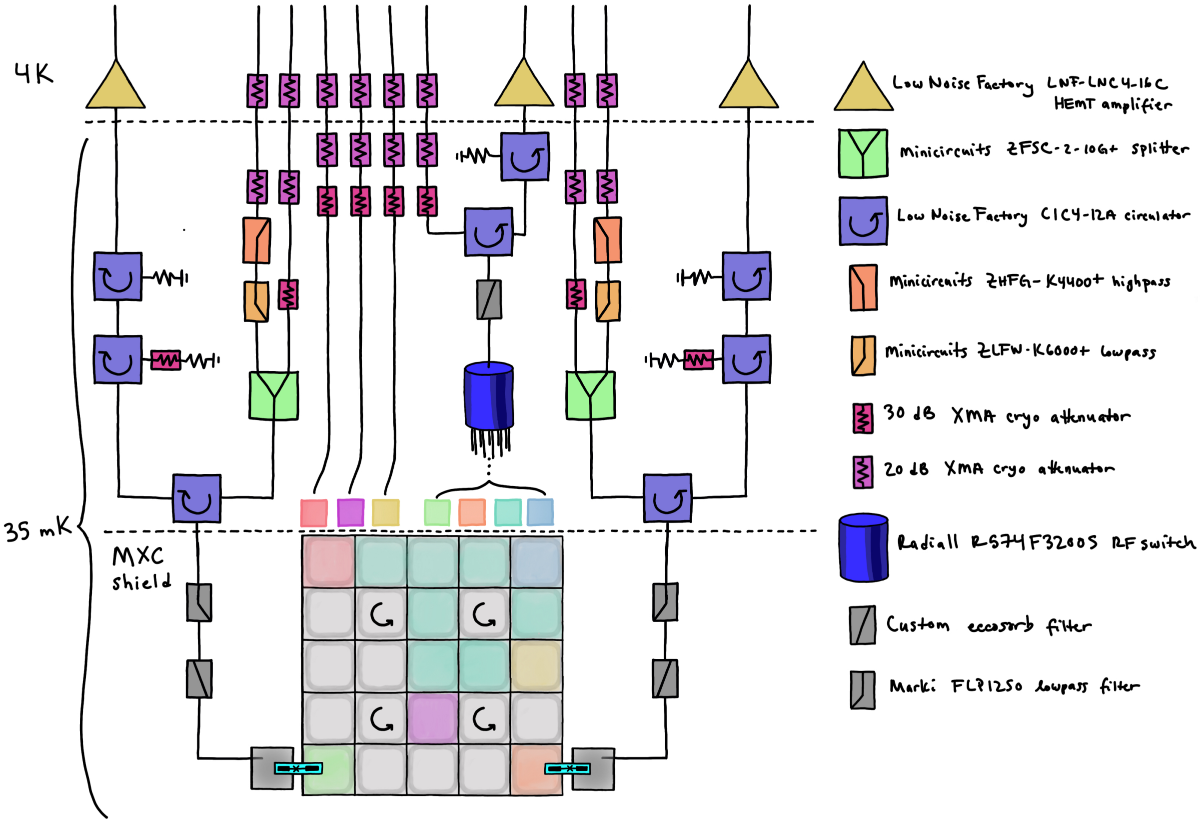

Figure 6.2: **Diagram of two-qubit setup within the dilution refrigerator.** Lattice sites highlighted in color are reached either by input-only lines or made accessible to reflection measurements via a 10-way RF switch installed after a circulator. We use antennas coupled to lattice sites to make transmission measruements of the lattice spectrum. Bottom dashed line illustrates the boundary of the mixing chamber shield. Filters on input lines used for multiphoton drives are shown in orange and yellow just above the RF combiners. Note that circulators used as isolators at output lines have a mix of terminators; those that go directly to terminator use cryogenic terminators from Quantum Microwave (QMC-CRYOTERM-0412) while those preceded by an attenuator use Minicircuits MCL-ANNE-50+ terminators that are not necessarily 50 Ω in a cryogenic setting. To end-run around this we subject any photons reaching these terminators and returning to the circulators to 60 dB of attenuation.

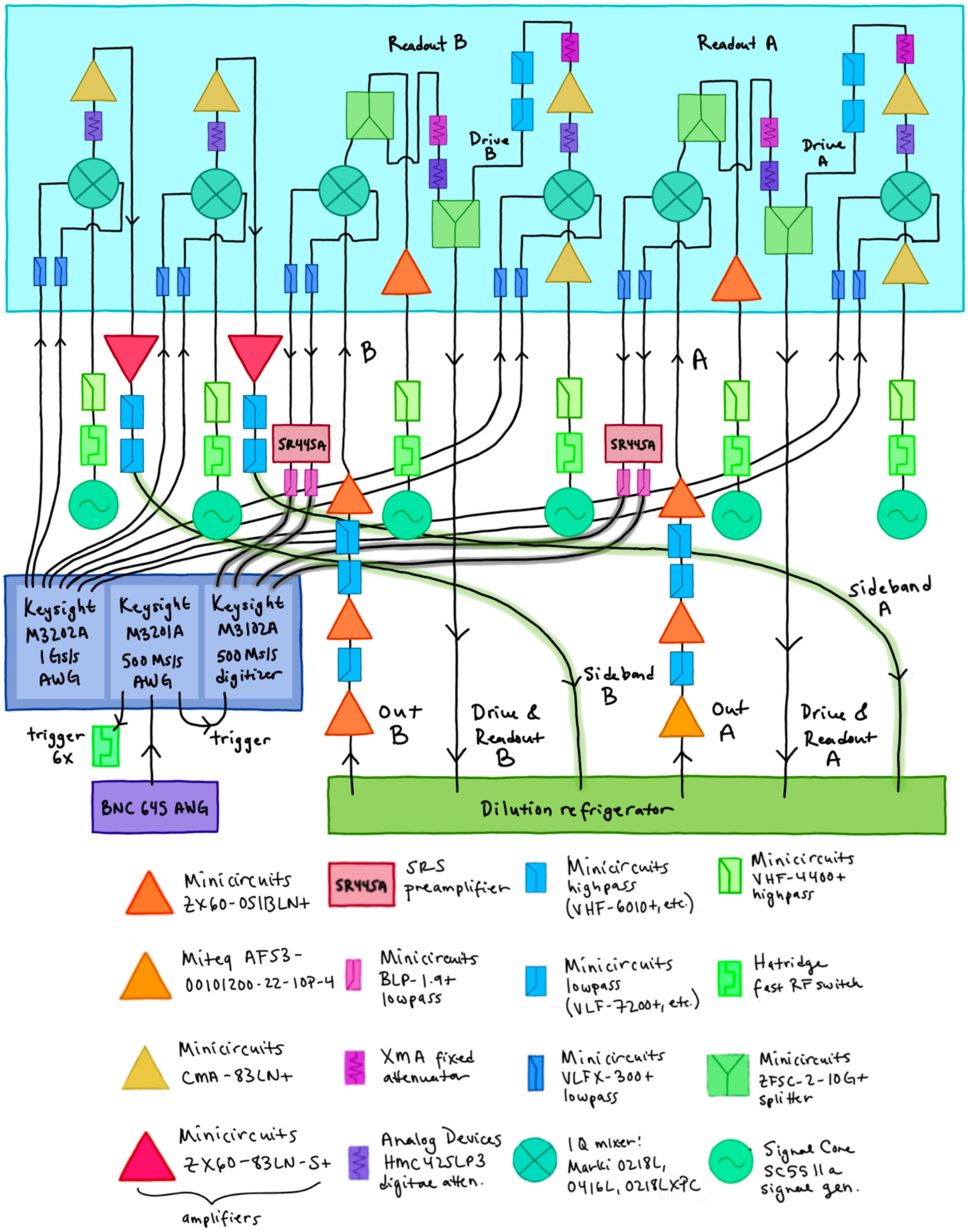

Figure 6.3: **Schematic of room-temperature measurement setup.** Amplification chains for signals exiting the dilution refrigerator are shown near bottom labeled as 'Out A' and 'Out B'. These signals are mixed down to DC by using a split-off portion of the readout tones, and fed to SRS preamplifiers before being digitized. Keysight M3...A cards are embedded in a Keysight PXIe chassis and triggered from a BNC 645 arbitrary waveform generator. The 500 Ms/s Keysight AWG triggers fast RF switches at the output of of the six LOs, which are followed by lowpass filters to eliminate transients from the switching.

of $\sim 18 - 20$ MHz. The hopping rate is the important figure to which one should compare disorder in onsite energies, as this determines when the resonator-resonator coupling is dominant over any smaller detuning ‘barrier’ that might frustrate transport and localize a photon. Although the utilty of room-temperature data is limited due to the possibly variable shifts of lattice cavity resonances upon cooldown, in Figure 6.4 we plot measured departures of each single-post cavity at room temperature from resonance with the chiral three-post sites.

After lattice retuning, the spectrum of the full tuned-up Harper-Hofstadter lattice was quite stable relative to the overall spectrum width ($\sim 120$ MHz) and the scale of the hopping rate; in Figure 6.5 we plot the ‘new’ spectrum over the old. The character and stability of the spectrum, along with wavepacket dynamics in the edge, are the best test of whether the lattice still has the topological properties we expect after a wait time and retuning. Lattice modes, measured at high power with the qubit saturated out, have shifted anywhere between 1 and 5 MHz below their historic frequencies from experiments earlier in this thesis.

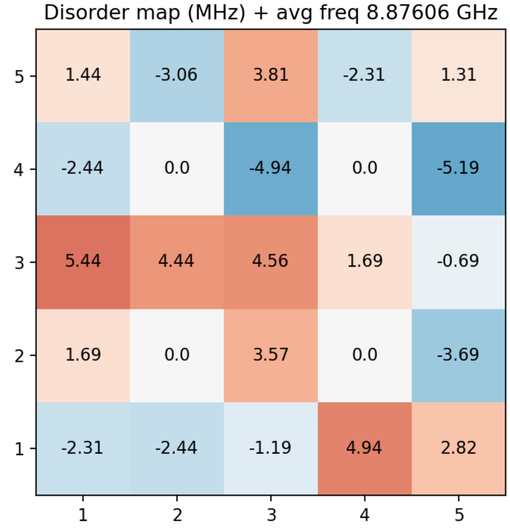

Disorder map (MHz) + avg freq 8.87606 GHz

| | 1 | 2 | 3 | 4 | 5 |
|---|---|---|---|---|---|
| 5 | 1.44 | -3.06 | 3.81 | -2.31 | 1.31 |
| 4 | -2.44 | 0.0 | -4.94 | 0.0 | -5.19 |
| 3 | 5.44 | 4.44 | 4.56 | 1.69 | -0.69 |
| 2 | 1.69 | 0.0 | 3.57 | 0.0 | -3.69 |
| 1 | -2.31 | -2.44 | -1.19 | 4.94 | 2.82 |

Figure 6.4: **Map of disorder in lattice site resonances at room temperature.** Chiral sites are presumed to be resonant and left without retuning due to the challenges of working with and measuring these sites.

Over the interim of several years, which included substantial exposure to air while the lattice was hanging in a dilution refrigerator open to atmosphere, the lifetimes of excitations in lattice modes remained around 3 $\mu$s. This is despite the understanding that niobium, unlike the tantalum which is now more commonly used for the pads of superconducting

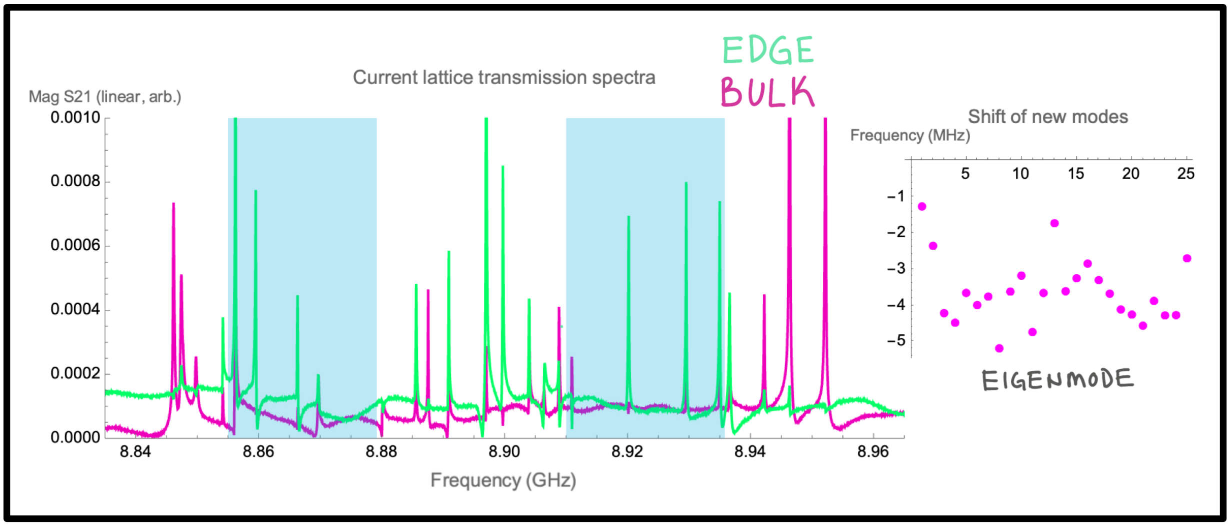

Figure 6.5: **Edge and bulk lattice spectra and shifts from historical values.** At **left**, we overplot current linear transmission (S21) spectra taken between pairs of edge and bulk lattice sites: strong green modes appear in the blue-highlighted edge regions and the pink bulk spectrum largely lacks associated bulk excitations at the same frequencies, confirming that these modes are predominantly edge-like. At **right**, we plot the shift of new modes relative to their old frequencies during measurements taken in the previous chapters.

transmon qubits, can grow a penetrating oxide that becomes thicker and thicker with sustained exposure to oxygen. The stability of lattice excitation lifetimes, profiled by ringdown measurement (see Figure 6.7), suggests that the permanent magnetic field used to bias the YIG spheres is ultimately the limiting factor in lattice photon lifetime. In his thesis [137], Clai Owens suggested options to improve lattice engineering in order to further localize the regime of flux penetration necessary to bias the YIG spheres, which could raise lattice photon lifetimes to be more on par with the at-minimum super-10-$\mu$s lifetimes expected of excited states of even very regular superconducting transmon qubits at this point in time.

To characterize the lifetimes of lattice modes and to probe lattice dynamics in order to ensure that the 'chiral' lattice was still chiral (i.e. hosted non-reciprocal transport of wavepackets confined, at least somewhat, to the lattice edge – see similar transport measurements in Figure 3.8), we built a room-temperature setup which could perform pulsed heterodyne measurements on excitations inhabiting the lattice. Standard pulsed measurements that we perform on qubits' readout resonators are homodyne measurements – we supply a square-pulse readout tone gated by upmixing with shaped output of a fast arbitrary waveform generator, and downmix the signal exiting the refrigerator with a signal split off from the same local oscillator which generates the readout pulse, resulting in an analog DC signal for the readout amplitude that gets amplified, filtered, and fed to a digitizer. This setup is illustrated in Figure 6.6.

In this situation where we sought to profile fast dynamics of lattice photons, rather than taking continuous-wave transmission spectra, we needed to use IQ mixers and fast arbitrary waveform generators (AWGs) to shape the relevant fast pulses. This meant that the resulting shaped pulses had been mixed up by the IF frequencies from the pulse-shaping AWG tones, causing the frequencies of emitted pulses to be 1 IF (selected to be 100-200 MHz depending on the frequency targeted with the same carrier signal) higher than the local oscillator frequencies. This meant that downmixing with the local oscillator returned the output signals to 100-200 MHz, rather than to DC, requiring heterodyne measurement of these outputs. Our fast (1GS/s) digitizers accommodated incoming signals at these frequencies, and we could elect to either digitally downmix *post hoc* (see David Schuster's thesis [174]), or simply analyze on top of the signal carrier frequencies.

In Figure 6.7, we plot a scan of 'ringdown' measurements taken across the lattice spectrum: in each case, we supply a long square pulse to inject a stable state of many photons into one lattice site, and then perform reflection measurements on a second lattice site spatially removed from the first in order to assess the second site's degree of excitation in time. Zooming in to several single-frequency slices of the ringdown scan in Figure 6.7, we fit approximate lifetimes $T_1$ for several relevant lattice eigenmodes. Performing fast pulsed linear measurements of the lattice in this way provides flexible and broad access to probing lattice dynamics in the many-photon limit!

We use this same setup to characterize the dynamics of wavepackets prepared in the lattice

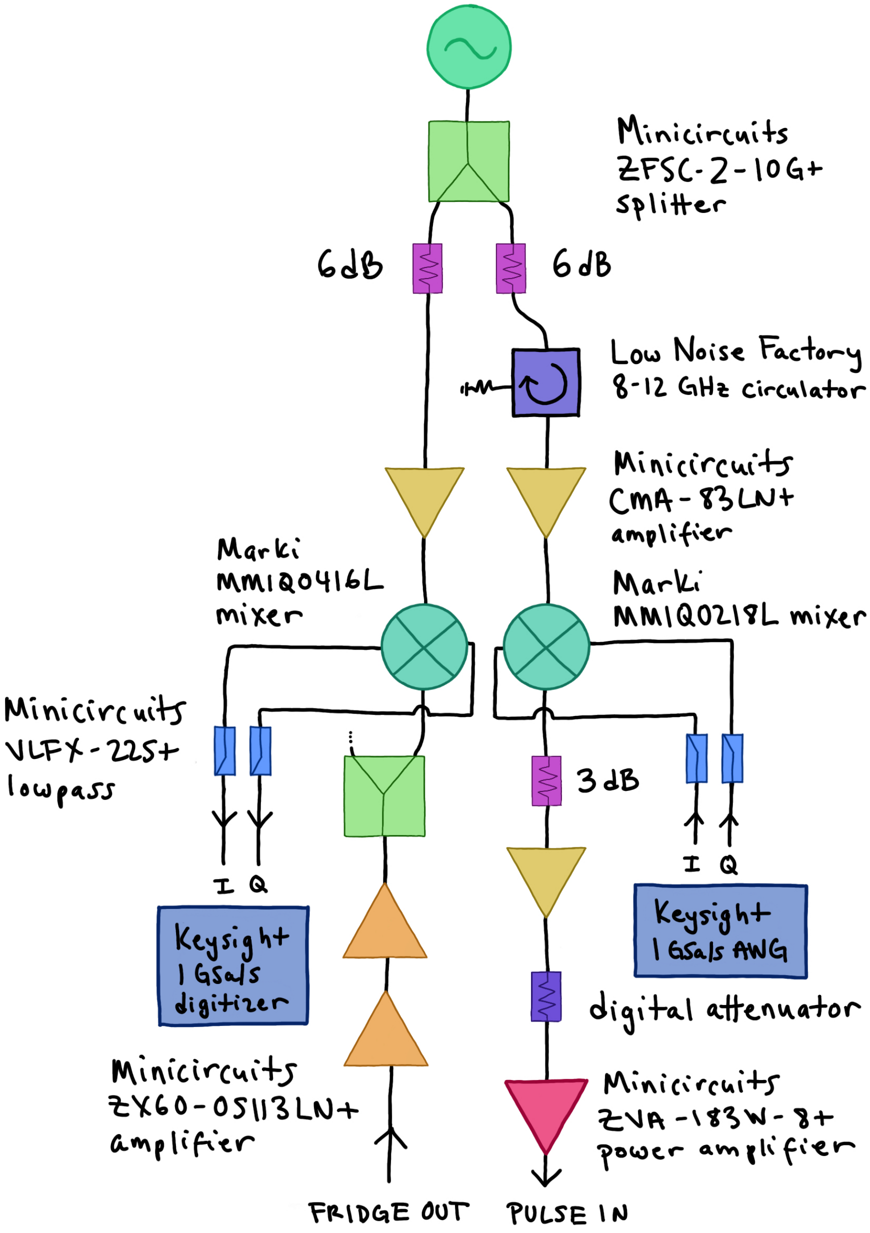

Figure 6.6: **Room-temperature setup for heterodyne measurements of lattice dynamics.** A single continuous signal generator (at top) is split; one portion is shaped via IQ mixing with shaped IF tones supplied from a Keysight 1 Gs/s arbitrary waveform generator to produce a square or Gaussian fast pulse needed for measurements. The second portion of the split-off tone is used to downmix signals exiting the refrigerator, bringing them to the IF carrier frequency used for pulse mixing, which is then lowpass filtered and digitized.

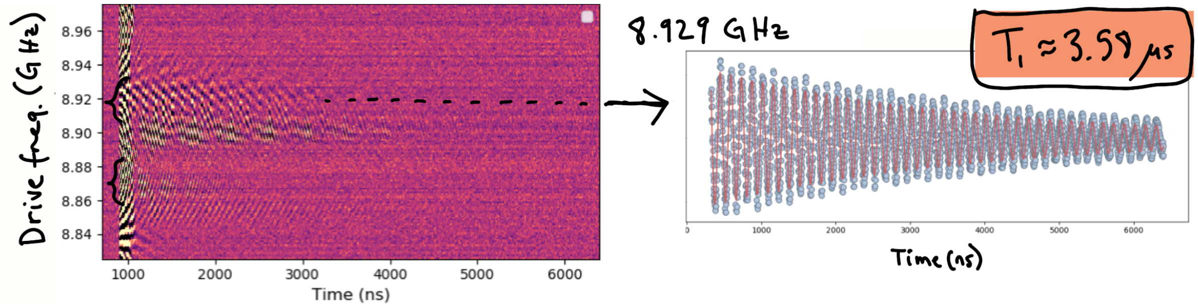

Figure 6.7: **Ringdown measurement scans.** At **left**, sweeping the IQ mixing frequencies output by the pulse-shaping AWG, we apply a 25 ns $\sigma$ Gaussian pulse to the lattice corner at a range of frequencies and make heterodyne measurements of reflected power on another lattice edge site. Color scale is arbitrary and linear. Scanning the pulse frequency across the lattice band reveals oscillations as a wavepacket circles in the two edge channels, bracketed in black. The central oscillation is from excitation movement in a set of edge-like modes near the Dirac mode at the lattice center. Moire interference patterns arise from the different IF frequencies serving as carriers to digitized signals at each scan point; we hold the local oscillator frequency constant and sweep pulse frequencies by relying on the AWG. At **right**, we examine a scan slice on-resonance with the upper edge channel and fit a $T_1$ for excitation decay of $\sim 3.6\mu$s. Decay is faster in the lower edge channel due to idiosyncrasies of lower-gap edge-mode quality factors unique to this particular cooldown.

edge: by supplying a fast Gaussian pulse (like that used for measurements in Figure 4.11) of length $4\sigma = 100$ ns, we synthesize wavepackets in the lattice edge channels by exciting sets of modes. Due to challenges with the particular refrigerator cooldown when these data were taken (rolling low-Q background modes spoiled the quality factors of some lattice eigenmodes), lower-channel wavepackets consist predominantly of excitations in two modes.

Figure 6.8 plots time traces of excitations in three of the lattice corner sites after a Gaussian pulse is applied to one corner, launching a circulating wavepacket. The Fourier transforms of onsite reflection show weak Gaussian envelopes centered around the 120/170 MHz heterodyne frequency that represents the central frequency of the applied pulse in the lower/upper band gap, with sharp spikes in excitation evidencing stronger transmission through the lattice eigenmodes on top of the low-grade envelope. We see that the round-trip time for a wavepacket in the lower-frequency, slower-group-velocity edge channel is $\sim 270$ ns.

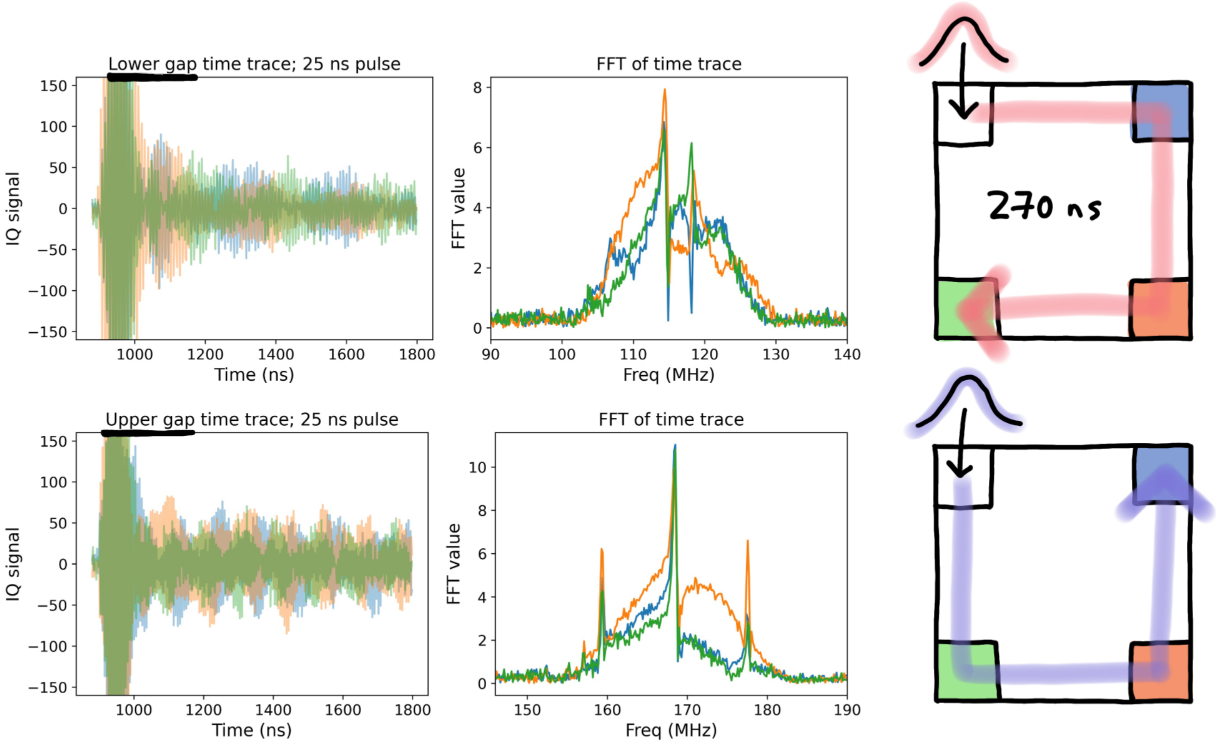

Figure 6.8: **Wavepacket dynamics in the lattice edge.** At **left**, time traces of heterodyne measurements (without the carrier digitally rotated off) of transmission of a Gaussian pulse to three lattice corner sites are plotted in green, orange, and blue. After a large initial spike in transmission due to the applied pulse itself, the wavepacket left propagating in each lattice edge channel sequentially excites the lattice corner sites in order. We can use these data to approximate the round-trip time of a wavepacket in each lattice edge. Note that excitations in the lower and upper gap propagate in opposite directions based on the ordering of green, blue, and orange peaks. At **center**, we plot the Fourier transform of this data centered on the carrier frequencies remaining after each signal is downmixed with its source local oscillator. A Gaussian envelope in frequency traces the energetic extent of the initial Gaussian transmission spike, and tall narrow lines evidence more effective transmission through the lattice modes. Note that these data were taken on a cooldown when the lifetimes of some lower-gap modes were spoiled, so one can easily perceive the participation of only two modes in the lower-gap Fourier transform plot. At **right**, schematic diagrams of the lattice corners illustrate how the data in the leftmost plots provide evidence of opposite-direction chiral wavepacket propagation in the two chiral edge channels of this toplogical lattice.

## 6.3 Measurements with two qubits

### *6.3.1 Transmon characterization*

Two transmon qubits are coupled to the lattice edge sites separated by one quarter-edge (depicted in Figure 6.1), using separate niobium resonators for qubit control and readout. Both fixed-frequency, with niobium capacitive pads and Al / $Al_2O_3$ / Al Josephson junctions, these qubits were fabricated by me in the University of Chicago Pritzker Nanofabrication Facility using modifications on a standard lab recipe for Manhattan-style junctions (see Appendix D.3).

These qubits' transition frequencies, ultimately $\omega_q/2\pi \approx 7.8$ GHz, sit far detuned from resonance with the lattice spectrum (centered at $\approx 9$ GHz) and $\sim 100$ MHz detuned from each other. Parameters for the qubits, labeled 'Alice' and 'Bob', are shown in table 6.1 – these were measured in an early cooldown with lattice corners cut off from coupling to the rest of the lattice, and shifted in later cooldowns. Note that $\chi$ quoted here is half of the full-scale $2\chi$ dispersive shift between qubit and resonator.

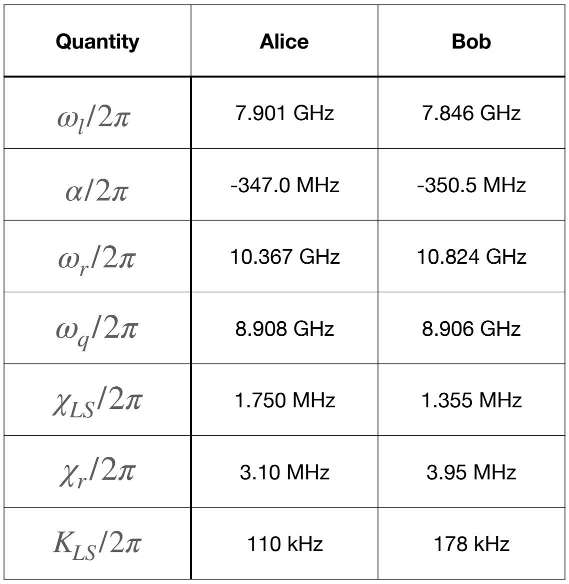

| Quantity | Alice | Bob |
|---|---|---|
| $\omega_l/2\pi$ | 7.901 GHz | 7.846 GHz |
| $\alpha/2\pi$ | -347.0 MHz | -350.5 MHz |
| $\omega_r/2\pi$ | 10.367 GHz | 10.824 GHz |
| $\omega_q/2\pi$ | 8.908 GHz | 8.906 GHz |
| $\chi_{LS}/2\pi$ | 1.750 MHz | 1.355 MHz |
| $\chi_r/2\pi$ | 3.10 MHz | 3.95 MHz |
| $K_{LS}/2\pi$ | 110 kHz | 178 kHz |

Table 6.1: **Parameters of qubits Alice and Bob, lattice sites, and readout resonators.** These measurements were taken with lattice corner sites decoupled from the rest of the lattice using detuning screws placed in the adjacent sites, so subscripts $LS$ refer to each lattice corner site alone.

The goal of this initial cooldown was to characterize the bare coupling rate between each qubit and its associated lattice corner site, reflected in values of $\chi_{LS}$. Once the lattice is tuned up and each qubit couples to a range of eigenmodes instead of to a single cavity mode, this full-scale coupling evades measurement. Its bare value is a figure of core importance as this sets the scale for expected bare couplings between qubits and individual lattice modes, and accordingly sets the theoretical upper limits of driven effective coupling rates $\tilde{g}$ between qubit and lattice spectrum. Much of my nanofabrication iteration was driven by securing parameters of these fixed-frequency qubits that generated a $\chi_{LS}$ large enough to support swap dynamics between qubit and lattice that were fast enough to beat the round-trip time of an excitation in the chiral lattice edge.

Qubit $T_1$ values were initially 9.5/10 $\mu$s in early cooldowns of this system; coupling to mysterious and idiosyncratic decay channels lowered their ultimate $T_1$ times to around 5 $\mu$s for the measurements taken to conclude this thesis. Alongside this change, the $|f\rangle$ state of qubit Bob in particular displayed a lower-than expected lifetime, necessitating changes to simulation parameters in order to best fit swap oscillations between $|f, 0\rangle$ and $|g, 1\rangle$ (see Section 6.6.4).

It is worth considering, at least for due diligence, what introduction of a nonlinearity via coupling-in of the transmon might due to the formerly linear cavity modes. We can calculate [52] the approximate self-Kerr shift (the resonator's energetic shift in response to itself being populated with photons) of a single cavity mode populated with $n$ photons coupled to that qubit:

$$\frac{-\alpha g^4}{\Delta^3} n^2 \tag{6.1}$$

Here $g$ is the qubit-cavity coupling, $\Delta = \omega_c - \omega_q$ is the qubit-cavity detuning, and $\alpha$ is the absolute value of the qubit anharmonicity. A back-of-the-envelope calculation puts this figure in the tens of kHz for low photon number, so we can effectively neglect it when considering measured shifts since our drive pulses span a broader frequency regime (see Appendix A) and will thus remain resonant with target cavity processes, even if we have same-direction shifts from two qubits at play.

We can also calculate [52] an approximate cross-Kerr interaction, the energy shift that modes mutually experience via coupling through a nonlinearity, between two cavities (e.g. the readout resonator and some lattice eigenmode, or a set of lattice eigenmodes) coupled to the same three-level transmon in the dispersive limit:

$$2g_1^2 g_2^2 \frac{-\alpha(\Delta_1+\Delta_2)}{\Delta_1^2\Delta_2^2(\Delta_1+\Delta_2-\alpha)} \tag{6.2}$$

A similar order-of-magnitude calculation suggests that this will remain negligible relative to other energy scales we care about like drive envelopes and linewidths.

To further explore our shift expectations, we experimentally probe the strength of the cross-Kerr interactions between a pair of transmons coupled to the lattice by $\pi$-pulsing one to its $|e\rangle$ state and then performing a Ramsey measurement of the frequency $\omega_q$ of the other qubit's first transition. As the undressed qubit resonances are over 1 GHz detuned from the lattice eigenmodes, we find any frequency shift small enough to be unmeasurable given system parameters.

### 6.3.2 Confusion matrix for readout optimization

To improve the readout fidelities of both qubits, we apply a confusion matrix to the results of any qubit measurement. In a measurement of a single qubit, the core action is deciding whether the qubit is in state $|\uparrow\rangle$ or state $|\downarrow\rangle$. We can choose the nature of $|\uparrow\rangle$ and $|\downarrow\rangle$ in the same way that it's possible to measure electron spin polarizations along different directions in the iconic Stern-Gerlach experiment. In single or two-qubit tomography, long sequences of pulses are run before many rounds of measurement to select a different measurement bases in order to locate the state of the qubit on the Bloch sphere as opposed to just along an axis of choice [41].

The confusion matrix is a $2\times 2$ matrix transformation applied to the vector $(a|\uparrow\rangle, b|\downarrow\rangle)$ representing the counts of a many-shot measurement in which the qubit state is assigned to states $|\uparrow\rangle$ and $|\downarrow\rangle$. To calibrate this matrix, we prepare the qubit in targeted states $|\uparrow\rangle$ and $|\downarrow\rangle$ and then, averaging over many experimental runs, calculate how much of the time we correctly assign the measured qubit state to its known prepared state, and how much of the time our measurement process gets ‘confused’ by assignment of a measured qubit state to the incorrect outcome bin. From knowledge about the preparation and measurement, we can calculate a matrix that characterizes the conversion rates between prepared states and measured states:

$$\begin{bmatrix} \text{counts } |\downarrow\rangle \\ \text{counts } |\uparrow\rangle \end{bmatrix} = \begin{array}{ccc} & \text{prep } |\downarrow\rangle & \text{prep } |\uparrow\rangle \\ \text{get } |\downarrow\rangle & A & B \\ \text{get } |\uparrow\rangle & C & D \end{array} \begin{bmatrix} \text{prep } |\downarrow\rangle \\ \text{prep } |\uparrow\rangle \end{bmatrix} \tag{6.3}$$

If the above ‘confusion’ matrix maps between known states and measurement results, applying its inverse to a set of results $(a|\uparrow\rangle, b|\downarrow\rangle)$ of a more complicated measurement, in which we do not simply prepare a known state and immediately read it out, ‘de-confuses’ the results of that more complicated measurement by removing the pre-characterized effects of errors and state overlaps accrued during the post-preparation readout process.

$$\begin{bmatrix} \text{‘real’ } |\downarrow\rangle \\ \text{‘real’ } |\uparrow\rangle \end{bmatrix} = \frac{1}{AD - BC} \begin{array}{ccc} & \text{get } |\downarrow\rangle & \text{get } |\uparrow\rangle \\ \text{prep } |\downarrow\rangle & D & -B \\ \text{prep } |\uparrow\rangle & -C & A \end{array} \begin{bmatrix} \text{a } |\uparrow\rangle \\ \text{b } |\downarrow\rangle \end{bmatrix} \tag{6.4}$$

The confusion matrix has no traction on errors or problems accumulated before readout, and it’s best to run its calibration alongside every actual measurement in order to effectively cope with experimental drifts. Application of the confusion matrix to our setup, which displayed limited readout fidelities due at least in part to antenna coupling issues, improved readout fidelities for qubits Alice and Bob from $\approx 9$ and 20 to $\approx 15$ and 40 percent respectively.

### *6.3.3 Sideband cooling*

The qubits in our setup were natively very ‘hot’: the thermal population of their excited states was substantial enough to pose problems. Temperature measurements performed using the classic method of comparing the amplitudes of $|e\rangle \leftrightarrow |f\rangle$ Rabi oscillations measured with and without exciting the transmon to its $|e\rangle$ state beforehand suggested that qubit Bob saw a temperature of over 230 mK before interventions were made.

Assuming a two-state system, we can calculate a Boltzmann factor, representing the proportion of times the qubit is measured its $|e\rangle$ state over an ensemble of runs, from just a ratio of the averaged populations in $|g\rangle$ and $|e\rangle$ [192]:

$$P(|e\rangle)/P(|g\rangle) = e^{-\frac{h(\omega_e - \omega_g)}{2\pi k_B T}} \tag{6.5}$$

For a multilevel system, it would be necessary to fit populations to a Boltzmann distribution [62], but we stick with simply two levels.

This thermal population proved to be a substantial impediment to making clean measurements of each qubit’s state; as an example, measurements trying to trace the Stark shift of the $|g\rangle \leftrightarrow |e\rangle$ transition under strong four-wave drive initially produced incomprehensible results as enough $|f\rangle$ state population was already present that this four-wave drive excited coherent interactions between lattice and thermal excitations in the qubit. Excess thermal population in the readout resonators, also, meant that while profiling the qubit transitions using two-tone continuous-wave spectroscopy [166], these transitions appeared not as single lines but as number-split distributions as the qubit transitions dispersively shifted in response to readout resonator photons.

To address the unhelpful qubit thermal populations, we used Raman sideband cooling to relocate excess thermal photonic population from the $|e\rangle$ state of the qubit (the first, and thus most, populated by thermal effects exciting the qubit above its ground state) to some of the many conveniently-available lattice eigenmodes. We already had access to a drive scheme for moving photons from qubit to lattice, deployed throughout this thesis to intentionally generate single excitations in the lattice by removing excitations from a qubit's $|f\rangle$ state. Anticipating that the average thermal photon number $\bar{n}$ in the qubit did not surpass 1, we applied an $|e\rangle \leftrightarrow |f\rangle$ $\pi$ pulse to each qubit before applying a strong four-wave drive calibrated to resonantly swap an excitation into a lattice eigenmode of choice.

Pechal et al. [145], who originated this all-microwave qubit-cavity coupling approach for fixed-frequency transmons, used the same sideband cooling protocol. Several other all-microwave-drive cooling protocols exist (see Figure 6.10): Geerlings et al. [61] introduce a driven reset protocol for transmons coupled to resonators that requires the cavity linewidth $\kappa > \Gamma_{up} = P(|e\rangle)/T_1$, where $P(|e\rangle)$ is the equilibrium excited state population of the qubit and $T_1$ is its excited state lifetime.

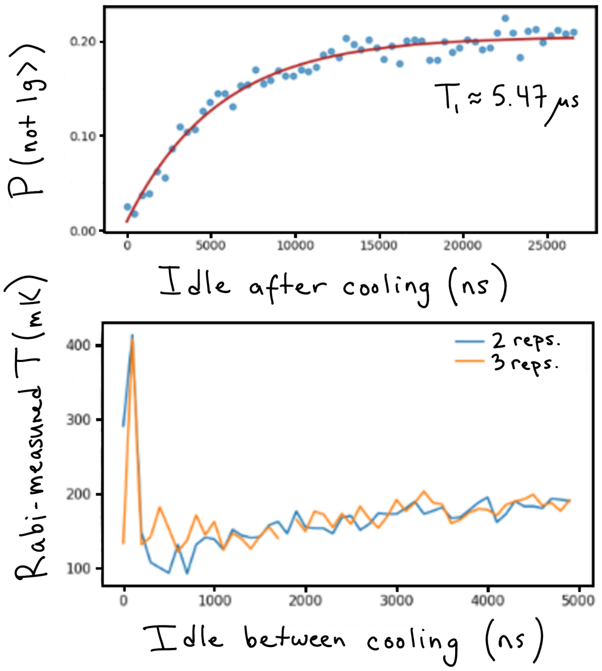

Figure 6.9: **Effect of sideband cooling.** At **top**, the probability of qubit Bob's presence in an excited state is tracked after the conclusion of sideband cooling. Excited-state population saturates at around 20 percent. At **bottom**, we test the ultimate qubit temperature after placing different idle times between different numbers of rounds of sideband cooling.

In this protocol, two drives are applied simultaneously, one at frequency $\omega_{ge}^0$ of the bare qubit transition and the other at $\omega_c^g$ chosen to place photons in the cavity if the qubit is in its ground state. This latter drive displaces the cavity to $|\alpha\rangle$ and the combined state to $|g, \alpha\rangle$, prohibiting resonant excitation of the qubit out of its ground state at $\omega_{ge}^0$. Here the qubit only excites spontaneously at rate $\Gamma_{up}$, whereas the system decays from $|e, \alpha\rangle$

(where it would start if $|e\rangle$ was thermally populated and the displacment drive applied) to $|e, 0\rangle$ at the more rapid rate $1/\kappa$. The aforementioned Rabi drive at $\omega_{ge}^{0}$ then pushes the system $|e, 0\rangle$ to $|g, 0\rangle$. In this way, the system is driven to $|g, \alpha\rangle$ at rate $\kappa$; waiting around ten lifetimes $1/\kappa$ for cavity population to decay repeatedly should send the system to a steady state, the preparation fidelity of which is characterized by $\kappa/\Gamma_{up}$.

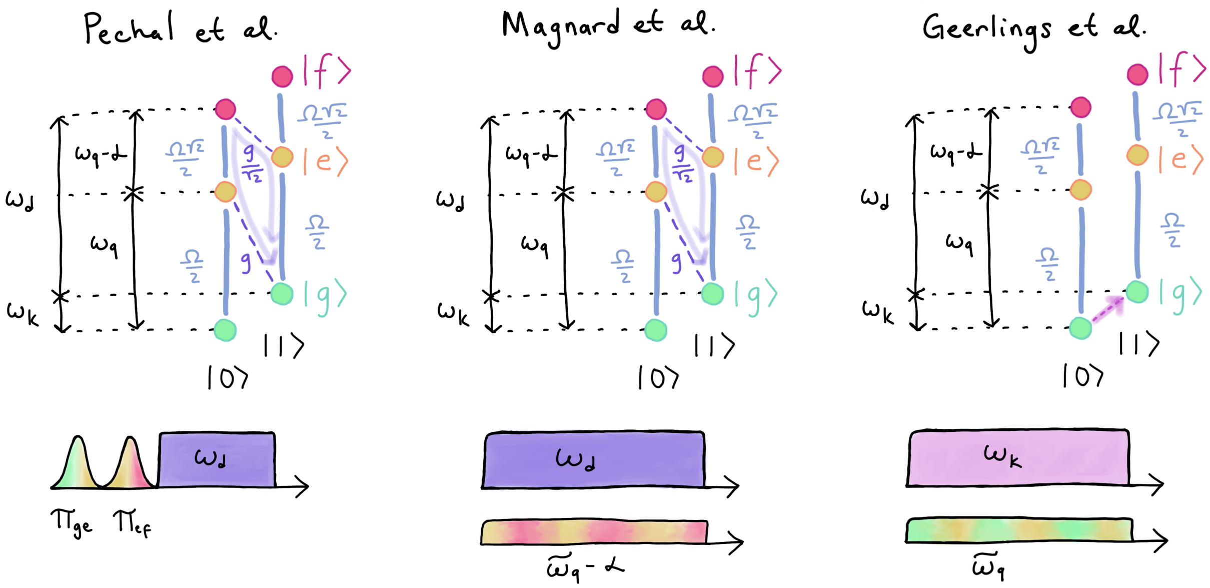

Figure 6.10: **Options for all-microwave-drive sideband cooling of fixed-frequency transmons.** Level diagram calls out states $|f, 0\rangle$ etc. and is represented in the lab frame; its style is adapted from Pechal et al. [145]. Horizontal state labels are Fock states in cavity mode $k$, vertical state labels pertain to the qubit.

Magnard et al. [112] also make use of the $|f, 0\rangle \leftrightarrow |g, 1\rangle$ microwave-driven transition to cool their qubits: their cooling rate is flexible regarding the value of the resonator's $\kappa$, as it's possible to compensate with strong multiphoton drives, an interesting advantage of this approach. These authors supply two simultaneous drives, $|f, 0\rangle \leftrightarrow |g, 1\rangle$ and $|e, 0\rangle \leftrightarrow |f, 0\rangle$, creating a $\lambda$ system that pours photons from $|e\rangle$ out to the environment. To achieve this they need to account for the Stark shift on the $|e, 0\rangle \leftrightarrow |f, 0\rangle$ transition due to application of the other (much stronger, as it accesses a higher-order process) drive, as well as the Stark shift on the $|f, 0\rangle \leftrightarrow |g, 1\rangle$ transition itself, and supply a tone that resonantly excites this transition at a frequency that would 'normally' be far off-resonance if the $|f,0\rangle \leftrightarrow |g,1\rangle$ Rabi drive were off. For us, calibrating the frequency of the $|e,0\rangle \leftrightarrow |f,0\rangle$ transition under drive strong enough to stimulate fast-enough Rabi oscillations between $|f,0\rangle$ and $|g,1\rangle$ proved challenging, so we stuck to preparing $|f,0\rangle$ with a $\pi_{ef}$ pulse on the qubit and then applying $|f,0\rangle \leftrightarrow |g,1\rangle$ drive sequentially.

As depicted in the bottom of Figure 6.9, we find that applying the cooling protocol two to three times is sufficient to cool each qubit to around 120 mK, near the limit available to us in making qubit temperature measurements due to measurement noise. A time trace of qubit population measured in the top plot reveals that we diminish the excited-state population of the qubit to less than 5 percent after cooling, and we trace out the approximate qubit $T_1$ by following its return to saturation at a thermal excited-state population of around 20 percent.

## 6.4 Single- and multi-mode coupling between emitters and the lattice edge

We launch a directional excitation into a chiral lattice edge channel by applying a multiphoton drive. As illustrated in the bottom of Figure 6.1, an applied classical drive, of strength $\xi_d$, 'tunes' a dressed excited state of a qubit on resonance with an eigenmode $\omega_{\text{mode}}$ within the lattice spectrum, exchanging two photons in a transmon with one photon in the lattice.

The coherent dynamics of swapping excitations between each qubit and lattice eigenmodes is displayed in Figure 6.11 for qubits $A$ and $B$, where we apply a multiphoton drive to sweep each qubit's dressed excited state across the lattice eigenspectrum. The effective coupling $\tilde{g}$ between qubit and lattice depends on the strength of the applied microwave drive. Figure 6.11 illustrates how the measured coherent swap rate of excitations in both qubits to a particular lattice mode increases with drive power. The qubit $A$ data includes more noise and artifacts from the digitizer, as $A$'s lower readout fidelity forced us to average more.

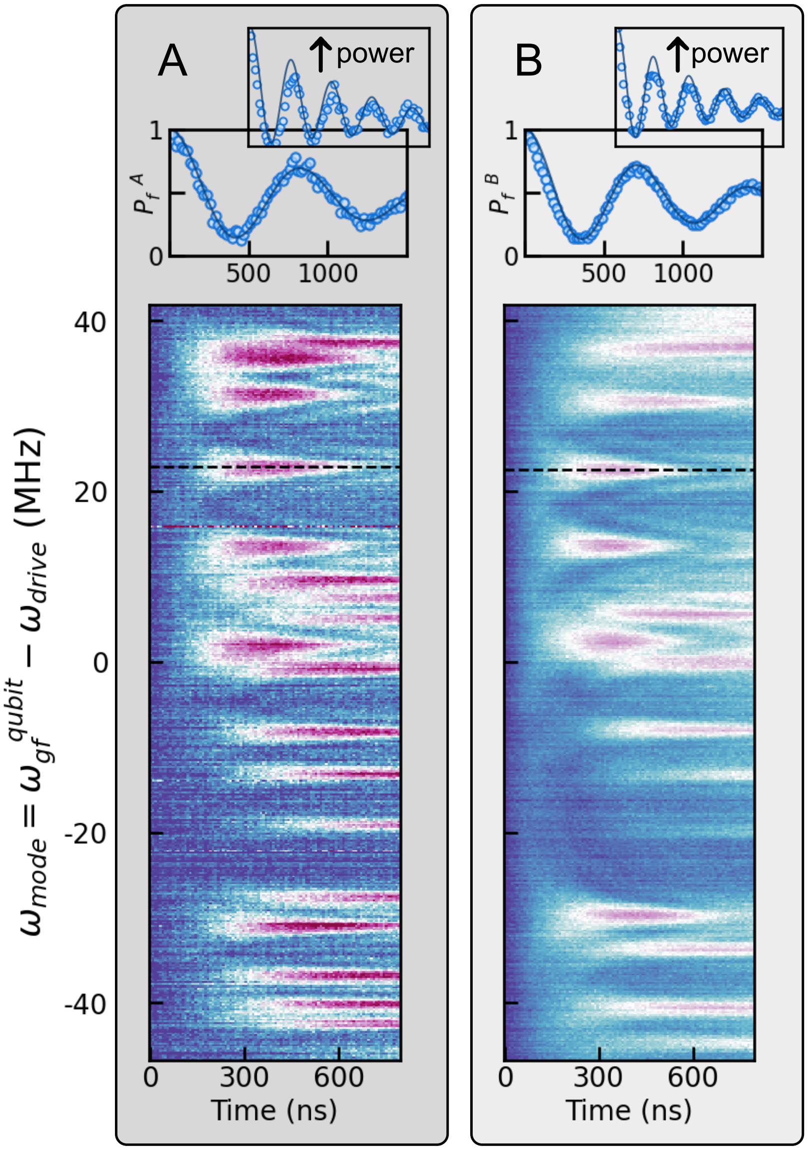

Figure 6.11: **Multiple emitters strongly coupled to the chiral lattice.** Slow Rabi oscillations demonstrating strong coupling between qubits A, B and lattice eigenmodes. In both columns, large insets at top are single-frequency slices of the respective bottom plots at the frequencies indicated by the dashed lines. Smaller insets at top show oscillations with a higher supplied drive power and thus higher effective Rabi rate between each qubit and the same lattice mode. Note that the frequencies $\omega_{mode}$ of individually identified lattice modes have shifted asymmetrically upward relative to those seen in an unperturbed lattice spectrum at low power; this is a result of Stark shifts on qubit transitions from the drive and Lamb shifts on the qubit as it is drawn near resonance with a forest of synthetic vacuum modes.

Because the qubits in this platform couple to the discrete eigenmodes of a 25-site cavity array, these experiments probe a regime intermediate between cavity quantum electrodynamics – which describes a qubit coupled to a single vacuum mode – and waveguide quantum electrodynamics, which sees an emitter coupled to a transmission line or photonic material with a more continuous density of states. To generate an edge-localized wavepacket propagating in an edge channel of this topological lattice, it is necessary to excite a superposition of edge eigenmodes, rather than emitting to some frequency continuum.

An analog of this form of coupling can be found in work exploring the super-strong coupling regime [118] of circuit and waveguide QED, in which coupling rates are so extreme, or the mode spacing so narrow, that a quantum emitter interfaces simultaneously with multiple discrete modes of an engineered photonic landscape [187, 23, 156, 93, 197, 8, 97]. In our case, the strong coupling is moderated by the applied microwave drive that ramps up the effective $\tilde{g}_k$ to specific modes $k$ rather than intrinsic to the bare interaction between qubit and lattice.

As we increase drive strengths past those which generate the $\tilde{g}$ in Figure 6.11, the ranges of drive frequency over which the qubits couple resonantly to individual lattice modes broaden and begin to overlap, so that supplying a drive at one frequency effects resonant coupling between qubit and multiple lattice modes simultaneously. This strong drive Stark shifts the qubit levels and a frequency-dependent Lamb shift on the dressed qubit excited state comes into play (see Section 6.6.1) as it is brought near resonance with elements of the synthetic multimode lattice vacuum [181, 139]. As our drive-based injection method results in Stark shifts on the scale of half the lattice bandwidth, we neglect the pulse shaping used in other work with this injection method to generate maximum swap efficiency (see Section 6.6.5).

The shifts imposed by increasing drive strength result in the resonances between qubit and the lattice edge modes which form the lower-frequency edge channel drawing closer together. This effect is illustrated in Figure 6.12b; Figure 6.12a shows the detection of a photon released from one qubit into one, two, and three of these lattice edge modes reached using three different drive powers. The coupling pulse frequencies and times at different drive powers are indicated by white dashed lines and circles in Figure 6.12b. Qualitatively different time-dependent retrieval of an excitation traces out the behavior of a photon in the lattice edge as it is sent through one static mode, a half-edge-localized two-mode pair, or a three-mode edge wavepacket.

When a photon is passed through one mode, we expect no noticeable time dynamics; the only fluctuations visible in $P_{\text{received}}$ appear as a small increase at low time due to the finite timescale of Rabi dynamics, and a decay stemming from the lifetime of an excitation in that lattice mode.

When a photon is driven into a superposition of modes, the envelope of the detected packet is well-modeled by a time-decaying sum of complex oscillations at the known eigenmode frequencies $\omega_1, \omega_2, \omega_3$ with relative phases that encode the phase winding of the edge channel between coupling sites:

$$A_{tot}|a_1 e^{i\omega_1 t} e^{i\frac{\pi}{2}} + a_2 e^{i\omega_2 t} e^{i\pi} + a_3 e^{i\omega_3 t} e^{i\frac{3\pi}{2}}|^2 e^{-t/\tau} + c$$

To model transport the ‘other way’ around in the same channel, we use a phase $\frac{3\pi}{2}$ to account for the wavepacket’s transit of three quarters of the lattice edge. Our protocols inject roughly half of a photon into the lattice in this case, and a 10-15% deviation from the prescribed relative phases can produce an excellent fit to the data.

In the middle row of Figure 6.12a, when a photon is passed through two edge modes, we observe a sinusoidal time-dynamics that comes from summing two modes in the equation above. A $5 \times 5$ snapshot of a simulated excitation in Figure 6.12a illustrates how a combination of two edge-like eigenmodes will be localized to half the lattice edge, resulting in sinusoidal time-dynamics for a chirally propagating packet.

At bottom in Figure 6.12a, a more complicated dynamics of asymmetrically-spaced peaks

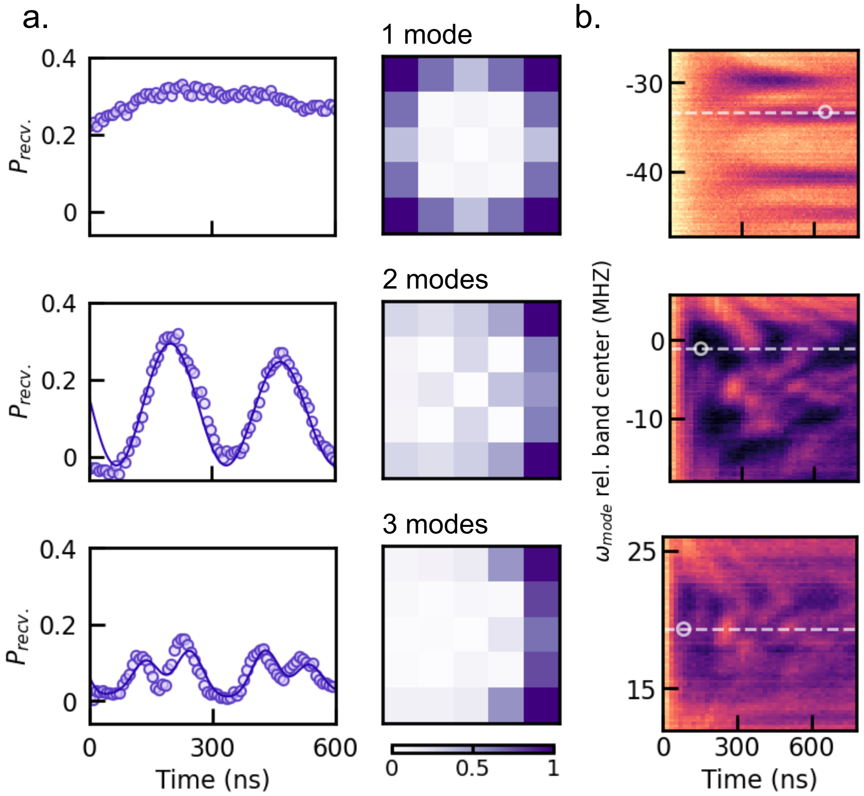

Figure 6.12: **Synthesizing wavepackets in an edge channel. a,** We send and receive single photons through 1, 2, and 3 lattice modes using the strong coupling of both quantum emitters to the chiral lattice. Trace plots in **a** show the population retrieved by qubit B resulting from this process. To couple to $> 1$ modes, we increase drive strength to both Stark shift sites of resonant coupling to lattice modes closer together in drive frequency and enable a higher effective Rabi rate $\tilde{g}$. We capitalize upon the increased Rabi rate to shorten drive pulses, broadening the frequency range over which we couple to connect with more eigenmodes. Swapping to more than 1 lattice eigenmode produces a wavepacket with some localization that propagates in time around the lattice edge. Square plots in **a** illustrate point-in-time snapshots of these excitation profiles, the time evolution of which inflects the time-resolved population in the receiving qubit. In **b,** we scan the frequency and length of drive pulses drawing the receiving qubit into resonance with the lattice spectrum. Dashed white lines and circles indicate pulse parameters used to produce data in **a**. Moving downward, as we increase drive strength, we see formerly distinct single-mode resonant processes cross, blur together, and eventually shift closer together in frequency (bottom plot) as the time for maximum swap of an excitation between qubit and lattice decreases with the increase in $\tilde{g}$.

emerges when a photon is driven into a weighted superposition of three edge modes, as expected from simulations of even a disorder-free Harper-Hofstadter model (see Section 6.5.2). Even neglecting reflections from lattice corners and the participation of edge modes in the bulk of this finite-size lattice, the nonlinear dispersion of wavepackets produced in low-eigenmode-number Chern lattices like this one is expected [194, 122] to cause a photonic qubit to effectively time bin itself as the packet splits apart while migrating along an edge channel.

## 6.5 Non-reciprocal transport in a chiral channel

Having injected excitations into, and detected excitations propagating in, a superposition of edge modes of this topological lattice, we use this chiral channel to demonstrate non-reciprocal transport between an emitting and a receiving qubit.

We use parameters for sending and receiving a photon like those used in the bottom section of Figure 6.12a. A cartoon of the pulse scheme is shown in Figure 6.13a; the time coordinate for dynamics is the delay between the starts of 75 ns sending and receiving pulses. Calibration of swap efficiency indicates that these parameters move $\sim$ 50% of the population from qubit A into the edge and similarly transfer $\sim$ 90% of population from qubit B to the lattice.

Figure 6.13b illustrates the protocol for demonstrating non-reciprocal transport: in the edge channel chosen for use, a photon sent from qubit A to B will will have traversed three quarters of the lattice edge, while a photon sent from B to A will have traversed one quarter. For an excitation constrained to propagate in an edge-localized chiral channel, we anticipate that the first peak of the photon sent from A to B will take three times as long to appear as one sent from B to A. Figure 6.13c shows measurement of this $\approx$ 3 to 1 ratio in delay of photonic transmission. This evidence of the expected time delay indicates that the lattice topology surmounts less dominant issues like incomplete localization of edge wavepackets to edge sites, scattering of excitations at lattice corners, and disorder in lattice site frequencies and couplings to support on-demand directional transport of a photon between emitters.

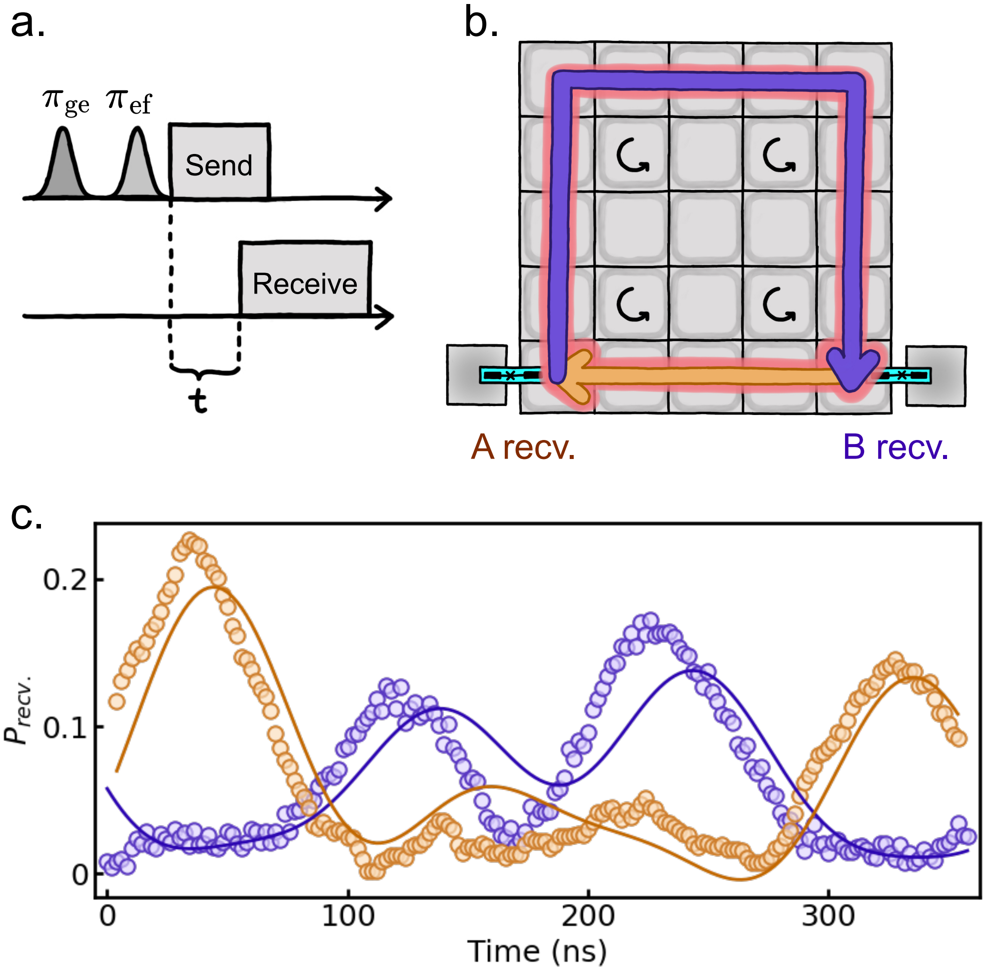

Figure 6.13: **Non-reciprocal transport in a chiral edge.** In **a** we depict the protocol for sending and receiving excitations through the chiral lattice: after preparing the sending qubit in its $|\mathrm{f}\rangle$ state, we supply a drive pulse to swap a photon into the lattice via the four-wave process detailed above. At some time delay $t$ thereafter, we begin a drive pulse to swap a photon out of the lattice and into the receiving qubit. The coordinate $t = 0$ occurs when both sending and receiving pulses begin simultaneously. **b** shows a schematic of transport through a chiral edge channel of the lattice with transport from B to A marked out in orange and transport from A to B in purple. In **c** we plot received population in each qubit following transport from A to B (purple) and B to A (orange). The initial orange peak appears approximately 3 times as early as the initial purple peak. The packet retrieved by B (purple trace) fragments in two peaks likely due to the combination of finite-size effects more apparent in a longer edge transport and the not-entirely-linear dispersion expected for this few-mode edge channel.

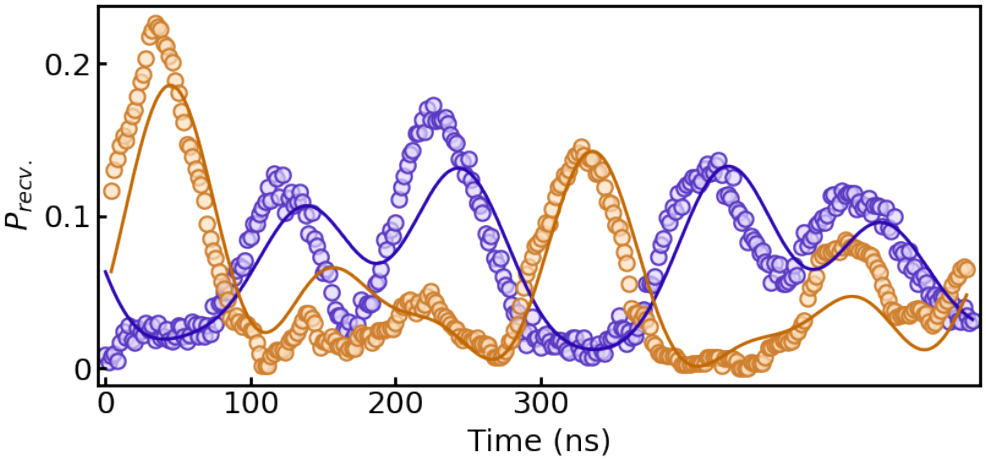

Figure 6.14: **Long-time non-reciprocal transport in a chiral edge.** We plot the data shown in Figure 6.13 out to longer time, showing further revivals in detected populations.

### *6.5.1 Protocol for Bell state preparation*

We sought to prepare a photon traveling in an edge wavepacket in a Bell state, an iconic form of maximally entangled quantum state, and characterize that state by calculating correlations in simultaneous measurements of both qubits. While we believe we executed this, our setup lacked long-term phase coherence between the pulses used to emit and detect said photon, and we lacked the time to alter the setup. We were thus unable to measure the off-diagonal elements of the two-qubit density matrix necessary to characterize the full quantum state. For those seeking to learn more about two-qubit tomography, Jerry Chow's thesis [41] provides a helpful introduction.

To attempt to prepare a Bell state, we prepared a qubit in its $|f\rangle$ state and then executed half a swap of that excitation between qubit and lattice. After waiting a delay time commensurate with the known delay for wavepacket transport, we performed a full swap out of the lattice to the second qubit.

$$\begin{aligned}|g,0,g\rangle \rightarrow \pi_{ge}, \pi_{ef} \rightarrow |f,0,g\rangle \rightarrow \text{ Half swap in } &\rightarrow \frac{|g,1,g\rangle + |f,0,g\rangle}{\sqrt{2}} \\ \rightarrow \text{ Evolution and propagation } \rightarrow \text{ Full swap out } &\rightarrow \frac{|g,0,f\rangle + |f,0,g\rangle}{\sqrt{2}}\end{aligned} \tag{6.6}$$

If we neglect the empty cavity and just consider the state of the qubits after this protocol, we find them in a Bell state:

$$\frac{|0,1\rangle + |1,0\rangle}{\sqrt{2}}. \tag{6.7}$$

We were able to perform the pulse sequences of two-qubit tomography, but lacked the phase coherence between the two swap pulses necessary to retain phase information [26], so were unable to effectively measure the ultimate quantum state.

### *6.5.2 Simulating edge channel emission and dynamics*

We use the Python package QuTiP to simulate the populations of qubits coupled to a disorder-free version of the Harper-Hofstadter lattice. We implement a $5 \times 5$ lattice model that incorporates both coupling through resonant modes on chiral sites and virtual coupling through the detuned backwards-chiral modes in thse sites, but keeps 'perfect' eigenfrequencies rather than incorporating those measured in the actual lattice spectrum which reflect lattice disorder. Generating a pair of two-level systems coupled to the lattice corners, we prepare an excitation in one and then turn on an effective coupling $\tilde{g}$ between that qubit and its lattice corner site. We shape $\tilde{g}$ with an idealized Gaussian time envelope.

Even with a smooth Gaussian ramp of $\tilde{g}$ between qubit and lattice corner, and even in this completely disorder-free limit, in which eigenenergies are different than those observed due to the lack of impact of said disorder, we still rapidly descend into wild-looking dynamics and some degree of wavepacket fragmentation due simply to the system's finite size.

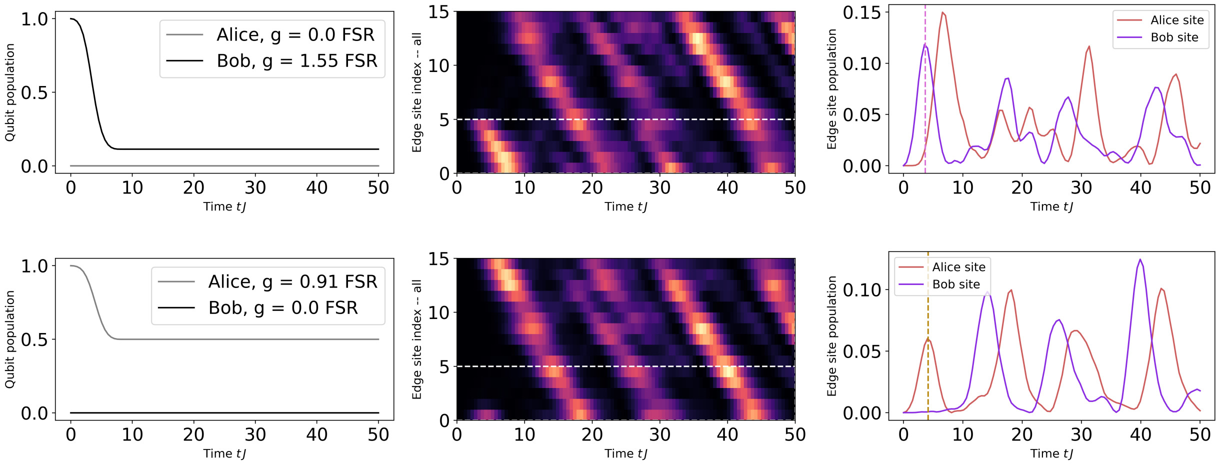

Figure 6.16: **Disorder-free simulations of dynamics in the lower-frequency edge channel.** Time axes in all plots are multiples of the hopping rate, here termed $J$ to distinguish it from time. FSR refers to the spacing between the two lattice edge modes we wish to most prominently excite. In the **top row**, we simulate emission of a photon from qubit Bob at the center of the lower-frequency lattice edge channel, setting effective g by matching it to the population we experimentally measure exiting the qubit. The **top middle panel** plots the path of the resulting lattice excitation around the lattice edge; a white dashed line highlights the index (5) of the edge site to which Bob is coupled, while Alice is coupled to site (1). The **top right panel** plots populations of edge sites to which the qubits are coupled. The vertical dashed line locates the maximum of the initially emitted excitation. In the **bottom row**, we perform the same set of simulations for emission from qubit Alice, again setting g by matching it to the measured population lost from the qubit. In the **bottom right panel**, a vertical dashed line again locates the maximum of the excitaiton initially released in the Alice-coupled edge site.

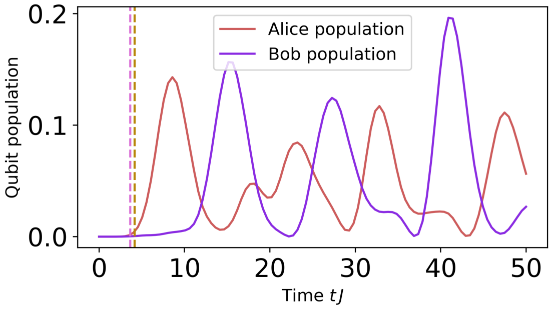

Figure 6.15: **Disorder-free simulation of qubit populations after detecting lattice wavepacket.** We simulate emitting a qubit from Alice and detecting it with Bob, and vice-versa. Dashed vertical lines flag the initial maxima of excitations on the sites immediately coupled to the emitting qubit. Calculating detection delays versus these lines, we detect with Bob an excitation propagating 'the long way' around the lattice edge 2.7 times later than we detect one propagating 'the short way' with Alice. This delay partly reflects coupling disparities in the simulation.

In this disorder-free simulation, which does not reflect the actual eigenenergies of lattice modes as measured, we find that the lower-edge-channel excitation takes $\approx$ 3.2 times as long to propagate 'the long way' around between lattice corner sites, compared to 'the short way' of a quarter lattice edge. As this difference in speed incorporates a disparity in effective couplings of the qubits to their lattice corners, it is likely an overestimate. Measuring the same delay using ultimate *qubit population* after using a second qubit to detect a photon propagating in the lattice, we find (Figure 6.15) that the lower-edge-channel excitation takes $\approx$ 2.7 times as long to propagate 'the long way' around the lattice edge. This is likely an underestimate, as the delay is calculated relative to the time maxima of wavepackets initially emitted into the lattice, so the quantity is itself inflected by the higher effective $g$ between the lattice and Bob. If we remove the disparity between qubit-lattice couplings $g$, eliminating the above asymmetries, we still see a delay of first peaks, relative to $t = 0$, that does not match the expected 3-to-1 ratio; it is not yet clear why this occurs in our simulation.

## 6.6 Exploration: the multiphoton swap process

Having presented the core result of this final chapter, we further discuss issues and subtleties that arose while attempting to use an all-microwave drive-based process to transfer excitations between a fixed-frequency qubit and a multimode cavity landscape. The major limitations of the experiments we sought to accomplish in the sections above are governed by the details surrounding the four-wave swap drive that follow.

### *6.6.1 Stark shifts due to four-wave drive*

The strong multiphoton drive which stimulates coherent interactions between qubit and lattice is applied through an antenna well-coupled to each qubit's readout resonator; while this tone is far off-resonance from the readout resonator, the strength of this drive is still substantial and the many off-resonant photons incident in the vicinity of each qubit can effectively Stark shift its levels.

We can characterize the Stark shift on a set of qubit levels due to the multiphoton drive by applying a long drive tone to the readout resonator at a chosen frequency, then supplying a long, slow $\pi$ pulse to attempt to excite the qubit between levels with fine frequency resolution while this drive is still ongoing, and reading out the state of the qubit after both drives conclude. By sweeping the frequency of the slow $\pi$ pulse, we can locate the frequency at which the qubit is 'excitable', characterizing the qubit transition's Stark shift. In Figure 6.17, we replicate classic-style shift-versus-amplitude plots [174] for qubit Bob, where we expect a quadratic dependence in the shift of the qubit line with increased drive amplitude.

We follow qubit Bob's $|g\rangle \leftrightarrow |e\rangle$ transition, sketching a parabola of the form $x = Cy^2$ to show that the line's shift qualitatively follows the classic quadratic shape. The small second peak on the left side at top of Figure 6.17 is spaced apart from the first by the qubit-readout resonator dispersive shift and is thus likely due to photonic population in the resonator. We also follow Bob's $|e\rangle \leftrightarrow |f\rangle$ transition, by applying a $\pi_{ge}$ pulse before the rest of this protocol begins. The scan of the $|e\rangle \leftrightarrow |f\rangle$ transition departs from a quadratic form at high power, likely because at high drive this transition ($\sim$ 7.5 GHz) is roughly 100 MHz less detuned from the 6.265 GHz drive.

This transition also shows a forest of avoided crossings as we pass through sites of resonant coupling between the $|f\rangle$ state of the multiphoton-driven qubit and the lattice eigenmodes. The frequency (6.265 GHz) selected for the multiphoton drive parks the qubit between sites of resonant interaction with a pair of edge modes in the upper gap. Increasing the drive power pushes the qubit transition frequencies $\omega_{ge}$ and $\omega_{ef}$ lower, so that following $\omega_{mode} = 2\omega_q - \alpha - \omega_D$, we gain on-resonance access to lower- and lower-frequency regimes of the lattice spectrum. As we go to higher drive power, we see a tighter-spaced regime of smaller avoided crossings, reflective of passing the dressed qubit through resonance with less-well-coupled and more-tightly-spaced bulk modes in the center of the lattice spectrum.

We further track the $|g\rangle \leftrightarrow |e\rangle$ transition of qubit Alice with four-wave drive amplitude; this transition displays a dispersive-shifted side-peak indicating photonic population in the readout resonator, and departs from quadratic behavior at higher drive power. This departure isconsistent with the understanding that the increasing prominence of higher-order effects causes the drive-dependent Stark shift to behave differently than standard lowest-order Jaynes-Cummings Stark shifts when this strong multiphoton drive enters the picture [210]. Differences in frequencies relevant to Alice (in particular, the drive is $\sim 200$ MHz closer to the qubit transition) might account for Alice's greater susceptibility to higher-order effects at strong drive. Shown in the middle of Figure 6.17, we draw a dotted line at the approximate drive amplitude used for transport measurements; we calibrated this drive amplitude by selecting the maximum value at which the effective swap rate $\tilde{g}$ increased predictably with drive rate, and ended up selecting a drive regime that qualitatively matches the turn-off from lowest-order behavior.

By comparing the frequencies of lattice modes in low-power linear spectra to the 'frequencies' of those same modes in lattice scans taken via four-wave swap drive, we can trace out what amounts to the Stark shift on the qubit's $|g\rangle \leftrightarrow |f\rangle$ transition under this multiphoton drive. $\omega_D = 2\omega_q - \alpha - \omega_{mode}$ is the drive frequency necessary to excite resonant interactions between qubit and lattice mode; measuring what appear to be frequencies $\omega_{mode}$ in chevron

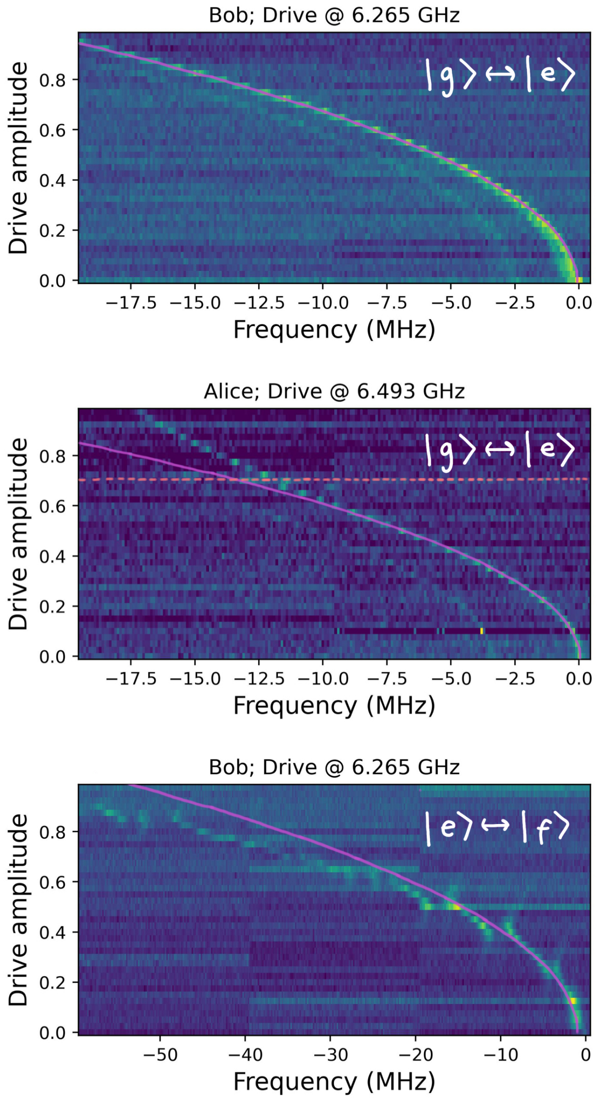

Figure 6.17: **Stark shifts on a pair of qubit transitions.** We profile the Stark shift on the qubits' transitions under four-wave swap drives of increasing amplitude. Color scales are linear, arbitrary, and profile the degree of qubit excitation. At **top**, Bob's $|g\rangle \leftrightarrow |e\rangle$ transition appears quadratic. At **middle**, Alice's $|g\rangle \leftrightarrow |e\rangle$ transition turns off a quadratic dependence on drive at higher amplitudes. At **bottom**, Bob's resonant $|e\rangle \leftrightarrow |f\rangle$ transition passes through an array of avoided crossings with lattice eigenmodes.

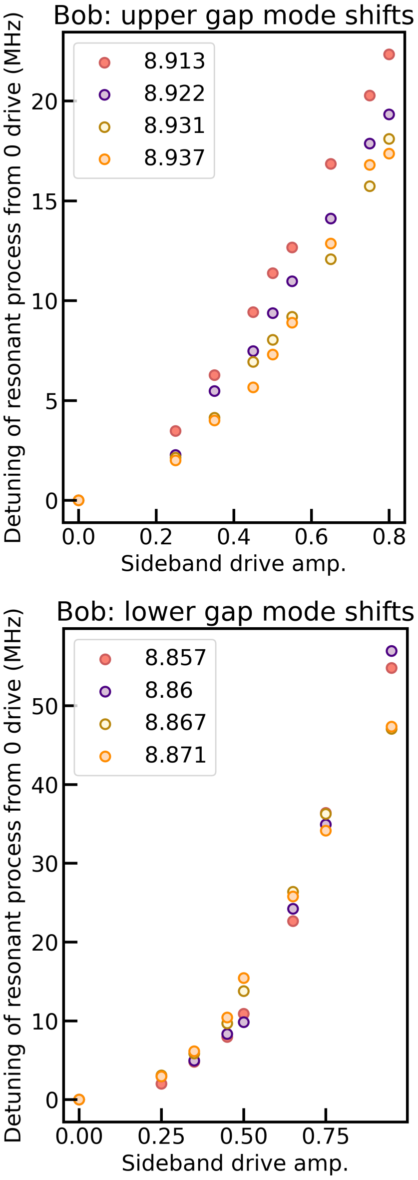

Figure 6.18: **Stark shifts on qubit Bob dressed to resonance with edge modes.** Shifts for modes in the lower gap appear more quadratic with amplitude than those in the upper gap, which are more challenging to trace in chevron spectra. We see that at high-power drives the lower-gap modes 'experience' Stark shifts of close to 60 MHz. Drive amplitudes are from an early setup and do not map onto their values in other measurements in this thesis.

spectra, we can ascribe the effective shift to the qubit instead. This shift, measured at a range of drive amplitudes, is plotted for lower- and upper-gap edge modes in Figure 6.18. The observed Stark shift of up to 60 MHz (for the lower gap) is an order of magnitude higher than the largest shifts addressed in at least one other implementation [76] of this drive process, and may be higher than shifts seen in broader general use.

The impacts of assorted shifts and what are likely increasingly arcane higher-order drive-based effects on the qubit at high power can also be seen through looking at chevron spectra of the whole lattice taken via multiphoton qubit-lattice swap. Some such spectra are shown in Figure 6.19, which examines three different drive amplitudes, multipliers 0.2, 0.5, and 0.7 of maximum drive amplitude, executed via mixing carrier with shaping tones from an arbitrary waveform generator. It is worth noting that while these spectra were taken at the same drive amplitude setting, differences in attentuation, antenna coupling, and resonance features of each actual drive line mean that these amplitudes are identical in name only.

These spectra can be compared to those pictured in Figure 6.11 which have an effective drive amplitude of 0.2 in this same scheme, which assigns a number to drive amplitude based on the fraction of full output voltage used at the arbitrary waveform generator which executes pulse shaping. At mid-range (0.5) drive amplitudes, we can still resolve many modes, and regions of resonant access overlap. At higher-range (0.7) drive amplitudes, the higher-frequency modes accessible to Alice begin to blur out, seemingly beyond what one expects just from increasing mode widening, likely a more pronounced effect of the strong drive on this qubit, which sits several hundred MHz closer in frequency to its four-wave drive.

In the non-reciprocal transport data, we work with effective drive amplitudes near 0.7; at these drive powers, the lower-channel lattice edge modes are shifted tightly together for easier access with a single-frequency drive, while still maintaining easily identifiable resonant swap patterns.

Zeytinoğlu et al. [210] model this same four-wave drive process and profile how effective

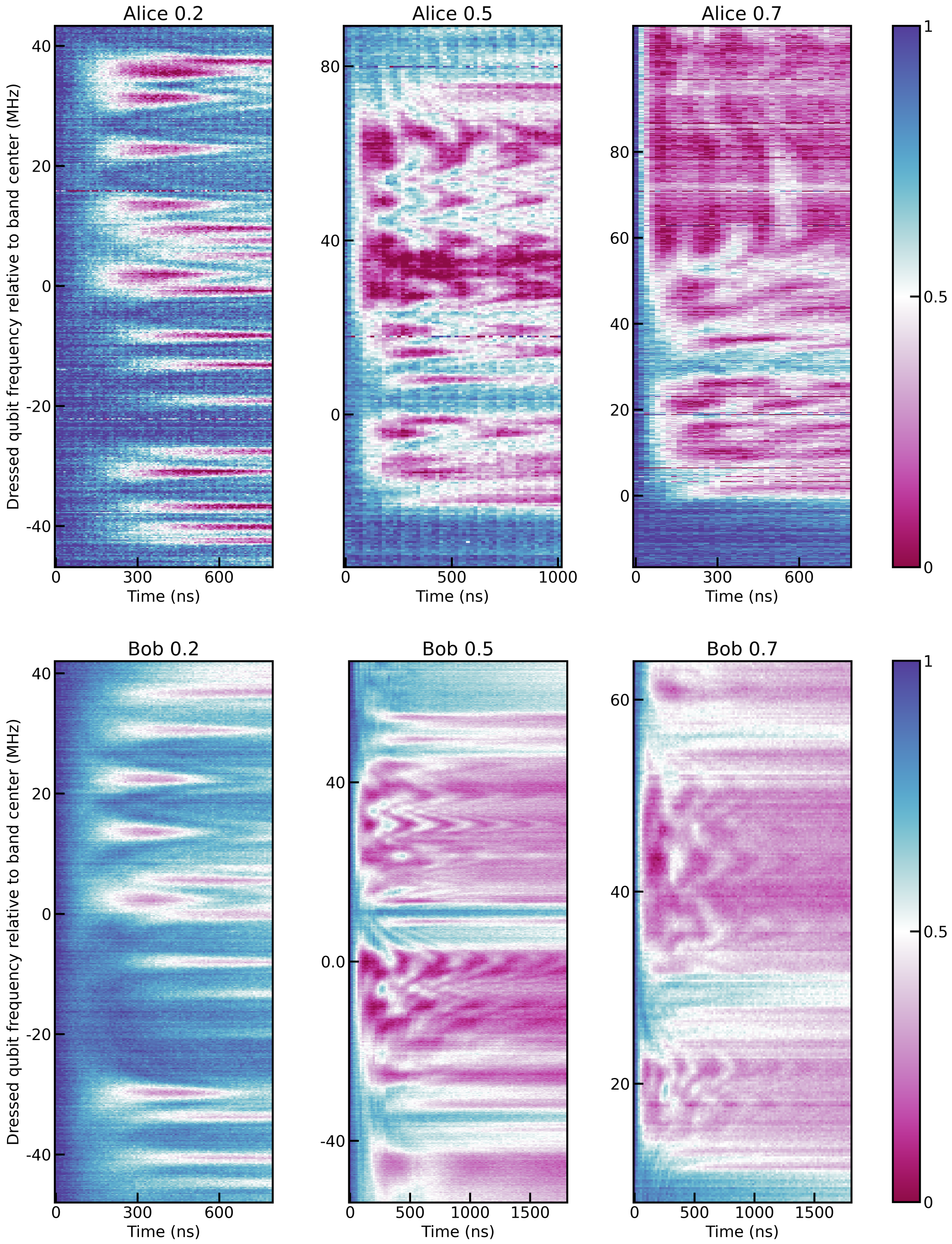

Figure 6.19: **Higher-power chevron scans.** Chevron plots trace on- and off-resonant four-wave interactions across the lattice spectrum. Note the frequency scaling on each vertical axis – all modes are shifted upwards with higher drive strength. Color scales are probability of each qubit being in its $|f\rangle$ state. Note that Bob has a narrower range of data values due to a calibration error, and also that different sub-plots have different time axes.

drive rate $\tilde{g}/2\pi$ falls off from its linear dependence on drive strength $\Omega/2\pi$ at strengths above 0.2 GHz due to the increasing impact of higher-order effects. This comports with the above qualitative indications that consistent behavior of the qubit levels at high drive powers is not a given. A rough calculation of the drive rate for a 5 MHz $\tilde{g}/2\pi$, a bare (overestimated) coupling $g/2\pi$ of 10 MHz between a transmon and some specific lattice mode, and approximate qubit and lattice mode parameters yields a drive strength $\Omega/2\pi$ several times this 0.2 GHz limit.

### 6.6.2 Drive parameter calibration

Given this idiosyncratic and detail-rich way in which the lattice spectrum, as 'seen' through four-wave operations with the qubit, changes in response to applied drive power, it is necessary to calibrate the drive parameters for transport measurements with an eye to what one hopes to achieve.

Holding the drive frequency fixed at the frequency used to excite a superposition of three edge eigenmodes, we perform an emission/detection experiment, generating a lattice excitation with one qubit and detecting it with the other after some time delay. If we vary both this delay and the lengths (identical for emission and detection) of the drive pulses, we can assess the regime of pulse lengths at which we successfully excite three

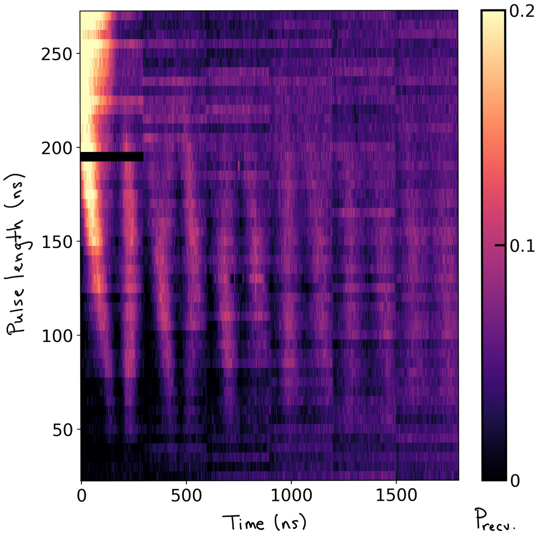

Figure 6.20: **Sweeping emission and detection pulse lengths.** We profile the population (scale on colorbar) of the detecting qubit after attempting to swap an excitation from one qubit to the lattice with an emission pulse, waiting some time (horizontal axis), and attempting to detect it with a second pulse in the second qubit. Advantageous pulse lengths are in the range of 70-90 ns. The dark stripe is data with a digitizer error. Measurements are performed with qubit Bob.

eigenmodes. Longer drive pulses are narrower in frequency, and even though we use square pulses (which Fourier transform to a sinc function with a menagerie of side lobes), drive pulses that are too long will simply fail to stretch across enough of frequency space to excite as many modes as shorter pulses. Pulses that are too short, though, will fail to inject the power necessary to effect emission and detection of excitations.

In Figure 6.20, we scan pulse lengths across a wide regime from far-too-long (longer than the ∼ 270 ns round-trip time of an excitation in this lattice edge channel, so that oscillations indicating departure and arrival of excitations at the detecting qubit simply wash out), through too-long (narrow enough in frequency that only one or two lattice modes are excited), through correct, to too-short (we fail to see any change in the detecting qubit population at all). As the pulse lengths shrink from too-long to correct, what were sinusoidal oscillations of the detecting qubit population, indicative of excitation of a set of 2 lattice modes, migrate to become asymmetrically spaced in time, a sign that more than 2 modes are being excited which reflects the bunching we see in data in Figure 6.13.

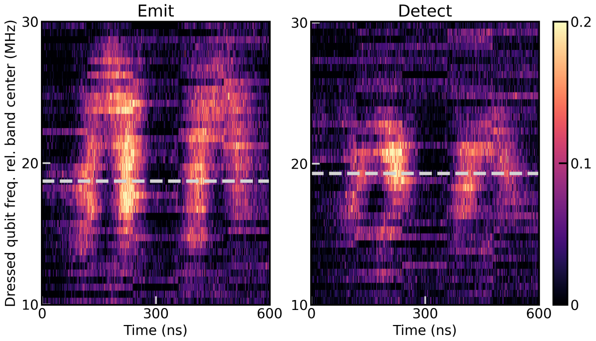

Figure 6.21: **Sweeping frequencies of emission and detection pulses.** Holding (optimized) pulse lengths steady and one pulse at its optimal frequency to excite transport through the lower-frequency chiral edge, we sweep the frequency of the other pulse and trace the dynamics of the resulting photonic population detected at the second qubit.

In Figure 6.21, we sweep the frequencies of emission and detection pulses to find those optimal for preparing and receiving a wavepacket transported through the lower-frequency chiral lattice edge. On-resonance with the frequencies that yield high population retrieval (white lines), a non-sinsuoidal oscillation appears in the photonic population retrieved by the detecting qubit. Off-resonance, yellow regions indicating retrieval peaks coalesce or disappear. Interestingly, the detection pulse is more sensitive than the emission pulse to detuning, likely an effect of non-ideal changes accumulated by a wavepacket propagating in a fundamentally time-reversal-symmetry-broken system. These behaviors are richly detailed and not entirely understood here.

We have shown, through scans of pulse frequency and length at a set of chosen drive powers, that we can exploit the rich and idiosyncratic physics of the disordered and imperfect lattice to locate good drive parameters for probing non-reciprocal transport.

### *6.6.3 Transport through the upper gap*

In addition to profiling non-reciprocal transport in the lower-frequency of the two chiral edge channels of this topological lattice, we seek to profile transport in the upper-frequency, opposite-direction chiral edge channel. Pulse calibration for these measurements works similarly to the methods detailed above. Our attempt to probe chiral transport in the upper-frequency chiral edge channel is less effective because the wider spacing of resonant interactions ($\approx 10$ MHz) between the qubit and modes in the upper-frequency edge channel means that it is more difficult to excite $> 2$ modes with a single-frequency drive in this channel. In Figure 6.22 we do manage to profile the dynamics of an excitation placed in a superposition of at least two of the upper-gap edge modes.

### *6.6.4 Modeling four-wave swap processes*

If we model the levels of a transmon like levels of a bosonic ladder, we expect the decay of the second excited qubit state ($|f\rangle$) to be twice that of the first ($|e\rangle$). This does not turn out to be the case for the qubits used in these experiments! In particular, qubit Bob displays an $|e\rangle$ state $T_1$ around $5\mu$s, but an $|f\rangle$ state $T_1$ near $2\mu$s. To better model oscillations in qubit population when each qubit is brought on resonance with a lattice eigenmode via multiphoton drive, we build a simple model of a qubit coupled to an oscillator in QuTiP

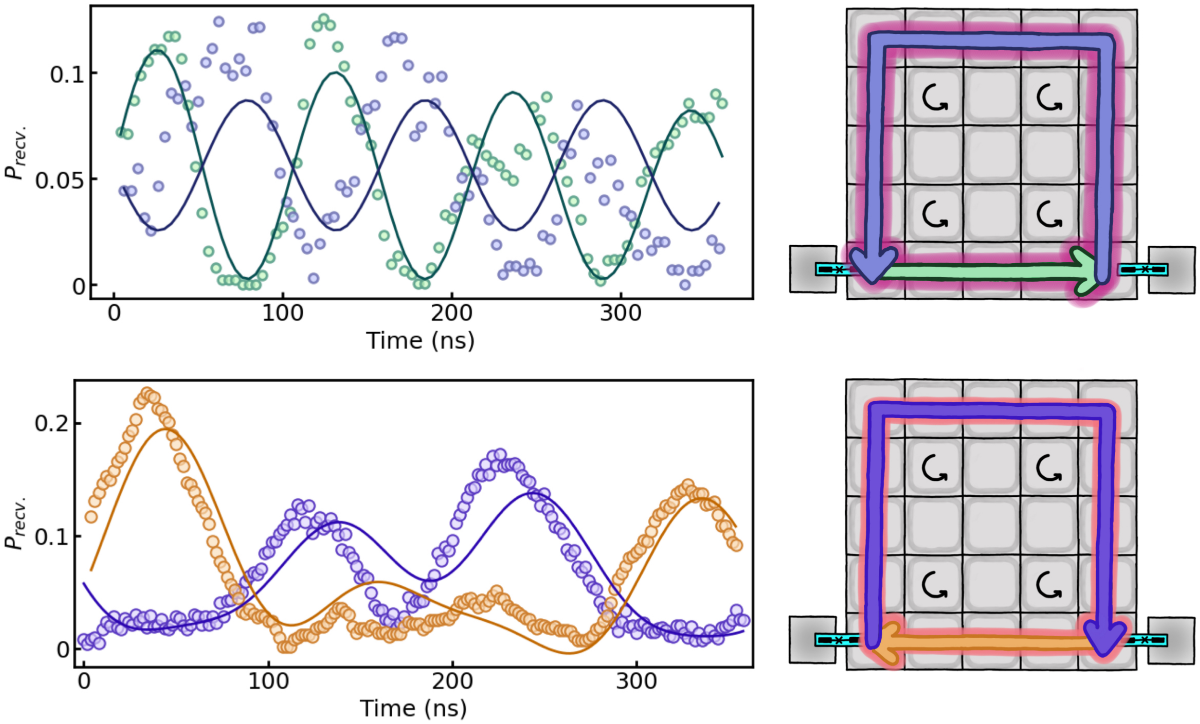

Figure 6.22: **Attempt at probing non-reciprocal transport in the upper-frequency chiral edge.** At **top**, we emit and detect photons using the upper-frequency edge channel of the chiral lattice. As edge modes are spaced further ($\approx$ 10 MHz) apart in this channel, and brought together less aggressively by shifts of resonant processes at strong drives, a single-frequency tone is less effective at exciting multiple modes and generating a localized wavepacket. We see largely sinusoidal behavior consistent with exciting a set of two lattice eigenmodes. Fits are two-mode versions of those described and carried out earlier in this chapter for lower-gap edge modes. At **bottom**, we include similar transport data from Figure 6.13 using three modes in the slower-dispersion lower-frequency edge channel for comparison. Lower-gap data are taken with more than three times as many averages, accounting for the noise difference in the two datasets.

which accounts for individual decay rates on different levels (see Appendix C).

In Figure 6.23, we produce fits from this model to Rabi oscillations between each resonantly-coupled qubit dressed excited state and a lattice mode of choice. Note that, at a range of drive amplitudes, the population present in qubit Bob never quite reaches 0 even on the first oscillation; this is an effect of the very rapid decay time of Bob's $|f\rangle$ state, which causes some population to be lost via decay even on route to the first minimum of Rabi oscillation. The simulations account for this more rapid decay and succeed in reproducing the nonzero minimum of Bob's first oscillation at both high and low drive powers.

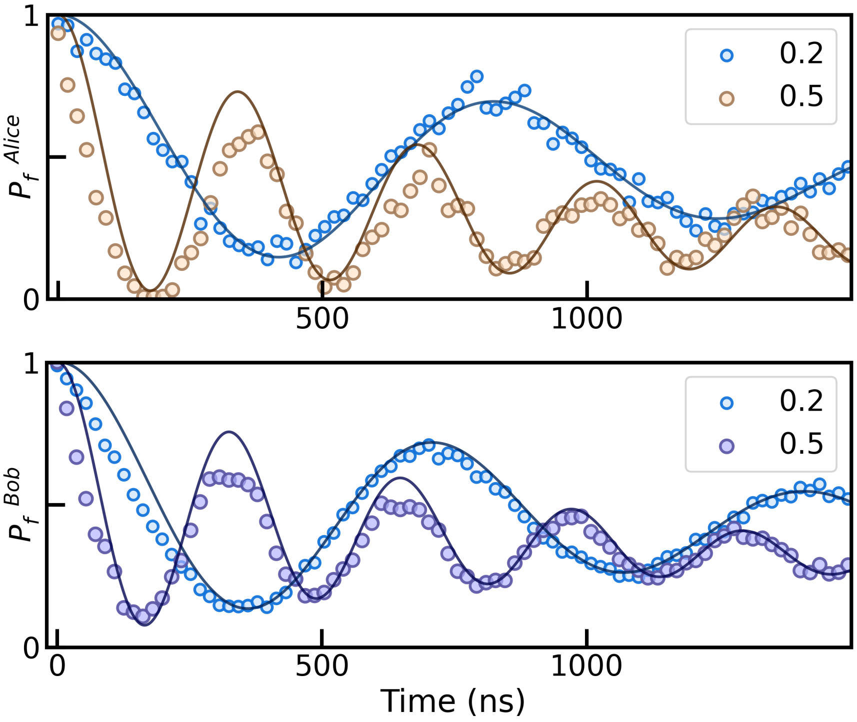

Figure 6.23: **Fits to resonant four-wave-driven Rabi oscillations.** Resonant dynamics between each qubit and the same mode are measured at two different drive amplitudes, and thus two different effective coupling rates $\tilde{g}$. We fit dynamics using a model of coupled qubit and resonator in QuTiP that incorporates non-ideal lifetimes in the $|f\rangle$ states of the qubits.

Irregularities in the shape of oscillations, especially notable in data taken at higher (0.5) drive amplitude, stem from the overlap between targeted modes and their neighbors that arises as resonant access to the modes broadens with higher drive power. The tops are cut off of some sinusoids due to interference patterns from overlapping access to multiple modes, visible as ripples in chevron plots.

### *6.6.5 Effects and challenges of four-wave swap*

It is the state of the art [91, 10, 26, 76, 167] to shape the amplitude of the multiphoton drive when using this four-wave process to couple a dressed excited state of a fixed-frequency qubit to a cavity mode or transmission line. We have found, however, that the Stark shifts on the qubit transition are so extreme as to prohibit amplitude modulation and the *effective* amplitude modulation that stems from providing drives at multiple frequencies simultaneously.

This is because, due to the exquisitely sensitive dependence of the qubit transition on the drive power in the regimes we must access to generate sub-200-ns dynamics, amplitude modulation of a drive pulse amounts to detuning the qubit by possibly several tens of MHz from the targeted resonant interaction. In that process of ring-up and ring-down of the full-scale Stark shift, the dressed excited state of the qubit also is dragged across resonance with some portion of the lattice band, risking unwanted interactions with un-targeted modes.

In Figure 6.24, we take the same scan of the lattice spectrum via multiphoton-driven qubit, using, in turn, square pulses, square pulses with 15 ns $\sigma$ Gaussian edges, and Gaussian pulses. Even with minor modification to a square pulse in the form of rounded edges with a Gaussian rise and fall, we see the accessed spectrum blur, asymmetrically, demonstrating striping that sweeps from the lower left up into the main part of the band structure. When Gaussian pulses are used, this blurring becomes so pronounced that the fine details of the lattice spectrum are obscured. This seems to be an effect of the qubit ‘dumping’ its population into unwanted locations en route to the target resonance.

When some shaped tone at a specific frequency is applied to the qubit, the qubit’s $|g\rangle \leftrightarrow |f\rangle$ transition Stark shifts onto resonance with the ultimate lattice frequency we seek to target. During the interim ring-up time, the qubit transition sits at a higher frequency;

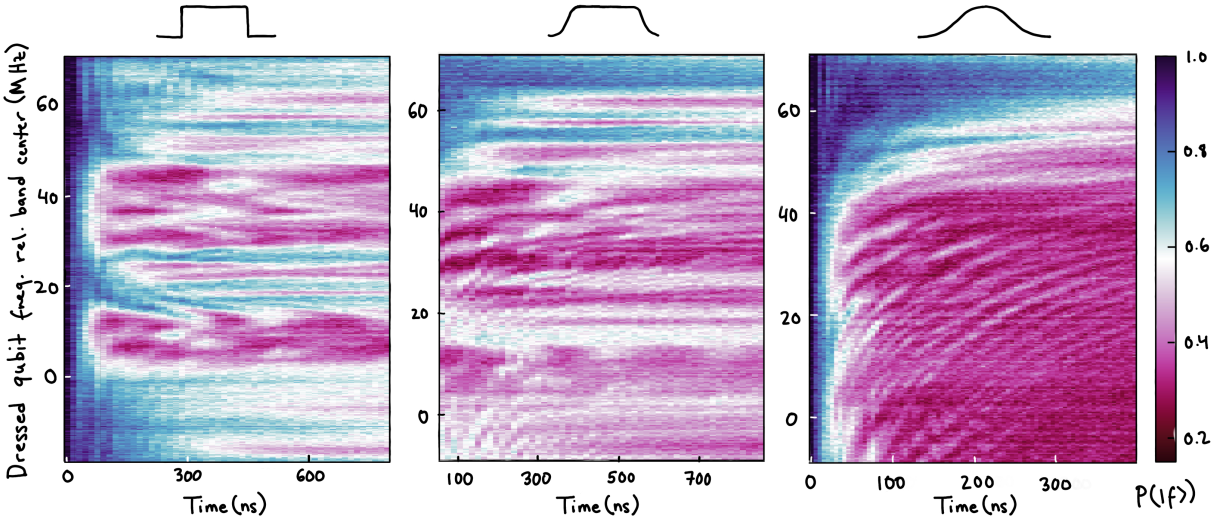

Figure 6.24: **Multiphoton-driven spectra with a range of pulse shapes.** We supply a strong multiphoton drive (amplitude label 0.6) to stimulate swapping of excitations between qubit Bob and lattice modes. Cartoons of the pulse shapes used sit above each plot. Colorbar represents population in the lattice-coupled qubit; minimum of 0.2 is due to prep. error.

as we target the lower-frequency edge channel in our transport experiments, the qubit has the opportunity to lose population as it passes through resonance with most of the lattice spectrum on route to the target frequency with fully rung-up drive.

Because of this limitation on access to resonant dynamics with shaped pulses, we restrict ourselves to using square pulses in the work done in this thesis. Others using the same four-wave process, in regimes with much weaker Stark shifts, have seen success in chirping the phases of their drive pulses in order to cut back on the scale of the Stark shift [76]: they modulate the phase $\phi_{\mathrm{f0g1}}(t)$ of the drive pulse $a_p(t)$ to produce

$$a_c(t) = a_p(t)e^{i\phi_{\mathrm{f0g1}}(t)} \tag{6.8}$$

with the phase modulated according to

$$\frac{d\phi_{\mathrm{f0g1}}(t)}{dt} = -\Delta_{\mathrm{f0g1}}(t) \tag{6.9}$$

where $-\Delta_{\mathrm{f0g1}}(t)$ is the Stark shift on the qubit due to the drive pulse at instantaneous time $t$. We can express this in terms of the coefficient $C_{ch}$ scaling the quadratic dependence of this Stark shift on the instantaneous pulse amplitude, which we can fit from data, resulting in chirped pulse:

$$a_c(t) = a_p(t) e^{-i \int_0^t C_{ch} |a_p(t')|^2 dt'} \tag{6.10}$$

This method might be helpful to the experiments described in this thesis, opening up the benefits of pulse shaping for maximizing population and optimizing shape of the wavepacket released into the chiral edge if the Stark shift can be effectively toned down. Ilves et al. [76] cancel out a maximum Stark shift $\Delta_{\mathrm{f0g1}}$ of 8 MHz; we would need to target $\sim$ 60 MHz, so more work would need to be done to ensure that this method remains effective at higher drives.

## 6.7 Conclusion

In this work, we strongly couple two transmon qubits to the edge of a topological photonic lattice and show the capacity to emit a microwave photon into, and detect it traveling in, a multi-mode chiral edge channel of this synthetic Chern insulator. We use this capacity to observe non-reciprocal transport between the quantum emitters coupled to the chiral lattice edge, leveraging strong couplings between emitters and photonic metamaterial to probe single-photon dynamics.

Immediate future work with this extant platform might employ tomographic measurements to explore the entanglement structure of long-traveling wavepackets that fragment in the chiral edge. Phase-modulating the swap drive might partially lessen the scale of its Stark shift on the qubit levels [145, 76], opening broader opportunities (see Section 6.6.5) for shaping temporal pulse envelopes to optimize photon transfer into the lattice [210, 91, 10].

Fine control of temporal envelopes of traveling wavepackets, alongside the native time-binning effect suggested [194, 122] to occur in a few-mode edge channel, would enable exploration, in a directional channel, of dual-rail time bin [76, 92] and multiphoton [10, 25] qubit encodings tractable with cavity-based tools for error correction. The natural time delay of directional excitations in the lattice edge also makes this platform an option for generating cluster states of light [149, 55] of the three-plus dimensions needed to approach fault-tolerant computation [159], especially since the sixteen-cavity lattice edge provides multiple possible sites of qubit-waveguide interaction.

The richness of a structure which admits many distinct couplings is a core advantage of this platform: coupling one additional qubit to the lattice bulk would engender Landau-photon polaritions [48, 49], opening pathways to explore the polaritonic physics of interest in photonic systems which combine topology with nonlinearity and gain [87, 11, 12]. Coupling more qubits to the lattice edge would enable attempts at driven-dissipative preparation of steady entangled states in many-emitter quantum electrodynamics with a chiral waveguide [184, 148, 102]. Introducing local parametric driving or reservoir engineering to (a) lattice site(s) could support production of long-range entangled states of light which gain structure from system topology [208, 151].

Scaling up the size of the lattice itself would mitigate issues with edge-state leakage into the bulk and the significance of scattering from lattice corners, further localizing wavepackets in chiral lattice edge channels serving as more-multimode topological waveguides. Scaling up the number of items coupled to this lattice, beyond introduction of a few specific emitters or sites of reservoir engineering, could affect the system globally, opening avenues to generation [157] and stabilization [82] of states of matter combining interactions with topology.

# CHAPTER 7

# OUTLOOK

The quarter-flux Harper-Hofstadter lattice for microwave photons, strongly coupled to multiple nonlinearities, which is the focus of this thesis provides a rich landscape of opportunities to investigate the interplay of topology and interactions. It offers the chance to both excite and probe single-photon dynamics in an engineered photonic system, a goal which is of interest nowadays both for quantum information applications and as a route to developing further techniques in topological photonics. We expand on the conclusion of the previous chapter and detail some potential next steps.

## 7.1 Further measurements to be made with this platform

- *Chirping of multiphoton drive.* As discussed in the previous chapter, chirping the phase of multiphoton swap-drive pulses could possibly diminish the substantial Stark shifts on qubit $|g\rangle \leftrightarrow |f\rangle$ transitions enough to enable the use of pulse shaping.

  The most obvious initial application of pulse shaping would be to permit multi-frequency drives, which inherently have some variable amplitude envelope due to the phase differences between the tones involved. Gaining access to resonant driving of multiple qubit-lattice mode interactions simultaneously would enable us to more effectively excite multiple $\sim$ 10 MHz spaced edge modes in the higher-frequency edge channel of the lattice, permitting synthesis of a genuinely multimode wavepacket propagating in the upper edge channel.

  There exists a wealth of work on optimizing pulse shaping, from the early days of flying qubits with photons in transmission lines [129, 10, 25]; others, working with continuum mode landscapes in waveguides, have calculated the exact pulse shape that is necessary in that context to generate Gaussian-envelope single-photon wavepackets.

As the work in this thesis probes a regime intermediate between continuum-waveguide and single-cavity-mode coupling, calculation of an optimized pulse shape would be more idiosyncratically dependent on the details of the exact lattice and its eigenspectrum. The finite-size effects present in this $5 \times 5$ lattice, notably wavepackets' tendency to bounce off of corners, would further complicate pulse shaping but would be tractable via simulation. It should be possible to model, for a disorder-free lattice, the perfect shape of pulse to optimize transfer efficiency of a photon into the lattice, circumventing the maximum 30 percent recovery rate of photons we observed after passage through the chiral edge. It should even be possible to model wavepacket decoherence by relying on known lattice mode frequencies and perhaps time-resolved measurements of excitations propagating along the edge; in that way, even if the emission and detection pulses are made asymmetric by lattice disorder, one could optimize for photon retrieval.

- *Two-qubit tomography.* In Section 6.5.1 we detailed the protocol to prepare the qubits in a Bell state via lattice edge wavepacket; we attempted this preparation, but were unable to measure its effectiveness. With limited time, we did not have access to the phase coherence between emission and detection pulses necessary to attain phase information on states in two-qubit tomography.

  Deploying phase-coherent emission and detection drives would be a fairly simple hardware modification, feasible by splitting both drives off of the same local oscillator with upmixing afterwards (emission and detection drives should be a maximum of 100-200 MHz detuned). Gaining access to two-qubit tomography would open avenues to explore the entanglement structure of traveling lattice wavepackets, which several authors [122, 194] suggest are functionally time-binned due to wavepacket bunching in a few-discrete-mode waveguide. While the imperfect and detailed nature of lattice edge transmission makes this platform a suboptimal venue to explore dual-rail time-bin qubit encoding on its own, this is an active subject of research interest in the circuit

QED community [92, 76].

- *Channel-channel scattering.* Each of the transmons Alice and Bob is coupled to both lattice edge channels; supplying a pair of detuned drives simultaneously could cause one such transmon to absorb a photon tunneling in one edge channel and emit it to the other. Probing mode-mode and channel-channel scattering through a qubit would be intrinsically entertaining, but might also be useful to construct an added (synthetic) dimension in the lattice, potentially altering the dimensionality of the effective lattice or of a photonic cluster state prepared in it. We discuss cluster states later in this chapter, but it's important to note that a single feedback event with one qubit is enough to generate a two-dimensional cluster state [149, 55], an outcome which this platform is very hypothetically already equipped to seek.

## 7.2 Improvements to the platform

- *Flux-tunable qubits.* If the above item regarding pulse chirping is ineffective at toning down the extreme scale of the Stark shift associated with the four-wave swap drive, it will become difficult to add further fixed-frequency qubits coupled to the lattice, due to the already-idiosyncratic nature of calibration needed to track mode-resonant drive frequencies that are equisitely sensitive to small changes in the drive. Recent work has been done at Yale to realize fast-flux delivery to circuits embedded in cavities [104], addressing the physical challenge of routing this flux to 3D transmon qubits embedded in chunks of superconducting material which works to screen changes in current.

  Flux tuning could be particularly exciting because of the potential for parametric modulation to bring the qubits on resonance with lattice modes; this would be a flexible method of gaining, and shutting off, access to coherent processes. Any increased speed of swap operations would help to generate excitations in the lattice on timescales much faster than the chiral edge round-trip, as opposed to only a few times faster. We could then more easily separate state preparation/detection from dynamics.

Dynamic control of flux bias within this platform, alongside associated circuit modifications, could also provide opportunity to access three-wave mixing [58, 59], avoiding the $\phi^4$ term in the Josephson Hamiltonian by using a three-wave process to produce lattice photons. This might support evasion of the giant Stark shift problem associated with our higher-order four-wave drive.

- *Scale the system up, on-chip.* Reaching larger lattice sizes would provide a more finely-populated set of discrete eigenmodes useful to synthesize wavepackets in each edge channel. At larger size, finite-size effects in the lattice, particularly the overlap of each edge eigenmode with the bulk, would be less prominent. While it is perhaps possible to scale up in the 3D architecture, there is limited room to grow before the experiment becomes curtailed by the size of a mixing chamber plate.

  Beyond increasing the size of a quarter-flux Harper-Hofstadter lattice, it might be interesting to explore other lattice dimensionalities and connectivities (the Kagome lattice? Synthetic gauge fields in higher dimensions, including synthetic ones?), taking advantage of the flexibility of engineering available to circuit QED systems. If executed in 3D, this would have to be done with attention to the size, shape, and spacing of milled cavities. Site-site couplings, which derive from evanescent overlap of adjacent cavity mode profiles, would be particularly hard to maintain. It might be preferable to realize a topological lattice in 2D on-chip – here the challenge of more complicated connectivities could still be difficult to execute, but access to vias and flip-chip architectures courtesy of superconducting bump-bonding between layers might provide more feasibly attainable flexibility in dimensions and connections.

  The challenge in moving to 2D would be in maintaining the synthetic gauge field without the convenience of YIG spheres, and this would likely need to be carried out via coupling modulation, as was the case in prior work showing chiral transport in a 2D qubit ring [170]. With the introduction of (somewhat narrow-band) 2D on-chip circulators [36, 15, 130] and other more inventive forms of generating non-reciprocity [202], though, it is possible that we might ‘plug in’ these pre-generated ideas to again engineer a topological lattice that sites its gauge field in local phase windings.

Overall, a larger topological lattice might be of interest for studying transport of polaritonic states in a broadly nonlinear lattice bulk, which requires multiple bulk nonlinearities in its proposal [49], or approaching the regime of investigating state localization and thermalization in a many-body quantum system. The ways in which topology, with its affordance of global structure and access to system-wide entanglement, might add subtlety to this study of many-body interacting systems are worth further consideration.

The advantage of moving to a 2D transmon lattice is that, rather than hoping to successfully introduce a 3D qubit coupled to each of many lattice cavities, we might instead design a circuit and immediately attain nonlinearity on each site, putting the platform in reach of exploring many-body physics in a topological landscape.

## 7.3 More qubits coupled to the lattice

- *2 and higher dimensional cluster states.* Other work, in particular using a slow-light waveguide with a ‘mirror’ at one end [55], has already realized two-dimensional photonic states in a circuit QED platform. However, given the interest of photonic cluster states to folks studying quantum communication [85], measurement-based quantum computing [160, 159], and entangled states of light in general, they are worth exploring further; the general formula of itinerant photon plus some set of light-matter interactions arrayed along a waveguide is an attractive one for thinking about both making quantum states of light and moving quantum information with those states.

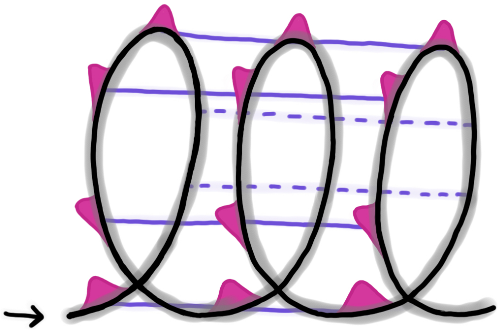

Figure 7.1: **Schematic of 2D cluster state.** Adapted from [55], this schematic depicts a two-dimensional cluster state formed from subsequent re-entangling events of photons propagating with some delay in a slow-light waveguide. A three-dimensional version of this graph state, constructed with more nodes of entanglement, to three dimensions is argued to be sufficient to produce a resource state for fault-tolerant measurement-based quantum computation [149, 159].

Raussendorf [159] argues that a three-dimensional photonic cluster state is sufficient to produce fault-tolerant quantum computation with a one-way quantum computer.

The extant platform already has, in theory, a slow-light waveguide in the form of the lattice edge coupled to multiple qubits. We have a round-trip time in the slow-propagating edge channel of 270 ns, compared to ∼75 ns dynamics timescales. We could, in theory, construct at least 3-dimensional cluster states with the platform as it exists presently: more than 2 re-entangling operations with a set of 2 qubits would suffice, which we might achieve by waiting multiple lattice round trips between operations.

The issue with this option is that the wavepackets in the chiral lattice on this scale have such wild behavior that tracing where, exactly, wavepackets are in the long term can prove a challenge. Increasing the lattice size, even if by just a few sites in each dimension, might help to constrain this wild behavior and make the chiral edge more useful for transport of actual local wavepackets.

Coupling even more qubits to the lattice edge would offer even more opportunities to entangle qubits with photons passing by in the edge channel, increasing capacities for generating multidimensional graph states of light. Having qubits on hand to help characterize these states would be helpful in doing proof-of-concept experiments realizing these states. But the ultimate lack of scalability of this 3D cavity lattice platform would prevent broader applicability.

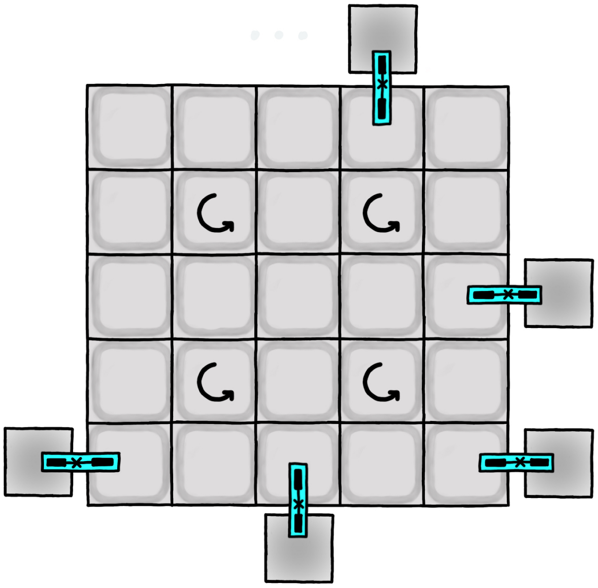

Figure 7.2: **Chiral waveguide QED with multiple qubits coupled to the chiral lattice edge.** We depict a set of further transmon qubits coupled at arbitrary sites along the edge of the 5 × 5 microwave Chern insulator. By siting transmons specifically on the edge, we can gain access to control and readout of these cavities via auxiliary cavities, also pictured.

- *Chiral waveguide QED with a bunch of emitters.* The chiral lattice edge, particularly in an expanded lattice, would provide an interesting playground to explore multi-emitter chiral quantum optics (see Figure 7.2 and the treatment of chiral waveguide quantum electrodynamics in Chapter 1). This is one of the most interesting and feasible directions of development for the chiral lattice platform – coupling qubits to bulk sites could prove challenging (see section to follow), but the lattice edge sites are much more accessible to introduction of further qubits, limited by capacities for qubit tuning and control that might be mitigated by the above-discussed introduction of fast flux bias.

A range of theoretical and experimental works in chiral quantum optics interrogate the physics of waveguide-mediated many-emitter interaction in situations where either the coupling structure [148, 102, 182, 81, 79] or the waveguide itself [158, 153, 29, 179] is chiral. Collective multi-emitter states mediated by a chiral waveguide, correlated photonic states propagating directionally through a landscape of super-wavelength-spaced strongly-coupled nonlinearities, and the driven-dissipative stabilization of large entangled states of light would be interesting to probe in the chiral edge alone while en route to the fractional quantum Hall limit. The fact that the chiral lattice platform sits in between a single-mode cavity and a continuum waveguide might add interest to this direction of exploration.

- *Couple qubit to the lattice bulk.* Coupling a transmon to one of the lattice sites located in the bulk (see Figure 7.3) could be accomplished by bringing the sapphire wafer upon which it sits through the underside of the lattice. The sites are purposefully designed to be tall enough that each cavity mode sees its electric field amplitude fall off exponentially towards the cavity top, making it infeasible to couple in a transmon from the lattice roof without pushing it far enough into the cavity to spoil its quality factor. As side-coupling locations of each bulk lattice site are consumed with nearest-neighbor tunnel couplings, we would need to access the cavity from its bottom, likely through the center of the quarter-wave post to preserve rotational symmetry, in order to introduce a bulk qubit.

  Were we to do this, we might generate and probe the behavior of a Landau-photon polariton in the Chern lattice [48, 49]; such a hybrid qubit-photon state, trapped by the strong synthetic gauge field, would be confined to localization in the bulk. This experiment would provide an accessible probe of single-polaritonic physics, which can be put in conversation with other work combining nonlinear materials with engineered photonic systems [31, 87], the continuum version of the multi-emitter physics described

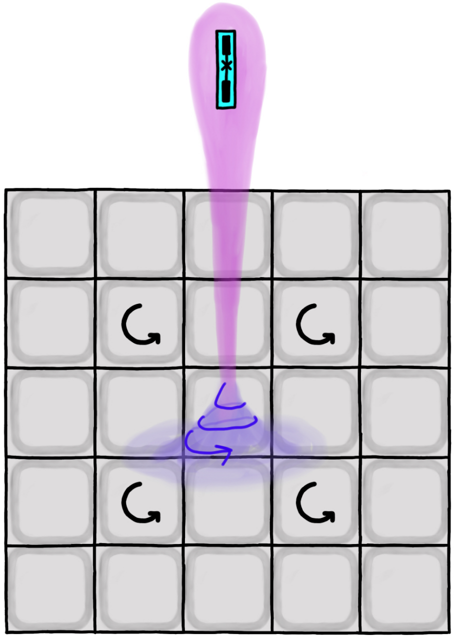

Figure 7.3: **Landau-photon polariton from coupling a qubit to the microwave Chern insulator bulk.** Adapted from [48], we depict the polariton (in purple), a quasiparticle formed by hybridization of a nonlinear transmon qubit and a photon confined to a Landau level in the bulk of the microwave Chern insulator. Using multiple emitters to generate multiple of these quasiparticles in the bulk, most feasible if the lattice were scaled up, might open up a rich landscape of non-nearest-neighbor interactions [48] and in combination with a synthetic electric field – a potential gradient – might also open the possibility of efficient emission, absorption, and directional bulk transport of excitations between qubits [49].

in the bullet point above. To execute this it would be necessary to develop good strategies for reading out states with the same qubit one used to do state preparation, unless one was willing to add further nonlinearities to the lattice bulk. Some theoretical proposals argue that the polaritonic states accessible when *multiple* emitters are coupled to the lattice bulk might host interesting behavior [17], including efficient state transport between emitters [49], but we would benefit from a larger lattice and larger lattice bulk to address this limit, as bulk sites one off the edge have some measurable edge-like mode participation.

- *Lend nonlinearity to all sites, approaching the fractional quantum Hall limit.* The initial motivation of the microwave Chern insulator studied throughout this thesis was as a superconducting-qubit-compatible photonic metamaterial which would admit coupling of qubits to enough lattice sites to accomplish substantial nonlinearity throughout the lattice. In this case, the Harper-Hofstadter lattice would host photon-photon interactions, opening up the chance to study the transport and interaction of excitations in a system that mimics the mechanism of the fractional quantum Hall effect. Measurements performed with this analog quantum simulator were intended to provide access to measurements of anyons, in particular the then as-yet-unseen non-Abelian anyons of interest for those working towards fault-tolerant quantum computation. Since that time, an analog simulation of fractional quantum Hall physics has been realized in cold atoms [108] and it has become apparent that coupling enough 3D transmon qubits to lattice sites to achieve the fractional quantum Hall limit, and then controlling them, is a likely prohibitive amount of effort. It seems like the routes immediately above and below this item leverage the special aspects of this circuit QED platform to greater effect.

## 7.4 Some futures in reservoir engineering

- *Single site of reservoir engineering or dissipative pairing.* The flexibility of this many-edge-site lattice with easy antenna access to be hooked up to various drives and circuits is probably the most interesting aspect of this particular topological photonic platform. The discussion of chiral waveguide quantum electrodynamics above brings up the expectation that, with a set of quantum emitters coupled to a shared chiral waveguide, it should be possible to dissipatively stabilize some entangled steady state of the whole system.

  A pair of recent papers offers a set of options for supplying a particular intervention at a specific location in a Chern lattice, which should be sufficient to achieve a global

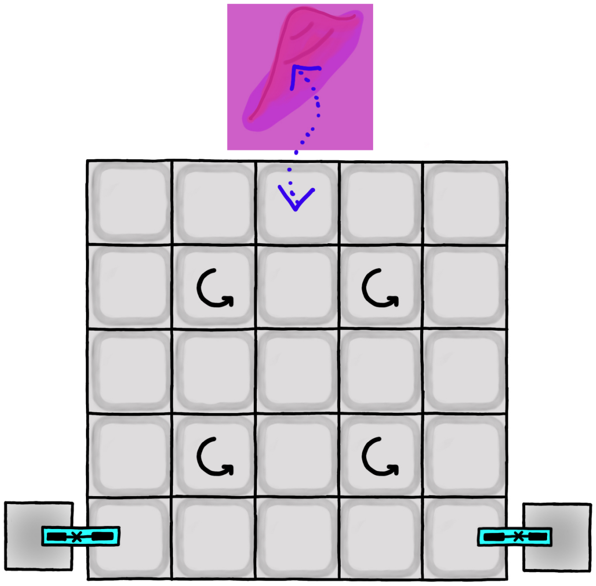

Figure 7.4: **Coupling of lattice site to a squeezed reservoir.** We depict, at top in pink, a reservoir of squeezed light coupled to a single site of the lattice edge. Yanay and Clerk [208] argue that this intervention in reservoir engineering could help to stabilize long-range entangled states of light in the Chern lattice that gain their structure from the metamaterial's topology.

response thanks to the system topology: Pocklington et al. [151] propose introduction of a (non-Hermitian) dissipative pairing operation to one pair of lattice sites, which at low power should stabilize an exponentially edge-localized steady state with the edge sites highly entangled, and at high power should introduce a novel instability. Yanay and Clerk [208] propose introduction of a squeezed reservoir coupled to a single lattice site; due to the symmetry of the Chern insulator Hamiltonian, this reservoir will stabilize a steady state, in which the correlation structure across the whole lattice will depend on the reservoir-engineering location chosen.

In both cases, introduction of a local interaction/reservoir, plus the symmetry of the Chern insulator, result in steady-state global correlations structured by that symmetry. This is illustrative of the close connection between topology and long-range entanglement [39], and investigating the entanglement structures accessible in a photonic Chern insulator via parsimonious driving or reservoir engineering might be of meaningful interest to future researchers seeking to manipulate and understand quantum light in topological photonic systems.

*Topological protection of correlated photons.* In extension of the section above, the support system lattice topology yields for correlated states can also be used to stabilize pre-squeezed states of light injected into some site of the lattice (e.g. from a Josephson parametric amplifier) purely in order to preserve those correlated states of light themselves. Past work has investigated the capacity of topological insulator edge states to protect correlated pairs of photons above the results that would be achievable without topological structure [123, 22, 200]. As the utility of this work seems to be rooted in scalability for quantum information handling, and the chiral lattice, as it stands, is eminently difficult to scale, this route is not the most valuable for future experimental work.

- *Interface with non-Hermitian processes.* This thesis has largely evaded discussing the combination of non-Hermitian physics with non-reciprocity, which is a rapidly expanding zone of interest, but it will now mention that a flowering of recent work [136, 155] has focused on combining topology with the non-Hermitian processes of gain and loss. Some experiments explore polaritonic physics [87] and lasing [11, 12] in topological systems made of nonlinear materials, while others build platforms from the ground up to work towards simulating a many-body non-Hermitian system [27]. Further work applies parametric driving to systems with topological edge modes, spurring amplification than can be harnessed for experimental use [144, 204]. This requires more thought, but it might be of interest to use the chiral lattice platform to support and explore topological amplification of light under drive.

# REFERENCES

[1] Alexei Alexeyevich Abrikosov. The magnetic properties of superconducting alloys. *Journal of Physics and Chemistry of Solids*, 2(3):199–208, 1957.

[2] Y. Aharonov and D. Bohm. Significance of electromagnetic potentials in the quantum theory. *Phys. Rev.*, 115:485–491, Aug 1959. doi:10.1103/PhysRev.115.485. URL `https://link.aps.org/doi/10.1103/PhysRev.115.485`.

[3] Google Quantum AI and Collaborators. Non-Abelian braiding of graph vertices in a superconducting processor. *Nature*, 618:264–269, Jun 2023. doi:10.1038/s41586-023-05954-4. URL `https://doi.org/10.1038/s41586-023-05954-4`.

[4] M. Aidelsburger, M. Atala, M. Lohse, J. T. Barreiro, B. Paredes, and I. Bloch. Realization of the Hofstadter Hamiltonian with ultracold atoms in optical lattices. *Phys. Rev. Lett.*, 111:185301, Oct 2013. doi:10.1103/PhysRevLett.111.185301. URL `https://link.aps.org/doi/10.1103/PhysRevLett.111.185301`.

[5] M. Aidelsburger, M. Lohse, C. Schweizer, M. Atala, S. Barreiro, J. T. nad Nascimbène, N. R. Cooper, I. Bloch, and N. Goldman. Measuring the Chern number of Hofstadter bands with ultracold bosonic atoms. *Nature Physics*, 11:162–166, Feb 2015. doi:10.1038/nphys3171. URL `https://doi.org/10.1038/nphys3171`.

[6] Monika Aidelsburger. *Artificial gauge fields with ultracold atoms in optical lattices*. PhD thesis, Ludwig-Maximilians-Universitat Munich, 2015. URL `https://doi.org/10.1007/978-3-319-25829-4`.

[7] Brandon M Anderson, Ruichao Ma, Clai Owens, David I Schuster, and Jonathan Simon. Engineering topological many-body materials in microwave cavity arrays. *Physical Review X*, 6(4):041043, 2016.

[8] Ziqiao Ao, Sahel Ashhab, Fumiki Yoshihara, Tomoko Fuse, Kosuke Kakuyanagi, Shiro Saito, Takao Aoki, and Kouichi Semba. Extremely large Lamb shift in a deep-strongly coupled circuit QED system with a multimode resonator. *Scientific Reports*, 13:11340, Jul 2023. doi:10.1038/s41598-023-36547-w. URL `https://doi.org/10.1038/s41598-023-36547-w`.

[9] János K. Asbóth, Lázló Oroszlány, and András Pályi. *A Short Course on Topological Insulators: Band Structure and Edge States in One and Two Dimensions*. Springer International, 2016. doi:https://doi.org/10.1007/978-3-319-25607-8. URL `https://doi.org/10.1007/978-3-319-25607-8`.

[10] Christopher J. Axline, Luke D. Burkhart, Wolfgang Pfaff, Mengzhen Zhang, Kevin Chou, Philippe Campagne-Ibarcq, Philip Reinhold, Luigi Frunzio, S. M. Girvin, Liang Jiang, M. H. Devoret, and R. J. Schoelkopf. On-demand quantum state transfer and entanglement between remote microwave cavity memories. *Nature Physics*, 14:705–710, July 2018. doi:https://doi.org/10.1038/s41567-018-0115-y.

[11] Babak Bahari, Abdoulaye Ndao, Felipe Vallini, Abdelkrim El Amili, Yeshaiahu Fainman, and Boubacar Kanté. Nonreciprocal lasing in topological cavities of arbitrary geometries. *Science*, 358(6363):636–640, 2017. doi:10.1126/science.aao4551. URL `https://www.science.org/doi/abs/10.1126/science.aao4551`.

[12] Miguel A. Bandres, Steffen Wittek, Gal Harari, Midya Parto, Jinhan Ren, Mordechai Segev, Demetrios N. Christodoulides, and Mercedeh Khajavikhan. Topological insulator laser: Experiments. *Science*, 359(6381):eaar4005, 2018. doi:10.1126/science.aar4005. URL `https://www.science.org/doi/abs/10.1126/science.aar4005`.

[13] Sabyasachi Barik, Aziz Karasahin, Christopher Flower, Tao Cai, Hirokazu Miyake, Wade DeGottardi, Mohammad Hafezi, and Edo Waks. A topological quantum optics interface. *Science*, 359(6376):666–668, 2018. doi:10.1126/science.aaq0327. URL `https://www.science.org/doi/abs/10.1126/science.aaq0327`.

[14] Sabyasachi Barik, Aziz Karasahin, Sunil Mittal, Edo Waks, and Mohammad Hafezi. Chiral quantum optics using a topological resonator. *Phys. Rev. B*, 101:205303, May 2020. doi:10.1103/PhysRevB.101.205303. URL `https://link.aps.org/doi/10.1103/PhysRevB.101.205303`.

[15] S. Barzanjeh, M. Wulf, M. Peruzzo, M. Kalaee, P. B. Dieterle, O. Painter, and J. M. Fink. Mechanical on-chip microwave circulator. *Nature Communications*, 8, Oct 2017. doi:10.1038/s41467-017-01304-x. URL `https://doi.org/10.1038/s41467-017-01304-x`.

[16] Simon Baur, Daniel Tiarks, Gerhard Rempe, and Stephan Dürr. Single-photon switch based on Rydberg blockade. *Physical Review Letters*, 112(1):073901, 2014. doi:10.1103/PhysRevLett.112.073901. URL `https://link.aps.org/doi/10.1103/PhysRevLett.112.073901`.

[17] Miguel Bello and J. Ignacio Cirac. Topological effects in two-dimensional quantum emitter systems. *Phys. Rev. B*, 107:054301, Feb 2023. doi:10.1103/PhysRevB.107.054301. URL `https://link.aps.org/doi/10.1103/PhysRevB.107.054301`.

[18] Hannes Bernien, Sylvain Schwartz, Alexander Keesling, Harry Levine, Ahmed Omran, Hannes Pichler, Soonwon Choi, Alexander S. Zibrov, Manuel Endres, Markus Greiner, Vladan Vuletić, and Mikhail D. Lukin. Probing many-body dynamics on a 51-atom quantum simulator. *Nature*, 551:579–584, Nov 2017. doi:10.1038/nature24622. URL `https://doi.org/10.1038/nature24622`.

[19] Michael Victor Berry. Quantal phase factors accompanying adiabatic changes. *Proceedings of the Royal Society of London. A. Mathematical and Physical Sciences*, 392 (1802):45–57, 1984. doi:10.1098/rspa.1984.0023. URL `https://royalsocietypublishing.org/doi/abs/10.1098/rspa.1984.0023`.

[20] K. M. Birnbaum, A. Boca, R. Miller, A. D. Boozer, T. E. Northup, and H. J. Kimble. Photon blockade in an optical cavity with one trapped atom. *Nature*, 436:87–90, Jul 2005. doi:10.1038/nature03804. URL `https://doi.org/10.1038/nature03804`.

[21] Lev S. Bishop. *Circuit quantum electrodynamics*. PhD thesis, Yale University, 2010. URL `https://doi.org/10.48550/arXiv.1007.3520`.

[22] Andrea Blanco-Redondo, Bryn Bell, Dikla Oren, Benjamin J. Eggleton, and Mordechai Segev. Topological protection of biphoton states. *Science*, 362(6414):568–571, 2018. doi:10.1126/science.aau4296. URL `https://www.science.org/doi/abs/10.1126/science.aau4296`.

[23] Sal J. Bosman, Mario F. Gely, Vibhor Singh, Alessandro Bruno, Daniel Bothner, and Gary A. Steele. Multi-mode ultra-strong coupling in circuit quantum electrodynamics. *npj Quantum Information*, 3:46, Oct 2017. doi:10.1038/s41534-017-0046-y. URL `https://doi.org/10.1038/s41534-017-0046-y`.

[24] T. Brecht, M. Reagor, Y. Chu, W. Pfaff, C. Wang, L. Frunzio, M. H. Devoret, and R. J. Schoelkopf. Demonstration of superconducting micromachined cavities. *Applied Physics Letters*, 107(19):192603, 11 2015. doi:10.1063/1.4935541. URL `https://doi.org/10.1063/1.4935541`.

[25] Luke D. Burkhart, James D. Teoh, Yaxing Zhang, Christopher J. Axline, Luigi Frunzio, M.H. Devoret, Liang Jiang, S.M. Girvin, and R.J. Schoelkopf. Error-detected state transfer and entanglement in a superconducting quantum network. *PRX Quantum*, 2: 030321, Aug 2021. doi:10.1103/PRXQuantum.2.030321. URL `https://link.aps.org/doi/10.1103/PRXQuantum.2.030321`.

[26] Luke David Burkhart. *Error-Detected Networking for 3D Circuit Quantum Electrodynamics*. PhD thesis, Yale University, 2020. URL `https://rsl.yale.edu/sites/default/files/files/Luke%20Burkhart-Thesis-2020.pdf`.

[27] J. H. Busnaina, Z. Shi, A. McDonald, D. Dubyna, I. Nsanzineza, Jimmy S. C. Hung, C. W. Sandbo Chang, A. A. Clerk, and C. M. Wilson. Quantum simulation of the bosonic Kitaev chain. *arXiv*, 2023. URL `https://arxiv.org/abs/2309.06178`.

[28] W. Cai, J. Han, Feng Mei, Y. Xu, Y. Ma, X. Li, H. Wang, Y. P. Song, Zheng-Yuan Xue, Zhang-qi Yin, Suotang Jia, and Luyan Sun. Observation of topological magnon insulator states in a superconducting circuit. *Phys. Rev. Lett.*, 123:080501, Aug 2019. doi:10.1103/PhysRevLett.123.080501. URL `https://link.aps.org/doi/10.1103/PhysRevLett.123.080501`.

[29] G. Calajó and D. E. Chang. Emergence of solitons from many-body photon bound states in quantum nonlinear media. *Phys. Rev. Res.*, 4:023026, Apr 2022. doi:10.1103/PhysRevResearch.4.023026. URL `https://link.aps.org/doi/10.1103/PhysRevResearch.4.023026`.

[30] P. Campagne-Ibarcq, E. Zalys-Geller, A. Narla, S. Shankar, P. Reinhold, L. Burkhart, C. Axline, W. Pfaff, L. Frunzio, R. J. Schoelkopf, and M. H. Devoret. Deterministic remote entanglement of superconducting circuits through microwave two-photon transitions. *Phys. Rev. Lett.*, 120:200501, May 2018. doi:10.1103/PhysRevLett.120.200501. URL `https://link.aps.org/doi/10.1103/PhysRevLett.120.200501`.

[31] Iacopo Carusotto and Cristiano Ciuti. Quantum fluids of light. *Rev. Mod. Phys.*, 85: 299–366, Feb 2013. doi:10.1103/RevModPhys.85.299. URL `https://link.aps.org/doi/10.1103/RevModPhys.85.299`.

[32] Iacopo Carusotto, Andrew A Houck, Alicia J Kollár, Pedram Roushan, David I Schuster, and Jonathan Simon. Photonic materials in circuit quantum electrodynamics. *Nature Physics*, 16(3):268–279, 2020. doi:10.1038/s41567-020-0815-y. URL `https://doi.org/10.1038/s41567-020-0815-y`.

[33] Alexander Cerjan, Mohan Wang, Sheng Huang, Kevin P. Chen, and Mikael C. Rechtsman. Thouless pumping in disordered photonic systems. *Light: Science & Applications*, 9, Oct 2020. doi:10.1038/s41377-020-00408-2. URL `https://doi.org/10.1038/s41377-020-00408-2`.

[34] Srivatsan Chakram, Andrew E. Oriani, Ravi K. Naik, Akash V. Dixit, Kevin He, Ankur Agrawal, Hyeokshin Kwon, and David I. Schuster. Seamless high-$q$ microwave cavities for multimode circuit quantum electrodynamics. *Phys. Rev. Lett.*, 127:107701, Aug 2021. doi:10.1103/PhysRevLett.127.107701. URL `https://link.aps.org/doi/10.1103/PhysRevLett.127.107701`.

[35] Srivatsan Chakram, Kevin He, Akash V. Dixit, Andrew E. Oriani, Ravi K. Naik, Nelson Leung, Hyeokshin Kwon, Wen-Long Ma, Liang Jiang, and David I. Schuster. Multimode photon blockade. *Nature Physics*, 18, Aug 2022. doi:10.1038/s41567-022-01630-y. URL `https://doi.org/10.1038/s41567-022-01630-y`.

[36] Benjamin J. Chapman, Eric I. Rosenthal, Joseph Kerckhoff, Bradley A. Moores, Leila R. Vale, J. A. B. Mates, Gene C. Hilton, Kevin Lalumière, Alexandre Blais, and K. W. Lehnert. Widely tunable on-chip microwave circulator for superconducting quantum circuits. *Phys. Rev. X*, 7:041043, Nov 2017. doi:10.1103/PhysRevX.7.041043. URL `https://link.aps.org/doi/10.1103/PhysRevX.7.041043`.

[37] Udvas Chattopadhyay, Sunil Mittal, Mohammad Hafezi, and Y. D. Chong. Mode delocalization in disordered photonic Chern insulator. *Phys. Rev. B*, 103:214201, Jun 2021. doi:10.1103/PhysRevB.103.214201. URL `https://link.aps.org/doi/10.1103/PhysRevB.103.214201`.

[38] Wen-Jie Chen, Shao-Ji Jiang, Xiao-Dong Chen, Baocheng Zhu, Lei Zhou, Jian-Wen Dong, and C. T. Chan. Experimental realization of photonic topological insulator in a uniaxial metacrystal waveguide. *Nature Communications*, 5, Dec 2014. doi:10.1038/ncomms6782. URL `https://doi.org/10.1038/ncomms6782`.

[39] Xie Chen, Zheng-Cheng Gu, and Xiao-Gang Wen. Local unitary transformation, long-range quantum entanglement, wave function renormalization, and topological order. *Phys. Rev. B*, 82:155138, Oct 2010. doi:10.1103/PhysRevB.82.155138. URL `https://link.aps.org/doi/10.1103/PhysRevB.82.155138`.

[40] Xiaojun Cheng, Camille Jouvaud, Xiang Ni, S. Hossein Mousavi, Azriel Z. Genack, and Alexander B. Khanikaev. Robust reconfigurable electromagnetic pathways within a photonic topological insulator. *Nature Materials*, 15:542–548, May 2016. doi:10.1038/nmat4573. URL `https://doi.org/10.1038/nmat4573`.

[41] Jerry Moy Chow. *Quantum information processing with superconducting qubits*. PhD thesis, Yale University, 2010. URL `https://rsl.yale.edu/sites/default/files/files/RSL_Theses/jmcthesis.pdf`.

[42] J. I. Cirac, P. Zoller, H. J. Kimble, and H. Mabuchi. Quantum state transfer and entanglement distribution among distant nodes in a quantum network. *Phys. Rev. Lett.*, 78:3221–3224, Apr 1997. doi:10.1103/PhysRevLett.78.3221. URL `https://link.aps.org/doi/10.1103/PhysRevLett.78.3221`.

[43] J. Ignacio Cirac and Peter Zoller. Goals and opportunities in quantum simulation. *Nature Physics*, 8:264–266, Apr 2012. doi:10.1038/nphys2275. URL `https://doi.org/10.1038/nphys2275`.

[44] Roberta Citro and Monika Aidelsburger. Thouless pumping and topology. *Nature Reviews Physics*, 5:87–101, Feb 2023. doi:10.1038/s42254-022-00545-0. URL `https://doi.org/10.1038/s42254-022-00545-0`.

[45] Logan W. Clark, Nathan Schine, Claire Baum, Ningyuan Jia, and Jonathan Simon. Observation of Laughlin states made of light. *Nature*, 582:41–45, Jun 2020. doi:10.1038/s41586-020-2318-5. URL `https://doi.org/10.1038/s41586-020-2318-5`.

[46] N. R. Cooper. *Fractional quantum Hall states of bosons: properties and prospects for experimental realization*, pages 487–521. World Scientific, 2020. doi:10.1142/9789811217494_0010. URL `https://doi.org/10.1142/9789811217494_0010`.

[47] Andrew J. Daley, Immanuel Bloch, Christian Kokail, Stuart Flannigan, Natalie Pearson, Matthias Troyer, and Peter Zoller. Practical quantum advantage in quantum simulation. *Nature*, 670:667–676, Jul 2022. doi:10.1038/s41586-022-04940-6. URL `https://doi.org/10.1038/s41586-022-04940-6`.

[48] Daniele De Bernardis, Ze-Pei Cian, Iacopo Carusotto, Mohammad Hafezi, and Peter Rabl. Light-matter interactions in synthetic magnetic fields: Landau-photon polaritons. *Phys. Rev. Lett.*, 126:103603, Mar 2021. doi:10.1103/PhysRevLett.126.103603. URL `https://link.aps.org/doi/10.1103/PhysRevLett.126.103603`.

[49] Daniele De Bernardis, Francesco S. Piccioli, Peter Rabl, and Iacopo Carusotto. Chiral quantum optics in the bulk of photonic quantum hall systems. *PRX Quantum*, 4: 030306, Jul 2023. doi:10.1103/PRXQuantum.4.030306. URL `https://link.aps.org/doi/10.1103/PRXQuantum.4.030306`.

[50] C Dlaska, B Vermersch, and P Zoller. Robust quantum state transfer via topologically protected edge channels in dipolar arrays. *Quantum Science and Technology*, 2(1): 015001, jan 2017. doi:10.1088/2058-9565/2/1/015001. URL `https://dx.doi.org/10.1088/2058-9565/2/1/015001`.

[51] Avik Dutt, Qian Lin, Luqi Yuan, Momchil Minkov, Meng Xiao, and Shanhui Fan. A single photonic cavity with two independent physical synthetic dimensions. *Science*, 367(6473):59–64, 2020. doi:10.1126/science.aaz3071. URL `https://www.science.org/doi/abs/10.1126/science.aaz3071`.

[52] Matthew Elliott, Jaewoo Joo, and Eran Ginossar. Designing Kerr interactions using multiple superconducting qubit types in a single circuit. *New Journal of Physics*, 20 (2):023037, feb 2018. doi:10.1088/1367-2630/aa9243. URL `https://dx.doi.org/10.1088/1367-2630/aa9243`.

[53] Kejie Fang, Zongfu Yu, and Shanhui Fan. Realizing effective magnetic field for photons by controlling the phase of dynamic modulation. *Nature Photonics*, 6:782–787, Nov 2012. doi:10.1038/nphoton.2012.236. URL `https://doi.org/10.1038/nphoton.2012.236`.

[54] N. Fayard, L. Henriet, A. Asenjo-Garcia, and D. E. Chang. Many-body localization in waveguide quantum electrodynamics. *Phys. Rev. Res.*, 3:033233, Sep 2021. doi:10.1103/PhysRevResearch.3.033233. URL `https://link.aps.org/doi/10.1103/PhysRevResearch.3.033233`.

[55] Vinicius S. Ferreira, Gihwan Kim, Andreas Butler, Hannes Pichler, and Oskar Painter. Deterministic generation of multidimensional photonic cluster states with a single quantum emitter. *arXiv*, June 2022. doi:https://doi.org/10.48550/arXiv.2206.10076.

[56] Richard J. Fletcher, Airlia Shaffer, Cedric C. Wilson, Parth B. Patel, Zhenjie Yan, Valentin Crépel, Biswaroop Mukherjee, and Martin W. Zwierlein. Geometric squeezing into the lowest Landau level. *Science*, 372(6548):1318–1322, 2021. doi:10.1126/science.aba7202. URL `https://www.science.org/doi/abs/10.1126/science.aba7202`.

[57] A. Fragner, M. Göppl, J. M. Fink, M. Baur, R. Bianchetti, P. J. Leek, A. Blais, and A. Wallraff. Resolving vacuum fluctuations in an electrical circuit by measuring the Lamb shift. *Science*, 322:1357–1360, Nov 2008. doi:10.1126/science.1164482. URL `https://doi.org/10.1126/science.1164482`.

[58] N. E. Frattini, U. Vool, S. Shankar, A. Narla, K. M. Sliwa, and M. H. Devoret. 3-wave mixing Josephson dipole element. *Applied Physics Letters*, 110(22):222603, 05 2017. doi:10.1063/1.4984142. URL `https://doi.org/10.1063/1.4984142`.

[59] Nicholas Frattini. *Three-wave Mixing in Superconducting Circuits: Stabilizing Cats with SNAILs*. PhD thesis, Yale University, 2021. URL `https://elischolar.library.yale.edu/gsas_dissertations/332/`.

[60] Suhas Ganjam, Yanhao Wang, Yao Lu, Archan Banerjee, Chan U Lei, Lev Krayzman, Kim Kisslinger, Chenyu Zhou, Ruoshui Li, Yichen Jia, Mingzhao Liu, Luigi Frunzio, and Robert J. Schoelkopf. Surpassing millisecond coherence times in on-chip superconducting quantum memories by optimizing materials, processes, and circuit design, 2023.

[61] K. Geerlings, Z. Leghtas, I. M. Pop, S. Shankar, L. Frunzio, R. J. Schoelkopf, M. Mirrahimi, and M. H. Devoret. Demonstrating a driven reset protocol for a superconducting qubit. *Phys. Rev. Lett.*, 110:120501, Mar 2013. doi:10.1103/PhysRevLett.110.120501. URL `https://link.aps.org/doi/10.1103/PhysRevLett.110.120501`.

[62] Kurtis Lee Geerlings. *Improving coherence of superconducting qubits and resonators*. PhD thesis, Yale University, 2013. URL `https://www.proquest.com/docview/1495984234`.

[63] Sasan J. Ghaemsaidi, Michel Fruchart, and Severine Atis. Internal wave crystals. *arXiv:2111.07984*, 2021.

[64] Daniel Gottesman. Opportunities and challenges in fault-tolerant quantum computation. *arXiv:2210.15844*, 2022.

[65] Christian Gross and Immanuel Bloch. Quantum simulations with ultracold atoms in optical lattices. *Science*, 357(6355):995–1001, 2017. doi:10.1126/science.aal3837. URL `https://www.science.org/doi/abs/10.1126/science.aal3837`.

[66] M. Hafezi, S. Mittal, J. Fan, A. Migdall, and J. M. Taylor. Imaging topological edge states in silicon photonics. *Nature Photonics*, 7:1001–1005, Dec 2013. doi:10.1038/nphoton.2013.274. URL `https://doi.org/10.1038/nphoton.2013.274`.

[67] M. Hafezi, P. Adhikari, and J. M. Taylor. Chemical potential for light by parametric coupling. *Physical Review B*, 92:174305, Nov 2015. doi:10.1103/PhysRevB.92.174305. URL `http://link.aps.org/doi/10.1103/PhysRevB.92.174305`.

[68] Mohammad Hafezi, Eugene A. Demler, Mikhail D. Lukin, and Jacob M. Taylor. Robust optical delay lines with topological protection. *Nature Physics*, 7:907–912, Aug 2011. doi:10.1038/nphys2063. URL `https://www-nature-com.proxy.uchicago.edu/articles/nphys2063`.

[69] F. D. M. Haldane and S. Raghu. Possible realization of directional optical waveguides in photonic crystals with broken time-reversal symmetry. *Phys. Rev. Lett.*, 100:013904, Jan 2008. doi:10.1103/PhysRevLett.100.013904. URL `https://link.aps.org/doi/10.1103/PhysRevLett.100.013904`.

[70] Serge Haroche and Jean-Michel Raimond. *Exploring the Quantum: Atoms, Cavities, and Photons*. Oxford University Press, 2006. URL `https://doi-org.proxy.uchicago.edu/10.1093/acprof:oso/9780198509141.001.0001`.

[71] P. G. Harper. Single band motion of conduction electrons in a uniform magnetic field. *Proceedings of the Physical Society. Section A*, 68(10):874, Oct 1955. doi:10.1088/0370-1298/68/10/304. URL `https://dx.doi.org/10.1088/0370-1298/68/10/304`.

[72] M. Z. Hasan and C. L. Kane. Colloquium: Topological insulators. *Rev. Mod. Phys.*, 82:3045–3067, Nov 2010. doi:10.1103/RevModPhys.82.3045. URL `https://link.aps.org/doi/10.1103/RevModPhys.82.3045`.

[73] Douglas R. Hofstadter. Energy levels and wave functions of Bloch electrons in rational and irrational magnetic fields. *Phys. Rev. B*, 14:2239–2249, Sep 1976. doi:10.1103/PhysRevB.14.2239. URL `https://link.aps.org/doi/10.1103/PhysRevB.14.2239`.

[74] Andrew A. Houck, Hakan E. Türeci, and Jens Koch. On-chip quantum simulation with superconducting circuits. *Nature Physics*, 8:292–299, Apr 2012. doi:10.1038/nphys2251. URL `https://doi.org/10.1038/nphys2251`.

[75] Jimmy S. C. Hung, J. H. Busnaina, C. W. Sandbo Chang, A. M. Vadiraj, I. Nsanzineza, E. Solano, H. Alaeian, E. Rico, and C. M. Wilson. Quantum simulation of the bosonic Creutz ladder with a parametric cavity. *Phys. Rev. Lett.*, 127:100503, Sep 2021. doi:10.1103/PhysRevLett.127.100503. URL `https://link.aps.org/doi/10.1103/PhysRevLett.127.100503`.

[76] J. Ilves, S. Kono, Y. Sunada, S. Yamazaki, M. Kim, K. Koshino, and Y. Nakamura. On-demand generation and characterization of a microwave time-bin qubit. *npj Quantum Information*, 6, 2020. doi:10.1038/s41534-020-0266-4. URL `https://www.nature.com/articles/s41534-020-0266-4`.

[77] Mohsin Iqbal, Nathanan Tantivasadakarn, Ruben Verresen, Sara L. Campbell, Joan M. Dreiling, Caroline Figgatt, John P. Gaebler, Jacob Johansen, Michael Mills, Steven A. Moses, Juan M. Pino, Anthony Ransford, Mary Rowe, Peter Siegfried, Russell P. Stutz, Michael Foss-Feig, Ashvin Vishwanath, and Henrik Dreyer. Creation of non-Abelian topological order and anyons on a trapped-ion processor. *arXiv:2305.03766*, 2023.

[78] Ningyuan Jia, Clai Owens, Ariel Sommer, David Schuster, and Jonathan Simon. Time- and site-resolved dynamics in a topological circuit. *Physical Review X*, 5:021031, Jun 2015. doi:10.1103/PhysRevX.5.021031. URL `http://link.aps.org/doi/10.1103/PhysRevX.5.021031`.

[79] Chaitali Joshi, Frank Yang, and Mohammad Mirhosseini. Resonance fluorescence of a chiral artificial atom. *Phys. Rev. X*, 13:021039, Jun 2023. doi:10.1103/PhysRevX.13.021039. URL `https://link.aps.org/doi/10.1103/PhysRevX.13.021039`.

[80] Bharath Kannan, Max J. Ruckriegel, Daniel L. Campbell, Anton Frisk Kockum, Jochen Braumüller, David K. Kim, Morten Kjaergaard, Philip Krantz, Alexander Melville, Bethany M. Niedzielski, Antti Vepsäläinen, Roni Winik, Jonilyn L. Yoder, Franco Nori, Terry P. Orlando, Simon Gustavsson, and William D. Oliver. Waveguide quantum electrodynamics with superconducting artificial giant atoms. *Nature*, 583:775–779, July 2020. doi:10.1038/s41586-020-2529-9. URL `https://doi.org/10.1038/s41586-020-2529-9`.

[81] Bharath Kannan, Aziza Almanakly, Youngkyu Sung, Agustin di Paolo, David A. Rower, Jochen Braumüller, Alexander Melville, Bethany M. Niedzielski, Amir Karamlou, Kyle Serniak, Antti Vepsäläinen, Mollie E. Schwartz, Jonilyn L. Yoder, Roni Winik, Joel I-Jan Wang, Terry P. Orlando, Simon Gustavsson, Jeffrey A. Grover, and William D. Oliver. On-demand directional microwave photon emission using waveguide quantum electrodynamics. *Nature Physics*, 19:394–400, March 2023. doi:10.1038/s41567-022-01869-5. URL `https://doi.org/10.1038/s41567-022-01869-5`.

[82] Eliot Kapit, Mohammad Hafezi, and Steven H. Simon. Induced self-stabilization in fractional quantum Hall states of light. *Phys. Rev. X*, 4:031039, Sep 2014. doi:10.1103/PhysRevX.4.031039. URL `https://link.aps.org/doi/10.1103/PhysRevX.4.031039`.

[83] Amir H. Karamlou, Ilan T. Rosen, Sarah E. Muschinske, Cora N. Barrett, Agustin Di Paolo, Leon Ding, Patrick M. Harrington, Max Hays, Rabindra Das, David K. Kim, Bethany M. Niedzielski, Meghan Schuldt, Kyle Serniak, Mollie E. Schwartz, Jonilyn L. Yoder, Simon Gustavsson, Yariv Yanay, Jeffrey A. Grover, and William D. Oliver. Probing entanglement across the energy spectrum of a hard-core Bose-Hubbard lattice. *arXiv:2306.02571*, 2023.

[84] Eunjong Kim, Xueyue Zhang, Vinicius S. Ferreira, Jash Banker, Joseph K. Iverson, Alp Sipahigil, Miguel Bello, Alejandro González-Tudela, Mohammad Mirhosseini, and Oskar Painter. Quantum electrodynamics in a topological waveguide. *Phys. Rev. X*, 11:011015, Jan 2021. doi:10.1103/PhysRevX.11.011015. URL `https://link.aps.org/doi/10.1103/PhysRevX.11.011015`.

[85] H. J. Kimble. The quantum internet. *Nature*, 453, Jun 2008. doi:10.1038/nature07127. URL `https://doi.org/10.1038/nature07127`.

[86] A.Yu. Kitaev. Fault-tolerant quantum computation by anyons. *Annals of Physics*, 303 (1):2–30, 2003. ISSN 0003-4916. doi:https://doi.org/10.1016/S0003-4916(02)00018-0.

URL `https://www.sciencedirect.com/science/article/pii/S0003491602000180`.

[87] S. Klembt, T. H. Harder, O. A. Egorov, K. Winkler, R. Ge, M. A. Bandres, M. Emmerling, L. Worschech, T. C. H. Liew, M. Segev, C. Schneider, and S. Höfling. Exciton-polariton topological insulator. *Nature*, 562, Oct 2018. doi:10.1038/s41586-018-0601-5. URL `https://doi.org/10.1038/s41586-018-0601-5`.

[88] Jens Koch, Terri M. Yu, Jay Gambetta, A. A. Houck, D. I. Schuster, J. Majer, Alexandre Blais, M. H. Devoret, S. M. Girvin, and R. J. Schoelkopf. Charge-insensitive qubit design derived from the cooper pair box. *Phys. Rev. A*, 76:042319, Oct 2007. doi:10.1103/PhysRevA.76.042319. URL `https://link.aps.org/doi/10.1103/PhysRevA.76.042319`.

[89] Jens Koch, Andrew A. Houck, Karyn Le Hur, and S. M. Girvin. Time-reversal-symmetry breaking in circuit-QED-based photon lattices. *Phys. Rev. A*, 82:043811, Oct 2010. doi:10.1103/PhysRevA.82.043811. URL `https://link.aps.org/doi/10.1103/PhysRevA.82.043811`.

[90] Yaacov E. Kraus, Yoav Lahini, Zohar Ringel, Mor Verbin, and Oded Zilberberg. Topological states and adiabatic pumping in quasicrystals. *Phys. Rev. Lett.*, 109:106402, Sep 2012. doi:10.1103/PhysRevLett.109.106402. URL `https://link.aps.org/doi/10.1103/PhysRevLett.109.106402`.

[91] P. Kurpiers, P. Magnard, T. Walter, B. Royer, M. Pechal, J. Heinsoo, Y. Salathé, A. Akin, S. Storz, J.-C. Besse, S. Gasparinetti, A. Blais, and A. Wallraff. Deterministic quantum state transfer and remote entanglement using microwave photons. *Nature*, 558, 2018. doi:10.1038/s41586-018-0195-y. URL `https://doi.org/10.1038/s41586-018-0195-y`.

[92] P. Kurpiers, M. Pechal, B. Royer, P. Magnard, T. Walter, J. Heinsoo, Y. Salathé, A. Akin, S. Storz, J.-C. Besse, S. Gasparinetti, A. Blais, and A. Wallraff. Quantum communication with time-bin encoded microwave photons. *Phys. Rev. Appl.*, 12:044067, Oct 2019. doi:10.1103/PhysRevApplied.12.044067. URL `https://link.aps.org/doi/10.1103/PhysRevApplied.12.044067`.

[93] Roman Kuzmin, Nitish Mehta, Nicholas Grabon, Raymond Mencia, and Vladimir E. Manucharyan. Superstrong coupling in circuit quantum electrodynamics. *npj Quantum Information*, 5, Feb 2019. doi:10.1038/s41534-019-0134-2. URL `https://doi.org/10.1038/s41534-019-0134-2`.

[94] Dany Lachance-Quirion, Marc-Antoine Lemonde, Jean Olivier Simoneau, Lucas St-Jean, Pascal Lemieux, Sara Turcotte, Wyatt Wright, Amélie Lacroix, Joëlle Fréchette-Viens, Ross Shillito, Florian Hopfmueller, Maxime Tremblay, Nicholas E. Frattini, Julien Camirand Lemyre, and Philippe St-Jean. Autonomous quantum error correction of Gottesman-Kitaev-Preskill states. *arXiv:2310.11400*, 2023.

[95] Willis E. Lamb and Robert C. Retherford. Fine structure of the hydrogen atom by a microwave method. *Phys. Rev.*, 72:241–243, Aug 1947. doi:10.1103/PhysRev.72.241. URL `https://link.aps.org/doi/10.1103/PhysRev.72.241`.

[96] José Lebreuilly, Alberto Biella, Florent Storme, Davide Rossini, Rosario Fazio, Cristiano Ciuti, and Iacopo Carusotto. Stabilizing strongly correlated photon fluids with non-Markovian reservoirs. *Phys. Rev. A*, 96:033828, Sep 2017. doi:10.1103/PhysRevA.96.033828. URL `https://link.aps.org/doi/10.1103/PhysRevA.96.033828`.

[97] Daniel Lechner, Riccardo Pennetta, Martin Blaha, Philipp Schneeweiss, Arno Rauschenbeutel, and Jürgen Volz. Light-matter interaction at the transition between cavity and waveguide QED. *arXiv:2302.07161*, 2023.

[98] Nathan R. A. Lee, Marek Pechal, E. Alex Wollack, Patricio Arrangoiz-Arriola, Zhaoyou Wang, and Amir H. Safavi-Naeni. Propagation of microwave photons along a synthetic dimension. *Phys. Rev. A*, 101:053807, May 2020. doi:10.1103/PhysRevA.101.053807. URL `https://link.aps.org/doi/10.1103/PhysRevA.101.053807`.

[99] Z. Leghtas, S. Touzard, I. M. Pop, A. Kou, B. Vlastakis, A. Petrenko, K. M. Sliwa, A. Narla, S. Shankar, M. J. Hatridge, M. Reagor, L. Frunzio, R. J. Schoelkopf, M. Mirrahimi, and M. H. Devoret. Confining the state of light to a quantum manifold by engineered two-photon loss. *Science*, 347(6224):853–857, 2015. doi:10.1126/science.aaa2085. URL `https://www.science.org/doi/abs/10.1126/science.aaa2085`.

[100] N. Leung, Y. Lu, S. Chakram, R. K. Naik, N. Earnest, R. Ma, K. Jacobs, A. N. Cleland, and D. I. Schuster. Deterministic bidirectional communication and remote entanglement generation between superconducting qubits. *npj Quantum Information*, 5, Feb 2019. doi:10.1038/s41534-019-0128-0. URL `https://doi.org/10.1038/s41534-019-0128-0`.

[101] Yanbing Liu and Andrew A. Houck. Quantum electrodynamics near a photonic bandgap. *Nature Physics*, 13:48–52, Jan 2017. doi:10.1038/nphys3834. URL `https://doi.org/10.1038/nphys3834`.

[102] Peter Lodahl, Sahand Mahmoodian, Søren Stobbe, Arno Rauschenbeutel, Philipp Schneeweiss, Jürgen Volz, Hannes Pichler, and Peter Zoller. Chiral quantum optics. *Nature*, 541, Jan 2017. doi:10.1038/nature21037. URL `https://doi.org/10.1038/nature21037`.

[103] Ling Lu, John D. Joannopoulos, and Marin Soljačić. Topological photonics. *Nature Photonics*, 8:821–829, Nov 2014. doi:https://doi.org/10.1038/nphoton.2014.248. URL `https://doi.org/10.1038/nphoton.2014.248`.

[104] Yao Lu, Aniket Maiti, John W. O. Garmon, Suhas Ganjam, Yaxing Zhang, Jahan Claes, Luigi Frunzio, Steven M. Girvin, and Robert J. Schoelkopf. High-fidelity parametric beamsplitting with a parity-protected converter. *Nature Communications*, Sep 2023. doi:10.1038/s41467-023-41104-0. URL `https://doi.org/10.1038/s41467-023-41104-0`.

[105] Yuehui Lu, Ningyuan Jia, Lin Su, Clai Owens, Gediminas Juzeliūnas, David I Schuster, and Jonathan Simon. Probing the Berry curvature and Fermi arcs of a Weyl circuit. *Physical Review B*, 99(2):020302, 2019. doi:10.1103/PhysRevB.99.020302. URL `https://link.aps.org/doi/10.1103/PhysRevB.99.020302`.

[106] Daniil M. Lukin, Melissa A. Guidry, Joshua Yang, Misagh Ghezellou, Sattwik Deb Mishra, Hiroshi Abe, Takeshi Ohshima, Jawad Ul-Hassan, and Jelena Vučković. Two-emitter multimode cavity quantum electrodynamics in thin-film silicon carbide photonics. *Phys. Rev. X*, 13:011005, Jan 2023. doi:10.1103/PhysRevX.13.011005. URL `https://link.aps.org/doi/10.1103/PhysRevX.13.011005`.

[107] Eran Lustig, Steffen Weimann, Yonatan Plotnik, Yaakov Lumer, Miguel A. Bandres, Alexander Szameit, and Mordechai Segev. Photonic topological insulator in synthetic dimensions. *Nature*, 567(7748), Mar 2019. doi:10.1038/s41586-019-0943-7. URL `https://doi.org/10.1038/s41586-019-0943-7`.

[108] Julian Léonard, Sooshin Kim, Joyce Kwan, Perrin Segura, Fabian Grusdt, Cécile Repellin, Nathan Goldman, and Markus Greiner. Realization of a fractional quantum Hall state with ultracold atoms. *Nature*, 619:495–499, Jul 2023. doi:10.1038/s41586-023-06122-4. URL `https://doi.org/10.1038/s41586-023-06122-4`.

[109] Ruichao Ma, Clai Owens, Andrew Houck, David I. Schuster, and Jonathan Simon. Autonomous stabilizer for incompressible photon fluids and solids. *Phys. Rev. A*, 95:043811, Apr 2017. doi:10.1103/PhysRevA.95.043811. URL `https://link.aps.org/doi/10.1103/PhysRevA.95.043811`.

[110] Ruichao Ma, Brendan Saxberg, Clai Owens, Nelson Leung, Yao Lu, Jonathan Simon, and David I Schuster. A dissipatively stabilized Mott insulator of photons. *Nature*, 566(7742):51–57, 2019.

[111] Lukas J. Maczewsky, Julia M. Zeuner, Stefan Nolte, and Alexander Szameit. Observation of photonic anomalous Floquet topological insulators. *Nature Communications*, 8:13756, Jan 2017. doi:10.1038/ncomms13756. URL `https://doi.org/10.1038/ncomms13756`.

[112] P. Magnard, P. Kurpiers, B. Royer, T. Walter, J.-C. Besse, S. Gasparinetti, M. Pechal, J. Heinsoo, S. Storz, A. Blais, and A. Wallraff. Fast and unconditional all-microwave reset of a superconducting qubit. *Phys. Rev. Lett.*, 121:060502, Aug 2018. doi:10.1103/PhysRevLett.121.060502. URL `https://link.aps.org/doi/10.1103/PhysRevLett.121.060502`.

[113] Sahand Mahmoodian, Giuseppe Calajó, Darrick E. Chang, Klemens Hammerer, and Anders S. Sørensen. Dynamics of many-body photon bound states in chiral waveguide qed. *Phys. Rev. X*, 10:031011, Jul 2020. doi:10.1103/PhysRevX.10.031011. URL `https://link.aps.org/doi/10.1103/PhysRevX.10.031011`.

[114] Joseph D. Martin. What's in a name change? *Physics in Perspective*, 17:3–32, Mar 2015. doi:10.1007/s00016-014-0151-7. URL `https://doi.org/10.1007/s00016-014-0151-7`.

[115] Joseph D. Martin. When condensed-matter physics became king. *Physics Today*, 72(1): 30–37, 01 2019. doi:10.1063/PT.3.4110. URL `https://doi.org/10.1063/PT.3.4110`.

[116] Jeronimo G. C. Martinez, Christie S. Chiu, Basil M. Smitham, and Andrew A. Houck. Flat-band localization and interaction-induced delocalization of photons. *arXiv:2303.02170*, 2023.

[117] Joaquin Medina Dueñas, Gabriel O'Ryan Pérez, Carla Hermann-Avigliano, and Luis E. F. Foa Torres. Quadrature protection of squeezed states in a one-dimensional photonic topological insulator. *Quantum*, 5:526, August 2021. ISSN 2521-327X. doi:10.22331/q-2021-08-17-526. URL `https://doi.org/10.22331/q-2021-08-17-526`.

[118] D Meiser and P Meystre. Superstrong coupling regime of cavity quantum electrodynamics. *Physical Review A*, 74(6):065801, 2006.

[119] Joaquín Minguzzi, Zijie Zhu, Kilian Sandholzer, Anne-Sophie Walter, Konrad Viebahn, and Tilman Esslinger. Topological pumping in a Floquet-Bloch band. *Phys. Rev. Lett.*, 129:053201, Jul 2022. doi:10.1103/PhysRevLett.129.053201. URL `https://link.aps.org/doi/10.1103/PhysRevLett.129.053201`.

[120] R. Mitsch, C. Sayrin, B. Albrecht, P. Schneeweiss, and A. Rauschenbeutel. Quantum state-controlled directional spontaneous emission of photons into a nanophotonic waveguide. *Nature Communications*, 5, Dec 2014. doi:10.1038/ncomms6713. URL `https://doi.org/10.1038/ncomms6713`.

[121] S. Mittal, J. Fan, S. Faez, A. Migdall, J. M. Taylor, and M. Hafezi. Topologically robust transport of photons in a synthetic gauge field. *Phys. Rev. Lett.*, 113:087403, Aug 2014. doi:10.1103/PhysRevLett.113.087403. URL `https://link.aps.org/doi/10.1103/PhysRevLett.113.087403`.

[122] Sunil Mittal, Venkata Vikram Orre, and Mohammad Hafezi. Topologically robust transport of entangled photons in a 2D photonic system. *Opt. Express*, 24(14):15631–15641, Jul 2016. doi:10.1364/OE.24.015631. URL `https://opg.optica.org/oe/abstract.cfm?URI=oe-24-14-15631`.

[123] Sunil Mittal, Elizabeth A. Goldschmidt, and Mohammad Hafezi. A topological source of quantum light. *Nature*, 561:502–506, Sep 2018. doi:10.1038/s41586-018-0478-3. URL `https://doi.org/10.1038/s41586-018-0478-3`.

[124] Hirokazu Miyake, Georgios A. Siviloglou, Colin J. Kennedy, William Cody Burton, and Wolfgang Ketterle. Realizing the Harper Hamiltonian with laser-assisted tunneling in optical lattices. *Phys. Rev. Lett.*, 111:185302, Oct 2013. doi:10.1103/PhysRevLett.111.185302. URL `https://link.aps.org/doi/10.1103/PhysRevLett.111.185302`.

[125] David Morin. Waves (draft), Accessed 2023. URL `https://scholar.harvard.edu/david-morin/waves`. Online mansucript.

[126] Biswaroop Mukherjee, Airlia Shaffer, Parth B. Patel, Zhenjie Yan, Cedric C. Wilson, Valentin Crépel, Richard J. Fletcher, and Martin Zwierlein. Crystallization of bosonic quantum Hall states in a rotating quantum gas. *Nature*, 601:58–62, Jan 2022. doi:10.1038/s41586-021-04170-2. URL `https://doi.org/10.1038/s41586-021-04170-2`.

[127] Sebabrata Mukherjee and Mikael C. Rechtsman. Observation of Floquet solitons in a topological bandgap. *Science*, 368(6493):856–859, 2020. doi:10.1126/science.aba8725. URL `https://www.science.org/doi/abs/10.1126/science.aba8725`.

[128] Mahdi Naghiloo. *Exploring quantum dynamics and thermodynamics in superconducting circuits*. PhD thesis, Washington University in St. Louis, 2019. URL `https://doi.org/10.7936/mxyg-yr40`.

[129] A. Narla, S. Shankar, M. Hatridge, Z. Leghtas, K. M. Sliwa, E. Zalys-Geller, S. O. Mundhada, W. Pfaff, L. Frunzio, R. J. Schoelkopf, and M. H. Devoret. Robust concurrent remote entanglement between two superconducting qubits. *Phys. Rev. X*, 6:031036, Sep 2016. doi:10.1103/PhysRevX.6.031036. URL `https://link.aps.org/doi/10.1103/PhysRevX.6.031036`.

[130] Rohit Navarathna, Dat Thanh Le, Andrés Rosario Hamann, Hien Duy Nguyen, Thomas M. Stace, and Arkady Fedorov. Passive superconducting circulator on a chip. *Phys. Rev. Lett.*, 130:037001, Jan 2023. doi:10.1103/PhysRevLett.130.037001. URL `https://link.aps.org/doi/10.1103/PhysRevLett.130.037001`.

[131] Chetan Nayak, Steven H. Simon, Ady Stern, Michael Freedman, and Sankar Das Sarma. Non-Abelian anyons and topological quantum computation. *Rev. Mod. Phys.*, 80:1083–1159, Sep 2008. doi:10.1103/RevModPhys.80.1083. URL `https://link.aps.org/doi/10.1103/RevModPhys.80.1083`.

[132] Simon E. Nigg, Hanhee Paik, Brian Vlastakis, Gerhard Kirchmair, S. Shankar, Luigi Frunzio, M. H. Devoret, R. J. Schoelkopf, and S. M. Girvin. Black-box superconducting circuit quantization. *Physical Review Letters*, 108:240502, Jun 2012. doi:10.1103/PhysRevLett.108.240502. URL `https://link.aps.org/doi/10.1103/PhysRevLett.108.240502`.

[133] T. E. Northup and R. Blatt. Quantum information transfer using photons. *Nature Photonics*, 8:356–363, May 2014. doi:10.1038/nphoton.2014.53. URL `https://doi.org/10.1038/nphoton.2014.53`.

[134] Lukas Novotny. Strong coupling, energy splitting, and level crossings: A classical perspective. *American Journal of Physics*, 78(11):1199–1202, 11 2010. ISSN 0002-9505. doi:10.1119/1.3471177. URL `https://doi.org/10.1119/1.3471177`.

[135] Andrew Enrique Oriani. *Multimodal and ultra high-Q superconducting niobium cavities for circuit quantum electrodynamics*. PhD thesis, University of Chicago, 2022. URL `https://schusterlab.stanford.edu/static/pdfs/Oriani_Thesis.pdf`.

[136] Yasutomo Ota, Kenta Takata, Tomoki Ozawa, Alberto Amo, Zhetao Jia, Boubacar Kante, Masaya Notomi, Yasuhiko Arakawa, and Satoshi Iwamoto. Active topological photonics. *Nanophotonics*, 9(3):547–567, 2020. doi:10.1515/nanoph-2019-0376. URL `https://doi.org/10.1515/nanoph-2019-0376`.

[137] Clai Owens. *Creating quantum topological materials with 3D microwave photons*. PhD thesis, University of Chicago, 2019. URL `https://schusterlab.stanford.edu/static/pdfs/Owens_Thesis.pdf`.

[138] Clai Owens, Aman LaChapelle, Brendan Saxberg, Brandon M. Anderson, Ruichao Ma, Jonathan Simon, and David I. Schuster. Quarter-flux Hofstadter lattice in a qubit-compatible microwave cavity array. *Phys. Rev. A*, 97:013818, Jan 2018. doi:10.1103/PhysRevA.97.013818. URL `https://link.aps.org/doi/10.1103/PhysRevA.97.013818`.

[139] John Clai Owens, Margaret G. Panetta, Brendan Saxberg, Gabrielle Roberts, Srivatsan Chakram, Ruichao Ma, Andrei Vrajitoarea, Jonathan Simon, and David I. Schuster. Chiral cavity quantum electrodynamics. *Nature Physics*, 18, Jul 2022. doi:10.1038/s41567-022-01671-3. URL `https://doi.org/10.1038/s41567-022-01671-3`.

[140] Tomoki Ozawa, Hannah M. Price, Alberto Amo, Nathan Goldman, Mohammad Hafezi, Ling Lu, Mikael C. Rechtsman, David Schuster, Jonathan Simon, Oded Zilberberg, and Iacopo Carusotto. Topological photonics. *Rev. Mod. Phys.*, 91:015006, Mar 2019. doi:10.1103/RevModPhys.91.015006. URL `https://link.aps.org/doi/10.1103/RevModPhys.91.015006`.

[141] Hanhee Paik, D. I. Schuster, Lev S. Bishop, G. Kirchmair, G. Catelani, A. P. Sears, B. R. Johnson, M. J. Reagor, L. Frunzio, L. I. Glazman, S. M. Girvin, M. H. Devoret, and R. J. Schoelkopf. Observation of high coherence in Josephson junction qubits measured in a three-dimensional circuit QED architecture. *Phys. Rev. Lett.*, 107:240501, Dec 2011. doi:10.1103/PhysRevLett.107.240501. URL `https://link.aps.org/doi/10.1103/PhysRevLett.107.240501`.

[142] Margaret G. Panetta, Andrei Vrajitoarea, Gabrielle Roberts, John Clai Owens, Jonathan Simon, and David I. Schuster. Chiral transport between quantum emitters in a topological photonic metamaterial. Forthcoming, 2023.

[143] Vittorio Peano, Martin Houde, Christian Brendel, Florian Marquardt, and Aashish A. Clerk. Topological phase transitions and chiral inelastic transport induced by the squeezing of light. *Nature Communications*, 7, Mar 2016. doi:10.1038/ncomms10779. URL `https://doi.org/10.1038/ncomms10779`.

[144] Vittorio Peano, Martin Houde, Florian Marquardt, and Aashish A. Clerk. Topological quantum fluctuations and traveling wave amplifiers. *Phys. Rev. X*, 6:041026, Nov 2016. doi:10.1103/PhysRevX.6.041026. URL `https://link.aps.org/doi/10.1103/PhysRevX.6.041026`.

[145] M. Pechal, L. Huthmacher, C. Eichler, S. Zeytinoğlu, Jr. A. A. Abdumalikov, S. Berger, A. Wallraff, and S. Filipp. Microwave-controlled generation of shaped single photons in circuit quantum electrodynamics. *Physical Review X*, 4, Oct 2022. doi:10.1103/PhysRevX.4.041010.

[146] J. Perczel, J. Borregaard, D. E. Chang, S. F. Yelin, and M. D. Lukin. Topological quantum optics using atomlike emitter arrays coupled to photonic crystals. *Phys. Rev. Lett.*, 124:083603, Feb 2020. doi:10.1103/PhysRevLett.124.083603. URL `https://link.aps.org/doi/10.1103/PhysRevLett.124.083603`.

[147] Jan Petersen, Jurgen Volz, and Arno Rauschenbeutel. Chiral nanophotonic waveguide interface based on spin-orbit interaction of light. *Science*, 346(6205):67–71, Sep 2014. doi:10.1126/science.1257671. URL `https://www-science-org.proxy.uchicago.edu/doi/10.1126/science.1257671`.

[148] Hannes Pichler, Tomás Ramos, Andrew J. Daley, and Peter Zoller. Quantum optics of chiral spin networks. *Phys. Rev. A*, 91:042116, Apr 2015. doi:10.1103/PhysRevA.91.042116. URL `https://link.aps.org/doi/10.1103/PhysRevA.91.042116`.

[149] Hannes Pichler, Soonwon Choi, Peter Zoller, and Mikhail D. Lukin. Universal photonic quantum computation via time-delayed feedback. *PNAS*, 114, Oct 2017. doi:10.1073/pnas.1711003114. URL `https://doi.org/10.1073/pnas.1711003114`.

[150] Harris Pirie, Shuvom Sadhuka, Jennifer Wang, Radu Andrei, and Jennifer E. Hoffman. Topological phononic logic. *Phys. Rev. Lett.*, 128:015501, Jan 2022. doi:10.1103/PhysRevLett.128.015501. URL `https://link.aps.org/doi/10.1103/PhysRevLett.128.015501`.

[151] Andrew Pocklington, Yu-Xin Wang, and A. A. Clerk. Dissipative pairing interactions: Quantum instabilities, topological light, and volume-law entanglement. *Phys. Rev. Lett.*, 130:123602, Mar 2023. doi:10.1103/PhysRevLett.130.123602. URL `https://link.aps.org/doi/10.1103/PhysRevLett.130.123602`.

[152] Alexander V. Poshakinskiy, Janet Zhong, Yongguan Ke, Nikita A. Olekhno, Chaohong Lee, Yuri S. Kivshar, and Alexander S. Poddubny. Quantum hall phases emerging from atom–photon interactions. *npj Quantum Information*, 7, Feb 2021. doi:10.1038/s41534-021-00372-8. URL `https://www-nature-com.proxy.uchicago.edu/articles/s41534-021-00372-8`.

[153] Adarsh S. Prasad, Jakob Hinney, Sahand Mahmoodian, Klemens Hammerer, Samuel Rind, Philipp Schneeweiss, Anders S. Sørensen, Jürgen Volz, and Arno Rauschenbeutel. Correlating photons using the collective nonlinear response of atoms weakly coupled to an optical mode. *Nature Photonics*, 14:719–722, Dec 2020. doi:10.1038/s41566-020-0692-z. URL `https://doi.org/10.1038/s41566-020-0692-z`.

[154] John Preskill. Quantum Computing in the NISQ era and beyond. *Quantum*, 2:79, Aug 2018. doi:10.22331/q-2018-08-06-79. URL `https://doi.org/10.22331/q-2018-08-06-79`.

[155] Hannah Price, Yidong Chong, Alexander Khanikaev, Henning Schomerus, Lukas J Maczewsky, Mark Kremer, Matthias Heinrich, Alexander Szameit, Oded Zilberberg, Yihao Yang, Baile Zhang, Andrea Alù, Ronny Thomale, Iacopo Carusotto, Philippe St-Jean, Alberto Amo, Avik Dutt, Luqi Yuan, Shanhui Fan, Xuefan Yin, Chao Peng, Tomoki Ozawa, and Andrea Blanco-Redondo. Roadmap on topological photonics. *Journal of Physics: Photonics*, 4(3):032501, Jun 2022. doi:10.1088/2515-7647/ac4ee4. URL `https://dx.doi.org/10.1088/2515-7647/ac4ee4`.

[156] Javier Puertas Martínez, Sébastien Léger, Nicolas Gheeraert, Rémy Dassonneville, Luca Planat, Farshad Foroughi, Yuriy Krupko, Olivier Buisson, Cécile Naud, Wiebke Hasch-Guichard, Serge Florens, Izak Snyman, and Nicolas Roch. A tunable Josephson platform to explore many-body quantum optics in circuit-QED. *npj Quantum Information*, 5, Feb 2019. doi:10.1038/s41534-018-0104-0. URL `https://doi.org/10.1038/s41534-018-0104-0`.

[157] S. Raghu and F. D. M. Haldane. Analogs of quantum-Hall-effect edge states in photonic crystals. *Phys. Rev. A*, 78:033834, Sep 2008. doi:10.1103/PhysRevA.78.033834. URL `https://link.aps.org/doi/10.1103/PhysRevA.78.033834`.

[158] Tomás Ramos, Hannes Pichler, Andrew J. Daley, and Peter Zoller. Quantum spin dimers from chiral dissipation in cold-atom chains. *Phys. Rev. Lett.*, 113:237203, Dec 2014. doi:10.1103/PhysRevLett.113.237203. URL `https://link.aps.org/doi/10.1103/PhysRevLett.113.237203`.

[159] R Raussendorf, J Harrington, and K Goyal. Topological fault-tolerance in cluster state quantum computation. *New Journal of Physics*, 9(6):199, Jun 2007. doi:10.1088/1367-2630/9/6/199. URL `https://dx.doi.org/10.1088/1367-2630/9/6/199`.

[160] Robert Raussendorf, Daniel E. Browne, and Hans J. Briegel. Measurement-based quantum computation on cluster states. *Phys. Rev. A*, 68:022312, Aug 2003.

doi:10.1103/PhysRevA.68.022312. URL `https://link.aps.org/doi/10.1103/PhysRevA.68.022312`.

[161] Matthew Reagor, Hanhee Paik, Gianluigi Catelani, Luyan Sun, Christopher Axline, Eric Holland, Ioan M. Pop, Nicholas A. Masluk, Teresa Brecht, Luigi Frunzio, Michel H. Devoret, Leonid Glazman, and Robert J. Schoelkopf. Reaching 10ms single photon lifetimes for superconducting aluminum cavities. *Applied Physics Letters*, 102(19): 192604, 05 2013. doi:10.1063/1.4807015. URL `https://doi.org/10.1063/1.4807015`.

[162] Matthew Reagor, Wolfgang Pfaff, Christopher Axline, Reinier W. Heeres, Nissim Ofek, Katrina Sliwa, Eric Holland, Chen Wang, Jacob Blumoff, Kevin Chou, Michael J. Hatridge, Luigi Frunzio, Michel H. Devoret, Liang Jiang, and Robert J. Schoelkopf. Quantum memory with millisecond coherence in circuit QED. *Phys. Rev. B*, 94:014506, Jul 2016. doi:10.1103/PhysRevB.94.014506. URL `https://link.aps.org/doi/10.1103/PhysRevB.94.014506`.

[163] Matthew James Reagor. *Superconducting cavities for circuit quantum electrodynamics*. PhD thesis, Yale University, 2015. URL `https://rsl.yale.edu/sites/default/files/files/RSL_Theses/reagor-thesis-20151202.pdf`.

[164] Mikael C. Rechtsman, Julia M. Zeuner, Yonatan Plotnik, Yaakov Lumer, Daniel Podolsky, Felix Dreisow, Stefan Nolte, Mordechai Segev, and Alexander Szameit. Photonic Floquet topological insulators. *Nature*, 496:196–200, Apr 2013. doi:10.1038/nature12066. URL `https://doi.org/10.1038/nature12066`.

[165] Elena S. Redchenko, Alexander V. Poshakinskiy, Riya Sett, Martin Žemlička, Alexander N. Poddubny, and Johannes M. Fink. Tunable directional photon scattering from a pair of superconducting qubits. *Nature Communications*, 14, May 2023. doi:10.1038/s41467-023-38761-6. URL `https://doi.org/10.1038/s41467-023-38761-6`.

[166] Matthew David Reed. *Entanglement and quantum error correction with superconducting qubits*. PhD thesis, Yale University, 2013. URL `https://arxiv.org/abs/1311.6759`.

[167] Kevin Reuer, Jean-Claude Besse, Lucien Wernli, Paul Magnard, Philipp Kurpiers, Graham J. Norris, Andreas Wallraff, and Christopher Eichler. Realization of a universal quantum gate set for itinerant microwave photons. *Phys. Rev. X*, 12:011008, Jan 2022. doi:10.1103/PhysRevX.12.011008. URL `https://link.aps.org/doi/10.1103/PhysRevX.12.011008`.

[168] Gabrielle Roberts, Andrei Vrajitoarea, Brendan Saxberg, Margaret G. Panetta, Jonathan Simon, and David I. Schuster. Manybody interferometry of quantum fluids. *arXiv*, Sep 2023. doi:10.48550/arXiv.2309.05727. URL `https://doi.org/10.48550/arXiv.2309.05727`.

[169] Gabrielle L. C. Roberts. *Quantum fluids in a Bose-Hubbard circuit*. PhD thesis, University of Chicago, Dec 2023. Forthcoming.

[170] P. Roushan, C. Neill, A. Megrant, Y. Chen, R. Babbush, R. Barends, B. Campbell, Z. Chen, B. Chiaro, A. Dunsworth, A. Fowler, E. Jeffrey, J. Kelly, E. Lucero, J. Mutus, P. J. J. O'Malley, M. Neeley, C. Quintana, D. Sank, A. Vainsencher, J. Wenner, T. White, E. Kapit, H. Neven, and J. Martinis. Chiral ground-state currents of interacting photons in a synthetic magnetic field. *Nature Physics*, 13, Feb 2017. doi:10.1038/nphys3930. URL `https://doi.org/10.1038/nphys3930`.

[171] P. Roushan, C. Neill, J. Tangpanitanon, V. M. Bastidas, A. Megrant, R. Barends, Y. Chen, Z. Chen, B. Chiaro, A. Dunsworth, A. Fowler, B. Foxen, M. Giustina, E. Jeffrey, J. Kelly, E. Lucero, J. Mutus, M. Neeley, C. Quintana, D. Sank, A. Vainsencher, J. Wenner, T. White, H. Neven, D. G. Angelakis, and J. Martinis. Spectroscopic signatures of localization with interacting photons in superconducting qubits. *Science*, 358(6367):1175–1179, 2017. doi:10.1126/science.aao1401. URL `https://www.science.org/doi/abs/10.1126/science.aao1401`.

[172] Brendan Saxberg, Andrei Vrajitoarea, Gabrielle Roberts, Margaret G. Panetta, Jonathan Simon, and David I. Schuster. Disorder-assisted assembly of strongly correlated fluids of light. *Nature*, 612:435–441, Dec 2022. doi:10.1038/s41586-022-05357-x. URL `https://doi.org/10.1038/s41586-022-05357-x`.

[173] Nathan Schine, Albert Ryou, Andrey Gromov, Ariel Sommer, and Jonathan Simon. Synthetic Landau levels for photons. *Nature*, 534:671–675, Jun 2016. doi:10.1038/nature17943. URL `https://doi.org/10.1038/nature17943`.

[174] David Isaac Schuster. *Circuit quantum electrodynamics*. PhD thesis, Yale University, 2007. URL `https://www.proquest.com/dissertations-theses/circuit-quantum-electrodynamics/docview/304783718/se-2`.

[175] DI Schuster, Andrew Addison Houck, JA Schreier, A Wallraff, JM Gambetta, A Blais, L Frunzio, J Majer, B Johnson, MH Devoret, et al. Resolving photon number states in a superconducting circuit. *Nature*, 445(7127):515–518, 2007.

[176] Matteo Seclì, Tomoki Ozawa, Massimo Capone, and Iacopo Carusotto. Spatial and spectral mode-selection effects in topological lasers with frequency-dependent gain. *APL Photonics*, 6(5):050803, 05 2021. ISSN 2378-0967. doi:10.1063/5.0041124. URL `https://doi.org/10.1063/5.0041124`.

[177] Maksym Serbyn, Dmitry A. Abanin, and Zlatko Papić. Quantum many-body scars and weak breaking of ergodicity. *Nature Physics*, 17:675–685, Jun 2021. doi:10.1038/s41567-021-01230-2. URL `https://doi.org/10.1038/s41567-021-01230-2`.

[178] Suraj Shankar, Anton Souslov, Mark J. Bowick, M. Cristina Marchetti, and Vincenzo Vitelli. Topological active matter. *Nature Reviews Physics*, 4:380–398, Jun 2022.

doi:10.1038/s42254-022-00445-3. URL `https://doi.org/10.1038/s42254-022-00445-3`.

[179] Alexandra S. Sheremet, Mihail I. Petrov, Ivan V. Iorsh, Alexander V. Poshakinskiy, and Alexander N. Poddubny. Waveguide quantum electrodynamics: Collective radiance and photon-photon correlations. *Rev. Mod. Phys.*, 95:015002, Mar 2023. doi:10.1103/RevModPhys.95.015002. URL `https://link.aps.org/doi/10.1103/RevModPhys.95.015002`.

[180] Itay Shomroni, Serge Rosenblum, Yulia Lovsky, Orel Bechler, Gabriel Guendelman, and Barak Dayan. All-optical routing of single photons by a one-atom switch controlled by a single photon. *Science*, 345(6199):903–906, 2014. doi:10.1126/science.1254699. URL `https://www.science.org/doi/abs/10.1126/science.1254699`.

[181] Matti Silveri, Shumpei Masuda, Vasilii Sevriuk, Kuan Y. Tan, Máté Jenei, Eric Hyyppä, Fabian Hassler, Matti Partanen, Jan Goetz, Russell E. Lake, Leif Grönberg, and Mikko Möttönen. Broadband Lamb shift in an engineered quantum system. *Nature Physics*, 15:533–537, Jun 2019. doi:10.1038/s41567-019-0449-0. URL `https://doi.org/10.1038/s41567-019-0449-0`.

[182] Ariadna Soro and Anton Frisk Kockum. Chiral quantum optics with giant atoms. *Phys. Rev. A*, 105:023712, Feb 2022. doi:10.1103/PhysRevA.105.023712. URL `https://link.aps.org/doi/10.1103/PhysRevA.105.023712`.

[183] Dimitrios L. Sounas and Andrea Alù. Non-reciprocal photonics based on time modulation. *Nature Photonics*, 11, Dec 2017. doi:10.1038/s41566-017-0051-x. URL `https://doi.org/10.1038/s41566-017-0051-x`.

[184] K Stannigel, P Rabl, and P Zoller. Driven-dissipative preparation of entangled states in cascaded quantum-optical networks. *New Journal of Physics*, 14(6):063014, jun 2012. doi:10.1088/1367-2630/14/6/063014. URL `https://dx.doi.org/10.1088/1367-2630/14/6/063014`.

[185] Horst L. Stormer, Daniel C. Tsui, and Arthur C. Gossard. The fractional quantum Hall effect. *Rev. Mod. Phys.*, 71:S298–S305, Mar 1999. doi:10.1103/RevModPhys.71.S298. URL `https://link.aps.org/doi/10.1103/RevModPhys.71.S298`.

[186] Aziza Suleymanzade. *Millimeter wave photons for hybrid quantum systems.* PhD thesis, University of Chicago, 2021. URL `http://simonlab.stanford.edu/theses/SuleymanzadeAziza_PhDThesis.pdf`.

[187] Neereja M. Sundaresan, Yanbing Liu, Darius Sadri, László J. Szőcs, Devin L. Underwood, Moein Malekakhlagh, Hakan E. Türeci, and Andrew A. Houck. Beyond strong coupling in a multimode cavity. *Phys. Rev. X*, 5:021035, Jun 2015. doi:10.1103/PhysRevX.5.021035. URL `https://link.aps.org/doi/10.1103/PhysRevX.5.021035`.

[188] M. Eric Tai, Alexander Lukin, Matthew Rispoli, Robert Schittko, Tim Menke, Dan Borgnia, Philipp M. Preiss, Fabian Grusdt, Adam M. Kaufman, and Markus Greiner. Microscopy of the interacting Harper–Hofstadter model in the two-body limit. *Nature*, 546:519–523, Jun 2017. doi:10.1038/nature22811. URL `https://doi.org/10.1038/nature22811`.

[189] David Tong. *The Quantum Hall Effect.* TIFR Infosys Lectures, 2016. URL `https://www.damtp.cam.ac.uk/user/tong/qhe.html`. Online lecture notes.

[190] David Tong. David Tong: Lectures on solid state physics, 2017. URL `http://www.damtp.cam.ac.uk/user/tong/solidstate.html`. Online lecture notes.

[191] C. H. Valahu, V. C. Olaya-Agudelo, R. J. MacDonell, T. Navickas, A. D. Rao, M. J. Millican, J. B. Pérez-Sánchez, J. Yuen-Zhou, M. J. Biercuk, C. Hempel, T. R. Tan, and I. Kassal. Direct observation of geometric-phase interference in dynamics around a conical intersection. *Nature Chemistry*, 15:1503–1508, 11 2023. doi:10.1038/s41557-023-01300-3. URL `https://doi.org/10.1038/s41557-023-01300-3`.

[192] Sergio O. Valenzuela, William D. Oliver, David M. Berns, Karl K. Berggren, Leonid S. Levitov, and Terry P. Orlando. Microwave-induced cooling of a superconducting qubit. *Science*, 314(5805):1589–1592, 2006. doi:10.1126/science.1134008. URL `https://www.science.org/doi/abs/10.1126/science.1134008`.

[193] Arjan F. van Loo, Arkady Fedorov, Kevin Lalumière, Barry C. Sanders, Alexandre Blais, and Andreas Wallraff. Photon-mediated interactions between distant artificial atoms. *Science*, 342(6165):1494–1496, 2013. doi:10.1126/science.1244324. URL `https://www.science.org/doi/abs/10.1126/science.1244324`.

[194] C. Vega, D. Porras, and A. González-Tudela. Topological multimode waveguide QED. *Phys. Rev. Res.*, 5:023031, Apr 2023. doi:10.1103/PhysRevResearch.5.023031. URL `https://link.aps.org/doi/10.1103/PhysRevResearch.5.023031`.

[195] Karl Gerd H. Vollbrecht, Christine A. Muschik, and J. Ignacio Cirac. Entanglement distillation by dissipation and continuous quantum repeaters. *Phys. Rev. Lett.*, 107: 120502, Sep 2011. doi:10.1103/PhysRevLett.107.120502. URL `https://link.aps.org/doi/10.1103/PhysRevLett.107.120502`.

[196] Klaus von Klitzing. The quantized Hall effect. *Rev. Mod. Phys.*, 58:519–531, Jul 1986. doi:10.1103/RevModPhys.58.519. URL `https://link.aps.org/doi/10.1103/RevModPhys.58.519`.

[197] Andrei Vrajitoarea, Ron Belyansky, Rex Lundgren, Seth Whitsitt, Alexey V. Gorshkov, and Andrew A. Houck. Ultrastrong light-matter interaction in a photonic crystal. *arXiv:2209.14972*, Sep 2022.

[198] Christopher S. Wang, Nicholas E. Frattini, Benjamin J. Chapman, Shruti Puri, S. M. Girvin, Michel H. Devoret, and Robert J. Schoelkopf. Observation of wave-packet

branching through an engineered conical intersection. *Phys. Rev. X*, 13:011008, Jan 2023. doi:10.1103/PhysRevX.13.011008. URL `https://link.aps.org/doi/10.1103/PhysRevX.13.011008`.

[199] Christopher Shen Wang. *Bosonic quantum simulation in circuit quantum electrodynamics*. PhD thesis, Yale University, 2022. URL `https://elischolar.library.yale.edu/gsas_dissertations/674`.

[200] Michelle Wang, Cooper Doyle, Bryn Bell, Matthew J. Collins, Eric Magi, Benjamin J. Eggleton, Mordechai Segev, and Andrea Blanco-Redondo. Topologically protected entangled photonic states. *Nanophotonics*, 8(8):1327–1335, 2019. doi:doi:10.1515/nanoph-2019-0058. URL `https://doi.org/10.1515/nanoph-2019-0058`.

[201] Xin Wang, Ya-Fen Lin, Jia-Qi Li, Wen-Xiao Liu, and Hong-Rong Li. Chiral SQUID-metamaterial waveguide for circuit-QED. *New Journal of Physics*, 24(12):123010, dec 2022. doi:10.1088/1367-2630/aca87e. URL `https://dx.doi.org/10.1088/1367-2630/aca87e`.

[202] Yu-Xin Wang, Chen Wang, and Aashish A. Clerk. Quantum nonreciprocal interactions via dissipative gauge symmetry. *PRX Quantum*, 4:010306, Jan 2023. doi:10.1103/PRXQuantum.4.010306. URL `https://link.aps.org/doi/10.1103/PRXQuantum.4.010306`.

[203] Zheng Wang, Yidong Chong, J. D. Joannopoulos, and Marin Soljačić. Observation of unidirectional backscattering-immune topological electromagnetic states. *Nature*, 461: 772–775, Oct 2009. doi:10.1038/nature08293. URL `https://www-nature-com.proxy.uchicago.edu/articles/nature08293`.

[204] Clara C. Wanjura, Matteo Brunelli, and Andreas Nunnenkamp. Topological framework for directional amplification in driven-dissipative cavity arrays. *Nature Communications*, 11, Jun 2020. doi:10.1038/s41467-020-16863-9. URL `https://doi.org/10.1038/s41467-020-16863-9`.

[205] Gregory H. Wannier. Dynamics of band electrons in electric and magnetic fields. *Rev. Mod. Phys.*, 34:645–655, Oct 1962. doi:10.1103/RevModPhys.34.645. URL `https://link.aps.org/doi/10.1103/RevModPhys.34.645`.

[206] Eric W. Weisstein. Fourier Transform – Gaussian, Retrieved 2023. URL `https://mathworld.wolfram.com/FourierTransformGaussian.html`.

[207] Weixuan Xu, Baylor Fox-Kemper, Jung-Eun Lee, J. B. Marston, and Ziyan Zhu. Topological signature of stratospheric Poincare – gravity waves. *arXiv:2306.12191*, 2023.

[208] Yariv Yanay and Aashish A. Clerk. Reservoir engineering of bosonic lattices using chiral symmetry and localized dissipation. *Phys. Rev. A*, 98:043615, Oct 2018. doi:10.1103/PhysRevA.98.043615. URL `https://link.aps.org/doi/10.1103/PhysRevA.98.043615`.

[209] N.Y. Yao, C.R. Laumann, A.V. Gorshkov, H. Weimer, L. Jiang, J.I. Cirac, P. Zoller, and M.D. Lukin. Topologically protected quantum state transfer in a chiral spin liquid. *Nature Communications*, 4, Mar 2013. doi:10.1038/ncomms2531. URL `https://doi.org/10.1038/ncomms2531`.

[210] S. Zeytinoğlu, M. Pechal, S. Berger, A. A. Abdumalikov, A. Wallraff, and S. Filipp. Microwave-induced amplitude- and phase-tunable qubit-resonator coupling in circuit quantum electrodynamics. *Phys. Rev. A*, 91:043846, Apr 2015. doi:10.1103/PhysRevA.91.043846. URL `https://link.aps.org/doi/10.1103/PhysRevA.91.043846`.

[211] Xueyue Zhang. *Superconducting circuit architectures based on waveguide quantum electrodynamics*. PhD thesis, California Institute of Technology, 2023. URL `https://resolver.caltech.edu/CaltechTHESIS:03112023-174134421`.

[212] Xueyue Zhang, Eunjong Kim, Daniel K. Mark, Soonwon Choi, and Oskar Painter. A superconducting quantum simulator based on a photonic-bandgap metamaterial. *Science*, 379(6629):278–283, 2023. doi:10.1126/science.ade7651. URL `https://www.science.org/doi/abs/10.1126/science.ade7651`.

[213] Han Zhao, Xingdu Qiao, Tianwei Wu, Bikashkali Midya, Stefano Longhi, and Liang Feng. Non-Hermitian topological light steering. *Science*, 365(6458):1163–1166, 2019. doi:10.1126/science.aay1064. URL `https://www.science.org/doi/abs/10.1126/science.aay1064`.

[214] Youpeng Zhong, Hung-Shen Chang, Audrey Bienfait, Étienne Dumur, Ming-Han Chou, Christopher R. Conner, Joel Grebel, Rhys G. Povey, Haoxiong Yan, David I. Schuster, and Andrew N. Cleland. Deterministic multi-qubit entanglement in a quantum network. *Nature*, 590, Feb 2021. doi:10.1038/s41586-021-03288-7. URL `https://doi.org/10.1038/s41586-021-03288-7`.

[215] Oded Zilberberg, Sheng Huang, Jonathan Guglielmon, Mohan Wang, Kevin P. Chen, Yaacov E. Kraus, and Mikael C. Rechtsman. Photonic topological boundary pumping as a probe of 4D quantum Hall physics. *Nature*, 553:59–62, Jan 2018. doi:10.1038/nature25011. URL `https://doi.org/10.1038/nature25011`.

# APPENDIX A

# REMINDER SHEET FOR FREQUENCY-TIME CONVERSION

The subbasement of the Schuster lab at the University of Chicago had a piece of paper taped to the wall which reminded readers of where the factor of $2\pi$ went in the conversion between widths $\sigma$ of Gaussian pulse shapes in frequency and time. It became tiresome to rederive every time I was on a different floor and forgot, so I provide a reminder here:

$$\boxed{\sigma_f \sigma_t = \frac{1}{2\pi}} \tag{A.1}$$

We retrieve this from the Fourier transform of a generic Gaussian function in some dimension $x$ which Fourier transforms to $k$ [206]:

$$f(x) = e^{-ax^2} \quad FT \longrightarrow \quad F(k) = \int_{-\infty}^{\infty} e^{-ax^2} e^{-i2\pi kx} dx = \sqrt{\frac{\pi}{a}} e^{\frac{-\pi^2 k^2}{a}} \tag{A.2}$$

We can express a Gaussian function of time of unit height centered at zero as:

$$f(t) = e^{-\frac{1}{2}\frac{x^2}{\sigma_t^2}} \quad FT \longrightarrow \quad F(f) \propto e^{-\pi^2 f^2 2\sigma_t^2} = e^{-\frac{1}{2} f^2 (4\pi^2 \sigma_t^2)} = e^{-\frac{1}{2}\frac{f^2}{\sigma_f^2}} \tag{A.3}$$

We note that $\omega = 2\pi f$ and arrange the contents of the exponent on the right side of Equation A.3 to yield a $\sigma_f$. We expect that we should be able to express our result Gaussian in the same form as we started with, given that all we're specifying is a coordinate and a $\sigma$ in the exponent. Therefore,

$$\sigma_f^2 = \frac{1}{4\pi^2 \sigma_t^2} \quad \longrightarrow \quad \sigma_f \sigma_t = \frac{1}{2\pi} \tag{A.4}$$

# APPENDIX B

# CODE TO SIMULATE THE HARPER-HOFSTADTER LATTICE

## B.1 5 × 5 lattice, without backwards modes

Here we realize, in Mathematica, a 5 × 5 quarter-flux Harper-Hofstadter lattice. We keep the phase windings local to the chiral sites, modifying specifically the hoppings onto and off of the four lattice sites which host a YIG sphere.

```
(* Input specific Hamiltonian parameters! *)
J = 19.3*2 \[Pi]*10^6; (* Approximate hopping rate t *)
\[Phi] = 1/4*2 \[Pi];  (* Quarter-flux *)
\[Kappa] = 0;          (* No decay here *)
\[Omega]0 = 9.03699*2 \[Pi]*10^9;  (* Pick a lattice band center *)


(* List of coordinates of lattice sites *)
Size = 5;
siteindices = Flatten[Table[{ii, jj}, {ii, 1, Size}, {jj, 1, Size}], 1];
yigsiteindices = {{2, 2}, {2, 4}, {4, 2}, {4, 4}};
nInd = Length[siteindices];


(* Converts two-element lattice coordinate to single numerical index *)
getsiteindex[ii_, jj_] :=
  If[Length[#] > 0, #[[1, 1]], 0] &[Position[siteindices, {ii, jj}]];


(* Add diagonal elements to 25x25 Hamiltonian*)
HmatAnewgauge2 = Table[0, {nInd}, {nInd}];
For[ii = 1, ii <= Size, ii++,
```

```
 For[jj = 1, jj <= Size, jj++,
  curind = getsiteindex[ii, jj];
  HmatAnewgauge2[[curind, curind]] += \[Omega]0;]]

(* Add all site-site coupling amplitudes for 25x25*)
(* Horizontal hopping in odd-i rows, even-i rows *)
For[jj = 1, jj <= Size - 1,
 jj++,
 For[ii = 1, ii <= (Size + 1)/2, ii++,
  HmatAnewgauge2[[getsiteindex[2 ii - 1, jj],
    getsiteindex[2 ii - 1, jj + 1]]] += -J ;
  HmatAnewgauge2[[getsiteindex[2 ii - 1, jj + 1],
    getsiteindex[2 ii - 1, jj]]] += -J;
  ];
 For[ii = 1, ii <= (Size - 1)/2, ii++,
  HmatAnewgauge2[[getsiteindex[2 ii, jj],
    getsiteindex[2 ii, jj + 1]]] += -J ;
  HmatAnewgauge2[[getsiteindex[2 ii, jj + 1],
    getsiteindex[2 ii, jj]]] += -J;
  ]
 ]

(* Vertical hopping *)
For[jj = 1, jj <= (Size + 1)/2, jj++,
 For[ii = 1, ii <= Size - 1, ii++,
  HmatAnewgauge2[[getsiteindex[ii, 2 jj - 1],
```

```
    getsiteindex[ii + 1, 2 jj - 1]]] += -J;
  HmatAnewgauge2[[getsiteindex[ii + 1, 2 jj - 1],
    getsiteindex[ii, 2 jj - 1]]] += -J;
  ]
 ]

(* Vertical hopping  *)
For[jj = 1, jj <= (Size - 1)/2, jj++,
  For[ii = 1, ii <= (Size - 1)/2, ii++,
   HmatAnewgauge2[[getsiteindex[2 ii - 1, 2 jj],
     getsiteindex[2 ii, 2 jj]]] += -J;
   HmatAnewgauge2[[getsiteindex[2 ii, 2 jj],
     getsiteindex[2 ii - 1, 2 jj]]] += -J;
   ];
  For[ii = 1, ii <= (Size - 1)/2, ii++,
   HmatAnewgauge2[[getsiteindex[2 ii, 2 jj],
     getsiteindex[2 ii + 1, 2 jj]]] += -J;
   HmatAnewgauge2[[getsiteindex[2 ii + 1, 2 jj],
     getsiteindex[2 ii, 2 jj]]] += -J;
   ]
  ];

(* Multiply on complex phase from hoppings to/from YIG sites *)
For[mm = 1, mm <= Length[yigsiteindices], mm++,
 ii = yigsiteindices[[mm]][[1]];
 jj = yigsiteindices[[mm]][[2]];
```

```
(* Up tunneling, and conjugate*)
HmatAnewgauge2[[getsiteindex[ii, jj], getsiteindex[ii + 1, jj]]] *=
 Exp[I*2*\[Phi]];
HmatAnewgauge2[[getsiteindex[ii + 1, jj], getsiteindex[ii, jj]]] *=
 Exp[-I*2*\[Phi]];

(* Down tunneling, and conjugate*)
HmatAnewgauge2[[getsiteindex[ii, jj], getsiteindex[ii - 1, jj]]] *=
 Exp[I*0*\[Phi]];
HmatAnewgauge2[[getsiteindex[ii - 1, jj], getsiteindex[ii, jj]]] *=
 Exp[-I*0*\[Phi]];

(* Vertical tunneling top, boring and just for thoroughness*)
HmatAnewgauge2[[getsiteindex[ii, jj], getsiteindex[ii, jj + 1]]] *=
 Exp[I*\[Phi]];
HmatAnewgauge2[[getsiteindex[ii, jj + 1], getsiteindex[ii, jj]]] *=
 Exp[-I*\[Phi]];

(* Vertical tunneling bottom, conjugate also for thoroughness  *)
HmatAnewgauge2[[getsiteindex[ii, jj], getsiteindex[ii, jj - 1]]] *=
 Exp[I*3*\[Phi]] ;
HmatAnewgauge2[[getsiteindex[ii, jj - 1], getsiteindex[ii, jj]]] *=
 Exp[-I*3*\[Phi]];
]
```

```
eigenvalsAnewgauge2 = Reverse[Eigenvalues[HmatAnewgauge2]]
eigenvecsAnewgauge2 = Reverse[Eigenvectors[HmatAnewgauge2]];
```

## B.2 Numerical dynamics of wavepacket in perfect lattice

Here we can select a drive frequency $\omega_D$ and a one-sigma width, $\tau$, of a Gaussian drive pulse in time in order to prepare circulating wavepackets in the lattice. We include code for the high-frequency wavepacket, but one only needs to change $\omega_D$ to model the low-frequency wavepacket. If we change the variable $nInd$ to 29, we can also use this code to simulate dynamics in the modified lattice detailed in the following section.

```
nInd = 25;
MakeVariableList[preF_, sufF_, NN_] :=
Table[ToExpression[preF <> ToString[j] <> sufF], {j, NN}];
\[Psi]s = MakeVariableList["\[Psi]", "[t]", nInd];
d\[Psi]s = MakeVariableList["\[Psi]", "'[t]", nInd];

(* Initial condition is just... nothing *)
\[Psi]init = ConstantArray[0, nInd];
ICs = Thread[(\[Psi]s /. t -> 0) == \[Psi]init];

(* Drive on site 1, which should be {1,1}*)
\[Psi]drive = ConstantArray[0, nInd];
\[Psi]drive[[1]] = 1;
Print["\[Psi]drive=" <> ToString[\[Psi]drive]]
```

```
tmax = 1000/(10^9)


(* Drive freqs are 9.004, 9.064 GHz in lower and upper gap*)
\[Omega]D = -\[Omega]0 - 1.4 J ;
(* Time-sigma and center frequency of the drive envelope *)
\[Tau] = 2.42531/J;


drivefn = Exp[-((t - 3 \[Tau])^2)/(2 \[Tau]^2)];


EOMs = Thread[
   I d\[Psi]s == (HmatAnewgauge2 . \[Psi]s +
    10^10. \[Psi]drive *Exp[I \[Omega]D*t]*drivefn)];
EQNs = Join[EOMs, ICs];


(* Solve! *)
solns = NDSolve[EQNs, \[Psi]s, {t, 0, tmax}][[1]];
edgeindices2 = {1, 6, 11, 16, 21, 22, 23, 24, 25, 20, 15, 10, 5, 4, 3, 2};


\[Psi]sedge1 =
  Table[(Abs[\[Psi]s[[edgeindices2[[iii]]]] /. solns]^2), {iii , 1,
    Length[edgeindices2]}];


timetable1 =
  Table[((\[Psi]sedge1) /. t -> tt), {tt, 0, tmax, tmax/100}];
runaroundhi =
 Graphics[Raster[timetable1/Max[Max[timetable1]]], Frame -> True,
```

```
 Background -> White, AspectRatio -> 3/2,
 FrameStyle -> Thickness[0.0065],
 FrameTicks -> {{{{0, "0"}, {40, "400"}, {80, "800"} }, None}, {None,
     None}},
 FrameLabel -> {"Edge Site Index", "Time (ns)"},
 LabelStyle -> {Black, FontSize -> 22, FontFamily -> "Arial"}]
```

## B.3 Incorporating backwards chiral modes

To include coupling through more-detuned YIG site modes of opposite chirality, we increase the size of our Hamiltonian matrix to 29 × 29, and include an auxiliary set of 4 YIG sites that share the same coupling structure and rate to neighboring sites as the first 4, but are detuned in frequency.

```
AddExtraSites[\[Delta]_, \[Kappa]2_, HMat_] :=
 Module[{cs, blanktable,  biggerHmat, couplingsHmat},
  cs = J;
  blanktable = Table[0, 4, {nInd + 4}];
  For[ii = nInd + 1, ii <= nInd + 4, ii++,
   blanktable[[ii - nInd, ii]] += \[Omega]0 + \[Delta] +
     I \[Kappa]2/2];


  (* Add four columns of zeros to the right side of Hmat, verbosely *)
  biggerHmat =
   Transpose[Insert[Transpose[HMat], ConstantArray[0, 25], nInd + 1]];
  biggerHmat =
   Transpose[Insert[Transpose[biggerHmat], ConstantArray[0, 25], nInd + 1]];
  biggerHmat =
```

```
 Transpose[Insert[Transpose[biggerHmat], ConstantArray[0, 25], nInd + 1]];
biggerHmat =
 Transpose[Insert[Transpose[biggerHmat], ConstantArray[0, 25], nInd + 1]];

(* Now stick four fows of zeros on the bottom with the onsite
energies included on the global matrix diagonal*)

For[ii = 1, ii <= 4, ii++,
 biggerHmat = AppendTo[biggerHmat, blanktable[[ii]]]];

(* Instantiate couplingsHmat before you start actually putting the
couplings into it *)
couplingsHmat = biggerHmat;

For[mm = 1, mm <= 4, mm++,
 ii = yigsiteindices[[mm]][[1]];
 jj = yigsiteindices[[mm]][[2]];

 (* Up tunneling, and conjugate*)
 couplingsHmat[[25 + mm, getsiteindex[ii + 1, jj]]] += -J*
   Exp[I*2*\[Phi]];
 couplingsHmat[[getsiteindex[ii + 1, jj], 25 + mm]] += -J*
   Exp[-I*2*\[Phi]];

 (* Down tunneling, and conjugate*)
 couplingsHmat[[25 + mm, getsiteindex[ii - 1, jj]]] += -J*
```

```
    Exp[I*0*\[Phi]];
  couplingsHmat[[getsiteindex[ii - 1, jj], 25 + mm]] += -J*
    Exp[-I*0*\[Phi]];

  (* Vertical tunneling top, boring and just for thoroughness*)
  couplingsHmat[[25 + mm, getsiteindex[ii, jj + 1]]] += -J*
    Exp[I*3*\[Phi]];
  couplingsHmat[[getsiteindex[ii, jj + 1], 25 + mm]] += -J*
    Exp[-I*3*\[Phi]];

  (* Vertical tunneling bottom, conjugate also for thoroughness  *)
  couplingsHmat[[25 + mm, getsiteindex[ii, jj - 1]]] += -J*
    Exp[I*\[Phi]] ;
  couplingsHmat[[getsiteindex[ii, jj - 1], 25 + mm]] += -J*
    Exp[-I*\[Phi]];
  ];

 couplingsHmat]

(* Put backwards sites in 200 MHz detuned *)
bothHmatAnewgauge2 = AddExtraSites[200*2*Pi*10^6, 0, HmatAnewgauge2];

eigenvalsBothAnewgauge2 = Reverse[Eigenvalues[bothHmatAnewgauge2]]
eigenvecsBothAnewgauge2 = Reverse[Eigenvectors[bothHmatAnewgauge2]];
```

# APPENDIX C

# CODE TO SIMULATE MULTILEVEL SWAPS IN QUTIP

We found that due to the rapid $|f\rangle$ state decay of qubit Bob in particular, more rapid than would be expected from treating transmon levels basically like harmonic oscillator levels, we needed to simulate the $|f, 0\rangle \leftrightarrow |g, 1\rangle$ swapping between qubit and lattice mode in a way that accounted for the idiosyncratic decay rate of each transmon level. We wrote our own operators for each level transition, inspired by the treatment of operators here: `https://gist.github.com/AhmedSalaha/04eef0060068cd484fff2da06d2995de`.

```
# Bringing in t, Plist1 from data (t_evol, state_cor) taken in experiment
t = np.asarray(t_evol)
Plist1 = np.asarray(np.round(state_cor, 5))


# Parameters (MHz)
omega_c1 = (8921.3) * 2 * pi   # chiral mode 1
omega_q = 7764.2 * 2*pi        # frequency of chosen qubit
U = -351.4 * 2*pi              # anharmonicity of chosen qubit


kappa1 = 1/5.3 * 2 * pi     # cavity dissipation rate
                            # 1 is 1/kappa, the radial decay
gammaf = (1/1.4)            # qubit f dissipation rate
                            # The 2 is implied in the measurement
gammae = (1/4.9)            # qubit e dissipation rate


g1  = 0.708 * 2 * pi        # effective sideband coupling strength


omega_d = 2*omega_q + U  - omega_c1 # sideband drive with mode 1
```

```
# Cavity field operators

N = 3                                       # number of cav. Fock states

a = tensor(destroy(N), qeye(3))             # composite operator

vacuum = tensor(basis(N,0), basis(3,0))     # cavity and qubit vacuum


# Qubit operators

sm = tensor(qeye(N), destroy(3))                    # sigma minus on qubit

# Outer products

s00 = tensor(qeye(N), basis(3,0)*basis(3,0).dag())  # |0><0| in qubit

s01 = tensor(qeye(N), basis(3,0)*basis(3,1).dag())  # |0><1|

s12 = tensor(qeye(N), basis(3,1)*basis(3,2).dag())  # |1><2|

s11 = tensor(qeye(N), basis(3,1)*basis(3,1).dag())  # |1><1|

s22 = tensor(qeye(N), basis(3,2)*basis(3,2).dag())  # |2><2|


# Hamiltonian

# I'm not using ladder operators, but the bosonic-ladder factors of

# sqrt(2) get taken care of by measured T1.


# Rotating with drive

# wg |0><0| + we |1><1| + wf |2><2|

# Schrieffer-Wolff; see Lev Bishop thesis transformation to rotating frame,

# takes factor of state number on wd

HQ0 = (0 - 0*omega_d) * s00 + (omega_q - omega_d) * s11

+ (2*omega_q + U - 2*omega_d) * s22

HC0 = (omega_c1 - omega_d) * a.dag() * a
```

```
# g_eff a |2><1|1><0| + h.c.

Hswap = g1*a*s12.dag()*s01.dag() + g1*(a*s12.dag()*s01.dag()).dag()


# Do we still want to include the Kerr nonlinearity? I think we already

# include with the anharm terms, so no

# 0.5 U |2><1|1><0| |0><1|1><2| ???

HKerr = 0.5*U*(s12.dag() * s01.dag())*(s12.dag() * s01.dag()).dag()


H = HQ0 + HC0 + Hswap #+ HKerr


# Collapse operators

c_ops_list = [];

c_ops_list.append(np.sqrt(kappa1) * a)    # Cavity decay

c_ops_list.append(np.sqrt(gammaf) * s12)  # Decay |e><f|

c_ops_list.append(np.sqrt(gammae) * s01)  # Decay |g><e|


# Observables

Ncav1 = a.dag() * a

Nq = sm.dag() * sm

Pg = vacuum*vacuum.dag()

Pe = s01.dag() * vacuum * (s01.dag() * vacuum).dag()

Pf = (s12.dag()*s01.dag()*vacuum * (s12.dag()*s01.dag()*vacuum).dag())


exp_list = [Pg, Pe, Pf, Nq, Ncav1]
```

```
# ME dynamics: single drive freq

tlist = np.linspace(0, 1.8, 1001)

psi0 = s12.dag() * s01.dag() * vacuum # start in the f-state


output = mesolve(H, psi0, tlist, c_ops_list, exp_list, options=opts,

progress_bar=True)


pg = output.expect[0]

pe = output.expect[1]

pf = output.expect[2]

nq = output.expect[3]

n1 = output.expect[4]


# In plotting, use calibration data to assess how much of P(e) overlaps P(f)

# Adjust plotted V accordingly. As an example,

V = (pf + 1.208*pe)
```

# APPENDIX D

# TRANSMON NANOFABRICATION RECIPE

## D.1 Steps to fabricate a niobium optical layer

Fabrication was performed on 430 $\mu$m thick, 2 inch sapphire wafers, annealed prior to use. Deposition of niobium occurred in the same Plassys angled electron-beam evaporator used later for junction deposition. Optical lithography was carried out in a Heidelberg maskless laser writer.

Table D.1

| **Process step: approximate time** | **Sequential details** |
|---|---|
| Wafer clean: 45 min | Toluene: Sonicate 2/2/2 min at increasing speeds<br>Acetone: Sonicate 2/2/2 min at increasing speeds<br>Methanol: Sonicate 2/2/2 min at incr. speeds<br>IPA: Sonicate 2/2/2 min at increasing speeds<br>Spin dry<br>Inspect in microscope |
| Deposit Nb: 5 + 1 hours | Place wafer in Plassys load-lock chamber<br>Bake @ 200 C for 1 hour, gate valve closed<br>Open gate valve when load-lock cools<br>Pump down load-lock with deposition chamber<br>Total > 4 hrs bake and pumpdown<br>Deposit 75 nm Nb with wafer rotation |
| Spin photoresist: 10 min | AZ703, 3500 RPM, 1000 RPM/sec ramp, 45 sec |
| Soft bake: 1 min | Place on 95 C hot plate for 1 min |
| Prep Fl etch: 30 min (concurrent) | Start 2-step O2 clean in ICP etch machine |

| Continuation of Table D.1 | |
|---|---|
| | Precondition chamber with etch recipe, 1 min |
| Expose in Heidelberg: 10 min | Expose optical layer pattern<br>375 nm laser, dose 140 |
| Hard bake: 2 min | 95 C, 1:15 min |
| Develop: 5 min | AZ MIF 300, 1 min<br>DI quench, 10 sec<br>DI rinse, 2 min<br>Spin dry<br>Inspect in microscope to check develop |
| Fluorine etch: 30 min | Get new carrier wafer<br>Mount wafer on carrier with Fomblin oil<br>Run etch recipe, 3 min<br>Remove wafer from carrier and A+I clean carrier<br>Inspect etch in microscope |
| Strip photoresist: 1+ hour | Skip descum because omitting BHF here<br>Place in NMP<br>Warm with 80 C hot plate for > 40 mins |
| Clean wafer: 25 min | Sonicate in NMP in hot bath 5/5/5 min<br>Acetone: Sonicate 2/2, marinate 2 min<br>IPA: Sonicate 2/2, marinate 2 min<br>Vent vacuum bake oven<br>DI water rinse 2 min<br>Spin dry<br>Look in microscope; you're stuck with results! |

## D.2 Steps to fabricate Manhattan-style Al/$Al_2O_3$/Al junctions

Lithography was performed in a 100 kV Raith electron beam lithography system. Evaporation of junctions was performed in a Plassys angled electron-beam evaporator. An Angstrom Nexdep thermal evaporator was used to lay down a gold conduction layer prior to electron beam lithography, as the sapphire substrate used is not very conductive.

Table D.2

| **Process step: approximate time** | **Sequential details** |
|---|---|
| Vacuum bake: 15 min | Bake in vacuum oven used for HMDS prime<br>Include $N_2$ vent at end of recipe<br>Cool on bench in quartz holder 1-2 min |
| Clean spinner chuck: 5 min (concurrent) | Do this **every time**<br>Remove plastic o-ring using tweezers<br>Spray and scrub chuck with acetone<br>Spray and scrub chuck with IPA<br>Blow dry<br>Re-mount o-ring |
| Spin e-beam resist: 25 min | Check or write your own spin recipe **(see notes)**<br>Rest resist bottles from cabinet near the spinner<br>Prepare 2 pipettes prior to proceeding<br>Cover 2/3 wafer in MMA EL11<br>Spin @ 4000 RPM, 500 RPM/sec, 45 sec<br>Bake @ 180C for 5 min<br>Cool on cleaned bench for $>$ 20 sec<br>Cover 2/3 wafer in PMMA 950 A7<br>Spin 4000 RPM, 500 RPM/sec, 45 sec |

Continuation of Table D.2

| | |
|---|---|
| | Bake @ 180C for 5 min |
| Prep thermal evaporator: 5 min (concurrent) | Vent thermal evaporator during a bake<br>Load gold in evaporator during next bake |
| Evaporate conductive layer: 45 min | Depost 10 nm gold at 10 rpm<br>For smaller tungsten boat, try 0.5 Å per second |
| Electron beam lithography: 1.5 hrs | Wait to start prepping developer<br>Convert dxfs to gpfs using Beamer<br>Check dose multiplier and proximity effect file<br>Load and clamp wafer into its e-beam cassette<br>Do height check, $\theta$ correction of wafer<br>Write down marker coords. rel. Faraday cup<br>Double check that all clamps are screwed down<br>Load cassette into 100 kV Raith e-beam writer<br>Pump down<br>Marker alignment using relative coords.<br>Expose, dose 125-145×10, 3 nA beam |
| Prep e-beam developer: 5 min (concurrent) | Begin cooling during e-beam write<br>3:1 IPA:DI water in foil-covered beaker<br>Chill on hot plate set to 6 C<br>Maintain 45 mins from this to developing |
| Remove sample: 15 min | Vent Raith<br>Remove sample from e-beam cassette<br>Make sure that all clamps are screwed down<br>Inspect exposure sites in microscope<br>If bad, strip resist with NMP and go again |

| Continuation of Table D.2 | |
|---|---|
| Gold etch: 30 min | Gold etch 45 sec, a bit overkill given etch rates<br>DI water quench 10 sec<br>DI water rinse 2 min<br>Blow dry |
| Develop e-beam resist: 10 min | Place in chilled developer, 1.5 min, no agitation<br>100% IPA quench, 10 sec, **do not** spray water<br>Blow dry with alacrity<br>Inspect results of develop in microscope<br>Move quickly to load into Plassys |
| Deposit junctions: $>$ 7 hours | Align wafer on carrier **(see notes)**<br>Pump down to chamber pressure $\leq$ mid e-7 mbar<br>Ensure pumpdown $\geq$ 3.5 hrs<br>Highest usable pressure $\leq$ high e-7 mbar |
| Junction deposition: 2 + 1 hours | Ar + dynamic $O_2$ plasma etch<br>Etch turns off Penning gauge; restart script here<br>Ti evaporation, 4 min @ 0.2 nm/s to clean $O_2$<br>Triple angle ion mill with Ar<br>Ti evaporation, 4 min @ 0.2 nm/s<br>Al evap., 45° tilt, 90° rotation, 45 nm @ 1 nm/s<br>Static oxidation: 50 mbar for 15 min<br>Pump down chamber for 13 min<br>Ti evaporation, 4 min @ 0.2 nm/s to clean $O_2$<br>Al evap., 45° tilt, $90 + 90°$ rot., 115 nm @ 1 nm/s<br>Static oxidation: 3 mbar for 5 min<br>Leave junctions under vacuum for 20 min - 1 hr |

| Continuation of Table D.2 | |
|---|---|
| Spin dicing resist: 10 min | AZ703, 3500 RPM for 45 sec<br>Bake @ 95 C for 1 min<br>Can keep wafer for later dicing here<br>If wait is longer than a day, spin more resist |
| Dice: 1 hour | Point ionizing fan (on) at mounting plate<br>Mount wafer on dicing tape and ring @ 40 C<br>Make sure the blade is really 8A for sapphire<br>Make sure dicing saw water flow is properly set<br>Keep light on low power to avoid exposing resist<br>Run dicing recipe<br>De-mount ring+tape from saw under ionizing fan<br>Blow sample dry under ionizing fan<br>120 sec UV exposure to weaken grip of tape<br>Take ring, tape, and chips to solvent bay |
| De-mount chips from ring: 15 min | Place dicing ring on fabric wipe in solvent hood<br>Pour PG remover into a beaker nearby<br>Gently scoop under each chip with tweezer<br>Hold tweezer open with thumb, use bottom half<br>Depress tape into fabric wipe vs. peeling chip off<br>Place each chip into PG remover, stagger edges |
| Liftoff: 1-3 hours | Cover PG remover beaker<br>Place on 80 C hot plate for 1-3 hours<br>Avoid heated bath as water + NMP eat junctions<br>Do not lift off overnight |
| Clean chips: 45 min | Sonicate 40 sec on low in PG remover, 80 C bath |

| Continuation of Table D.2 | |
|---|---|
| | Spray with IPA while moving to acetone beaker<br>Acetone: sonicate 40 sec on low in cold bath<br>Spray with IPA while moving to IPA beaker<br>IPA: sonicate 40 sec on low in cold bath<br>Spray with IPA + move to second IPA beaker<br>Blow dry each chip with $N_2$ 10 sec after removing |
| Store chips | Use prepared polyethylene carrier from MTI<br>Pre-clean carrier with IPA, blow dry<br>Wrap chip holder in aluminum foil<br>Wait 12-24 hours after liftoff before measuring |

**Notes for spinning e-beam resist:**

- Test spin recipe with bare wafer for evenness – mount the wafer on the chuck, turn the vacuum on, and run your pre-checked recipe. Readjust as necessary to make sure that the spin runs flat. The spin-up of the wafer should look smooth and even, not wobbly.

- Prior to picking up resist, use $N_2$ gun to spray out insides and outside of pipette, aiming towards handle and away from tip. You may also spray off the wafer top, from an angle, making sure not to hold the (dirty) $N_2$ gun above the wafer itself.

- When applying resist, do so at the center of the wafer, avoiding bubbles. Once you start dripping resist, keep it up in a steady stream. Cover 1/2 to 2/3 of the wafer radius.

- The second spin is liable to get some PMMA on the back of your wafer. This is alright as long as the flecks are not big and lumpy. If too large, these might introduce too much unevenness when you seek to mount your wafer flat in the e-beam cassette.

- If you are worried about PMMA on the wafer back, *before* baking you can use cleanroom q-tips saturated in acetone, and then IPA, to try to scrub the un-baked resist off of the wafer back. Do this carefully, as it may introduce more harm than good.

**Notes for performing wafer alignment in the Plassys:**

- Align wafer flat to grid on the mounting cassette, and arrange the cassette so that the wafer flat is perpendicular to the mounting arm's axis of rotation.
- To accomplish this, it may be necessary to manually rotate the cassette in the user interface to get the flat fully perpendicular to this arm. 'Home' the stage thereafter to get rid of this rotation offset.
- After executing 'home' command, return to 'load' position and check that wafer flat is in the right place with planetary angle set to zero. This whole process may require some iteration but balance good alignment against the need to get the sample pumped down while the recently-exposed sample is fairly clean.
- You have a bit of wiggle room on alignment, courtesy of undercuts, as long as angled evaporation still fills your junction arm channels.
- If for some reason your e-beam exposure went wrong, if the area targeted for junctions is still covered and unexposed, it's possible to use the MMA/PMMA baked resist stack to protect the optical layer for some time. I have kept wafers covered with resist and gold, but un-exposed, for up to a week in the cleanroom without seeing an issue exposing ∼150 nm features nicely.

After making these transmon qubits on sapphire chips, one can measure the resistances across the junctions at room temperature, using the Ambegaokar-Baratoff relation [174] to draw a connection between room-temperature junction resistance and junction critical current. One may then draw a further connection between critical current and the Josephson energy $E_J$ that, when other system parameters are fixed, sets the qubit's transition frequency $\omega_{ge}$ and contributes to anharmonicity $\alpha$. As the size of the superconducting gap, $\Delta$, in the Ambegaokar-Baratoff relation is a bit of an empirical parameter that relates to materials properties, it is wise to calibrate a conversion factor between room-temperature junction resistance and $\omega_{ge}$ by testing fabricated transmons in a cooldown.

## D.3 Speculations regarding static

Nanofabrication involves sweeping such a large parameter space of process alterations, and navigating such a wide range of possible factors contributing to process drift, that it can be difficult to feel as though one is systematically troubleshooting specific problems.

I experienced pronounced issues with Josephson junctions shorting during my time in the cleanroom; my process was subtly different from others, as I did not perform any acid cleaning of the wafers and also used transmon designs with capacitive pads smaller than any others being fabricated in the lab at the time. Whatever the reason, the Josephson junctions that I fabricated seemed particularly sensitive to shorting, likely due to shock from electrostatic discharge. I made a pair of interventions simultaneously, one or both of which dramatically decreased the fraction of junctions which arrived shorted when their resistances were tested at room temperature: I operated an ionizing fan while mounting and de-mounting wafer and chips from the sticky tape used for dicing and switched to storing finished chips in polyethylene wafer holders rather than in a sticky holder that, while made with conductive gel, might have become less conductive upon continued exposure to atmosphere.